

Semiconductor-Based All-Optical Switching for Optical Time-Division Multiplexed Networks

by

Bryan S. Robinson

S. B., Massachusetts Institute of Technology
(1998)

M. Eng., Massachusetts Institute of Technology
(1998)

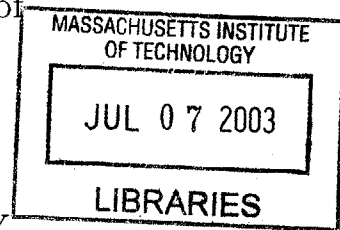
Submitted to the
Department of Electrical Engineering and Computer Science
in partial fulfillment of the requirements for the degree of

Doctor of Philosophy in Electrical Engineering

at the

MASSACHUSETTS INSTITUTE OF TECHNOLOGY

June 2003



© Massachusetts Institute of Technology 2003. All rights reserved.

Author

Department of Electrical Engineering and Computer Science

May 20, 2003

Certified by

Erich P. Ippen

Elihu Thomson Professor Of Electrical Engineering

Thesis Supervisor

Accepted by

Arthur C. Smith

Chairman, Department Committee on Graduate Students

ARCHIVES

Semiconductor-Based All-Optical Switching for Optical Time-Division Multiplexed Networks

by

Bryan S. Robinson

Submitted to the Department of Electrical Engineering and Computer Science
on May 22, 2003, in partial fulfillment of the
requirements for the degree of
Doctor of Philosophy in Electrical Engineering

Abstract

All-optical switching will likely be required for future optical networks operating at data rates which exceed electronic processing speeds. Switches utilizing nonlinearities in semiconductor optical amplifiers (SOA) are particularly attractive due to their compact size, low required switching energies, and high potential for integration. In this dissertation we investigate the practical application of such semiconductor-based all-optical switches in next-generation optical networks.

We present both theoretical and experimental studies of SOA-based interferometric switches. A detailed numerical model for the dynamic response of an SOA to an intensity-modulated optical signal is described. The model is validated using novel pump-probe techniques to measure the time-domain response of an SOA subject to various levels of saturation. The model is then used to evaluate the performance of three common SOA-based interferometric all-optical switches.

The use of SOAs in optical transmission systems has been limited due to the deleterious effects of pattern-dependent gain saturation. We develop a statistical model to study the system impact of variations of the SOA optical gain in response to a random intensity-modulated optical signal. We propose the use of pulse-position modulation (PPM) as a means for mitigating gain saturation effects in SOA-based optical processors. We present techniques for modulation and detection of optical PPM signals at data rates in excess of 100 Gbit/s. We demonstrate demultiplexing, wavelength conversion, and format conversion of optical PPM signals at data rates as high as 80 Gbit/s.

Finally, we report on experimental demonstrations of an optical interface for slotted OTDM networks. We implement head-end and transmitter nodes capable of producing fully loaded optical slots at an aggregate network data rate of 112.5 Gbit/s. We demonstrate a fully functional receiver node which utilizes semiconductor-based all-optical logic for synchronization, address processing, and rate conversion.

Thesis Supervisor: Erich P. Ippen

Title: Elihu Thomson Professor Of Electrical Engineering

Acknowledgments

The work described in this dissertation could not have been completed without the collective efforts of many individuals. First, I wish to acknowledge the great privilege that I have had in working with Professor Erich Ippen. His guidance in this work has been indispensable. I also wish to acknowledge Professor Rajeev Ram for serving on my thesis committee. While our meetings were brief, they were always fruitful.

I have thoroughly enjoyed working in collaboration with Dr. Scott Hamilton at Lincoln Laboratory. Aside from his innumerable contributions in the lab, Scott has been an excellent ambassador for our research efforts and he is largely responsible for the present success and continuation of the ultrafast optical processing research at Lincoln Laboratory. I am particularly grateful for his careful reading of this dissertation. I consider Scott a mentor, colleague, and friend of the highest caliber and I look forward to continuing our work together in the future.

Working at Lincoln Laboratory has been a wonderful experience. I thank Dr. Katie Hall for introducing me to the Laboratory. Her enthusiasm first inspired me to pursue research in this field. Her kind advice and encouragement through the years have kept me going. I am very grateful to Dr. Dan Moriarty for filling the void after Katie's departure and for teaching me a few important lessons on the risks of investing in start-up companies. Dr. John Moores was the source of many useful ideas in the development of the slotted OTDM network architecture described in this work. Jade Wang and Shelby Savage have made working in the lab a truly enjoyable experience. Jade is one of the coolest women that I know. Her consistently cheerful demeanor sets her apart from the typical MIT student. Shelby's mathematical expertise is unmatched, as is his ability to patiently listen to yet another one of my crazy ideas. He has offered many invaluable insights throughout this work. I thank Dr. Todd Ulmer, Dr. Tom Murphy, and Rich Younger for helping me maintain my sanity by providing many memorable hours of stimulating lunchroom conversation. Many others in the Optical Communications and Advanced Networks groups have contributed to this work. In particular, I wish to acknowledge Steve Bernstein, Dr. Dave Caplan, Dr.

Steve Chinn, Dr. Steve Constantine, Peg Danek, Chad Demers, Farhad Hakimi, Hosain Hakimi, Dr. Mark Kuznetsov, Doug Marquis, Naimish Patel, Dr. Jeff Roth, and Dr. Peter Schulz.

I am very grateful for the generous financial and material support that I have received from Lincoln Laboratory. While the organization at the Laboratory has changed much during my time there, their commitment to my research efforts has remained constant. I especially thank Dr. Bill Keicher for his continuing interest in my work and for giving me substantial freedom to pursue my research goals. I also gratefully acknowledge the financial support of the National Science Foundation and the IEEE Lasers and Electro-Optics Society.

Much credit is due to my family. My parents, Tom and Karen Lewis and Thom and Arnette Robinson, have been my inspiration. They have offered me nothing but love and unquestioning support in my pursuits. I thank my grandparents, Weldon and Lurline Robinson, for their constant prayers and encouragement. Their regular phone calls, e-mails, letters, articles, and care packages helped to bridge the distance between Boston and Dallas and made even the most difficult moments bearable. I also extend my deepest appreciation to the Ransoms, Jeff, Annette, Rachel and David, for welcoming me into their family and providing me with a home away from home for the last 9 years.

Most of all, I wish to acknowledge my wife, Sara. Any success that I can claim is a direct result of her tireless efforts behind the scenes. Sara is a model of God's grace and unconditional love, a wife of the noblest character. She is my source of joy in this world. My greatest hope is that I can serve her as well as she has served me.

Contents

1	Introduction	15
1.1	Optical Multiplexing Techniques	15
1.2	All-Optical Switching Requirements	18
1.3	Organization	19
	References	21
2	Semiconductor Optical Amplifiers	22
2.1	Introduction	22
2.2	Device Overview	23
2.3	Optical Gain in Semiconductors	25
2.4	Carrier-Induced Refractive Index	37
2.5	Carrier Dynamics in Semiconductors	40
2.6	Numerical Modeling	45
2.6.1	Calculation of Quasi-Fermi Energy and Carrier Temperature	50
2.6.2	Example Calculations	55
2.7	Difference-Frequency Sampling	58
2.8	Conclusions	65
	References	67
3	Semiconductor-Based All-Optical Switching	71
3.1	Introduction	71
3.2	Nonlinear Mach-Zehnder Interferometers	71
3.3	Semiconductor-Based Fiber Interferometers	74

3.3.1	Copropagating Ultrafast Nonlinear Interferometer	76
3.3.2	Counterpropagating Ultrafast Nonlinear Interferometer	81
3.3.3	Terahertz Optical Asymmetric Demultiplexer	84
3.4	Measurement of Switching Windows	89
3.5	Demultiplexing Performance Evaluation	95
3.6	Conclusions	98
	References	99
4	Gain Saturation in Semiconductor Optical Amplifiers	102
4.1	Introduction	102
4.2	Saturation Effects in OTDM Demultiplexing	104
4.3	Statistical Analysis of Gain Saturation	107
4.4	Reducing Pattern-Dependent Gain Saturation	117
4.4.1	Demonstration of All-Optical Wavelength Conversion at Trans- parency Point	119
4.4.2	Alternative Modulation Formats	122
4.5	Pulse-Position Modulation	123
4.5.1	PPM Waveform Generation	125
4.5.2	Demodulation and Detection of Optical PPM Signals	129
4.5.3	Spectral Efficiency	142
4.6	Demultiplexing of PPM Data	147
4.7	All-Optical Wavelength Conversion of OOK and PPM Data Formats	149
4.8	Conclusions	152
	References	153
5	Slotted OTDM Networking Demonstrations	159
5.1	Introduction	159
5.2	HLAN Architecture	161
5.3	Slotted OTDM System Implementation	165
5.4	Head-End	166
5.5	Transmitter	168

5.6	Receiver	173
5.6.1	Synchronization	173
5.6.2	Optical Address Processing	177
5.6.3	Rate Conversion	189
5.7	Conclusions	203
	References	205
6	Conclusion	210
6.1	Summary of Contributions	210
6.2	Optical Packet Switching	213
	References	219
A	Pulse Propagation in an Active Semiconductor Waveguide	221
	References	227
B	Chebyshev Approximation for the Reduced Fermi Energy	228
	References	229

List of Figures

1-1	Three optical multiplexing techniques: a) wavelength-division multiplexing, b) bit-interleaved time-division multiplexing, and c) slotted time-division multiplexing. Note that the shading in b) and c) is used to distinguish the different channels, not to indicate different transmission wavelengths.	16
2-1	A double-heterostructure semiconductor laser.	24
2-2	Absorption and emission processes in a semiconductor.	25
2-3	Direct bandgap semiconductor bandstructure.	26
2-4	Example gain curves calculated for a carrier density of $2 \cdot 10^{24} \text{ m}^{-3}$ and a lattice temperature of $T = 300 \text{ K}$. For the Lorentzian and hyperbolic secant lineshapes, a dephasing time of 100 fs is used. Table 2.1 lists the other parameters used in calculating these curves.	33
2-5	Calculated transparency wavelength as a function of the injected carrier density, N	35
2-6	Illustration of the dependence of semiconductor gain on carrier density and temperature. In a) the semiconductor gain is plotted for carrier densities of $N = 1.5, 1.75, 2, 2.25,$ and $2.5 \cdot 10^{24} \text{ m}^{-3}$ with carrier temperatures of $T_c = T_v = 300 \text{ K}$. In b), the gain is plotted for a carrier density of $N = 2 \cdot 10^{24} \text{ m}^{-3}$ and conduction band temperatures of $T_c = 300, 320, 340, 360, 380,$ and 400 K . The valence band carrier temperature is $T_v = 300 \text{ K}$	36
2-7	Illustration of the dependence of semiconductor refractive index on carrier density and temperature. The refractive index is calculated relative to a reference refractive index at a carrier density of $N = 2 \cdot 10^{24} \text{ m}^{-3}$ and a temperature of $T_c = T_v = 300 \text{ K}$. In a) the index is plotted for carrier densities of $N = 1.5, 1.75, 2, 2.25,$ and $2.5 \cdot 10^{24} \text{ m}^{-3}$ with carrier temperatures of $T_c = T_v = 300 \text{ K}$. In b), the index is plotted for a carrier density of $N = 2 \cdot 10^{24} \text{ m}^{-3}$ and conduction band temperatures of $T_c = 300, 320, 340, 360, 380,$ and 400 K . The valence band carrier temperature is $T_v = 300 \text{ K}$	39
2-8	Illustration of carrier dynamics in a semiconductor optical amplifier	40
2-9	Illustration of SOA with discretized longitudinal sections	46
2-10	Flow chart used for calculation of dynamic response of SOA.	47
2-11	The dimensionless parameter ν plotted as a function of the reduced Fermi energy, μ	52

2-12	Calculated SOA gain dynamics experienced by a 150 μ W continuous-wave probe a) copropagating and b) counterpropagating with respect to a 12.5-GHz repetition rate 2-ps pump pulse. The SOA current is 100 mA. The curves illustrate the gain dynamics in response to input pump pulse energies of 0.8, 1.6, 3.2, 8, 16, 32, 80, 160, 320, and 800 fJ.	57
2-13	Typical copropagating pump-probe experiment.	58
2-14	Experimental setup for characterization of gain transients in a semiconductor optical amplifier using difference-frequency sampling. MLFL: Mode-locked fiber laser; BPF: Optical bandpass filter; LPF: Electrical lowpass filter; DSO: Digital sampling oscilloscope	59
2-15	Frequency-domain illustration of difference-frequency sampling. The spectra of $\tilde{P}_{in}(f)$ and $\tilde{G}_{SOA}(f)$ are shown in a). These spectra are convolved to get the output spectrum, $\tilde{P}_{out}(f)$ shown in b). Note that the frequency axis scales differ in the two plots.	62
2-16	Cross-sectional diagram of an Alcatel 1901 SOA.	64
2-17	Experimental measurement of a) copropagating and b) counterpropagating gain dynamics in an Alcatel 1901 SOA with a bias current of 100 mA. The signal pulse energy is 0.8 fJ. Starting from the top, the curves represent the gain dynamics in response to a 12.5-GHz stream of 2-ps control pulses with energies of 0.8, 1.6, 3.2, 8, 16, 32, 80, 160, 320, and 800 fJ.	66
3-1	A nonlinear Mach-Zehnder interferometer.	72
3-2	A balanced Mach-Zehnder interferometer: a) schematic and b) principle of operation.	75
3-3	Schematic of a fiber implementation of the ultrafast nonlinear interferometer (UNI) in copropagating configuration. PMF: Polarization-maintaining fiber, SOA: Semiconductor optical amplifier, BPF: Optical bandpass filter.	77
3-4	Simulation of copropagating UNI operation. In a), the differential phase shift for the two signal pulse polarizations is shown for a temporal separation of $\tau = 5$ ps in the UNI. In b), the time-dependent transmission characteristics of the UNI are shown for signal pulse separations of $\tau = 2.5, 5, 10,$ and 16 ps.	80
3-5	Schematic of a fiber implementation of the UNI in a counterpropagating configuration.	81
3-6	Simulation of counterpropagating UNI operation. In a), the differential phase shift for the two signal pulse polarizations is shown for a temporal separation of $\tau = 5$ ps in the UNI. In b), the time-dependent transmission characteristics of the UNI are shown for signal pulse separations of $\tau = 2.5, 5, 10,$ and 16 ps.	83
3-7	Schematic of fiber implementation of the terahertz optical asymmetric demultiplexer (TOAD).	86

3-8	Simulation of TOAD operation. In a), the differential phase shift for the two signal pulses is shown for a loop asymmetry of $\tau = 5$ ps in the TOAD. In b), the time-dependent transmission characteristics of the TOAD are shown for loop asymmetries of $\tau = 2.5, 5, 10, 16$ ps. . . .	88
3-9	Two techniques for characterizing the switching window of an optical switch. In a), the switching window is measured via cross-correlation with the control pulse. In b), the switching window is measured via difference-frequency sampling.	90
3-10	Switching windows for a copropagating UNI with signal pulse offsets of a) 16 ps and b) 5 ps measured using difference-frequency sampling.	92
3-11	Switching windows for a counterpropagating UNI with signal pulse offsets of a) 16 ps and b) 5 ps measured using difference-frequency sampling.	93
3-12	Switching windows for TOAD with SOA asymmetries of a) 11 ps and b) 4 ps measured using difference-frequency sampling.	94
3-13	Experimental setup for 100-Gbit/s demultiplexing using the UNI and the TOAD.	96
3-14	Bit-error rate analysis of demultiplexed output of a) TOAD and b) UNI switches operating at aggregate data rates of 25-, 50-, and 100-Gbit/s.	97
4-1	Experimental setup for demultiplexing a 10-Gbit/s signal from a 40-Gbit/s data stream. MLFL: Mode-locked fiber laser, ODL: Optical delay line, OTDM MUX: Free-space optical time-division multiplexer, OOK: On-off-keyed modulator, PPG: Pulse-pattern generator, DSO: Digital sampling oscilloscope.	104
4-2	Waveforms at input and output of 40-Gbit/s-to-10-Gbit/s demultiplexer measured using a digital sampling oscilloscope.	105
4-3	Optical transmission system employing a semiconductor optical amplifier for in-line amplification.	108
4-4	Probability density for the sampled integrated gain in an SOA in response to a) a 10-Gbit/s random OOK-modulated data stream with a pulse energy of 100 fJ and b) a 100-Gbit/s random OOK-modulated data stream with a pulse energy of 10 fJ.	113
4-5	Calculated bit-error rate for 10-Gbit/s and 100-Gbit/s transmission systems including the effects of gain saturation in an in-line SOA. The pulse extinction ratio at the SOA input is infinite.	114
4-6	Calculated bit-error rate as a function of the receiver input power for 10 Gbit/s and 100 Gbit/s transmission systems with finite extinction ratios of 30 dB and 20 dB at the transmitter.	116
4-7	Experimental setup for all-optical wavelength conversion using an ultrafast nonlinear interferometer.	120
4-8	Wavelength conversion of a 10-Gbit/s signal using a semiconductor optical amplifier biased at the transparency point.	121

4-9	Two configurations for producing optical binary PPM waveforms using an electro-optic modulator. In a), the PPM delay is introduced prior to modulation. In b), the PPM delay is introduced after modulation.	126
4-10	Experimental autocorrelation of a 10-Gbit/s pseudo-random binary PPM sequence using 2-ps optical pulses. The PPM delay is 6.25 ps, allowing OTDM multiplexing to rates as high as 80 Gbit/s.	128
4-11	An optical M -ary PPM waveform modulator ($M = 2^k$) constructed using k 2x2 switches and a logarithmic series of delay lines.	129
4-12	Maximum likelihood direct detection M -ary PPM receiver for equal a priori symbol probabilities.	130
4-13	Calculated bit-error rate for an ideal noncoherent M -ary PPM receiver as a function of the number of photons per bit at the receiver input.	137
4-14	Required number of photons per bit to achieve a BER of 10^{-9} as a function of the number of bits per transmitted symbol, $k = \log_2 M$.	138
4-15	Receiver power penalty at a bit-error rate of 10^{-9} as a function of the pulse extinction ratio at the transmitter.	139
4-16	Receiver sensitivity as a function of the transmitted pulse extinction ratio.	140
4-17	A PPM receiver with an optical front-end.	141
4-18	Calculated power spectral densities for NRZ and PPM waveforms with a raised cosine pulse shape. The PSD is plotted as a function of the frequency normalized to the data rate.	146
4-19	Waveforms at input and output of 40-Gbit/s-to-10-Gbit/s PPM UNI demultiplexer measured using a digital sampling oscilloscope. The UNI is used for both demultiplexing and format-conversion from PPM to OOK modulation.	148
4-20	Experimental setup for OOK/PPM wavelength conversion.	150
4-21	Bit-error rate performance of wavelength conversion of OOK and PPM waveforms of various pattern lengths.	151
5-1	Helical local area network consisting of a head-end and three users connected via a unidirectional folded bus. Here, a folded linear bus is shown. A helical-shaped bus is also possible, but it may be less practical to implement. XMT: Transmitter, RCV: Receiver, GBW: Guaranteed Bandwidth, BOD: Bandwidth-on-Demand.	163
5-2	HLAN receiver block diagram. The heavy lines represent optical connections, while the light lines represent electrical connections.	164
5-3	Illustration of slot structure for an empty and a full slot.	167
5-4	Head-end experimental implementation. MLFL: Mode-locked fiber laser; EOM: Electro-optic intensity modulator; EDFA: Erbium-doped fiber amplifier.	168
5-5	Head-end waveform trace. A single pulse is eliminated from the 12.5-GHz global clock stream every 100 ns to demarcate the beginning of a slot.	169

5-6	Transmitter experimental implementation. PPM: Pulse-position modulator; MUX: Passive OTDM multiplexer; EDFA: Erbium-doped fiber amplifier; ODL: Tunable optical delay line.	170
5-7	Experimental waveforms demonstrating transmitter operation at aggregate media rates of a) 50 Gbit/s and b) 112.5 Gbit/s. The 50-Gbit/s waveform is measured using a 40-GHz photodiode and a digital sampling oscilloscope. The 112.5-Gbit/s waveform is measured via cross-correlation with a 12.5-GHz stream of 2.5-ps optical pulses. . . .	172
5-8	Block diagram of synchronization unit for a receiver node in a slotted OTDM network. The UNI output provides a slot-synchronization signal as well as a feedback to the dithering phase-locked loop (DPLL) which is used for bit synchronization.	175
5-9	Output pulse from slot-synchronization UNI operating at an aggregate media rate of 112.5 Gbit/s.	176
5-10	Block diagram of address processor for slotted OTDM receiver node.	178
5-11	4-bit PPM optical address generator.	179
5-12	Experimental trace of a 4-bit PPM local address, [1001]. The address rate is 12.5 Gbit/s. The PPM delay is set to 4.4 ps, or one-half of the bit-period at the aggregate media rate of 112.5 Gbit/s.	180
5-13	Two techniques for detecting a 4-bit address match. In the parallel comparator, a), four 2-input XOR gates and one 4-input AND gate are required. In b), the process is serialized, requiring a single 2-input XOR gate and two 2-input AND gates.	182
5-14	Experimental setup for demonstrating address matching functionality using PPM XOR in a UNI at 12.5 Gbit/s. MLFL: Mode-locked fiber laser; BPF: Bandpass filter; ODL: Optical delay line; PPG: Pulse-pattern generator; DSO: Digital sampling oscilloscope.	184
5-15	Waveforms from all-optical address matching demonstration at 12.5 Gbit/s. The control and signal inputs to the UNI each consist of a repeating stream of 3-bit complementary binary PPM addresses, A and B, where $A = [101]$ and $B = [010]$. A 20-ps PPM delay is used. When the addresses on the inputs match, the NOT XOR output of the UNI produces three match bits. When they do not match, no match bits are produced.	185
5-16	Experimental waveforms at output of address-comparison UNI operating at an address rate of 12.5 Gbit/s with an aggregate media rate of 112.5 Gbit/s. The network addresses are compared with a local receiver address of [1001]. The waveforms are measured on a digital sampling oscilloscope with a 30-GHz photodiode.	188
5-17	Simulated 12.5 Gbit/s receiver eye diagrams at output of address comparison XOR gate after direct-detection and filtering for a) OOK and b) PPM data formats.	189
5-18	Techniques for optical rate conversion of OTDM slots: a) serial-to-serial conversion, b) serial-to-parallel conversion.	190

5-19	Demultiplexing of OTDM PPM data at rates up to 80 Gbit/s with the aggregate data input to the signal port of the UNI. The experimental setup is shown in a). MLFL: Mode-locked fiber laser. PPM: Pulse-position modulator. DPLL: Dithering phase-locked loop; MUX: OTDM passive multiplexer; PRBS: Pseudo-random binary sequence. In b), an illustration of the switch operation at 40 Gbit/s is provided. Each control pulse opens a switching window for the signal path. Only signal pulses that are coincident with a switching window pass to the output of the switch.	193
5-20	Bit-error-rate performance for demultiplexing from aggregate PPM data rates of 10, 20, 40 and 80 Gbit/s on signal input to UNI.	194
5-21	Demultiplexing of OTDM PPM data at rates up to 80 Gbit/s with the aggregate data input to the control port of the UNI. The experimental setup is shown in a). MLFL: Mode-locked fiber laser. PPM: Pulse-position modulator. DPLL: Dithering phase-locked loop; MUX: OTDM passive multiplexer; PRBS: Pseudo-random binary sequence. In b), an illustration of the switch operation at 40 Gbit/s is provided. Each control pulse opens a switching window for the signal path. Only signal pulses that are coincident with a switching window pass to the output of the switch.	196
5-22	Bit-error-rate performance for demultiplexing from aggregate PPM data rates of 10, 20, 40, and 80 Gbit/s on control input to UNI.	197
5-23	Origin of intersymbol interference in demultiplexing of 80-Gbit/s PPM data using a UNI with 5-ps signal pulse separation. The filled pulses represent the signal input to the UNI while the unfilled pulses represent the control input.	198
5-24	Schematic for slotted OTDM rate conversion utilizing multiple wavelength demultiplexing in a single UNI. WDM: Wavelength-division multiplexer.	199
5-25	Schematic of experimental setup for multiple-wavelength demultiplexing of 20-Gbit/s aggregate data on control input of UNI. MLFL: Mode-locked fiber laser; PPM: Pulse-position modulator; ODL: Optical delay line; MUX: OTDM passive multiplexer; PRBS: Pseudo-random binary sequence.	200
5-26	Bit-error rate test results at UNI output for multiple-wavelength demultiplexing of a 20-Gbit/s OTDM signal. The solid symbols represent single-wavelength operation and the open symbols represent multiple wavelength operation.	202
6-1	Schematic of a generalized optical packet switch.	214
6-2	Four operational states of an ultrafast cross-bar switch.	217
6-3	All-optical synchronization with an ultrafast nonlinear interferometer.	218

List of Tables

2.1	Semiconductor parameters used in gain calculations.	33
2.2	Device parameters used in simulations.	55
B.1	Coefficients used in Chebyshev expansion for $\mu(\nu)$	229

Chapter 1

Introduction

The ever-increasing demand for bandwidth in existing global networks has prompted much research into the efficient utilization of available bandwidth in optical fiber transmission systems. Advances in optical fiber processing technologies have made the entire band of wavelengths from 1280 nm to 1625 nm available for low-loss transmission over long distances (< 0.4 dB/km). Thus, a single fiber can provide nearly 50 THz of accessible communications bandwidth. This bandwidth greatly exceeds electronic processing capabilities. Consequently, various technologies have been developed to partition the available bandwidth in an optical fiber among a number of transceivers operating at electronic rates. An important design issue facing system developers is how to best utilize this enormous capacity to efficiently provide the resources needed to meet the demands of future networks.

1.1 Optical Multiplexing Techniques

There are several optical techniques for multiplexing traffic from electronic-rate nodes. Three of these are illustrated in Figure 1-1. Present commercial efforts are focused on the development of wavelength-division multiplexed (WDM) systems. In a WDM network, the aggregate bandwidth of the fiber transmission system is divided among a number of transceivers operating on distinct carrier wavelengths. These transceivers typically operate at electronics-limited rates of 2.5-10 Gbit/s with 40 Gbit/s WDM

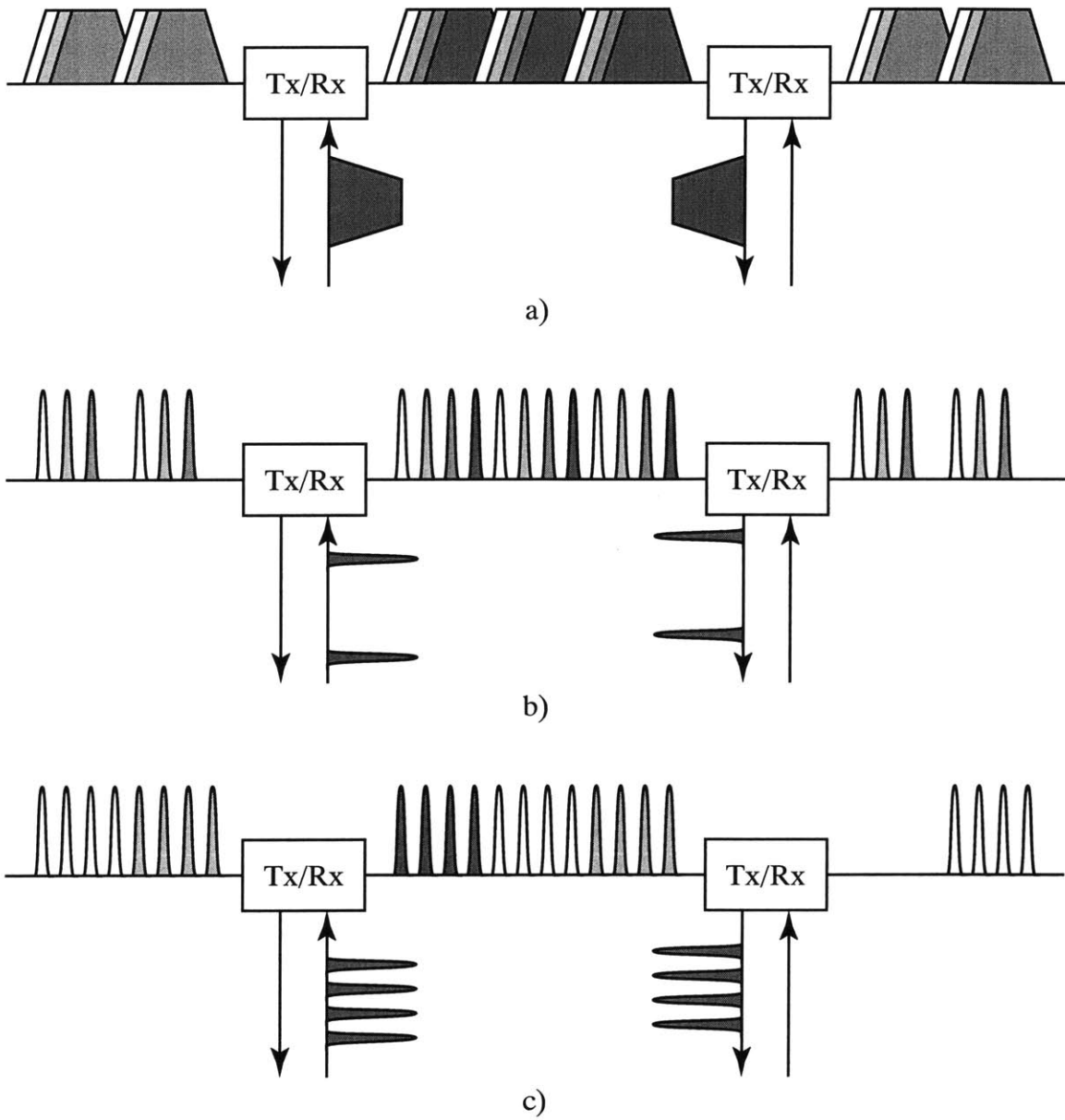


Figure 1-1: Three optical multiplexing techniques: a) wavelength-division multiplexing, b) bit-interleaved time-division multiplexing, and c) slotted time-division multiplexing. Note that the shading in b) and c) is used to distinguish the different channels, not to indicate different transmission wavelengths.

systems currently under development. Hundreds of these transceivers operating on independent wavelengths can be multiplexed on a single fiber providing point-to-point connectivity at electronic data rates. Physical-layer component technology for WDM networks is quite mature. Commercially available systems can provide capacities of up to 3.2 Tbit/s on a single fiber for unregenerated transmission distances of up to 2000 km [1.1]. Research demonstrations have achieved capacities as high as 10.92 Tbit/s [1.2] in a single fiber with spectral efficiencies as high as 1.28 bit/s/Hz [1.3].

An alternative method for utilizing the available bandwidth of an optical fiber is the use of optical time-division multiplexing (OTDM) techniques. In OTDM networks, multiple transceivers utilize fiber bandwidth by modulating a single carrier wavelength at aggregate data rates of 100 Gbit/s or higher. Current OTDM systems may be broadly classified as either bit-interleaved or slotted systems. In a bit-interleaved OTDM network, transceivers modulate data onto short optical pulses at electronic rates (~ 10 Gbit/s). Because the pulse duration is much shorter than the bit period, modulated pulse streams from several transceivers can be temporally interleaved to form a single modulated signal at an aggregate data rate which exceeds electronic processing capabilities (> 100 Gbit/s).

WDM and bit-interleaved OTDM networks are similar in that they are essentially circuit-switched networks at the optical layer. This architecture is necessary because the time required to initiate a new path between transceivers in the network is generally long compared to typical packet durations on the network. In a WDM network, changing the network topology requires a change in the wavelength selection of transmitters and receivers. In a bit-interleaved OTDM system, changing the timing of the interleaved channels is required. Since current technologies for implementing these changes are slow compared to typical packet durations, packet-switching services are generally provided electronically.

By contrast, slotted OTDM networks offer the potential for providing packet-switched network services at the optical layer. In a slotted OTDM system, individual transceivers are capable of bursting data onto the network at the aggregate OTDM bit-rate. The various transceivers share access to a single ultrafast channel by trans-

mitting in distinct time slots at the aggregate network data rate. Bandwidth may be allocated by a centralized processor which assigns specific time slots to the different transceivers on the network. However, scheduling is complicated by the fact that several packets may be in flight simultaneously on the network. The helical local area network (HLAN) [1.4, 1.5] has been proposed as a possible architecture for a slotted OTDM network which addresses these concerns.

Slotted OTDM networks can potentially provide many advantages over WDM and bit-interleaved OTDM networks. As mentioned above, they can be used to provide photonic packet-switching at data rates which exceed electronic processing capabilities. Medium access control is simplified in slotted OTDM networks and they can provide a variety of services including both guaranteed bandwidth and flexible bandwidth-on-demand. Additionally, in a slotted OTDM network, bandwidth may be allocated among transceivers with a much higher degree of granularity than in WDM and bit-interleaved OTDM networks. This leads to more efficient utilization of the available bandwidth and makes slotted OTDM networks ideal candidates for future high-capacity optical networks.

1.2 All-Optical Switching Requirements

Challenges in implementing bit-interleaved and slotted OTDM networks arise due to the fact that these networks require switching and logic operations at the aggregate bit-rate of the system. In the case of bit-interleaved OTDM networks, demultiplexers are required at the receivers to separate the fractional bandwidth destined for a particular node from the stream of data at the aggregate rate. As the aggregate data rate of the network is typically much higher than electronic processing rates, demultiplexing is usually performed in the optical domain, using all-optical logic gates. After demultiplexing, the data rate is lower and further processing may be done in electronics after detection. All-optical switches utilizing nonlinearities in optical fiber have been used to demonstrate bit-interleaved OTDM systems operating at data-rates as high as 1.28 Tbit/s [1.6].

Slotted OTDM networks must operate on slots in which the information arrives at the aggregate data rate of the network. This requires additional logical functionality in the optical domain prior to electronic detection at the receiver. Local transceiver clocks must be synchronized to network slot- and bit-clocks. Headers on incoming slots must be processed optically to determine their destination. Finally, data in incoming slots must be rate-converted to electronic data rates prior to detection and electronic processing at the receiver. These operations require the use of several layers of all-optical logic in the slotted OTDM transceiver.

To date, many different switch designs which can accomplish these tasks have been proposed. These switches are often based on an interferometric design employing an intensity-dependent refractive index in a waveguide. In most demonstrations, the nonlinear waveguide is either an optical fiber or a semiconductor. Semiconductor-based switches are particularly attractive for several reasons. First, they tend to be very compact. Typical interaction lengths in a semiconductor-based switch are on the order of ~ 1 mm. Moreover, semiconductor-based switches utilizing active waveguides, such as semiconductor optical amplifiers (SOA), require low switching energies. All-optical switching in semiconductor-based interferometers has been demonstrated with control pulse energies of a few fJ. Finally, semiconductor-based switches can be readily integrated using existing semiconductor processing technologies. Thus, they offer the potential for developing highly functional integrated electronic and photonic processing nodes in a compact package.

1.3 Organization

The work presented in this dissertation focuses on the practical implementation of semiconductor-based all-optical switches with emphasis on their application in slotted OTDM networks. The dissertation is organized as follows:

In Chapter 2, we review background theory on the gain and index dynamics of semiconductor optical amplifiers. We develop a numerical model for the dynamic response of a semiconductor gain medium which may be used to describe pulse

propagation in an SOA under the heavily saturated conditions which arise in typical all-optical switching applications. Next, we present experiments which utilize a difference-frequency pump-probe technique to measure the dynamic gain response of an SOA.

In Chapter 3, we discuss interferometric optical switching techniques employing semiconductor optical amplifiers. We discuss three common fiber interferometer configurations. Techniques for experimentally measuring the switching windows for these devices are demonstrated and the configurations are compared in an OTDM demultiplexing experiment.

In Chapter 4, we address the problems of gain saturation in semiconductor-based all-optical switches. We develop a statistical model for studying the system impact of data-pattern-dependent gain-saturation. We review techniques which have been employed for mitigation of gain saturation problems in semiconductor optical amplifiers. Finally, we propose the use of pulse-position modulation (PPM) as a data format which effectively eliminates the problems of gain saturation, while still enabling all-optical switching using standard interferometric techniques. We demonstrate the use of PPM in several all-optical switching experiments.

In Chapter 5, we describe efforts to utilize the ultrafast optical logic functionality provided by semiconductor-based switches to enable basic physical layer functionality in a slotted OTDM network. We discuss the design and experimental verification of the optical interface for various functional nodes in an HLAN network. We present designs of simplified head-end and transmitter nodes. These nodes simulate the transmission of fully-loaded network slots and test the operation of the receiver node. Finally, we describe the implementation of a fully-functional optical interface for a receiver node. This node utilizes optical logic gates for the three primary tasks required for physical layer access in an ultrahigh speed multiaccess network: synchronization, header processing, and data-rate conversion.

We conclude in Chapter 6 with a summary of the contributions of this work and a discussion of possible directions for future work in this area.

References

- [1.1] Corvis, “CorWave LR.” <http://www.corvis.com>.
- [1.2] K. Fukuchi, T. Kasamatsu, M. Morie, R. Ohhira, T. Ito, K. Sekiya, D. Ogasahara, and T. Ono, “10.92 Tb/s (273 x 40 Gb/s triple-band/ultra-dense WDM optical repeatered transmission experiment,” in *Conference on Optical Fiber Communication*, 2001.
- [1.3] S. Bigo, Y. Fignac, G. Charlet, W. Idler, S. Borne, H. Gross, R. Dischler, W. Poehlmann, P. Tran, C. Simonneau, D. Bayart, G. Veith, A. Jourdan, and J.-P. Hamaide, “10.2 Tbit/s (256x42.7 Gbit/s PDM/WDM) transmission over 100 km TeraLight fiber with 1.28 bit/s/hz spectral efficiency,” in *Conference on Optical Fiber Communication*, pp. PD25–1–3, 2001.
- [1.4] S. G. Finn, “HLAN– an architecture for optical multi-access networks,” in *IEEE/LEOS 1995 Summer Topical Meetings*, pp. 45–6, 1995.
- [1.5] R. A. Barry, V. W. S. Chan, K. L. Hall, E. S. Kintzer, J. D. Moores, K. A. Rauschenbach, E. A. Swanson, L. E. Adams, C. R. Doerr, S. G. Finn, H. A. Haus, E. P. Ippen, W. S. Wong, and M. Hane, “All-optical network consortium–ultrafast TDM networks,” *JLT/JSAC Special Issue on Optical Networks*, vol. 14, no. 5, p. 999, 1996.
- [1.6] M. Nakazawa, T. Yamamoto, and K. R. Tamura, “1.28 bit/s-70 km OTDM transmission using third- and fourth-order simultaneous dispersion compensation with a phase modulator,” *Electron. Lett.*, vol. 36, pp. 2027–9, November 2000.

Chapter 2

Semiconductor Optical Amplifiers

2.1 Introduction

Semiconductor optical amplifiers (SOA) have many potential applications in optical networks. SOAs were originally developed to provide in-line amplification in optical transmission systems. Because of their poor noise performance and relatively low saturated output power compared to erbium-doped fiber amplifiers, SOAs are rarely considered for this application in long haul-transmission networks today. However, they have a number of unique properties which make them useful for other applications in optical networks. For instance, SOAs fabricated in the quaternary semiconductor InGaAsP, lattice-matched to InP, can have a bandgap anywhere in the range from 1.1 μm to 1.65 μm . Thus, they can provide gain over the entire low-loss spectrum of an optical fiber. Additionally, SOAs are very compact and easily integrated with existing semiconductor processing technologies, making them useful in the development of integrated photonic processing nodes for a variety of network applications. Finally, the fast nonlinear gain dynamics in an SOA make them attractive candidates in a variety of nonlinear processing applications, such as wavelength conversion, regeneration and ultrafast switching in an optical network.

In this chapter, we develop a numerical model which may be used to study the performance of semiconductor optical amplifiers in nonlinear switching applications. We begin with a brief overview of device structures for semiconductor lasers and

semiconductor optical amplifiers. Then, we describe the gain and refractive index in a semiconductor optical amplifier which arise from the interaction of an optical field with the free carriers in the active region of the device. Next, we develop a theoretical model for the temporal dynamics of the carrier density and energy density in a semiconductor waveguide in response to an optical pulse. We present a numerical method for calculating the dynamic response of the SOA which includes the frequency-dependent nature of the gain and index transients. Finally, we validate the qualitative predictions of the model using experimental pump-probe measurements on an InGaAsP semiconductor optical amplifier.

2.2 Device Overview

The first homojunction semiconductor lasers were made using simple p - n junctions in a direct bandgap semiconductor such as GaAs [2.1–2.3]. In these devices, free carriers are injected across the junction by passing a current through the forward-biased diode. These carriers create an inverted population where light can be amplified via the stimulated emission which accompanies the recombination of an electron in the conduction band with a hole in the valence band of the semiconductor. This region where optical interactions with the inverted population take place is referred to as the active region. In a homojunction device, the depth of the active region in a direction normal to the junction is determined by the carrier diffusion lengths in the semiconductor and is typically on the order of $\sim 1 \mu\text{m}$. Consequently, the volume of the active region in a homojunction laser is large and high currents are required to achieve a population inversion in the region.

Modern semiconductor laser devices are typically heterostructures where several different semiconductor materials are combined to improve device performance. In the simplest such device, the double heterostructure (DH) laser, the active region consists of a material with a narrow band gap which resides between two cladding layers with wider band gap as shown in Figure 2-1. The heterostructure design improves laser performance in several ways. First, carriers injected by passing a current through the

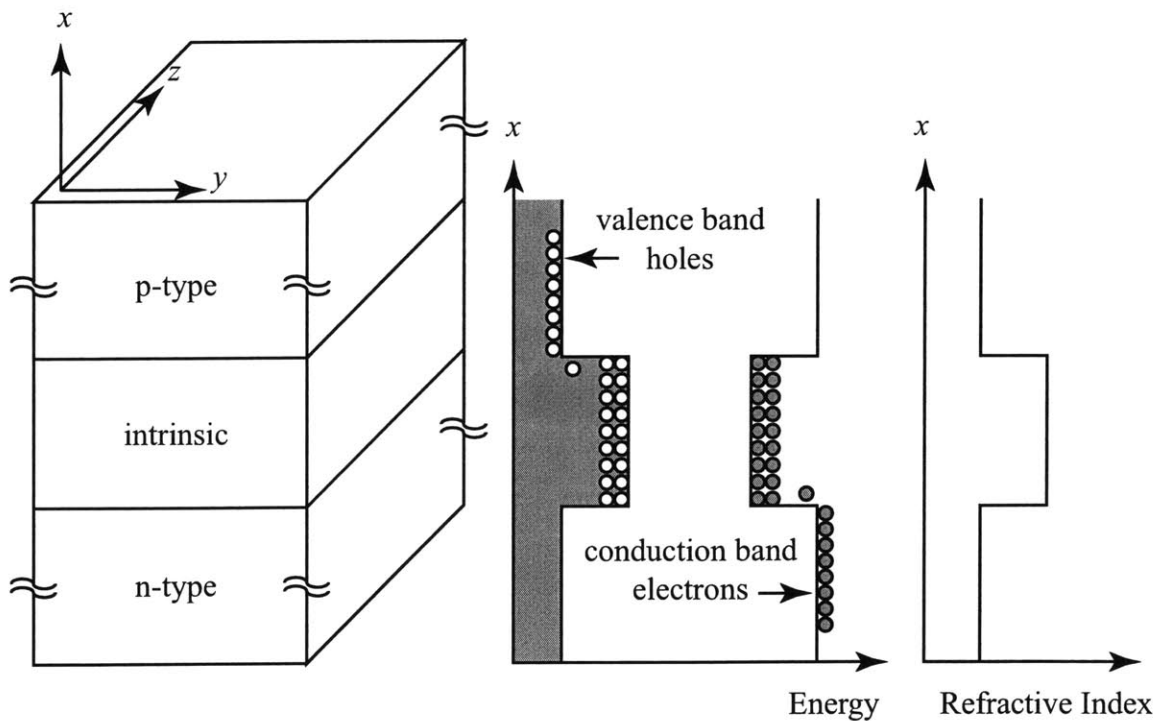


Figure 2-1: A double-heterostructure semiconductor laser.

diode are confined to the active region due to the potential barriers provided by the wide band gap materials. This makes it possible to achieve a population inversion with current densities which are much lower than those required in a homojunction laser. Additionally, the higher index of the lower band gap material relative to the cladding layers serves to confine the optical field, leading to a better mode overlap between the active region and the optical mode. These two features of the DH lasers enabled the development of the first practical semiconductor lasers which could operate continuously at room temperature [2.4, 2.5].

The double-heterostructure laser gives the designer more freedom in specifying the parameters of the active region. For instance, the thickness of the active region may be reduced to lower the current required to achieve inversion. The active region in bulk semiconductor devices today is typically around $0.1\text{-}0.2\ \mu\text{m}$ thick. Quantum well devices can have active layer thicknesses on the order of a few nanometers. Additionally, the doping of the active region can be varied relative to the cladding

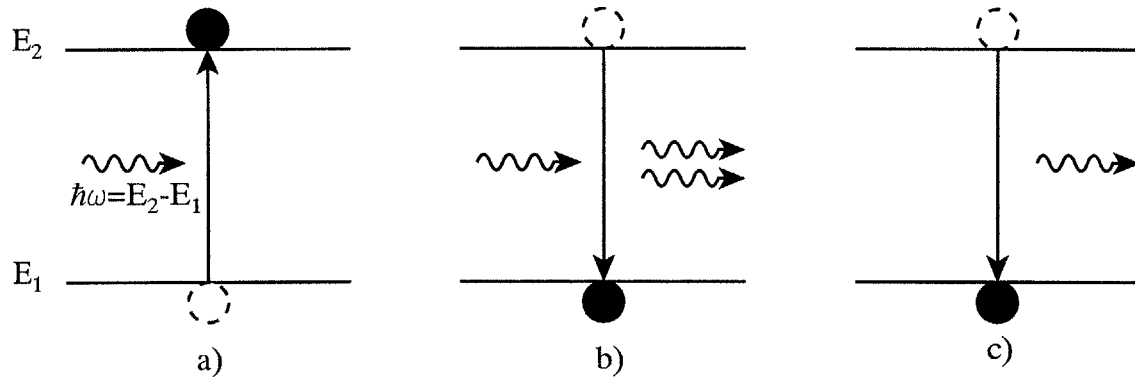


Figure 2-2: Absorption and emission processes in a semiconductor.

regions (which are doped to form the p - n junction). In particular, the active region can be lightly doped or even intrinsic.

A semiconductor laser is made by creating a waveguide in the active region which provides lateral confinement for the optical mode. The input and output facets of the device are cleaved normal to the waveguide to provide reflectivity for the laser cavity. A traveling-wave semiconductor optical amplifier is made by modifying the semiconductor laser design to reduce reflections from the facets. This may be accomplished by cleaving the input and output facets at an angle which is not normal to the waveguide and applying an anti-reflection coating to the facets.

2.3 Optical Gain in Semiconductors

Gain in a semiconductor arises from the exchange of energy between the photons in the incident optical field and the electrons and holes in the semiconductor. This occurs via the processes of absorption, stimulated emission, and spontaneous emission, depicted in Figure 2-2 for a two-level system. When an electron absorbs the energy in a photon, it is excited to a higher energy level, leaving behind a hole at the lower energy level. Conversely, an electron at a high energy level may recombine with a hole at a lower energy level, emitting a photon in the process. When this process is initiated by an existing photon in the semiconductor, it is called stimulated emission.

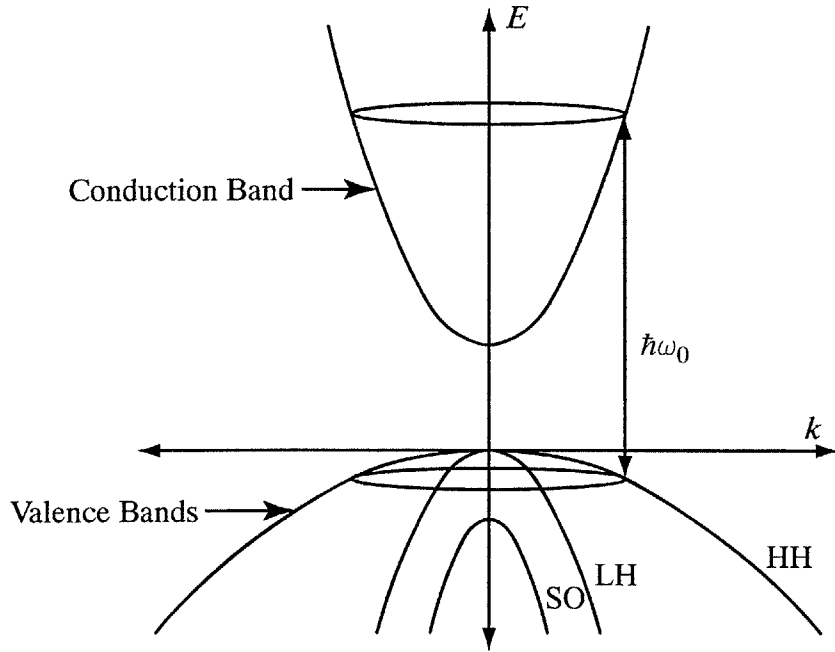


Figure 2-3: Direct bandgap semiconductor bandstructure.

Otherwise, it is called spontaneous emission.

In order to describe optical gain in a semiconductor, we must first describe the distribution of electrons and holes among the available energy states in the semiconductor. Charge carriers in an undoped bulk semiconductor reside in a periodic potential defined by the atoms in the periodic semiconductor lattice. Consequently, the carrier energy eigenstates have definite momentum and are described by the Bloch functions, parameterized by the wave vector, \vec{k} [2.6]. Due to the close proximity of atoms in the semiconductor lattice, the allowed electronic energy states form near-continuous bands. Figure 2-3 illustrates the typical band structure in a direct bandgap semiconductor near $\vec{k} = 0$. The valence bands consist of the highest occupied energy states at temperature $T = 0$. Near $\vec{k} = 0$, there are three valence bands containing carriers which may participate in optical interactions: the heavy-hole band, the light-hole band, and the split-off band. The heavy-hole band and the light-hole bands are degenerate at $\vec{k} = 0$. Above the valence bands, the lowest band of allowed energies is the conduction band. The energy difference between the highest energy valence band

state and the lowest energy conduction band state is known as the bandgap of the semiconductor.

In the effective mass approximation, the energy bands near $\vec{k} = 0$, are approximated by a parabolic relationship between the energy, E , and momentum, \vec{k} . The energy of a conduction band electron is thus given by

$$E_c(\vec{k}) = \frac{\hbar^2 k^2}{2m_c}, \quad (2.1)$$

where $k = |\vec{k}|$ and m_c is the effective mass of an electron in the conduction band. Similarly, for a hole in one of the valence bands, the energy is defined in terms of the hole effective mass, m_v , as

$$E_v(\vec{k}) = \frac{\hbar^2 k^2}{2m_v}. \quad (2.2)$$

Note that in each of these equations the energy is referenced to the band edge and is positive into the band. Each of the three valence bands has its own effective mass. We denote the effective masses of the heavy hole, light hole, and split-off bands as m_{hh} , m_{lh} , and m_{so} . Due to the differences in their effective masses, the number of free carriers in the heavy-hole valence band is typically much larger than the number of free carriers in the light-hole and split-off valence bands. Thus, in the following discussion, we only consider interactions between the holes in the heavy-hole band and electrons in the conduction band.

Electrons in a semiconductor are subject to the Pauli-exclusion principle. Therefore, at most two electrons (with opposite spin states) can occupy the same energy state simultaneously. The distribution of electrons among the available energy states is thus described by the Fermi-Dirac statistics. The probability that an electron occupies a state with energy E is given by the Fermi-Dirac distribution function

$$f_e(E) = \frac{1}{1 + \exp\left(\frac{E - E_F}{k_B T}\right)}. \quad (2.3)$$

Here, T is the temperature of the electrons and k_B is the Boltzmann constant. The energy E_F is known as the Fermi energy. At the Fermi energy, the probability of occupation is precisely 1/2.

At thermal equilibrium, the carriers in both the conduction and the valence band are characterized by a single Fermi energy. However, when carriers are injected via external means, such as an electrical current in a junction diode or optical excitation, the two bands may form separate “quasi-Fermi levels.” These quasi-Fermi levels arise due to the fact that the time required for energy to redistribute among carriers within a particular band via mechanisms such as carrier-carrier scattering is, in general, much shorter than the time required for energy to redistribute between the two bands. This latter redistribution of energy is limited by the recombination times of the semiconductor and is typically on the order of a few hundred picoseconds to several nanoseconds. We denote the quasi-Fermi energies in the conduction and valence bands as E_{F_c} and E_{F_v} , respectively. These energies are defined relative to the minimum energy in the respective band with the energy being positive into the band (as in Equations 2.1 and 2.2). Thus, the conduction band electron occupation probability is expressed as

$$f_c(E_c) = \frac{1}{1 + \exp\left(\frac{E_c - E_{F_c}}{k_B T_c}\right)} \quad (2.4)$$

and the valence band electron occupation probability is

$$f_v(E_v) = \frac{1}{1 + \exp\left(\frac{E_{F_v} - E_v}{k_B T_v}\right)}, \quad (2.5)$$

where T_c and T_v are the temperatures of the carriers in the conduction and valence band, respectively.

The density of states for a particular band, $\rho(E)$, is defined such that $\rho(E)dE$ quantifies the number of available electron energy states per unit volume in the range $(E, E + dE)$. Using the parabolic band shapes defined in Equations 2.1 and 2.2, and noting that, in a semiconductor with volume V , each momentum state occupies a

volume of $(2\pi)^3/V$ in k -space, we find that the density of states in the conduction band is

$$\rho_c(E_c) = \frac{1}{2\pi^2} \left(\frac{2m_c}{\hbar^2} \right)^{3/2} E_c^{1/2}. \quad (2.6)$$

Similarly, in the valence band, we find

$$\rho_v(E_v) = \frac{1}{2\pi^2} \left(\frac{2m_v}{\hbar^2} \right)^{3/2} E_v^{1/2}. \quad (2.7)$$

Note that a factor of 2 has been added to each of these densities to account for the two electron spin states.

The density of carriers per unit energy in a band is given by the product of the density of states and the occupation probability. We can now find the total electron density in the conduction band, N , by integrating the density of carriers over all possible energies

$$N = \int_0^\infty \rho_c(E_c) f_c(E_c) dE_c \quad (2.8)$$

The density of holes in the valence band, P , is obtained in a similar manner

$$P = \int_0^\infty \rho_v(E_v) [1 - f_v(E_v)] dE_v. \quad (2.9)$$

Assuming charge neutrality in the active region, the number of electrons in the conduction band must be equal to the number of holes in the valence band (i.e. $N = P$). If the carrier temperature and carrier density are known, Equations 2.8 and 2.9 can be used to obtain the quasi-Fermi levels for the two bands. Once the quasi-Fermi levels for the bands are known, the statistical distribution of the carriers is completely specified.

We can now calculate the gain of the semiconductor by considering the rates of transitions between the various electron states in the valence and conduction bands. An incident optical field experiences gain when the rate of stimulated emission exceeds

the rate of stimulated absorption. For an electron in a two-level system with an upper state energy, E_2 , and a lower state energy, E_1 , the rate of transitions from the upper state to the lower state under the influence of an incident photon flux, $v_g S$, may be calculated using Fermi's golden rule [2.7]

$$R_{21} = \frac{\pi q^2 \hbar}{m_0^2 n_g c \epsilon_0 \hbar \omega_0} |M_{12}|^2 f_2 (1 - f_1) \delta(E_2 - E_1 - \hbar \omega_0) v_g S, \quad (2.10)$$

where m_0 is the electron mass, n_g is the group index, $\hbar \omega_0$ is the photon energy, f_2 is the electron occupation probability for the upper state, and f_1 is the electron occupation probability for the lower state. If the upper and lower energy state kets are $|\Psi_2\rangle$ and $|\Psi_1\rangle$, respectively, then the matrix element representing the electron-photon interaction, $|M_{12}|^2$, is defined as

$$|M_{12}|^2 = |\langle \Psi_1 | \exp(i \vec{k}_p \cdot \vec{r}) \hat{e} \cdot \mathbf{p} | \Psi_2 \rangle|^2, \quad (2.11)$$

where \vec{k}_p is the photon wave vector, \hat{e} is the electric field polarization, and \mathbf{p} is the momentum operator. The rate of absorption may be expressed in a similar fashion

$$R_{12} = \frac{\pi q^2 \hbar}{m_0^2 n_g c \epsilon_0 \hbar \omega_0} |M_{12}|^2 f_1 (1 - f_2) \delta(E_2 - E_1 - \hbar \omega_0) v_g S. \quad (2.12)$$

The net gain per unit length for the two-level transition is given by the net rate of photon emission (i.e. the stimulated emission rate minus the absorption rate) normalized by the semiconductor volume and the photon flux

$$\begin{aligned} g_{21} &= \frac{1}{V} \frac{R_{21} - R_{12}}{v_g S} \\ &= \frac{1}{V} \frac{\pi q^2 \hbar}{m_0^2 n_g c \epsilon_0 \hbar \omega_0} |M_{12}|^2 (f_2 - f_1) \delta(E_2 - E_1 - \hbar \omega_0). \end{aligned} \quad (2.13)$$

The effect of spectral broadening due to the dipole dephasing time may be included by replacing the delta function in Equation 2.13 with the desired line shape function, $\mathcal{L}(E_2 - E_1 - \hbar \omega_0)$. The lineshape is usually parameterized by the dipole dephasing

time, τ_2 . Commonly used lineshapes include the Lorentzian

$$\mathcal{L}(E) = \frac{1}{\pi} \frac{\hbar/\tau_2}{(\hbar/\tau_2)^2 + E^2} \quad (2.14)$$

and the hyperbolic secant

$$\mathcal{L}(E) = \frac{\tau_2}{\pi\hbar} \operatorname{sech}\left(\frac{E\tau_2}{\hbar}\right). \quad (2.15)$$

As discussed above, there are many possible states for an electron in the conduction or valence band of a semiconductor. The total gain for a signal with photon energy $\hbar\omega_0$ must be calculated by summing the gain expressed in Equation 2.13 over all possible transitions between the conduction band and valence band

$$g(\hbar\omega_0) = \frac{\pi q^2 \hbar}{m_0^2 n_g c \epsilon_0 \hbar \omega_0} \sum_{\vec{k}_c} \sum_{\vec{k}_v} |M_{\vec{k}_c \vec{k}_v}|^2 \left[f_c(E_c(\vec{k}_c)) - f_v(E_v(\vec{k}_v)) \right] \cdot \delta(E_g + E_c(\vec{k}_c) + E_v(\vec{k}_v) - \hbar\omega_0) \quad (2.16)$$

This equation can be simplified by noting that, since the Bloch electron states have definite momentum, the matrix element, $|M_{\vec{k}_c \vec{k}_v}|^2$, is nonzero only when $\vec{k}_c = \vec{k}_v + \vec{k}_p$ (indeed, this condition is required for conservation of momentum). Since the photon momentum is generally much smaller than the electron momentum, this requirement becomes $\vec{k}_c \approx \vec{k}_v$. Thus, only vertical transitions between the bands are allowed. This is known as the k -selection rule. With strict k -selection, Equation 2.16 reduces to

$$g(\hbar\omega_0) = \frac{\pi q^2 \hbar}{m_0^2 n_g c \epsilon_0 \hbar \omega_0} |M_{\text{avg}}|^2 \rho_{\text{red}}(\hbar\omega_0 - E_g) [f_c(E_{r,c}) - f_v(E_{r,v})], \quad (2.17)$$

where m_r is the reduced mass for the transition,

$$m_r = \frac{m_v m_c}{m_v + m_c}, \quad (2.18)$$

and ρ_{red} is the reduced density of states,

$$\rho_{\text{red}}(E) = \frac{1}{2\pi^2} \left(\frac{2m_r}{\hbar^2} \right)^{3/2} E^{1/2}. \quad (2.19)$$

The reduced energies in the conduction and valence band are

$$E_{r,c} = \frac{m_r}{m_c} (\hbar\omega_0 - E_g) \quad (2.20)$$

$$E_{r,v} = \frac{m_r}{m_v} (\hbar\omega_0 - E_g). \quad (2.21)$$

$|M_{\text{avg}}|^2$ is the average of the momentum matrix element over all possible electron momentum directions. It can be calculated using perturbation techniques near $\vec{k} = 0$ to give [2.8]

$$|M_{\text{avg}}|^2 = \frac{m_0}{6} \left(\frac{m_0}{m^*} - 1 \right) \frac{E_g(E_g + \Delta)}{(E_g + \frac{2}{3}\Delta)}, \quad (2.22)$$

where Δ is the spin-orbital split-off energy. The effect of lineshape broadening may be included by convolving the gain given in Equation 2.17 with the desired lineshape function, $\mathcal{L}(E)$.

Figure 2-4 shows examples of a gain spectrum calculated using Equation 2.17 for a bulk $\text{In}_{1-x}\text{Ga}_x\text{As}_y\text{P}_{1-y}/\text{InP}$ semiconductor with a carrier density of $N = 2 \cdot 10^{24} \text{ m}^{-3}$ and carrier temperatures of $T_c = T_v = 300 \text{ K}$. Other parameters used in calculating this curve are given in Table 2.1. The solid curve shows the gain calculated using the delta-function line shape. For comparison, the remaining two curves show the gain calculated when a Lorentzian and hyperbolic secant lineshape with a dephasing time of 100 fs is used. The curves are plotted as a function of the photon wavelength, $\lambda = 2\pi c/\omega_0$.

For this semiconductor, the bandgap corresponds to a wavelength of $\lambda_g = 1565 \text{ nm}$. Photon energies below the bandgap (corresponding to wavelengths longer than 1565 nm) experience neither gain nor loss due to interband interactions with the free carriers in the semiconductor. Photon energies slightly above the bandgap experience

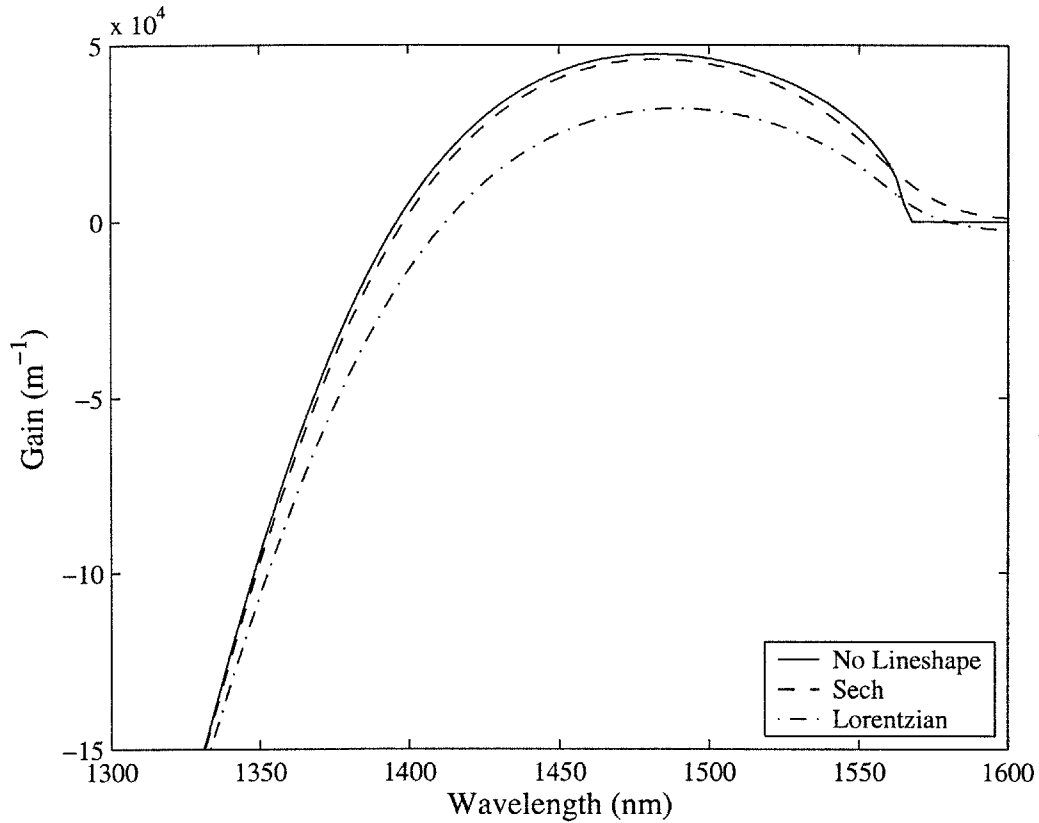


Figure 2-4: Example gain curves calculated for a carrier density of $2 \cdot 10^{24} \text{ m}^{-3}$ and a lattice temperature of $T = 300 \text{ K}$. For the Lorentzian and hyperbolic secant lineshapes, a dephasing time of 100 fs is used. Table 2.1 lists the other parameters used in calculating these curves.

Description	Symbol	Value	Units
Molar fraction As	y	0.92	—
Molar fraction Ga	x	0.4286	—
Free electron mass	m_0	$9.109 \cdot 10^{-31}$	kg
Electron effective mass	m_c	$0.0441 \cdot m_0$	kg
Heavy hole mass	m_{hh}	$0.4354 \cdot m_0$	kg
Light hole mass	m_{lh}	$0.0563 \cdot m_0$	kg
Energy gap	E_g	$1.2698 \cdot 10^{-19}$	J
Dipole dephasing time	τ_2	$1 \cdot 10^{-13}$	s
Split-off energy	Δ	$5.1331 \cdot 10^{-20}$	J
Index	n	3.508	—

Table 2.1: Semiconductor parameters used in gain calculations.

gain due to net stimulated emission in the semiconductor. Photon energies well above the bandgap energy experience loss due to net stimulated absorption. The energy at which the gain spectrum crosses over from net stimulated emission to net absorption is called the transparency point. In this case, the transparency point corresponds to a wavelength of approximately 1396 nm. From Equation 2.17, we find that the transparency point is the photon energy for which $f_c - f_v = 0$. Using Equations 2.4 and 2.5, we find that the transparency energy is related to the quasi-Fermi energies in the bands as $E_{tr} = E_g + E_{Fc} + E_{Fv}$. Thus, photon energies, $\hbar\omega_0$ which experience gain satisfy

$$E_g < \hbar\omega_0 < E_g + E_{Fc} + E_{Fv}. \quad (2.23)$$

This is known as the Bernard-Duraffourg condition for net stimulated emission [2.9]. Figure 2-5 shows the calculated transparency point, $E_g + E_{Fc} + E_{Fv}$, as a function of the injected carrier density, N . For carrier densities less than $N_{tr} = 7.4 \cdot 10^{23} \text{ m}^{-3}$, the transparency wavelength is below the bandgap. Thus, for carrier densities below N_{tr} , there are no photon energies which experience gain in the semiconductor. N_{tr} is referred to as the transparency carrier density.

From Equations 2.4, 2.5, and 2.17, we find that when the carriers in the conduction band and valence bands are at quasi-equilibrium (i.e. their energy distribution is described by the Fermi-Dirac statistics), the gain at a particular wavelength is described in terms of four parameters: the quasi-Fermi energies in the conduction and valence bands and the carrier temperatures in the two bands. At a specified carrier temperature, the quasi-Fermi levels in both the conduction and valence bands may be calculated for a particular carrier density, N , using Equations 2.8 and 2.9. In Figure 2-6 a), we show the calculated gain for various carrier densities with a fixed carrier temperature of $T_c = T_v = 300 \text{ K}$. In Figure 2-6 b), we show the calculated gain for various carrier temperatures at a fixed carrier density of $N = 2 \cdot 10^{24} \text{ m}^{-3}$. In both of these calculations, a hyperbolic secant lineshape with a dephasing time of $\tau_2 = 100 \text{ fs}$ has been used.

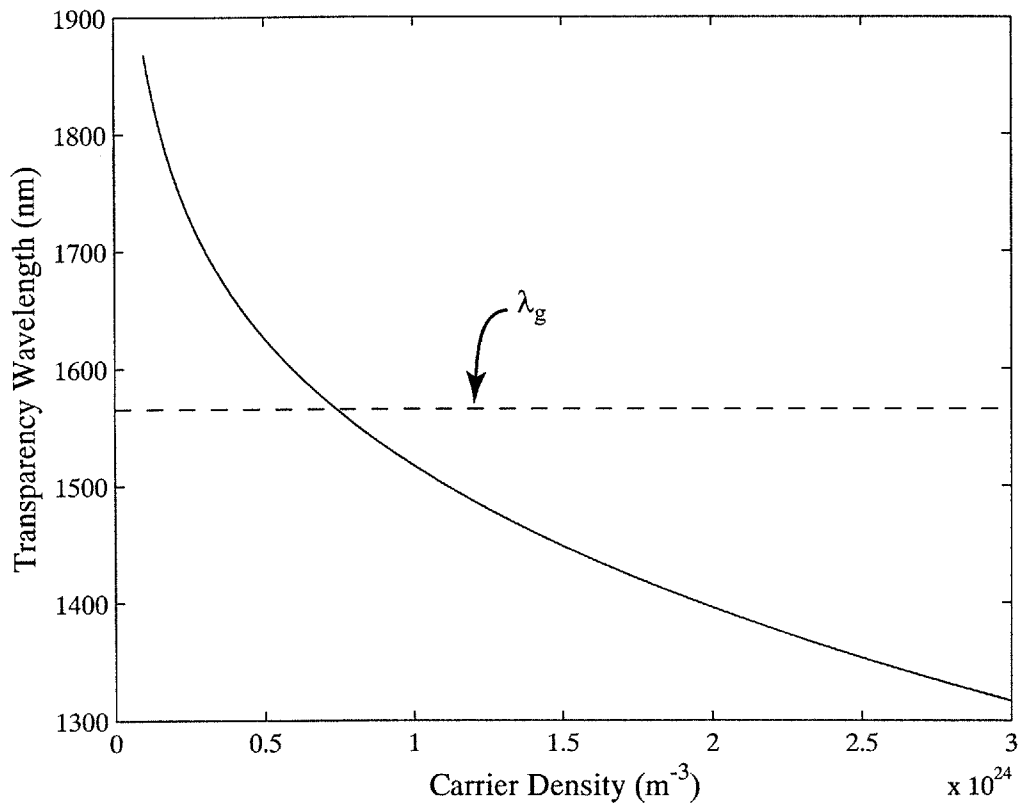


Figure 2-5: Calculated transparency wavelength as a function of the injected carrier density, N .

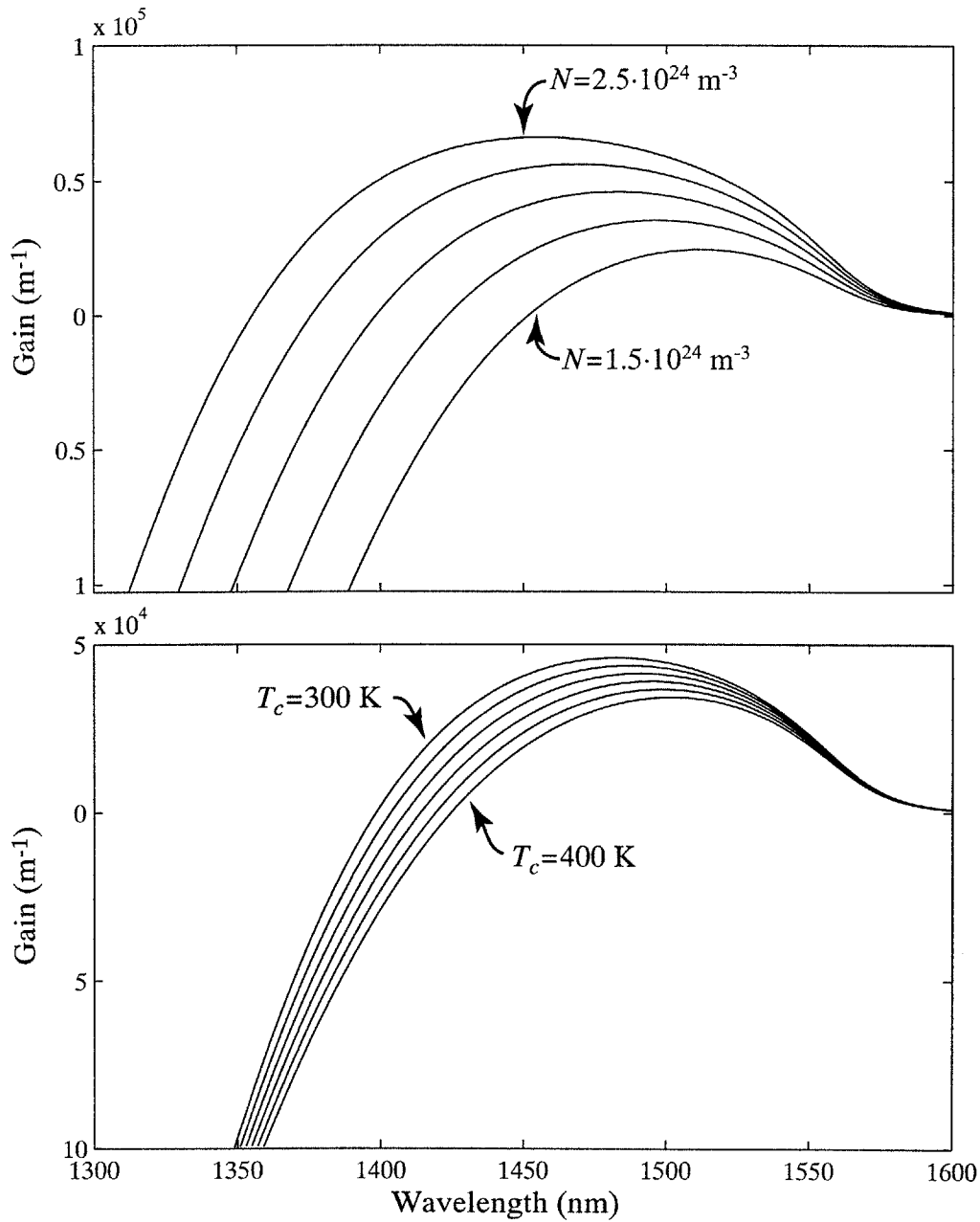


Figure 2-6: Illustration of the dependence of semiconductor gain on carrier density and temperature. In a) the semiconductor gain is plotted for carrier densities of $N = 1.5, 1.75, 2, 2.25,$ and $2.5 \cdot 10^{24} \text{ m}^{-3}$ with carrier temperatures of $T_c = T_v = 300 \text{ K}$. In b), the gain is plotted for a carrier density of $N = 2 \cdot 10^{24} \text{ m}^{-3}$ and conduction band temperatures of $T_c = 300, 320, 340, 360, 380,$ and 400 K . The valence band carrier temperature is $T_v = 300 \text{ K}$.

We note that simplified models for the carrier density dependent gain have been employed. For instance, the gain is often approximated using the transparency carrier density, N_{tr} , as [2.7]

$$g(N) = a_0(N - N_{tr}) \quad (2.24)$$

where a_0 is the so-called differential gain parameter. This model can be quite accurate for the gain at the peak of the gain spectrum for various carrier densities. Since it is linear, it can often be utilized to obtain analytic approximations for device performance. It also greatly reduces the computational complexity involved in numerical simulations of device performance. However, this model does not include the wavelength dependence of the gain and is therefore only accurate for calculations involving a single optical wavelength. Moreover, since the gain peak shifts to shorter wavelengths as the carrier density is increased, this model is only accurate for small changes in the carrier density around a particular operating point.

A much-improved empirical model which employs a third-order polynomial to approximate the wavelength dependence of the gain has recently been presented [2.10]. This model has been used to model device gain over a wide range of carrier densities ($0.8 \cdot 10^{24} \text{m}^{-3}$ to $3.25 \cdot 10^{24} \text{m}^{-3}$) and a wide range of wavelengths (1450 nm to 1650 nm). The model does not describe the effects of temperature on the material gain, however. These effects are particularly important when studying the dynamic response of a semiconductor to optical pulses with durations less than a few picoseconds.

2.4 Carrier-Induced Refractive Index

The carrier-induced refractive index in a semiconductor may be related to the carrier-induced gain (or absorption) via the Kramers-Kronig relations [2.11, 2.12]. The Kramers-Kronig relations are a direct result of the causal, bounded nature of the material response to an incident electromagnetic field. They state that the refractive

index in a medium, $n(\omega)$, is related to the gain, $g(\omega)$, via the integral transformation

$$n(\omega) = 1 - \frac{c}{\pi} \mathcal{P} \int_0^\infty \frac{g(\Omega)}{\Omega^2 - \omega^2} d\Omega, \quad (2.25)$$

where \mathcal{P} indicates the Cauchy principal value of the integral. A concise derivation of this result, along with a review of its applications to nonlinear optics, may be found in [2.13].

Calculation of the refractive index using Equation 2.25 requires calculation of the frequency-dependent gain for all frequencies. In this case, the two-band model for the gain described in Section 2.3 is not sufficient and the gain and absorption due to electron transitions between higher energy bands must also be considered. However, the applications considered in this work do not require calculation of the total refractive index. Rather, we are primarily interested in calculating the change in refractive index associated with changes in the carrier distributions of the conduction and valence bands. In this case, the change in refractive index, $\Delta n(\omega)$, may be specified in terms of the associated change in gain, $\Delta g(\omega)$, as

$$\Delta n(\omega) = -\frac{c}{\pi} \int_0^\infty \frac{\Delta g(\Omega)}{\Omega^2 - \omega^2} d\Omega'. \quad (2.26)$$

Note that the changes in gain due to stimulated emission and carrier heating are generally confined to a small range of frequencies near the bandgap frequency of the semiconductor. Thus, $\Delta g(\omega) \approx 0$ for $\omega < \omega_L$ and $\omega > \omega_H$. Therefore, contributions to the refractive index due to transitions between higher energy bands in the semiconductor may be neglected in Equation 2.26.

Figure 2-7 illustrates the changes in the refractive index, $\Delta n(\omega)$ which arise due to changes in the carrier density and carrier temperatures in a semiconductor. The refractive index is calculated relative to the refractive index at a carrier density of $2 \cdot 10^{24} \text{ m}^{-3}$ and a temperature of 300 K. Figure 2-7 a) shows the changes in refractive index due to changes in the carrier density at a fixed carrier temperature. Figure 2-7 b) shows the changes in refractive index associated with changes in the electron population temperature for a fixed carrier density and hole temperature.

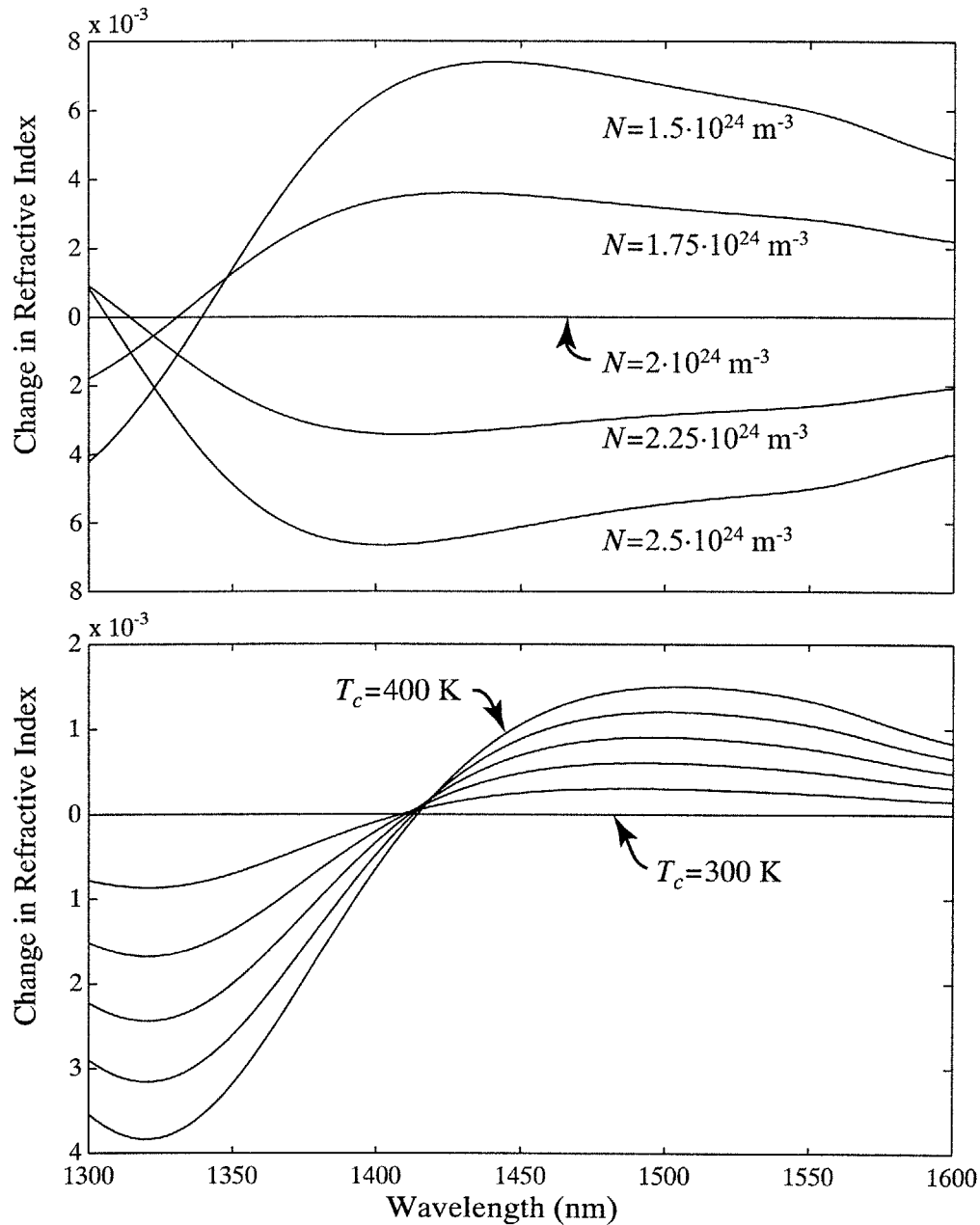


Figure 2-7: Illustration of the dependence of semiconductor refractive index on carrier density and temperature. The refractive index is calculated relative to a reference refractive index at a carrier density of $N = 2 \cdot 10^{24} \text{ m}^{-3}$ and a temperature of $T_c = T_v = 300 \text{ K}$. In a) the index is plotted for carrier densities of $N = 1.5, 1.75, 2, 2.25,$ and $2.5 \cdot 10^{24} \text{ m}^{-3}$ with carrier temperatures of $T_c = T_v = 300 \text{ K}$. In b), the index is plotted for a carrier density of $N = 2 \cdot 10^{24} \text{ m}^{-3}$ and conduction band temperatures of $T_c = 300, 320, 340, 360, 380,$ and 400 K . The valence band carrier temperature is $T_v = 300 \text{ K}$.

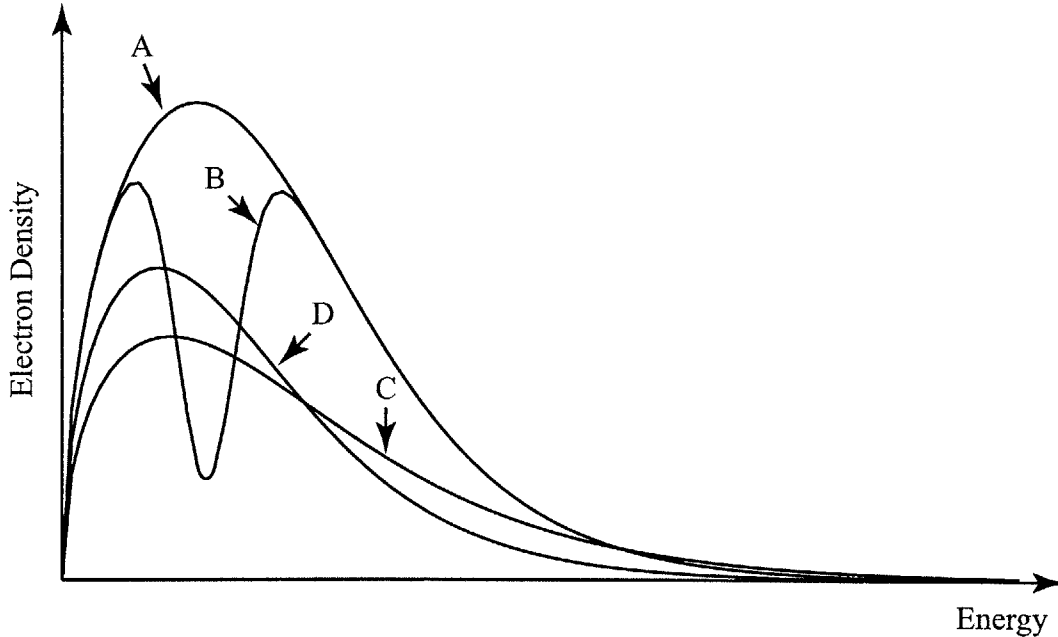


Figure 2-8: Illustration of carrier dynamics in a semiconductor optical amplifier

2.5 Carrier Dynamics in Semiconductors

The model presented above provides a useful description of the gain (or absorption) that arises in a semiconductor due to the interband interaction of an optical field with the carrier populations of the semiconductor. In this section, we extend this model to describe the dynamic effects caused by a time-varying optical intensity propagating in a semiconductor optical amplifier. The dynamic gain changes in InGaAsP semiconductor optical amplifiers have been studied extensively, both theoretically (e.g. [2.14], and references therein) and experimentally (e.g. [2.15], and references therein). These effects are primarily due to changes in the distribution of carriers in the bands. These changes are depicted in Figure 2-8. Curve A shows the steady state distribution of conduction band electrons in the semiconductor (given by $f_c(E)\rho_c(E)$). As discussed in the previous section, this distribution is described by a Fermi-Dirac distribution of electrons among the available energy levels. The distribution is a function of the quasi-Fermi energy, E_{Fc} , and the temperature of the electrons, T_c .

The transmission of a short optical pulse at a wavelength which experiences gain

in the semiconductor modifies the distribution of carriers as shown in Curve B. This distribution differs from the steady state distribution in three ways. First, carriers are depleted in a narrow energy region corresponding to the electron momentum, k , where the energy difference between the conduction and valence Bloch states is equal to the photon energy of the optical excitation. This nonuniform depletion of carriers at a specific energy level is known as spectral hole burning and is a consequence of the inhomogeneously broadened nature of the semiconductor gain medium. Second, the electron density has decreased due to recombination from stimulated emission. Finally, the total energy density of the electron population has been altered due to the removal of electrons via stimulated recombination and the injection of high-energy electrons via free carrier absorption.

This non-equilibrium distribution of carriers then relaxes to a Fermi-Dirac distribution via carrier-carrier scattering processes after a period of $\sim 50 - 100$ fs. This carrier density is shown in Curve C. The quasi-Fermi level and temperature of this distribution differ from the original distribution. The total carrier density remains depleted from its original level. Thus, the quasi-Fermi level of this distribution will be smaller than the unsaturated quasi-Fermi level. Additionally, the temperature of the remaining carriers is generally elevated above the lattice temperature. There are several explanations for this carrier heating. First, free carrier absorption increases the total energy density of the electron population by exciting carriers to higher energies within the band. Second, recombination via stimulated emission removes carriers near the band edge which are generally “cooler” than the average carrier in the band. These effects on the energy density are collectively referred to as “carrier heating” [2.16].

Next, the distribution “cools” to the lattice temperature via electron-phonon scattering. This happens over a period of $\sim 500 - 1000$ fs and the resulting carrier distribution is shown in Curve D. At this point, the carrier temperature has relaxed to the lattice temperature, but the quasi-Fermi energy for the population remains reduced due to the depleted number of carriers in the band. Finally, the depleted population recovers to the original unsaturated carrier density shown in Curve A via electrical

or optical injection of free carriers into the active region. The rate of this recovery is determined by the rate of injection of free carriers and the spontaneous recombination rates in the active region, typically ~ 100 ps – 1 ns.

We restrict the present analysis to the propagation of optical pulses with durations greater than a few hundred femtoseconds. Thus, the effect of spectral hole burning may be treated adiabatically [2.17]. In this case, we can assume that the carriers are always described by Fermi-Dirac distributions and their dynamics can be modeled by considering the evolution of the Fermi-energies and the carrier temperatures. The effects of carrier depletion and carrier heating are described using rate equations for the carrier density and the carrier energy density. Here, we express the rate equations phenomenologically, although similar equations may be obtained via a more formal semiclassical derivation using the density matrix [2.14].

The evolution of the carrier density, $N(z, t)$, at a longitudinal point, z , in the amplifier is described by the rate equation

$$\frac{\partial N}{\partial t} = \frac{\eta I}{qV} - R(N) + D\nabla^2 N - v_g g S. \quad (2.27)$$

The first term on the right-hand side of Equation 2.27 represents the rate of injection of free carriers into the active region of volume V from the current, I , with efficiency η . We assume that the current is uniform along the length and width of the active region. The second term represents the spontaneous recombination rate in the semiconductor. The third term describes the effects of carrier diffusion. For the present discussion, we will neglect the effect of this diffusion term and assume that the carrier density is uniform across the transverse dimensions of the active region. This is justified due to the slow nature of the diffusion process in comparison to the other processes considered. The last term in Equation 2.27 represents the rate of recombination due to stimulated emission. Here, v_g is the group velocity of the optical signal, g is the semiconductor gain at the photon energy, and S is the incident photon density.

The spontaneous recombination term in Equation 2.27 is a sum of the recombination rates due to processes such as nonradiative recombination at defects, spontaneous

emission, and Auger recombination. Recombination at surfaces and defects in the active region produce a nonradiative recombination rate that is directly proportional to the density of electrons, $R_{\text{nr}} = A_{\text{nr}}N$. The rate of recombination due to spontaneous emission is proportional to the product of the electron density in the conduction band, N , and the hole density in the valence band, P [2.18]. In the case of an intrinsic semiconductor, $N = P$, so the total rate of spontaneous emission is given by $R_{\text{spon}} = B_{\text{spon}}N^2$. Auger recombination occurs when an electron recombines with a hole and the energy released from that recombination excites a second electron (hole) to a higher energy level within the conduction (valence) band. Auger recombination can be a very important process in narrow-gap semiconductors. It has recently been used to explain the observation of longitudinal carrier temperature variations of over 60K in semiconductor optical amplifiers operating at 1.55 μm [2.19]. The calculated rate of Auger recombination is approximately $R_{\text{aug}} = C_{\text{aug}}N^3$ [2.20]. Room temperature measurements of the Auger recombination constant in InGaAsP at 1.55 μm give $C_{\text{aug}} \approx 7.5 \cdot 10^{-41} \text{m}^6/\text{s}$ [2.21]. Thus, the total rate of recombination from processes other than stimulated emission is expressed as

$$R(N) = A_{\text{nr}}N + B_{\text{spon}}N^2 + C_{\text{aug}}N^3. \quad (2.28)$$

For small perturbations in the carrier density, the spontaneous emission rate is sometimes expressed as $R(N) = N/\tau_c$. In this case, τ_c is the carrier lifetime and is approximately equal to the amount of time required for the carrier density to recover to its unsaturated level. Typical values for τ_c range from several hundred picoseconds to a few nanoseconds. Since these lifetimes are generally longer than the bit period in OTDM transmission systems, the carrier density saturation fluctuates with the data pattern, leading to undesirable pulse amplitude modulation at the output of the amplifier. We address these effects in more detail in Chapter 4.

Temperature dynamics in the semiconductor may be modeled using the carrier energy density. The carrier energy density represents the total energy per unit volume in a particular band. The energy density for electrons in the conduction band, $U_c(z, t)$,

is

$$U_c = \int_0^\infty E_c \rho_c(E_c) f_c(E_c) dE_c. \quad (2.29)$$

Similarly, for holes in the valence band, we can express the energy density as

$$U_v = \int_0^\infty E_v \rho_v(E_v) [1 - f_v(E_v)] dE_v. \quad (2.30)$$

Because, the effective masses of the valence and conduction bands differ, the energy density of the electrons in the conduction band will generally be different from the energy density of the holes in the valence band. The larger effective mass of the valence band holes implies that the occupied states will be concentrated near the band edge leading to a smaller energy density in the valence band than in the conduction band.

The evolution of the carrier energy density for the conduction or valence band is described by the rate equation

$$\frac{\partial U_{\{c,v\}}}{\partial t} = \sigma_{\{c,v\}} N \hbar \omega_0 v_g S - g E_{\{c,v\}} v_g S - \frac{U_{\{c,v\}} - U_{\{c,v\}}^L}{\tau_{h\{c,v\}}}. \quad (2.31)$$

The first term on the right-hand side of Equation 2.31 describes the effect of free carrier absorption on the energy density. The rate of free carrier absorption per unit volume is expressed as a product of the absorption cross-section, $\sigma_{\{c,v\}}$, the carrier density, N , and the photon flux, $v_g S$. Each photon absorbed contributes an energy of $\hbar \omega_0$ to the total energy density. The second term in equation 2.31 describes the effect of stimulated emission on the energy density. Each stimulated emission event removes an electron with energy $E_{\{c,v\}}$ from the population. The final term in Equation 2.31 describes the relaxation of the energy density to the lattice-temperature energy density, $U_{\{c,v\}}^L$. Note that the lattice-temperature energy density is dependent on the carrier density, N . The rate of this relaxation is determined by the electron-phonon interaction time, $\tau_{h\{c,v\}}$. Typically, $\tau_{h\{c,v\}} < 1$ ps.

Equations 2.27 and 2.31 describe the evolution of the carrier density, $N(z, t)$, and the energy densities, $U_{\{c,v\}}(z, t)$, respectively, in response to an incident photon flux,

$S(z, t)$, with photon energy $\hbar\omega_0$. The quasi-Fermi levels and carrier temperatures for the bands can be determined from the carrier density and the energy density using Equations 2.8, 2.9, 2.29, and 2.30. Thus, the gain and index in the semiconductor, $g(z, t)$ and $n(z, t)$, can be determined as a function of $N(z, t)$ and $U_{\{c,v\}}(z, t)$. The propagation of the photon density, $S(z, t)$, in a reference frame traveling with at the group velocity of the signal is described by the traveling wave equation

$$\frac{\partial S}{\partial z} = (\Gamma g(z, t) - \alpha_{\text{int}})S, \quad (2.32)$$

where Γ is the confinement factor for the waveguide and α_{int} is the internal loss of the waveguide. The phase of the of the field is described by

$$\frac{\partial \phi}{\partial z} = \frac{2\pi}{\lambda}n(z, t), \quad (2.33)$$

where λ is the wavelength of the incident field. These propagation equations are derived in more detail in Appendix A. Together, Equations 2.27, 2.31, 2.32, and 2.33 constitute a general model for describing the propagation of optical pulses in a semiconductor optical amplifier.

2.6 Numerical Modeling

In order to calculate the dynamic response of the SOA to a specified signal at the input, $S(0, t)$, the dynamic equations presented above must be solved numerically. To do this, we discretize the equations in time, t , and the longitudinal coordinate, z . Specifically, the SOA is divided into longitudinal segments of length Δz , as shown in Figure 2-9. In each segment, the dynamic variables describing the semiconductor state, N , U_c , and U_v , are assumed to have no variation with respect to the longitudinal coordinate, z . Thus, the segments must be short enough so that variations in the incident optical intensity are small over the length of the segment. In order to calculate the effects of counterpropagating fields in the SOA, the time discretization, Δt , is related to Δz by $\Delta t = \Delta z/v_g$. Thus, Δt is equal to the propagation time for the field

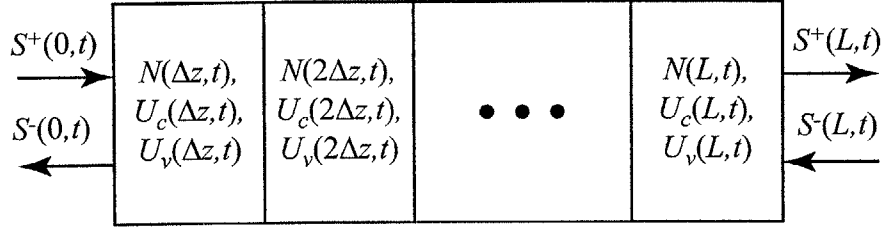


Figure 2-9: Illustration of SOA with discretized longitudinal sections

in a single segment. In solving these equations, we assume that the signal propagating from left to right, $S^+(z, t)$, is much more intense than the counterpropagating signal, $S^-(z, t)$. The equations are then solved by first determining the dynamic response of the SOA with only the signal $S^+(z, t)$ at the input. Then, the effect of the dynamic SOA response is calculated for the counterpropagating signal, assuming that it does not further saturate the state variables.

Figure 2-10 shows a flow chart illustrating the procedure used to calculate the dynamic response of the SOA in each segment. In the j -th segment, the state variables are calculated as a function of time by numerically integrating Equations 2.27 and 2.31 with the photon density $S^+((j-1)\Delta z, t)$ as the input. In the process of integrating these equations, the small signal gain, $g(j\Delta z, t)$, must be calculated for each time step, $k\Delta t$. This is done by first propagating the state variables, N , U_c , and U_v . At each time step, the semiconductor statistical parameters, $E_{F\{c,v\}}$ and $T_{\{c,v\}}$, are calculated by inverting the Fermi integrals in Equations 2.8, 2.9, 2.29, and 2.30. A computationally efficient technique for performing this inversion is described in Section 2.6.1, below. The frequency-dependent gain for the segment can then be calculated using Equation 2.17. Since calculation of the refractive index using the Kramers-Kronig relations is very time consuming, a look-up table is used to determine the refractive index at each step. After the gain for each time step in the segment is determined, the photon density at the output of the segment is calculated as

$$S(j\Delta z, k\Delta t) = S((j-1)\Delta z, k\Delta t) \exp [(\Gamma g(j\Delta z, k\Delta t) - \alpha_{\text{int}}) \Delta z] \quad (2.34)$$

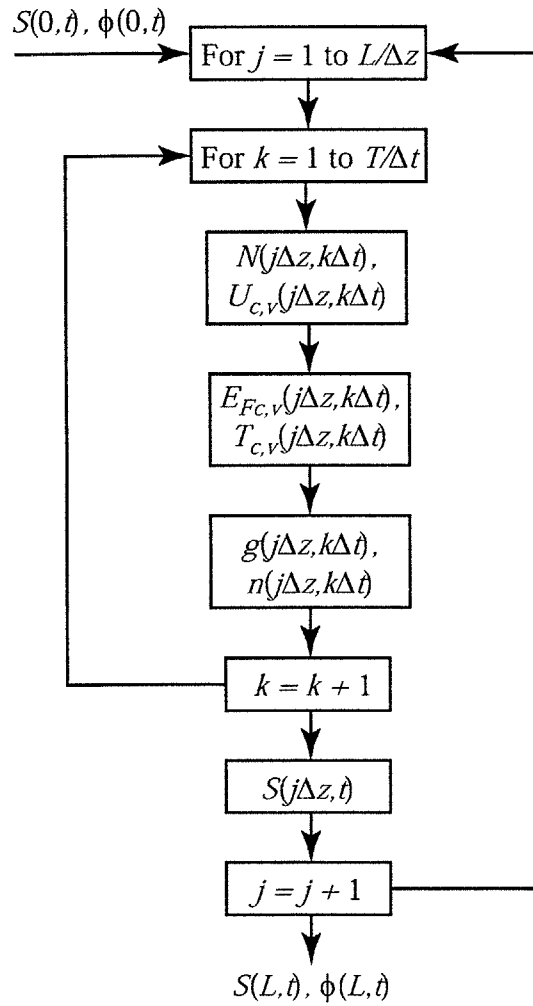


Figure 2-10: Flow chart used for calculation of dynamic response of SOA.

At the output of the amplifier, the photon density and phase shift for the copropagating fields are given by

$$S^+(L, k\Delta t) = S(0, k\Delta t) \exp \left[\sum_{j=1}^{L/\Delta z} (\Gamma g(j\Delta z, k\Delta t) - \alpha_{\text{int}}) \Delta z \right] \quad (2.35)$$

and

$$\phi^+(L, k\Delta t) = \frac{2\pi}{\lambda} \sum_{j=1}^{L/\Delta z} n(j\Delta z, k\Delta t) \Delta z. \quad (2.36)$$

Similarly, the photon density and phase shift for the counterpropagating fields may be expressed as

$$S^-(L, k\Delta t) = S(0, k\Delta t) \exp \left[\sum_{j=1}^{L/\Delta z} (\Gamma g(j\Delta z, k\Delta t + 2(L - j\Delta z)/v_g) - \alpha_{\text{int}}) \Delta z \right] \quad (2.37)$$

and

$$\phi^-(L, k\Delta t) = \frac{2\pi}{\lambda} \sum_{j=1}^{L/\Delta z} n(j\Delta z, k\Delta t + 2(L - j\Delta z)/v_g) \Delta z. \quad (2.38)$$

Before continuing our discussion, let us review a few of the primary assumptions made in the development of this numerical model. First, we have neglected certain saturation effects, such as spectral hole burning and two photon absorption. These effects play an important role in the propagation of high-intensity subpicosecond pulses in SOAs (see, for example, [2.22]). However, the optical pulses considered in this work are typically several picoseconds in duration. So, these effects can either be treated adiabatically (i.e. as an instantaneous intensity-dependent reduction in the gain) or neglected entirely. In the calculations presented below, the optical pulse intensities are low enough that, even in the adiabatic approximation, spectral hole burning effects on pulse propagation are negligible.

We have also assumed that the primary saturation effects are due to the strong pump signal propagating from left to right in the SOA. We have neglected the saturation effects due to the counterpropagating fields. Additionally, we have neglected the effects of amplified spontaneous emission (ASE) in the amplifier. These assumptions are valid in typical optical switching applications where a strong pump signal propagates in one direction in the amplifier and the effects of this pump are observed using a low intensity probe pulse. In this situation, the saturation effects of the counterpropagating signals and ASE are negligible in comparison to the pump-induced transients. However, for long SOAs (> 1 mm), or weaker input signals, counterpropagating ASE can lead to reduced gain at the input side of the amplifier. We note that the model described here, which includes the frequency-dependence of the saturated gain, can be easily modified to describe the propagation of guided ASE in the waveguide.

Finally, we have assumed that the injected current density is uniform along the length of the SOA. Since the model allows for longitudinal variations in the carrier densities and the associated longitudinal variations in the junction voltage (which may be determined as a function of the quasi-Fermi level separation between the bands), neglecting longitudinal variations in the injection current is tantamount to assuming an infinite contact resistance to the semiconductor device. Recently, static models have been proposed which more accurately describe the effects of a finite contact resistance [2.23].

In spite of these numerous assumptions this numerical model provides an accurate description of the gain transients which arise in a typical semiconductor-based all-optical switch. Below, we describe the utilization of this model to predict gain transients in a commercially available SOA. The predictions of the model are validated using experimental pump-probe measurements of the gain transients.

2.6.1 Calculation of Quasi-Fermi Energy and Carrier Temperature

As discussed in Section 2.3, when the carrier distributions in the valence and conduction bands are described by Fermi-Dirac statistics, the optical gain in a semiconductor is a function of the quasi-Fermi energies and temperatures in the conduction and valence bands. In the rate equation analysis presented above, the state of the carrier populations in the bands is described by the carrier number density, $N(z, t)$, and the carrier energy density, $U_{\{c,v\}}(z, t)$. Thus, in order to determine the gain at a particular point in the amplifier, the Fermi energies and carrier temperatures in the bands must be calculated for a specified N and U . This task is done by solving Equations 2.8, 2.9, 2.29, and 2.30 for $E_{F\{c,v\}}$ and $T_{\{c,v\}}$. Since this calculation is identical for the conduction band and the valence band, we shall drop the subscript $\{c, v\}$ notation in the following discussion. We first rewrite these Equation 2.8 (or Equation 2.9) as

$$N = \frac{1}{4} \left(\frac{2m}{\pi \hbar^2} \right)^{3/2} (k_B T)^{3/2} \mathcal{F}_{1/2}(\mu) \quad (2.39)$$

and Equation 2.29 (or 2.30) as

$$U = \frac{3}{8} \left(\frac{2m}{\pi \hbar^2} \right)^{3/2} (k_B T)^{5/2} \mathcal{F}_{3/2}(\mu), \quad (2.40)$$

where m is the effective mass of the free carriers in the band under consideration and $\mu = E_F/k_B T$ is the reduced quasi-Fermi energy for the band. The generalized Fermi-Dirac integral of order k is defined as

$$\mathcal{F}_k(\mu) = \frac{1}{\Gamma(k+1)} \int_0^\infty \frac{\epsilon^k}{1 + \exp(\epsilon - \mu)} d\epsilon, \quad (2.41)$$

where $\Gamma(x)$ is the Gamma function. The Fermi-Dirac integrals, especially those of half-integer order, arise often in the study of fermions. Consequently, techniques for numerical evaluation of the Fermi-Dirac integrals have received much attention (see, for example, [2.24–2.27] and references therein). Efficient algorithms for the

inversion of the Fermi-Dirac integral of order 1/2 have also been developed to allow calculation of the Fermi energy for a specified carrier density [2.28–2.30]. However, these algorithms require prior knowledge of the carrier temperature and, therefore, do not apply directly to the problem considered here.

We wish to solve Equations 2.39 and 2.40 for the carrier temperature, T , and the reduced Fermi energy, μ . To do this, we first define a dimensionless quantity ν which is a function of the carrier density, N , and the energy density, U , but is only explicitly dependent on the reduced Fermi energy, μ :

$$\begin{aligned}\nu(\mu) &= 2 \left(\frac{3\pi\hbar^2}{m} \right)^3 \frac{N^5(\mu, T)}{U^3(\mu, T)} \\ &= \frac{\mathcal{F}_{1/2}^5(\mu)}{\mathcal{F}_{3/2}^3(\mu)}\end{aligned}\tag{2.42}$$

For a specified, ν , which may be calculated, given N and U , we wish to find the corresponding reduced Fermi energy, $\mu = \mu(\nu)$, by inverting Equation 2.42. In general, this inversion must be done numerically.

Figure 2-11 shows the quantity ν plotted as a function of μ . We note several features of $\nu(\mu)$ which may be useful in solving for μ . First, ν is a monotonically increasing function of μ . Thus, it can be inverted. Moreover, this feature makes efficient inversion of the function via table lookup possible, although this is not the technique used here. Additionally, the range of ν is limited to $(0, 250/9\pi)$. The lower bound of this range is obtained by noting that the Fermi-Dirac integrals are always non-negative and tend toward 0 as $\mu \rightarrow -\infty$. The upper bound is found by observing that as $\mu \rightarrow \infty$,

$$\mathcal{F}_k(\mu) \rightarrow \frac{1}{\Gamma(k+1)} \frac{\mu^{k+1}}{(k+1)}.\tag{2.43}$$

To calculate $\mu(\nu)$, we use an approximation based on Chebyshev polynomials similar to the technique employed by Macleod to calculate the Fermi-Dirac integrals [2.27]. First, we note that the Fermi-Dirac integrals can be represented using power series for certain ranges of μ . For the nondegenerate case ($\mu < 0$) with $k > -1$, the

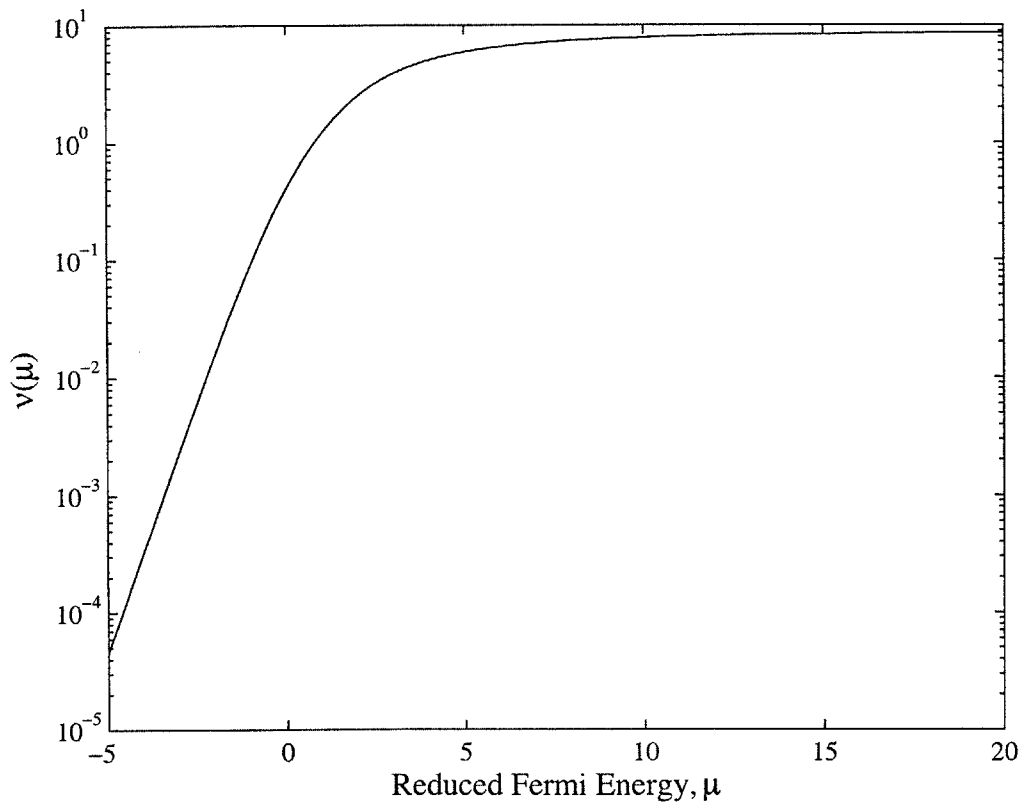


Figure 2-11: The dimensionless parameter ν plotted as a function of the reduced Fermi energy, μ .

integrand in Equation 2.41 can be expanded as a convergent Taylor series in $\exp(\mu - \epsilon)$ to obtain

$$\mathcal{F}_k(\mu) = \sum_{n=1}^{\infty} (-1)^{n-1} \frac{\exp(n\mu)}{n^{k+1}}. \quad (2.44)$$

For μ near 0, a Taylor series expansion of $\mathcal{F}_k(\mu)$ around $\mu = 0$ gives a convergent series for $-\pi < \mu < \pi$ [2.25],

$$\mathcal{F}_k(\mu) = \sum_{n=0}^{\infty} \frac{(1 - 2^{n-k})\zeta(k+1-n)}{n!} \mu^n, \quad (2.45)$$

where $\zeta(x)$ is the Riemann zeta function [2.31]. For the degenerate case ($\mu > 0$), no convergent series expression for $\mathcal{F}_k(\mu)$ is known. However, the following asymptotic expansion, due to Sommerfeld [2.32], is valid for half-integer k

$$\mathcal{F}_k(\mu) \sim \frac{\mu^{k+1}}{\Gamma(k+2)} \left(1 + \sum_{n=1}^{\infty} a_{2n} \mu^{-2n} \right), \quad (2.46)$$

where

$$a_{2n} = \frac{(1 - 2^{1-2n})(k+1)!(2\pi)^{2n} |B_{2n}|}{(k+1-2n)! (2n)!}, \quad (2.47)$$

and B_{2n} are the even Bernoulli numbers [2.31]. This asymptotic expression was later generalized to all possible values of k by Dingle [2.25].

Since $\nu(\mu)$ is a monotonically increasing function of μ , the ranges of μ for which Equations 2.44, 2.45, and 2.46 are valid have corresponding continuous ranges for ν . Specifically, $\mu < 0$ implies $\nu < \nu(0)$, $-\pi < \mu < \pi$ implies $\nu(-\pi) < \nu < \nu(\pi)$, and $\mu > 0$ implies $\nu > \nu(0)$. To find $\mu(\nu)$ for each of these ranges of ν , the corresponding series expansion for $\mathcal{F}_k(\mu)$ may be substituted into Equation 2.42 to obtain a series expression for ν in terms of powers of μ . Reversion of this series to solve for μ suggests

the following forms for a Chebyshev polynomial approximation of $\mu(\nu)$

$$\mu(\nu) = \begin{cases} \frac{1}{2} \ln \nu + \sqrt{\nu} g_1(t_1(\sqrt{\nu})), & \text{if } 0 < \nu \leq a, \\ g_2(t_2(\nu)), & \text{if } a < \nu \leq b, \\ \frac{1}{\sqrt{\nu_{\max} - \nu}} g_3(t_3(\nu_{\max} - \nu)), & \text{if } b < \nu < \nu_{\max}, \end{cases} \quad (2.48)$$

where $\nu_{\max} = 250/9\pi$ and the g_i are truncated series of Chebyshev polynomials. The functions $t_i(x)$ map the range of x into the interval $[-1, 1]$. In accordance with the discussion above, the limits for the different expansions, a and b , must be chosen so that $\nu(-\pi) < a < \nu(0)$ and $\nu(0) < b < \nu(\pi)$. Ideally, a and b should be chosen to optimize the approximation in terms of accuracy and required time for computation. For this work, we select $a = 0.4$ and $b = 3$. For these choices of a and b , we determine the minimum number of terms required in the Chebyshev polynomial series to give the desired relative error performance of 10^{-5} . Due to the method we have employed in determining the form of the Chebyshev series expansions for $\mu(\nu)$, very few terms are needed to meet this performance criterion. For g_1 , g_2 , and g_3 we find that 5, 16, and 8 terms are required, respectively. The details of these terms are included in Appendix B.

After calculating the reduced Fermi energy, the carrier temperature may be obtained using Equation 2.39

$$T = \frac{2mk_B}{\pi\hbar^2} \left(\frac{4N}{\mathcal{F}_{1/2}(\mu)} \right)^{2/3}. \quad (2.49)$$

In calculating T , we use Macleod's algorithm [2.27] to calculate the Fermi-Dirac integral, $\mathcal{F}_{1/2}(\mu)$, to floating point precision.

We have extensively evaluated the error performance of this estimation procedure. For specified μ and T , carrier densities and energy densities were calculated and Equations 2.48 and 2.49 were then used to calculate estimated values of the reduced Fermi energy and the carrier temperature. Over a range of temperatures $200 < T < 500$ and reduced Fermi energies $-8 < \mu < 17$ (corresponding to carrier densities

Description	Notation	Value	Units
Length	L	$8 \cdot 10^{-4}$	m
Cross-sectional area	A	$2.4 \cdot 10^{-13}$	m^2
Optical confinement factor	Γ	0.4	—
Internal loss	α_{int}	3000	m^{-1}
Input, output coupling loss	$\eta_{\text{in}}, \eta_{\text{out}}$	3	dB
Nonradiative recombination constant	A_{nr}	$5 \cdot 10^8$	s^{-1}
Bimolecular recombination constant	B_{spon}	$1 \cdot 10^{-16}$	$\text{m}^3 \text{s}^{-1}$
Auger recombination constant	C_{aug}	$5 \cdot 10^{-41}$	$\text{m}^6 \text{s}^{-1}$
Lattice temperature	T_L	300	K
FCA cross-section, conduction band	σ_c	$4 \cdot 10^{-22}$	m^2
FCA cross-section, valence band	σ_v	0	m^2
Electron-phonon scattering time	$\tau_{\{c,v\}}$	$1 \cdot 10^{-12}$	s
Pump Wavelength	λ_{pump}	$1.545 \cdot 10^{-6}$	m
Probe Wavelength	λ_{probe}	$1.550 \cdot 10^{-6}$	m

Table 2.2: Device parameters used in simulations.

between 10^{20} and 10^{25} m^{-3} over this temperature range), the maximum relative error in the estimated Fermi energy and carrier temperature was less than 10^{-5} . This range of values more than covers the operating range for an SOA in a typical all-optical switching application.

2.6.2 Example Calculations

We have used this model to simulate the effects of a strong pump pulse on the transmission of a weaker probe signal in an SOA. For these calculations, we assume that the pump pulse is a 2-ps Gaussian pulse with a center frequency of 1545 nm. To simulate the saturation effects encountered in our optical switching experiments, we set the pump pulse repetition rate to 12.5 GHz. Since the 80-ps period for the pump pulses is much shorter than the recovery time for the carrier density dynamics, the carrier density never recovers to its unsaturated level. The probe in the simulation is a continuous-wave signal with an average input power of 150 μW and a center frequency of 1550 nm. In this manner, the gain dynamics induced by the pump pulse can be observed directly on the signal envelope at the output of the SOA. Table 2.2

lists the other SOA parameters used in the simulation. The device parameters are taken from published literature on the Alcatel SOA described in Section 2.7.

In Figure 2-12 we show the simulated gain experienced by the probe signal in the SOA. We have performed the simulation for both copropagating and counterpropagating pump and probe signals. In the calculations, the pump pulse energy is varied from 0.8 fJ to 800 fJ. The arrival of the pump pulse is accompanied by a reduction in the signal gain due to saturation of the carrier density and carrier heating. The carrier heating is observed as a fast depletion in the gain which recovers with a 1-ps time constant. The carrier density saturation recovers much more slowly. Because the carrier density does not fully recover in a single period, the gain becomes more saturated as the pump pulse energy is increased.

The shape of the gain transients for the copropagating experiment and the counterpropagating experiment differ substantially. This difference is primarily due to longitudinal variations in the SOA gain. In the copropagating case, the probe signal propagates along with the pump pulse, leading to a fast gain transient with a rise time proportional to the pump pulse duration (2 ps). In the counterpropagating case, the rise time for the gain transient is much slower. This can be explained by observing that, as the pump and probe signals counterpropagate in the SOA, the pump pulse passes through a probe field of duration equal to two times the transit time of the SOA. Thus, the time delay between the probe field that exits the SOA just as the pump pulse is entering (and, therefore, only begins to experience the effects of the pump-pulse-induced saturation) and the probe field that enters the SOA just as the pump pulse is exiting (and, therefore, experiences the fully saturated SOA) is equal to twice the transit time of the SOA. Therefore, the SOA transit time limits the minimum risetime for the gain transients in a counterpropagating configuration. In Chapter 3 we study the impact that these transients have on the performance of semiconductor-based all-optical switches.

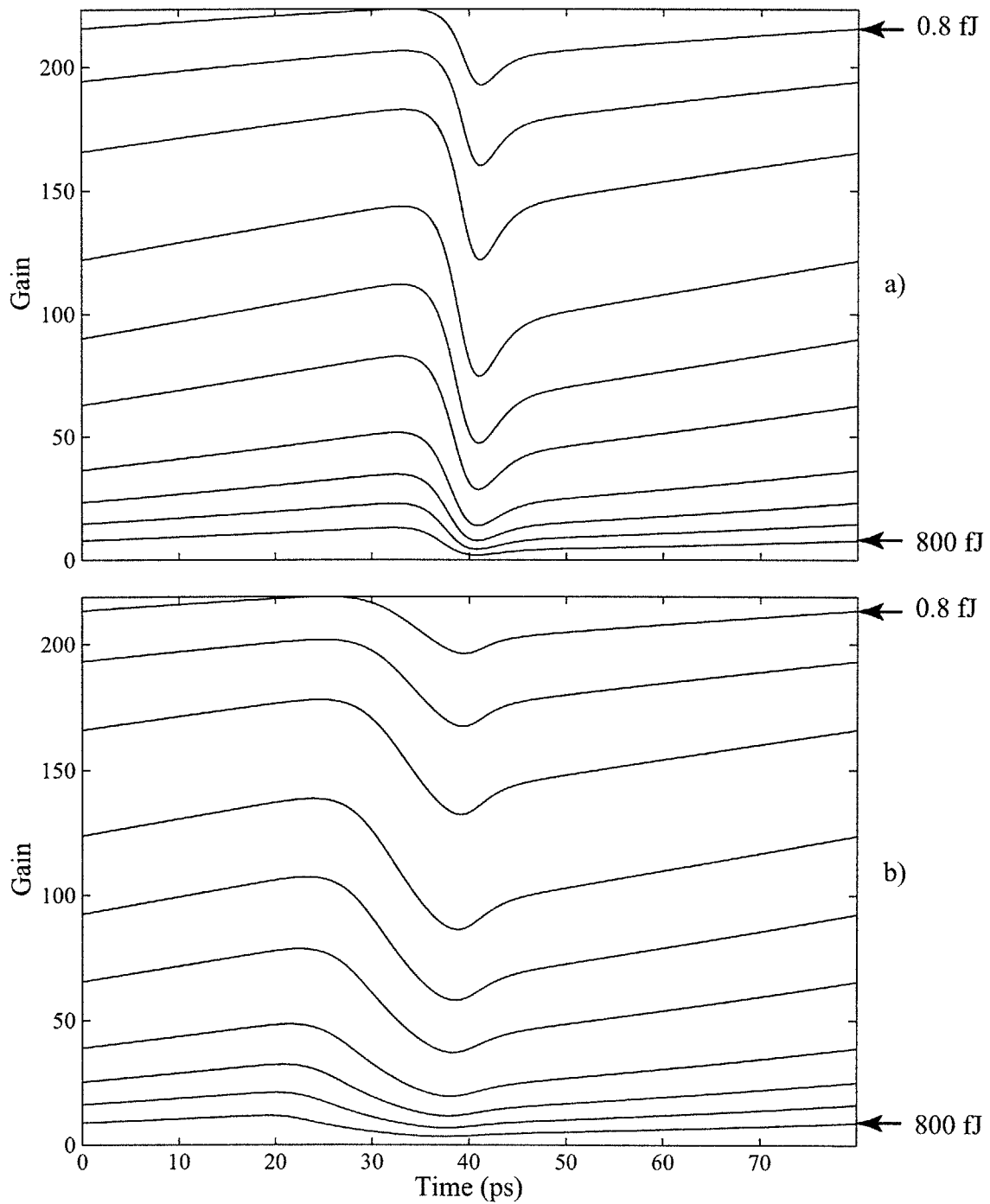


Figure 2-12: Calculated SOA gain dynamics experienced by a $150 \mu\text{W}$ continuous-wave probe a) copropagating and b) counterpropagating with respect to a 12.5-GHz repetition rate 2-ps pump pulse. The SOA current is 100 mA. The curves illustrate the gain dynamics in response to input pump pulse energies of 0.8, 1.6, 3.2, 8, 16, 32, 80, 160, 320, and 800 fJ.

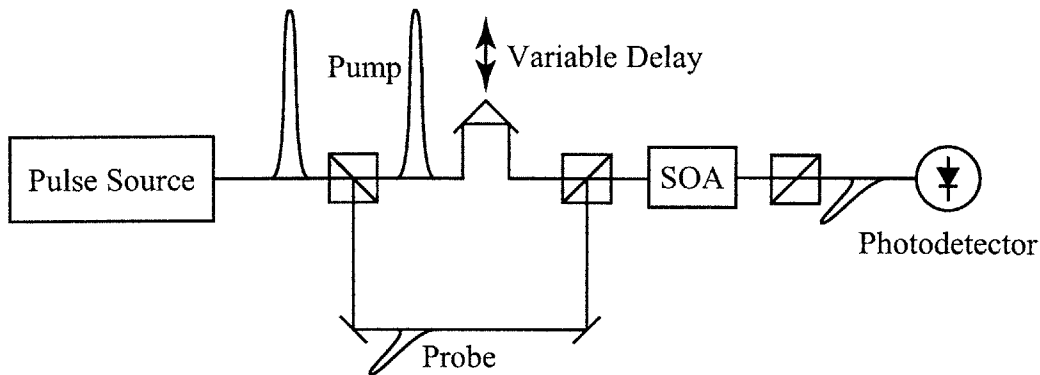


Figure 2-13: Typical copropagating pump-probe experiment.

2.7 Difference-Frequency Sampling

Because the ultrafast response of a semiconductor occurs on time-scales much too short for direct measurement using existing electronic test equipment, novel techniques must be employed to indirectly observe the time-domain response of the semiconductor. Typically, the ultrafast optical response of a material is observed using pump-probe techniques employing optical pulses with durations much shorter than the temporal response of the material [2.33]. This technique, illustrated in Figure 2-13, has been used to characterize the temporal transmission response of InGaAsP semiconductor optical amplifiers with sub-picosecond timing resolution [2.15, 2.22]. In these experiments, a high-intensity pump pulse propagating through the SOA waveguide induces changes in the transmission response of the material. A probe pulse copropagates with the pump pulse in the waveguide. Since the pump-pulse-induced gain transients are slow in comparison to the temporal width of the probe pulse, the probe pulse effectively samples the gain of the semiconductor at a specific time relative to the pump pulse. At the output of the waveguide, the effects of the pump pulse on the transmission of the probe pulse are observed. By varying the relative delay between the pump and probe pulses, the ultrafast temporal response of the semiconductor may be observed.

For the experimental work described here, we employ a different pump-probe technique, called difference-frequency sampling (DFS). A schematic of the experimental

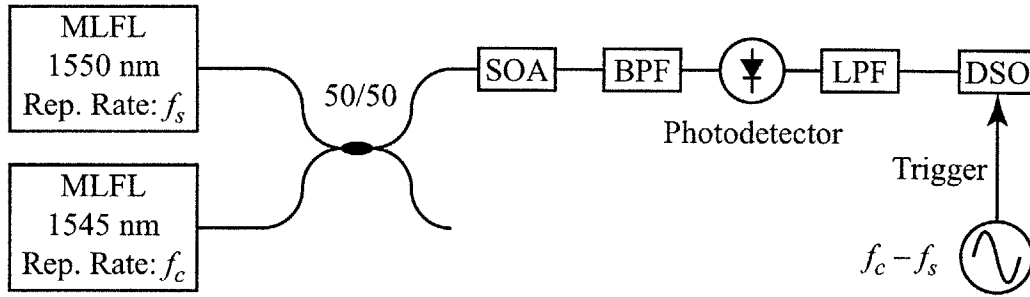


Figure 2-14: Experimental setup for characterization of gain transients in a semiconductor optical amplifier using difference-frequency sampling. MLFL: Mode-locked fiber laser; BPF: Optical bandpass filter; LPF: Electrical lowpass filter; DSO: Digital sampling oscilloscope

setup for using DFS to measure the gain transients in a semiconductor optical amplifier is shown in Figure 2-14. Consistent with the terminology used when discussing optical switching in the remainder of this dissertation, we shall refer to the pump pulses as “control” pulses and the probe pulses as “signal” pulses in the following discussion. The control pulses in the DFS experiment are provided by a mode-locked fiber laser producing a periodic stream of optical pulses with repetition rate f_c . The low-intensity signal pulses are provided by a second mode-locked fiber laser producing a periodic stream of optical pulses at a repetition rate of $f_s = f_c - \Delta f$. The two pulse streams are combined in a 50/50 fiber coupler and input to the SOA. Because of the offset frequency, Δf , between the control and signal pulse streams, the signal pulses slowly walk through the control pulses over a period of $1/\Delta f$. Consequently each signal pulse samples the gain transient induced by the control pulse at a slightly later time than the previous signal pulse. At the output of the SOA, the pulse streams are passed through a bandpass filter to remove the control pulses. The signal pulses are then photodetected with a slow detector (modeled in Figure 2-14 as a detector and a low pass filter) and the output is measured using a digital sampling oscilloscope.

Before providing a detailed analysis of the difference frequency sampling technique, we first note a few of its advantages over traditional pump-probe techniques. For instance, DFS uses no mechanical delay lines. This eases the alignment requirements as compared to a typical pump-probe experiment. In fact, using mode-locked

fiber lasers for pump sources, DFS can be implemented entirely in fiber, thereby completely eliminating free-space alignment issues. DFS also offers the advantage of fast acquisition times. In a typical pump-probe experiment, acquisition times are limited by the speed at which the variable optical delay can be moved. With DFS, the acquisition time is inversely proportional to the frequency offset. For a 1-kHz frequency offset, the acquisition time is 1 ms. One difficulty in implementing DFS is that it requires two pulse sources whose repetition rates can be tuned independently. Additionally, it may be difficult to “chop” the probe signal to improve the sensitivity of the measurement, as is often done in pump-probe measurements. For the high-saturation experiments described here, increased sensitivity is not an important issue, since the probe signal powers are easily detected at the SOA output.

To analyze the difference-frequency sampling technique, we begin by describing the signal pulse stream at the SOA input as

$$P_{\text{in}}(t) = \sum_{n=-\infty}^{\infty} p(t - nT_s), \quad (2.50)$$

where $T_s = 1/f_s$ is the signal pulse period and $p(t)$ is the intensity profile of the pulse. At the output of the SOA, the signal pulse stream is given by

$$P_{\text{out}}(t) = P_{\text{in}}(t)G_{\text{SOA}}(t), \quad (2.51)$$

where the gain of the amplifier, $G_{\text{SOA}}(t)$, is the integrated gain over the length of the SOA

$$G_{\text{SOA}}(t) = \exp \left[\int_0^L (\Gamma g(t, z) - \alpha_{\text{int}}) dz \right]. \quad (2.52)$$

We assume that the signal pulse intensity is much lower than the control pulse intensity. Thus, the gain transients in the SOA are primarily due to the control pulses

and are periodic with period $T_c = 1/f_c$. Then, we may write

$$G_{\text{SOA}}(t) = \sum_{m=-\infty}^{\infty} G(t - mT_c), \quad (2.53)$$

where $G(t)$ is the periodic gain transient induced by the control pulses.

Difference-frequency sampling is best understood in the frequency domain. Substituting Equations 2.50 and 2.53 into Equation 2.51 and taking the Fourier transform of the result, we find

$$\tilde{P}_{\text{out}}(f) = \left[\tilde{P}(f)f_s \sum_{n=-\infty}^{\infty} \delta(f - nf_s) \right] \otimes \left[\tilde{G}(f)f_c \sum_{m=-\infty}^{\infty} \delta(f - mf_c) \right], \quad (2.54)$$

where $\tilde{P}(f)$ and $\tilde{G}(f)$ are the Fourier transforms of the pulse intensity profile and the periodic gain profile, respectively. Evaluating the convolution integral and noting that $f_s = f_c - \Delta f$ we find

$$\begin{aligned} \tilde{P}_{\text{out}}(f) &= f_s f_c \sum_{n=-\infty}^{\infty} \sum_{m=-\infty}^{\infty} \tilde{P}(nf_s) \tilde{G}(mf_c) \delta(f - (n+m)f_c + n\Delta f) \\ &= f_s f_c \sum_{j=-\infty}^{\infty} \tilde{P}\left(-\frac{f_s}{\Delta f}f + j\frac{f_s f_c}{\Delta f}\right) \tilde{G}\left(\frac{f_c}{\Delta f}f - j\frac{f_s f_c}{\Delta f}\right) \\ &\quad \cdot \sum_{m=-\infty}^{\infty} \delta(f - jf_s - m\Delta f), \end{aligned} \quad (2.55)$$

where $j = m + n$. This output spectrum is illustrated in Figure 2-15.

At this point, it is useful to apply some constraints on the difference frequency, Δf . Assuming that the periodic gain transient $G(t)$, is band-limited to some interval $-f_G < f < f_G$, we require that the difference frequency satisfy

$$\Delta f < \frac{f_s f_c}{2f_G} \quad (2.56)$$

This is equivalent to the Nyquist sampling criterion and is necessary to avoid aliasing

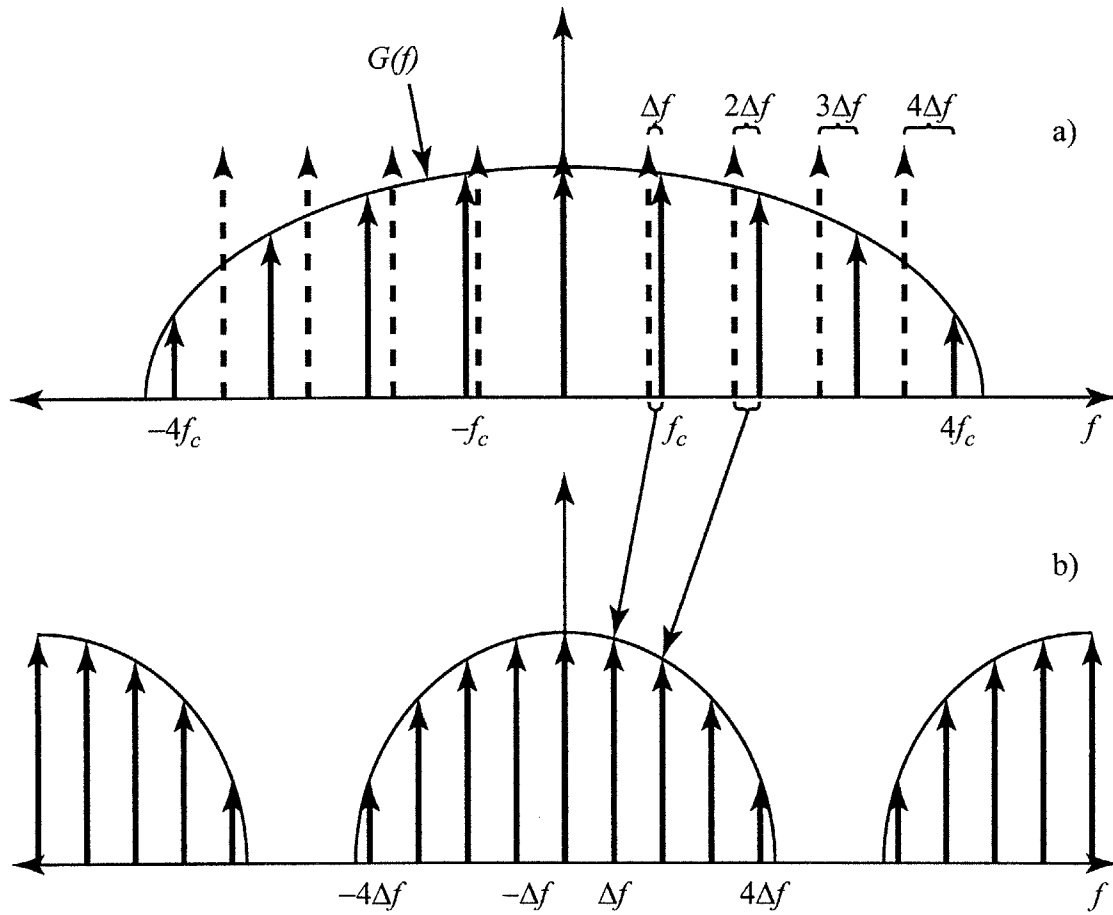


Figure 2-15: Frequency-domain illustration of difference-frequency sampling. The spectra of $\tilde{P}_{in}(f)$ and $\tilde{G}_{SOA}(f)$ are shown in a). These spectra are convolved to get the output spectrum, $\tilde{P}_{out}(f)$ shown in b). Note that the frequency axis scales differ in the two plots.

caused by undersampling. Additionally, the electrical bandwidth, f_E must satisfy

$$\frac{\Delta f f_G}{f_c} < f_E < \frac{f_c}{2}. \quad (2.57)$$

Note that the minimum required electrical bandwidth can be made arbitrarily small by decreasing the offset frequency, Δf . When these two conditions are satisfied, the output of the lowpass electrical filter consists of only the $j = 0$ terms in the summation of Equation 2.55

$$\tilde{P}_{\text{filt}}(f) = f_s f_c \tilde{P}\left(-\frac{f_s}{\Delta f} f\right) \tilde{G}\left(\frac{f_c}{\Delta f} f\right) \sum_{m=-\infty}^{\infty} \delta(f - m\Delta f) \quad (2.58)$$

Taking the inverse Fourier transform of Equation 2.58 we obtain the filtered output

$$P_{\text{filt}}(t) = \left[p\left(-\frac{\Delta f}{f_s} t\right) \right] \otimes \left[G\left(\frac{\Delta f}{f_c} t\right) \right] \otimes \left[\sum_{n=-\infty}^{\infty} \delta\left(t - \frac{n}{\Delta f}\right) \right]. \quad (2.59)$$

Thus, the output consists of a periodic train of the gain response function, $G(t)$, convolved with the sampling pulse shape and magnified in time by a factor of $f_c/\Delta f$.

We have used this technique to characterize the gain dynamics in a fiber-coupled commercial SOA (Alcatel 1901), shown in Figure 2-16 [2.34, 2.35]. The device is a separate confinement heterostructure. The active region of the SOA is a low-temperature-grown bulk InGaAsP crystal, providing an internal gain of up to 30 dB. The active region is 0.2 μm thick and 1.2 μm wide, providing an optical confinement factor of $\Gamma = 0.4$. The gain of the SOA is made polarization insensitive by applying a tensile strain of $\sim 0.15\%$ in the active region. At the input and output of the device, the active region is tapered to evanescently couple to a passive waveguide which expands the optical mode for better coupling to optical fiber. The input and output facets are angle-cleaved at 7 degrees and anti-reflection coated to reduce optical feedback in the SOA cavity.

In the DFS measurement, the control pulses were provided by an actively mode-locked fiber laser producing a 12.5-GHz stream of 2-ps pulses with a center wavelength

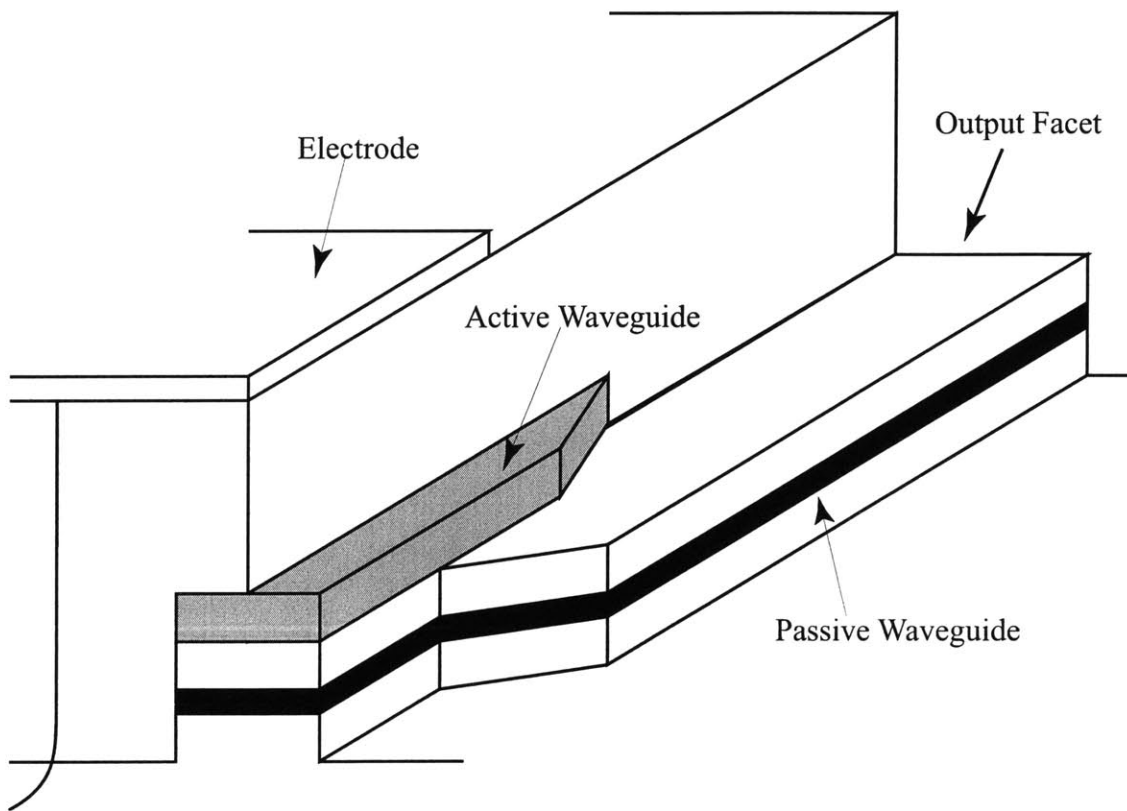


Figure 2-16: Cross-sectional diagram of an Alcatel 1901 SOA.

of 1545 nm. The signal pulses were provided by a second actively mode-locked fiber laser producing a stream of 2-ps pulses at 1550 nm. The offset frequency for the measurement was set to 50 Hz. The signal pulse energy was fixed at 0.8 fJ, while the control pulse energy was varied from 0.8 to 800 fJ. The bias current to the SOA was 100 mA. For the copropagating measurement, the experimental setup is identical to that shown in Figure 2-14. For the counterpropagating measurement, the 50/50 coupler and the signal laser are moved to the other side of the SOA. The experimental results for copropagating and counterpropagating signal and control pulses are shown in Figure 2-17. They show good qualitative agreement with the simulation results in Figure 2-12. Note, however, that the average power of the signal (probe) differs in the calculated and measured results. For the calculation, we used an average probe power of 150 μW , whereas the average signal power in the DFS measurement was 10 μW . The results are similar due to the fact that the signal pulses in the DFS measurement induce both carrier density and carrier temperature saturation. On the other hand, the continuous-wave probe in the calculation induces primarily carrier density saturation. Thus, in the calculation, higher probe powers are required to simulate the saturation induced by the signal pulses in the DFS measurement.

2.8 Conclusions

We have presented a numerical model for the dynamic gain and index saturation in a semiconductor optical amplifier. Our aim in developing this model was to accurately describe the response of the SOA using as few fitting parameters as possible. In doing this, we create a versatile model which can be used to both explain experimentally observed phenomena as well as optimize experimental operating parameters. The model presented here is distinguished from previously reported dynamic models by the way in which the SOA state is described. Other models attempt to describe the state of the SOA using the carrier density, which is a physical parameter, and the carrier temperatures in the conduction and valence bands, which are statistical parameters. The evolution of statistical parameters, such as the carrier temperature,

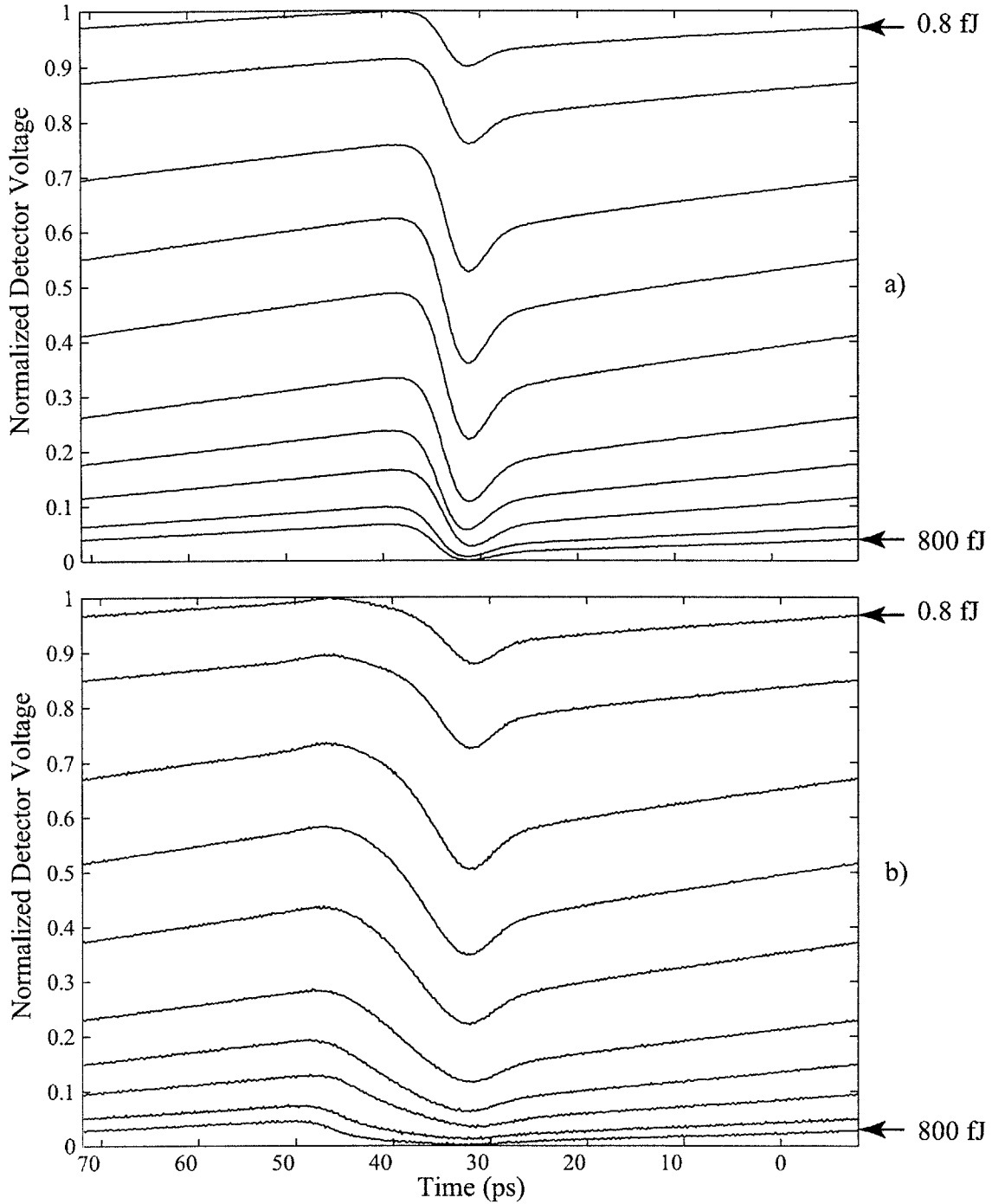


Figure 2-17: Experimental measurement of a) copropagating and b) counterpropagating gain dynamics in an Alcatel 1901 SOA with a bias current of 100 mA. The signal pulse energy is 0.8 fJ. Starting from the top, the curves represent the gain dynamics in response to a 12.5-GHz stream of 2-ps control pulses with energies of 0.8, 1.6, 3.2, 8, 16, 32, 80, 160, 320, and 800 fJ.

in response to an incident optical field can only be described using perturbational techniques. Consequently, these models are only accurate for small changes in the SOA state near a specified operating point.

In the model developed here, we describe the state of the SOA entirely using physical parameters such as the carrier density and the carrier energy density. The evolution of these physical parameters in response to an incident optical field is straightforward to express and calculate. We have presented an efficient numerical technique for inverting the Fermi-Dirac integrals to obtain the the statistical parameters needed to describe the distribution of carriers in the bands of the SOA. Once these statistical parameters are known, the frequency-dependent gain of the SOA may be directly calculated. This model provides an accurate description of the dynamic gain effects in the SOA for a wide range of saturation levels.

To test the validity of the model for operating conditions similar to those encountered in an SOA-based all-optical switch, we have performed pump-probe measurements of the gain in the SOA. To simulate the gain transients which may be encountered in an all-optical demultiplexing experiment, we used 2-ps pump pulses at a repetition rate of 12.5 GHz. The gain transients were measured for pump pulse energies ranging from 0.8 fJ to 800 fJ and found to be in good agreement with the predictions of the model.

References

- [2.1] R. N. Hall, G. E. Fenner, J. D. Kingsley, T. J. Soltys, and R. O. Carlson, "Coherent light emission from GaAs junctions," *Phys. Rev. Lett.*, vol. 9, pp. 366–8, November 1962.
- [2.2] M. I. Nathan, W. P. Dumke, G. Burns, J. F. H. Dill, and G. Lasher, "Stimulated emission of radiation from GaAs p - n junctions," *Appl. Phys. Lett.*, vol. 1, pp. 62–3, November 1962.
- [2.3] T. M. Quist, R. H. Rediker, R. J. Keyes, W. E. Krag, B. Lax, A. L. McWhorter, and H. J. Zeigler, "Semiconductor maser of GaAs," *Appl. Phys. Lett.*, vol. 1, pp. 91–2, December 1962.

- [2.4] Z. I. Alferov, V. M. Andreev, D. Z. Garbuzov, Y. V. Zhilyaev, E. P. Morozov, E. L. Portnoi, and V. G. Trofim, "Investigation of the influence of the AlAs-GaAs heterostructure parameters on the laser threshold current and realization of continuous emission at room temperature," *Fiz. Tekh. Poluprovodn.*, vol. 4, pp. 1826–9, September 1970.
- [2.5] I. Hayashi, M. B. Panish, P. W. Foy, and S. Sumski, "Junction lasers which operate continuously at room temperature," *Appl. Phys. Lett.*, vol. 17, pp. 109–11, August 1970.
- [2.6] N. W. Ashcroft and N. D. Mermin, *Solid State Physics*. Saunders College Publishing, 1976.
- [2.7] G. P. Agrawal and N. K. Dutta, *Semiconductor Lasers*. New York: Van Nostrand Reinhold, 2nd edition ed., 1993.
- [2.8] R. H. Yan, S. W. Corzine, L. A. Coldren, and I. Suimune, "Corrections to the expression for gain in GaAs," *IEEE J. Quantum Electron.*, vol. 26, pp. 213–6, February 1990.
- [2.9] M. G. A. Bernard and G. Duraffourg, "Laser condition in semiconductors," *Phys. Stat. Solidi*, vol. 1, pp. 699–703, 1961.
- [2.10] J. Leuthold, M. Mayer, J. Eckner, G. Guekos, H. Melchior, and C. Zellweger, "Material gain of bulk 1.55 μm InGaAsP/InP semiconductor optical amplifiers approximated by a polynomial model," *J. Appl. Phys.*, vol. 87, pp. 618–20, January 2000.
- [2.11] H. A. Kramers, "La diffusion de la lumière par les atomes," *Atti Congr. Int. Fis. Como*, vol. 2, pp. 545–557, 1927.
- [2.12] R. L. Krönig, "On the theory of dispersion of X-rays," *J. Opt. Soc. Am. Rev. Scient. Instrum.*, vol. 12, pp. 547–557, 1926.
- [2.13] D. C. Hutchings, M. Sheik-Bahae, D. J. Hagan, and E. W. Van Stryland, "Kramers-Krönig relations in nonlinear optics," *Opt. and Quantum Electron.*, vol. 24, no. 1, pp. 1–30, 1992.
- [2.14] J. Mørk and J. Mark, "Time-resolved spectroscopy of semiconductor laser devices: Experiments and modelling," in *Physics and Simulation of Optoelectronic Devices III, Proc. SPIE 2399* (M. Osinski and W. W. Chow, eds.), pp. 146–59, 1995.
- [2.15] K. L. Hall, *Femtosecond Nonlinearities in InGaAsP Diode Lasers*. PhD thesis, Massachusetts Institute of Technology, May 1993.
- [2.16] M. P. Kesler and E. P. Ippen, "Subpicosecond gain dynamics for GaAlAs laser diodes," *Appl. Phys. Lett.*, vol. 51, pp. 1765–7, November 1987.

- [2.17] J. Mørk and A. Mecozzi, “Theory of nondegenerate four-wave mixing between pulses in a semiconductor waveguide,” *IEEE J. Quantum Electron.*, vol. 33, pp. 545–55, April 1997.
- [2.18] G. Lasher and F. Stern, “Spontaneous and stimulated recombination radiation in semiconductors,” *Phys. Rev.*, vol. 133, pp. A553–63, January 1964.
- [2.19] J. N. Fehr, M. A. Dupertuis, T. P. Hessler, L. Kappei, D. Marti, F. Salleras, M. S. Nomura, B. Deveaud, J. Emery, and B. Dagens, “Hot phonons and Auger related carrier heating in semiconductor optical amplifiers,” *IEEE J. Quantum Electron.*, vol. 38, pp. 674–81, June 2002.
- [2.20] N. K. Dutta and R. J. Nelson, “The case for Auger recombination in $\text{In}_{1-x}\text{Ga}_x\text{As}_y\text{P}_{1-y}$,” *J. Appl. Phys.*, vol. 53, pp. 74–92, January 1982.
- [2.21] E. Wintner and E. P. Ippen, “Nonlinear carrier dynamics in $\text{Ga}_x\text{In}_{1-x}\text{As}_y\text{P}_{1-y}$,” *Appl. Phys. Lett.*, vol. 44, pp. 999–1001, May 1984.
- [2.22] K. L. Hall, G. Lenz, A. M. Darwish, and E. P. Ippen, “Subpicosecond gain and index nonlinearities in InGaAsP diode lasers,” *Opt. Comm.*, vol. 111, pp. 589–612, October 1994.
- [2.23] J. L. Pleumeekers, M. A. Dupertuis, T. Hessler, P. E. Selbmann, S. Haacke, and B. Deveaud, “Longitudinal spatial hole burning and associated nonlinear gain in gain-clamped semiconductor optical amplifiers,” *IEEE J. Quantum Electron.*, vol. 34, pp. 879–86, May 1998.
- [2.24] J. McDougall and E. C. Stoner, “The computation of Fermi-Dirac functions,” *Phil. Trans. Roy. Soc. London*, vol. 237, pp. 67–104, February 1938.
- [2.25] R. B. Dingle, “The Fermi-Dirac integrals,” *Appl. Sci. Res. Section B*, vol. 6, pp. 225–39, 1957.
- [2.26] W. J. Cody and H. C. Thacher, “Rational Chebyshev approximations for fermi-dirac integrals of orders $-1/2$, $1/2$, and $3/2$,” *Math. Comput.*, vol. 21, pp. 30–40, 1967.
- [2.27] A. J. Macleod, “Algorithm 779: Fermi-Dirac functions of order $-1/2$, $1/2$, $3/2$, $5/2$,” *ACM Trans. Math. Softw.*, vol. 24, pp. 1–12, March 1998.
- [2.28] N. G. Nilsson, “An accurate approximation of the generalized Einstein relation for degenerate semiconductors,” *Phys. Status Solidi*, vol. 19, pp. K75–8, September 1973.
- [2.29] W. B. Joyce and R. W. Dixon, “Analytic approximations for the Fermi energy of an ideal Fermi gas,” *Appl. Phys. Lett.*, vol. 31, pp. 354–6, September 1977.
- [2.30] H. Van Cong and G. Debais, “A simple accurate expression of the reduced Fermi energy for any reduced carrier density,” *J. Appl. Phys.*, vol. 73, pp. 1545–6, February 1993.

- [2.31] M. Abramowitz and I. A. Stegun, eds., *Handbook of Mathematical Functions*. Mineola, NY: Dover Publications, Inc., 1964.
- [2.32] A. Sommerfeld, "Zur Elektronentheorie der Metalle auf Grund der Fermischen Statistik," *Z. Phys.*, vol. 47, pp. 1–32, 1928.
- [2.33] E. P. Ippen and C. V. Shank, "Techniques for measurement," in *Ultrashort Light Pulses: Picosecond Techniques and Applications*, vol. 18 of *Topics in Applied Physics*, pp. 83–122, Berlin: Springer-Verlag, 1977.
- [2.34] J. Emery, P. Doussi re, L. Goldstein, F. Pommereau, C. Fortin, R. Ngo, N. Tschertner, J. Lafragette, P. Aubert, and F. Brillouet, "New, process tolerant, high performance 1.55 μm polarization insensitive semiconductor optical amplifier based on low tensile bulk GaInAsP," in *22nd European Conference on Optical Communication - ECOC'96*, pp. 3.165–3.168, 1996.
- [2.35] J. Emery, T. Ducellier, M. Bachmann, P. Doussi re, F. Pommereau, R. Ngo, F. Gaborit, L. Goldstein, G. Laube, and J. Barrau, "High performance 1.55 μm polarisation insensitive semiconductor optical amplifier based on low-tensile-strained bulk GaInAsP," *Electron. Lett.*, vol. 33, pp. 1083–4, June 1997.

Chapter 3

Semiconductor-Based All-Optical Switching

3.1 Introduction

In this chapter, we give an overview of high-speed semiconductor-based interferometric all-optical switching techniques. We begin with a discussion of the nonlinear Mach-Zehnder interferometer. We then describe three semiconductor-based single-arm interferometer designs which are commonly employed for switching applications. The differences in these switch topologies are highlighted and their impact on the operational characteristics of the switch is discussed. Next, we present experimental techniques for measuring the switching window of an all-optical switch. Finally, we compare the performance of the ultrafast nonlinear interferometer and the terahertz optical asymmetric demultiplexer in a 100-Gbit/s demultiplexing experiment.

3.2 Nonlinear Mach-Zehnder Interferometers

In this work, we will focus on interferometric all-optical switch architectures. The most straightforward interferometric all-optical switch is the nonlinear Mach-Zehnder [3.1], shown in Figure 3-1. Signal pulses entering on the left are split into two pulses of equal intensity via a 50/50 beam splitter at the input. Pulses in the lower arm

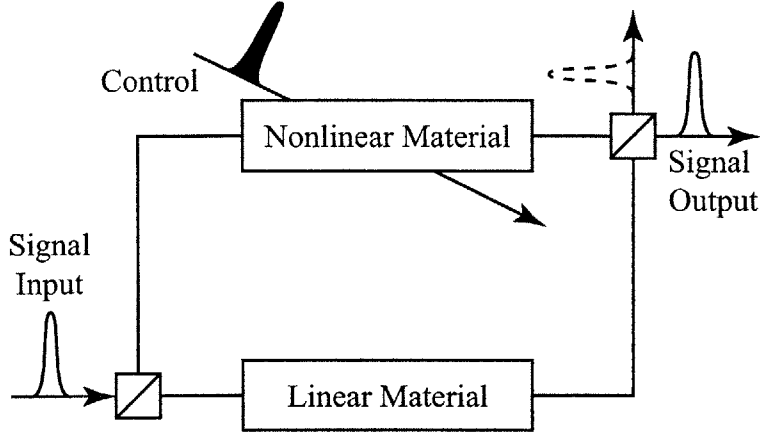


Figure 3-1: A nonlinear Mach-Zehnder interferometer.

travel through a linear material with a refractive index, n_l . Since the phase velocity of light traveling through this material is $v_l = c/n_l$, the phase change accumulated by the pulse propagating through this material is given by

$$\phi_l = \int_0^{L_l} \frac{2\pi}{\lambda} n_l dz = \frac{2\pi}{\lambda} n_l L_l, \quad (3.1)$$

where λ is the free-space center wavelength of the optical pulse and L is the propagation distance in the material.

Pulses in the upper arm travel through a nonlinear material. This material has a refractive index that is intensity dependent. In this case, an intense control pulse can be used to change the refractive index of the material. In the presence of a control pulse, the refractive index will generally vary as a function of time and position in the material. We write the refractive index as $n_{nl} = n_b + \Delta n(z, t)$, where n_b is the background refractive index and $\Delta n(z, t)$ is the change in refractive index due to the control pulse. The phase accumulated by the pulse as it propagates through this arm is then found to be

$$\begin{aligned} \phi_{nl}(t) &= \int_0^{L_{nl}} \frac{2\pi}{\lambda} n_{nl}(z, t) dz \\ &= \frac{2\pi}{\lambda} n_b L_{nl} + \int_0^{L_{nl}} \frac{2\pi}{\lambda} \Delta n(z, t) dz, \end{aligned} \quad (3.2)$$

where L_{nl} is the propagation distance in the nonlinear material.

When the two pulses are interfered at the output, the output intensity is proportional to the relative phase shift in the two arms

$$\begin{aligned}
 I_{\text{out}}(t) &= I_{\text{in}}(t) |1 + \exp\{j[\phi_1 - \phi_{\text{nl}}(t)]\}|^2 \\
 &= I_{\text{in}}(t) \cos^2\left(\frac{\phi_1 - \phi_{\text{nl}}(t)}{2}\right) \\
 &= I_{\text{in}}(t) \cos^2\left(\frac{\phi_{\text{bias}} - \Delta\phi(t)}{2}\right).
 \end{aligned} \tag{3.3}$$

Here, we have defined the bias phase shift, $\phi_{\text{bias}} = \frac{2\pi}{\lambda}(n_1 L_1 - n_b L_{\text{nl}} + \Delta L)$, where ΔL is the difference in the free-space path lengths of the two arms. The bias phase accounts for phase differences between the two arms owing to differences in path lengths and the linear refractive indices in the two arms.

For an instantaneous nonlinear response, such as that in an optical fiber, the nonlinear phase shift may be written as

$$\Delta\phi(t) = \frac{2\pi}{\lambda} n_2 I_c(t) L_{\text{nl}}, \tag{3.4}$$

where n_2 is the nonlinear refractive index and $I_c(t)$ is the intensity of the control pulse which copropagates with the signal pulse. Since the nonlinear phase shift is directly related to the intensity of the control pulse, we can control the output intensity of the signal pulses by adjusting the intensities of the control pulses.

By appropriately setting the bias phase, we can switch the signal pulses ON or OFF using the control pulses. For instance, suppose that there is no bias phase, $\phi_{\text{bias}} = 0$. Then, in the absence of a control pulse ($I_c = 0$), the signal pulse intensity at the output of the interferometer is equal to the signal pulse intensity at the input (neglecting losses in the interferometer). If we introduce a control pulse into the second arm with sufficient intensity such that $\Delta\phi = \pi$, the output signal pulses are completely switched OFF ($I_{\text{out}} = 0$). In this case, the pulse energy has been redirected to the dump port on the output beam splitter. If the signal pulse stream is an unmodulated clock with a repetition rate equal to the data rate of the control pulses,

the output of the switch is the logical inverse of the control input. Alternatively, we can set the bias phase to π and use the presence of a control pulse to switch the signal pulses ON, performing a logical AND function between the two pulse streams.

The nonlinear Mach-Zehnder interferometer described above, while attractive for its simplicity, is not a very practical design for an all-optical switch in most applications. For example, problems arise when one considers that the response of the nonlinear material may not be instantaneous. As discussed in Chapter 2, the nonlinear response in a semiconductor optical amplifier due to saturation of the carrier density may require several nanoseconds to recover. In this case, the nonlinear Mach-Zehnder interferometer will remain unbalanced for the duration of the carrier density recovery time. This would potentially limit switching rates to ~ 1 GHz, at best.

These problems can be alleviated by using a balanced interferometer design, like that shown in Figure 3-2 a) [3.2]. The balanced interferometer is similar to the nonlinear Mach-Zehnder interferometer, only both arms contain a nonlinear material. A diagram illustrating the operation of the balanced interferometer is shown in Figure 3-2 b). A control pulse is used to change the refractive index in both arms of the interferometer. However, the control pulse in the lower arm is delayed by a time τ relative to the upper arm. The nonlinear refractive index recovery time is assumed to be slow compared to τ . Thus, when the control pulse is incident on the nonlinear material in the upper arm, the interferometer is imbalanced by the differential phase shift between the two arms. However, the refractive index difference is canceled after the control pulse induces a nonlinear refractive index change in the lower arm. Thus, the interferometer is only imbalanced for a short period of duration τ . In this manner, the duration of the control-pulse-induced imbalance can be made much shorter than the carrier lifetime in the semiconductor, enabling switching at higher data rates.

3.3 Semiconductor-Based Fiber Interferometers

The Mach-Zehnder design discussed above suffers additional problems due to the spatial separation between the two arms. Because the signal pulses travel through

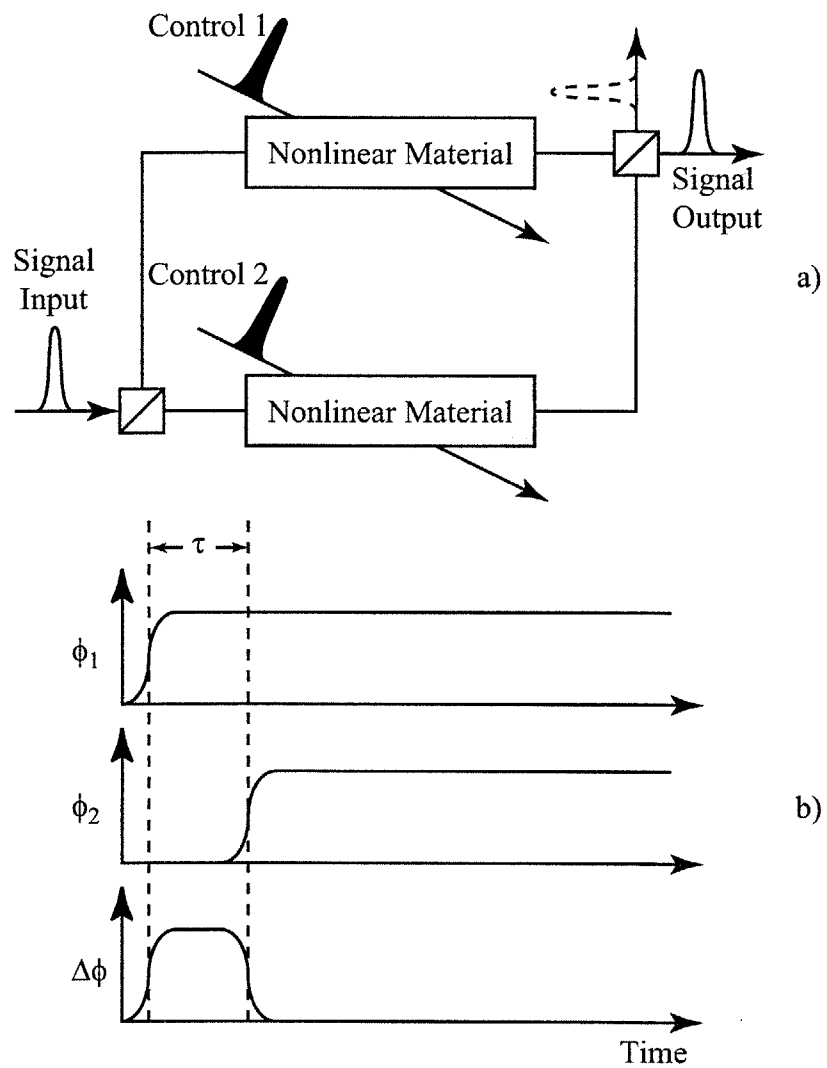


Figure 3-2: A balanced Mach-Zehnder interferometer: a) schematic and b) principle of operation.

two spatially separated paths, the switch may be imbalanced by thermal or acoustic variations between the two arms. These variations may affect the relative path lengths through which the signal pulses travel, causing unintentional changes in the bias phase of the interferometer, ϕ_{bias} . This leads to unpredictable switching behavior. These problems can be reduced by using active path length stabilization. However, such a solution is generally difficult and experimentally unsatisfactory.

Two practical solutions can be used to mitigate these problems. The first is to scale the interferometric structure to a size where the spatial separation between the arms is small enough that acoustic and thermal variations between the arms are negligible. Recently, semiconductor optical amplifiers have been integrated in compact balanced interferometric switching structures using hybrid [3.3] and monolithic [3.4] integration techniques. Alternatively, fiber interferometers may be assembled from discrete components using a single-arm interferometer (SAI) design [3.5]. In a single-arm interferometer, both signal pulses propagate along the same spatial path. They are distinguished by their direction of propagation or temporal separation. Below, we describe the operation of three possible fiber implementations of single-arm interferometers: the copropagating ultrafast nonlinear interferometer (UNI), the counter propagating UNI, and the terahertz asymmetric optical demultiplexer (TOAD).

3.3.1 Copropagating Ultrafast Nonlinear Interferometer

One example of a semiconductor-based single-arm fiber interferometer is the ultrafast nonlinear interferometer (UNI) [3.6]. The UNI was derived from a time-division interferometer that was originally designed to reduce the effects of thermal and acoustic variation in fiber-based all-optical switches [3.5, 3.7]. This interferometer design was later used for pump-probe experiments in AlGaAs [3.8, 3.9]. The time-division interferometer is essentially a single-arm nonlinear Mach-Zehnder interferometer where the signal pulses are distinguished by being orthogonally polarized and temporally separated. Since both signal pulses propagate along the same transmission path, the interferometer is immune to instabilities caused by refractive index changes which are slow compared to the temporal separation between the signal pulses. This geometry

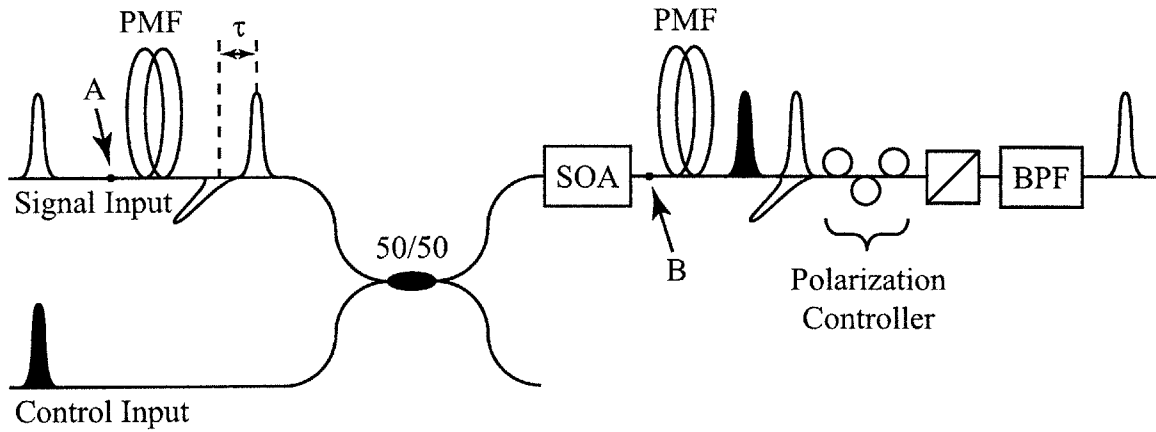


Figure 3-3: Schematic of a fiber implementation of the ultrafast nonlinear interferometer (UNI) in copropagating configuration. PMF: Polarization-maintaining fiber, SOA: Semiconductor optical amplifier, BPF: Optical bandpass filter.

was adapted for semiconductor-based switching applications using free-space optical delays to provide the temporal delay between the signal pulses [3.10]. The UNI is an all-fiber implementation of the time-domain interferometer.

A copropagating configuration of the UNI is shown in Figure 3-3. Entering signal pulses travel through a polarizer (not shown). At the output of the polarizer, the signal pulses are linearly polarized at 45 degrees with respect to the fast and slow axes of a length of birefringent polarization-maintaining fiber (PMF) which acts as a polarization-sensitive delay. After traversing the PMF, the temporally-separated orthogonally-polarized signal pulses pass through a 50/50 coupler where the control pulse is introduced. These pulses then travel through the semiconductor optical amplifier (SOA) where a nonlinear phase shift is acquired by the signal polarization that is overlapped by the control pulse. The two signal pulse polarizations are temporally recombined in a second length of PMF. The orthogonally polarized signal pulses are then interfered in a second polarizer. Finally, the control pulses are filtered out using a fiber-coupled band-pass filter leaving only the signal pulse at the output.

In practice, a fiber-coupled polarization-sensitive isolator is typically used in place of the polarizer at the output of the interferometer. This serves as both a polarizer and an isolator to prevent reflections on the output side of the interferometer from affecting

its operation. The polarization controller shown is used to set the bias phase of the interferometer. When the fiber used in the non-PMF portions of the interferometer is standard single-mode fiber (i.e. not polarization-maintaining), additional polarization controllers are needed at the points labeled A and B in order to properly align the signal polarization to the PMF birefringent axes.

Note that the UNI is essentially a polarization switch. Incoming signal pulses are linearly polarized. At the output of the second length of PMF in the switch, the signal pulse polarization will be either unchanged or orthogonal to the original signal pulse polarization, depending on the absence or presence of the control pulse. The polarizer at the switch output is then used to route the signal pulses according to their polarization. Realization of this polarization-switching capability of the UNI enables the switch to be used as an ultrafast cross-bar switch [3.11]. In this configuration, the two inputs to the cross-bar are orthogonally polarized at the signal input of the UNI. Both inputs are linearly polarized at 45 degrees relative to the fast and slow axes of the BRF. At the output of the switch, the two inputs will either remain on the same polarizations (bar state), or be flipped to the orthogonal polarizations (cross state), depending on the state of the control pulse.

The time-dependent transmissivity of an optical switch is defined as $T_s(t) = S_{\text{out}}(t)/S_{\text{in}}(t)$, where $S_{\text{in}}(t)$ is the input photon density at the signal wavelength. For the copropagating UNI, this transmissivity may be expressed as

$$T_s(t) = \frac{1}{4} \left\{ G_s^+(t) + G_s^+(t - \tau) + 2\sqrt{G_s^+(t)G_s^+(t - \tau)} \cos(\phi_s^+(t) - \phi_s^+(t - \tau) + \phi_{\text{bias}}) \right\} \quad (3.5)$$

Here, τ is the temporal separation between the signal pulses in the UNI and $G_s^+(t)$ and $\phi_s^+(t)$ are the gain and phase shift experienced by the signal propagating in the same direction as the control signal. Using the notation from Chapter 2, $G_s^+(t)$ and $\phi_s^+(t)$ may be expressed in terms of the small signal gain and refractive index in the

reference frame of the control pulse, $g(z, t, \omega_s)$ and $n(z, t, \omega_s)$, as

$$G_s^+(t) = \exp \left[\int_0^L (\Gamma g(z, t, \omega_s) - \alpha_{\text{int}}) dz \right], \quad (3.6)$$

and

$$\phi_s^+(t) = \frac{2\pi}{\lambda_s} \int_0^L n(z, t, \omega_s) dz, \quad (3.7)$$

where L is the SOA length, Γ is the confinement factor for the optical mode, α_{int} is the internal loss of the SOA waveguide, ω_s is the angular frequency of the signal pulse carrier, and λ_s is the signal wavelength.

Figure 3-4 a) shows a simulation of the differential phase delay experienced by the two orthogonal signal pulses in a copropagating UNI. This simulation was performed using the SOA model described in Chapter 2. In this calculation, the 2.5-ps control pulses arrive at a constant repetition rate of 12.5 GHz. The signal pulses are separated by 5 ps in the UNI. We assume that the phase shift experienced by the signal pulse field is polarization independent. Thus, apart from a relative delay related to the signal pulse separation, the control-pulse-induced phase shifts in the two signal polarizations are identical. Because the signal fields copropagate with the control pulse, the rise time for this phase shift is governed by the control pulse width. The control pulse energy in this calculation was set to provide a π phase shift.

Figure 3-4 b) shows the transmissivity of the copropagating UNI, calculated using Equation 3.5, for various values of the signal pulse separation, τ . This transmissivity function of the switch is often referred to as the “switching window.” In calculating these switching windows, the bias phase, ϕ_{bias} , has been adjusted to maximize the contrast ratio of the switch. The duration of the switching window sets an upper limit on the data rate at which the switch can operate. In the UNI, this duration is directly related to the temporal separation between the signal pulses in the switch, τ . Note that the amplitude of the switching response is reduced slightly for $\tau = 2.5$ ps. This is due to the fact that the temporal separation between the signal polarizations is comparable to the control pulse duration in this case. The minimum achievable

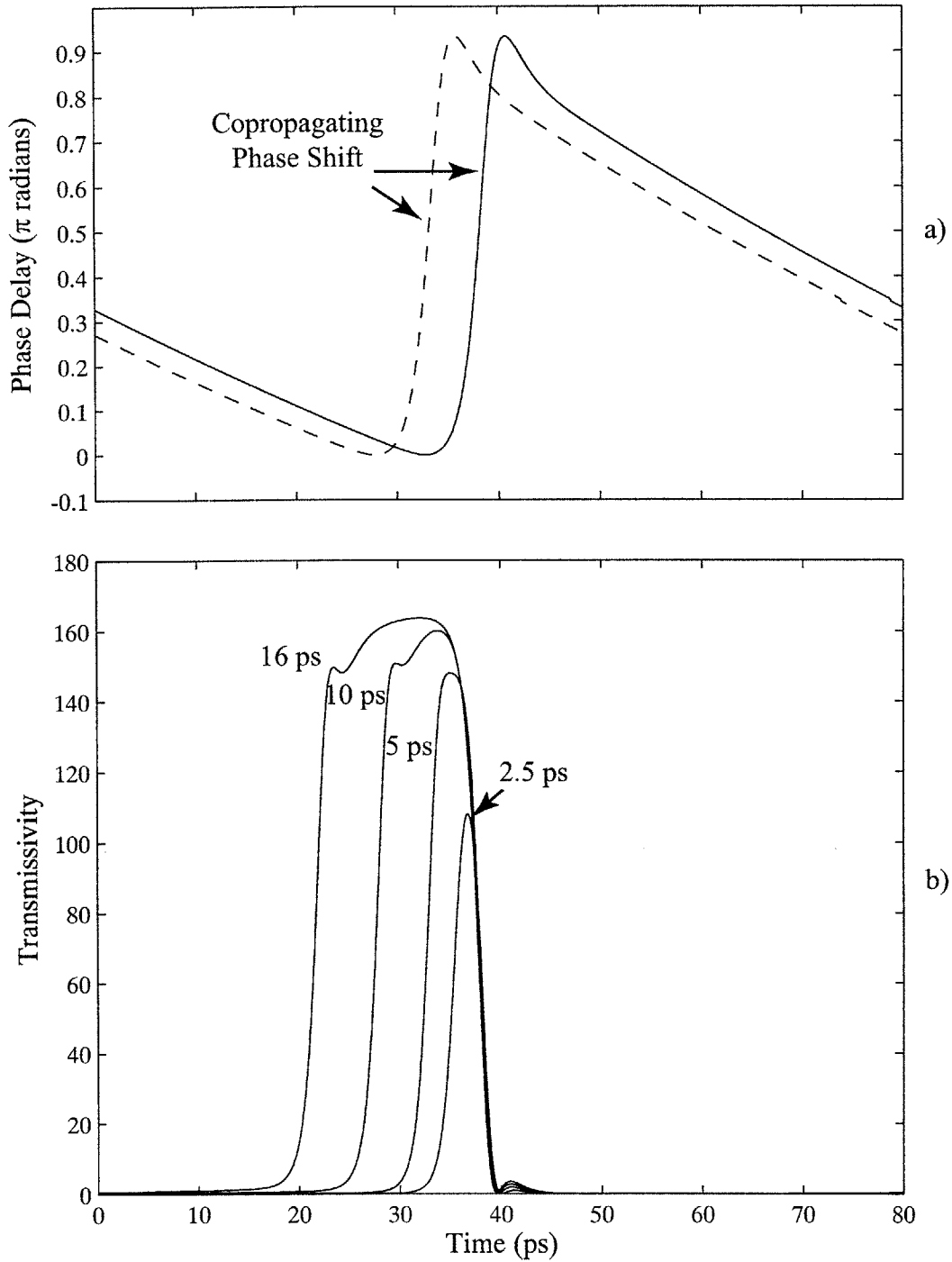


Figure 3-4: Simulation of copropagating UNI operation. In a), the differential phase shift for the two signal pulse polarizations is shown for a temporal separation of $\tau = 5$ ps in the UNI. In b), the time-dependent transmission characteristics of the UNI are shown for signal pulse separations of $\tau = 2.5, 5, 10,$ and 16 ps.

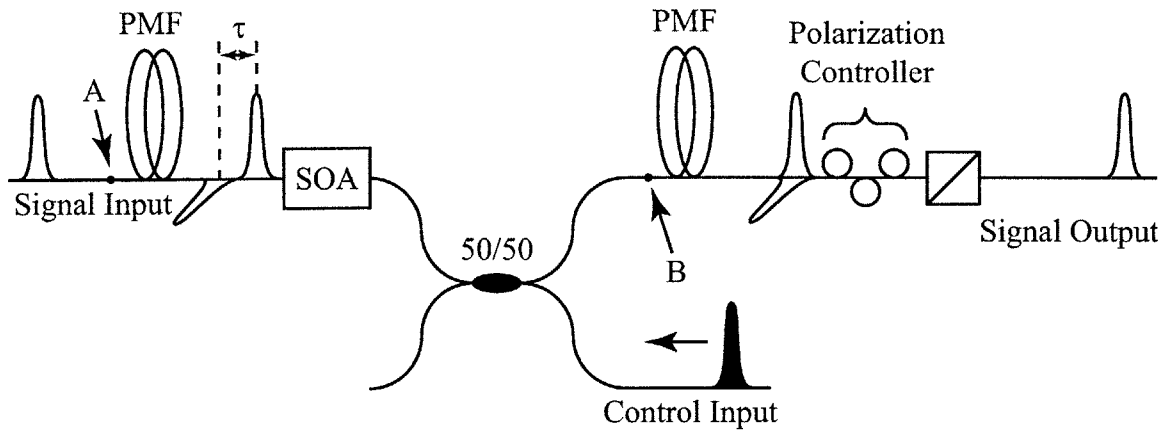


Figure 3-5: Schematic of a fiber implementation of the UNI in a counterpropagating configuration.

switching window duration for the copropagating UNI is limited by the rise time for the differential phase shift seen by the two signal polarizations. In comparison with the other fiber interferometers discussed here, the copropagating UNI offers the advantage of fast turn-on and turn-off times. This is due to the copropagating geometry where the rise time of the control-pulse-induced differential phase shift observed by the signal pulses is limited only by the duration of the control pulse. By reducing the temporal width of the control pulse, the window may be made arbitrarily short in duration (limited by the SOA gain bandwidth). This makes the copropagating UNI particularly suitable for ultrahigh-speed bitwise logic applications. Logical AND functionality has been demonstrated using this switch configuration at data rates as high as 100 Gbit/s [3.12]. The UNI has also been demonstrated for use as an all-optical 3R regenerator at data rates as high as 80 Gbit/s [3.13].

3.3.2 Counterpropagating Ultrafast Nonlinear Interferometer

The UNI can also be configured in a counterpropagating geometry as shown in Figure 3-5 [3.14]. In this configuration, entering signal pulses travel through a polarizer (not shown). At the output of the polarizer, the signal pulses are linearly polarized at 45

degrees with respect to the fast and slow axes of a length of PMF which acts as a polarization-sensitive delay. After traversing the PMF, the signal pulses pass through the SOA. Control pulses, counterpropagating with respect to the signal pulses, are introduced via a 50/50 coupler. The control pulses are timed to provide a differential phase shift between the two signal pulse polarizations as the pulses propagate through the SOA. At the output of the 50/50 coupler, the two signal pulse polarizations are temporally recombined in a second length of PMF. The orthogonally polarized signal pulses are then interfered in a second polarizer before exiting the switch. Because the control pulse is not present at the switch output, no bandpass filter is required in this configuration.

The transmissivity of the counterpropagating UNI may be expressed as

$$T_s(t) = \frac{1}{4} \left\{ G_s^-(t) + G_s^-(t - \tau) + 2\sqrt{G_s^-(t)G_s^-(t - \tau)} \cos(\phi_s^-(t) - \phi_s^-(t - \tau) + \phi_{\text{bias}}) \right\} \quad (3.8)$$

Here, $G_s^-(t)$ and $\phi_s^-(t)$ are the gain and phase shift experienced by a signal which counterpropagates relative to the control pulse. Using the notation from Chapter 2, $G_s^-(t)$ and $\phi_s^-(t)$ may be expressed in terms of the small signal gain and refractive index in the reference frame of the control pulse, $g(z, t, \omega_s)$ and $n(z, t, \omega_s)$, as

$$G_s^-(t) = \exp \left[\int_0^L (\Gamma g(z, t + 2(L - z)/v_g, \omega_s) - \alpha_{\text{int}}) dz \right], \quad (3.9)$$

and

$$\phi_s^-(t) = \frac{2\pi}{\lambda_s} \int_0^L n(z, t + 2(L - z)/v_g, \omega_s) dz. \quad (3.10)$$

Figure 3-6 shows the simulated transmission characteristics of the counterpropagating UNI. Figure 3-6 a) shows the differential phase shift experienced by the two signal polarizations. Both signal polarizations counterpropagate relative to the control pulse. Thus, as discussed in Chapter 2 the rise time for the differential phase shift is approximately twice the transit time for the SOA. For the 800- μm SOA in this

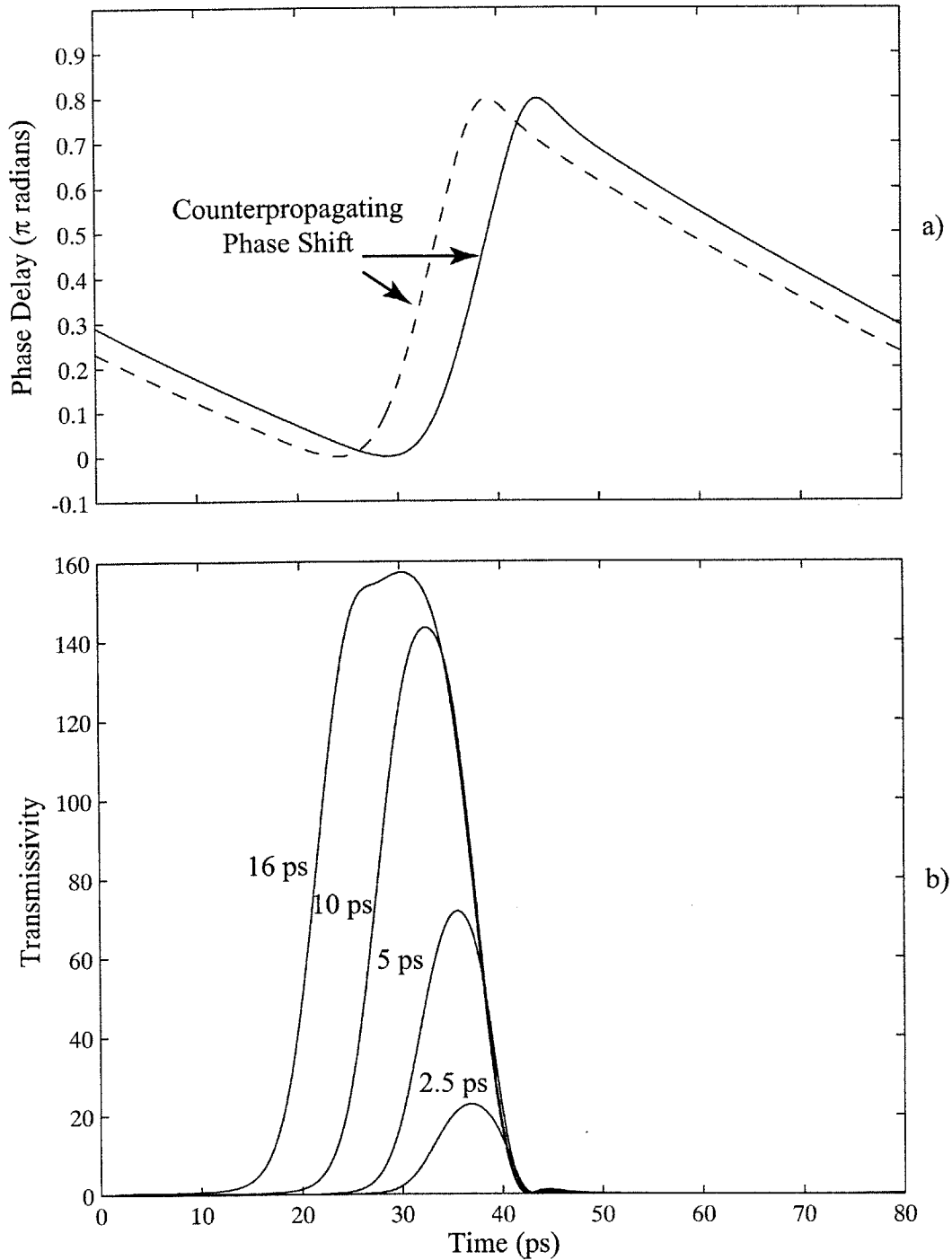


Figure 3-6: Simulation of counterpropagating UNI operation. In a), the differential phase shift for the two signal pulse polarizations is shown for a temporal separation of $\tau = 5$ ps in the UNI. In b), the time-dependent transmission characteristics of the UNI are shown for signal pulse separations of $\tau = 2.5, 5, 10,$ and 16 ps.

calculation, this duration is approximately 18 ps. Figure 3-6 b) shows the calculated switching windows for the counterpropagating UNI. For comparable signal pulse separations, the switching window for the counterpropagating UNI is longer than that of the copropagating UNI due to the slower rise time of the differential phase shift. Moreover, because of this slow response, the amplitude of the switching response of the counterpropagating UNI decreases as the signal pulse separation is reduced below the SOA transit time. Thus, the ultimate operational speed of the counterpropagating UNI is limited by the SOA transit time. Faster operation can be obtained with a shorter SOA. However, reducing the SOA length reduces the switch efficiency and requires higher energy control pulses.

In spite of these speed limitations, the counterpropagating UNI does have some distinct advantages over the copropagating UNI. In particular, since the signal pulses and control pulse do not propagate along the same path, a bandpass filter is not required to distinguish between the two at the switch output. In fact, in this configuration, the signal and control pulses can even have the same wavelength. This feature is particularly useful for applications such as 3-R regeneration, where wavelength changes are undesirable. Additionally, the counterpropagating UNI enables cascading of multiple switches, since the signal output from the switch can be used as either the signal or control input to another switch. Such cascability is required for complex logic operations. Infinite cascading capability has been effectively demonstrated for the counterpropagating UNI acting as a recirculating shift register at 40 Gbit/s [3.15].

3.3.3 Terahertz Optical Asymmetric Demultiplexer

The terahertz optical asymmetric demultiplexer (TOAD) (sometimes referred to as the semiconductor laser amplifier in an optical loop mirror, or SLALOM) is a slightly different form of the single-arm fiber interferometer. It is essentially a nonlinear Sagnac interferometer. A Sagnac interferometer consists of a loop, wherein the two signal pulses propagate in opposite directions. The pulses are then interfered in a coupler at the output of the loop. Many all-optical switching demonstrations have been performed using a nonlinear Sagnac interferometer with silica fiber as the nonlinear

medium, referred to as a nonlinear optical loop mirror (NOLM) [3.16]. In these interferometers, the asymmetry required for switching is obtained by introducing a control pulse into the loop which copropagates relative to one signal pulse and counterpropagates relative to the other. The copropagating pulse experiences a large nonlinear phase shift relative to the counterpropagating pulse. The SLALOM [3.17, 3.18] modifies this design by adding an asymmetrically-placed SOA in the loop. The SOA increases the magnitude of the control-pulse-induced nonlinear phase shift, thereby reducing the required propagation distance in the fiber loop. The TOAD [3.19] further modifies this design by reducing the SOA offset from the center of the loop such that the transit time of the asymmetry is substantially less than the SOA recovery time. In this way, the fast rise time of the nonlinear response in the SOA can be utilized to generate a switching window that is much shorter than the SOA recovery time.

A fiber implementation of the TOAD is shown in Figure 3-7. Signal pulses entering from the lower right side of the switch pass through a 50/50 coupler at the input to the Sagnac loop. The two pulses at the output of the 50/50 coupler then counterpropagate through the loop. A control pulse is introduced via a 50/50 or WDM coupler in the loop. The control pulse copropagates with one signal pulse and counterpropagates relative to the other signal pulse. This asymmetry, alone, is enough to get a differential phase shift from nonlinear effects in the SOA which have durations shorter than the SOA transit time. However, in practice, an additional asymmetry is added by offsetting the SOA from the center of the loop. Thus, the two signal pulses enter the SOA at different times relative to the control pulse. This loop asymmetry allows slower nonlinear effects, such as those due to carrier density changes in the SOA, to be utilized in obtaining a differential phase shift between the two signal pulses. The polarization controller in the loop is used to adjust the birefringence of the loop, thereby adding a fixed relative phase shift between the two signal pulses. After traversing the loop, the two signal pulses are recombined in the 50/50 coupler. If they are in phase, they will be directed to the output port. If they are out of phase, they will be reflected back to the input port.

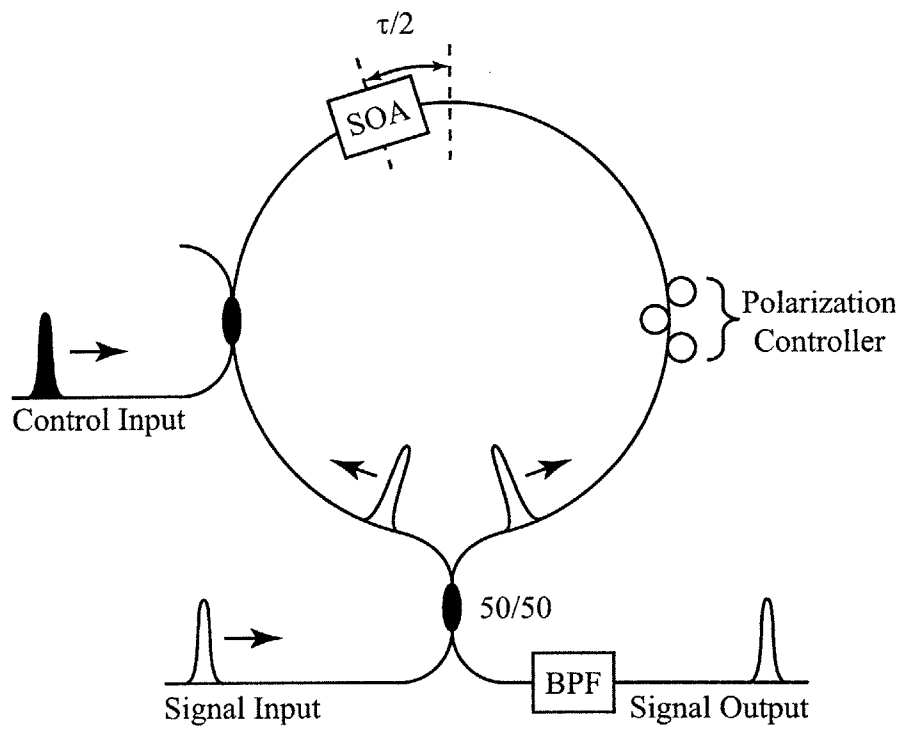


Figure 3-7: Schematic of fiber implementation of the terahertz optical asymmetric demultiplexer (TOAD).

Because the TOAD does not require a polarization sensitive delay, it is quite versatile in terms of possible wavelength and polarization assignments for the control and signal pulses. In principle, the TOAD can be made to operate independent of the signal and control polarizations. This mode of operation requires that the signal and control pulses be at different wavelengths so that a bandpass filter may be used to distinguish them at the output of the switch. On the other hand, if the incoming signal polarization is fixed, one can make the control pulse polarization orthogonal to the signal. In this configuration, the signal and control inputs may operate at the same wavelength and a polarizer may be used to distinguish between the two at the switch output.

Since one signal pulse copropagates with the control pulse and one signal pulse counterpropagates relative to the control pulse, the transmissivity of the TOAD may be expressed as [3.20]

$$T_s(t) = \frac{1}{4} \left\{ G_s^+(t) + G_s^-(t - \tau) + 2\sqrt{G_s^+(t)G_s^-(t - \tau)} \cos(\phi_s^+(t) - \phi_s^-(t - \tau) + \phi_{\text{bias}}) \right\}, \quad (3.11)$$

where τ represents the loop asymmetry arising SOA offset from the loop center and $G_s^+(t)$, $\phi_s^+(t)$, $G_s^-(t)$, and $\phi_s^-(t)$ are defined in Equations 3.6, 3.7, 3.9, and 3.10.

Figure 3-8 illustrates the switching characteristics of the TOAD. In 3-8 a), the differential phase delays seen by the two signal pulses is shown. The phase shift of the copropagating pulse has a fast rise time, similar to the copropagating UNI, while the phase shift of the counterpropagating pulse has a rise time that is limited by the SOA transit time, similar to the counterpropagating UNI. Figure 3-8 b) shows the TOAD switching windows for various values of the loop asymmetry, τ . As discussed above, because the direction of the control pulse itself causes an asymmetry in the loop, the switching window is non-zero, even when $\tau = 0$. In principle, since the fall time of the switching window is limited only by the control pulse duration, the TOAD switching window can be shorter than the counterpropagating UNI switching window. However, the shortest possible switching window in the TOAD is still limited by the

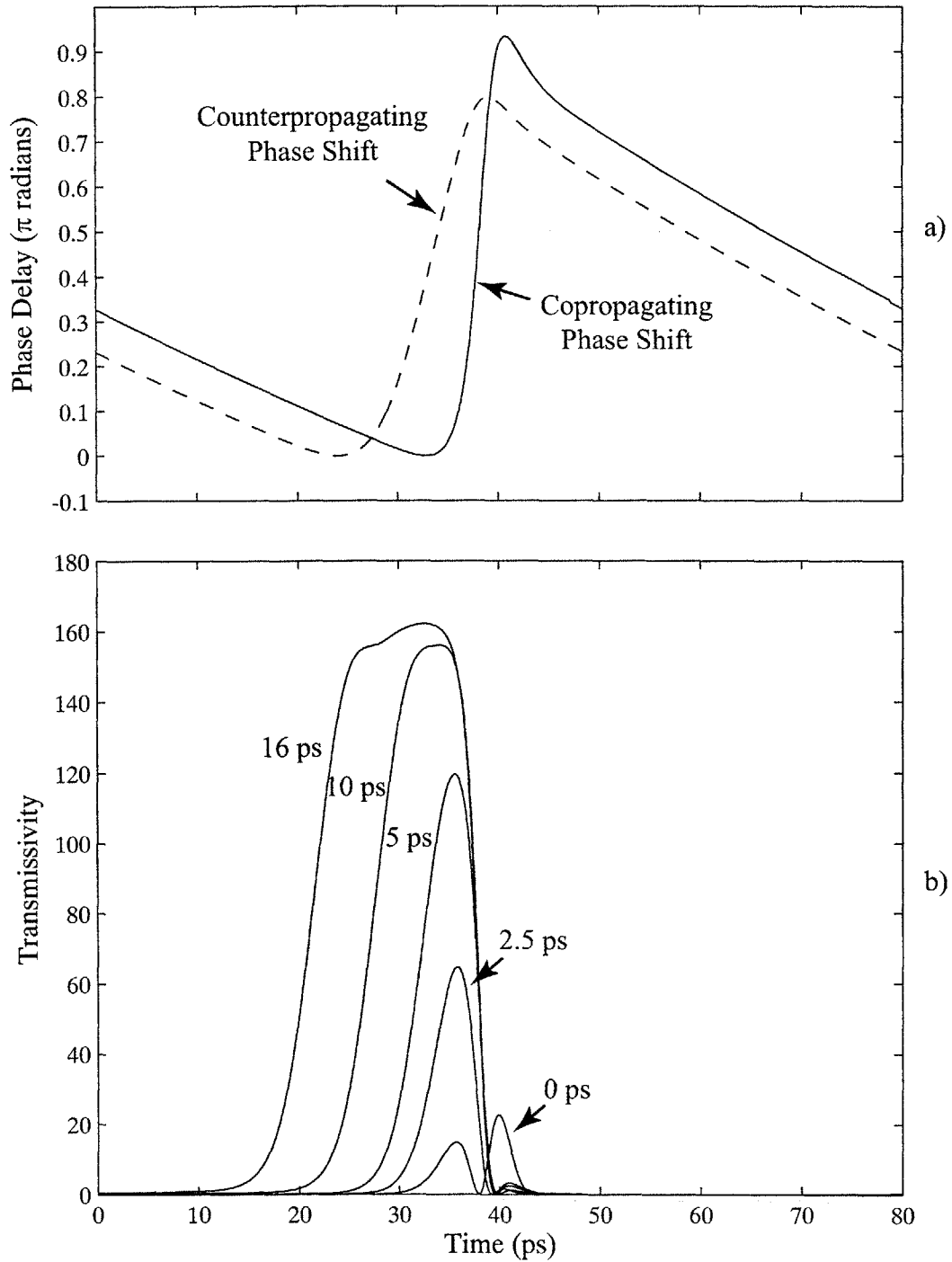


Figure 3-8: Simulation of TOAD operation. In a), the differential phase shift for the two signal pulses is shown for a loop asymmetry of $\tau = 5$ ps in the TOAD. In b), the time-dependent transmission characteristics of the TOAD are shown for loop asymmetries of $\tau = 2.5, 5, 10, 16$ ps.

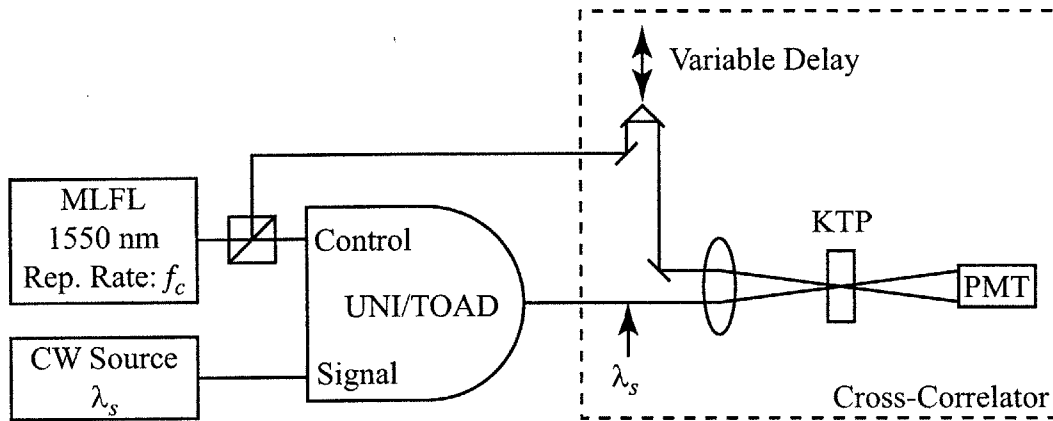
rise time which is proportional to the SOA transit time.

In spite of this potential limitation, the TOAD has been demonstrated in OTDM demultiplexing applications at data rates as high as 160 Gbit/s [3.21]. A modified TOAD configuration has also been used to achieve all-optical XOR functionality. This functionality has been used to demonstrate an all-optical parity checker [3.22] and an all-optical pseudo-random binary sequence generator [3.23]. The XOR configuration “unbalances” the interferometer, however, and operational data rates for these experiments were limited to ~ 1 Gbit/s.

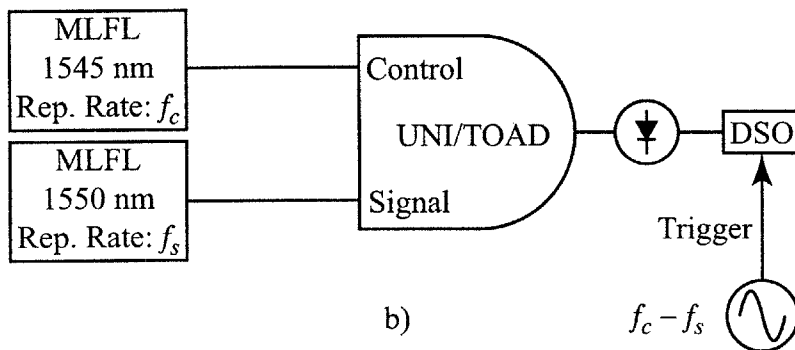
3.4 Measurement of Switching Windows

We have investigated two techniques for measuring the switching window of an all-optical switch. These techniques are illustrated in Figure 3-9. The first technique, shown in Figure 3-9 a), uses optical cross-correlation to measure the switching window induced by a control pulse [3.24]. A continuous-wave (CW) laser is used for the signal input to the switch. The control input is provided by a mode-locked fiber laser. At the output of the switch, the switching window is modulated onto the CW signal. The transients in the switching window are too fast to observe electronically, so the output signal is sampled in an optical cross-correlator based on sum-frequency generation in a KTP crystal. The sampling pulses for the cross-correlator are obtained by tapping off a portion of the control pulse energy at the input to the switch. When a tunable CW source is used for the signal input to the switch, this technique can be used to easily measure the frequency-dependence of the switch transmission characteristics.

An alternative measurement technique is shown in Figure 3-9 b). This measurement technique is based on the difference-frequency sampling (DFS) technique described in Section 2.7. The control and signal inputs to the switch are provided by two mode-locked fiber lasers. These lasers produce ~ 2.5 -ps pulses at 1545 nm and 1550 nm. The repetition rate of the signal laser, f_s , is slightly lower than the repetition rate of the control laser, f_c . Thus the signal pulses slowly walk through the control pulses over a period of $1/(f_c - f_s)$. The nonlinear interaction between



a)



b)

Figure 3-9: Two techniques for characterizing the switching window of an optical switch. In a), the switching window is measured via cross-correlation with the control pulse. In b), the switching window is measured via difference-frequency sampling.

the two pulse streams in the optical switch leads to intensity beating at the difference frequency, $f_c - f_s$. The temporal profile of the switching window can be measured by observing the envelope of this beating with a photodetector and a digital sampling oscilloscope (DSO).

This technique offers a number of advantages over the cross-correlation technique. First, since the optical pulses used at the input of the switch in the DFS measurement are very similar to the pulses used in a typical switching demonstration, the switching window obtained provides an accurate prediction of the switch performance in an actual switching application. Additionally, since the DFS technique requires no mechanical delays, no bulk optic alignment is required. Moreover, the DFS technique does not require nonlinear frequency conversion. With the cross-correlation technique, high-energy sampling pulses must be used in order to compensate for the relatively low intensity of the output signal from the optical switch and the low conversion efficiency of the sum-frequency process. With DFS, the intensity of the output signal from the switch is measured directly using a photodetector. Sensitivity can be improved by using optical preamplification prior to detection. Since the detected signal of interest is confined to fairly low frequencies (as determined by the offset frequency in the measurement), electrical amplification may also be utilized with minimal distortion. Finally, the measurement time for the DFS technique is much shorter than that required for the cross-correlation technique. For a 1-kHz frequency offset between the signal and control pulses, the entire switching window is mapped in 1 ms. This fast acquisition time is extremely useful in aligning polarization controllers in the switch, for example, since the effects of adjusting the polarization can be observed in near real-time.

Figures 3-10, 3-11, and 3-12 show measurements of the switching windows for a copropagating UNI, a counterpropagating UNI, and a TOAD obtained using the DFS technique. The repetition rate for the control pulses is 12.5 GHz and the frequency offset for the signal pulses is 1 kHz. The signal and control pulse energies in these measurements were 4 and 40 fJ, respectively. The finite extinction ratio observed in the measurements is primarily due to imperfect alignment of the signal polarizations in

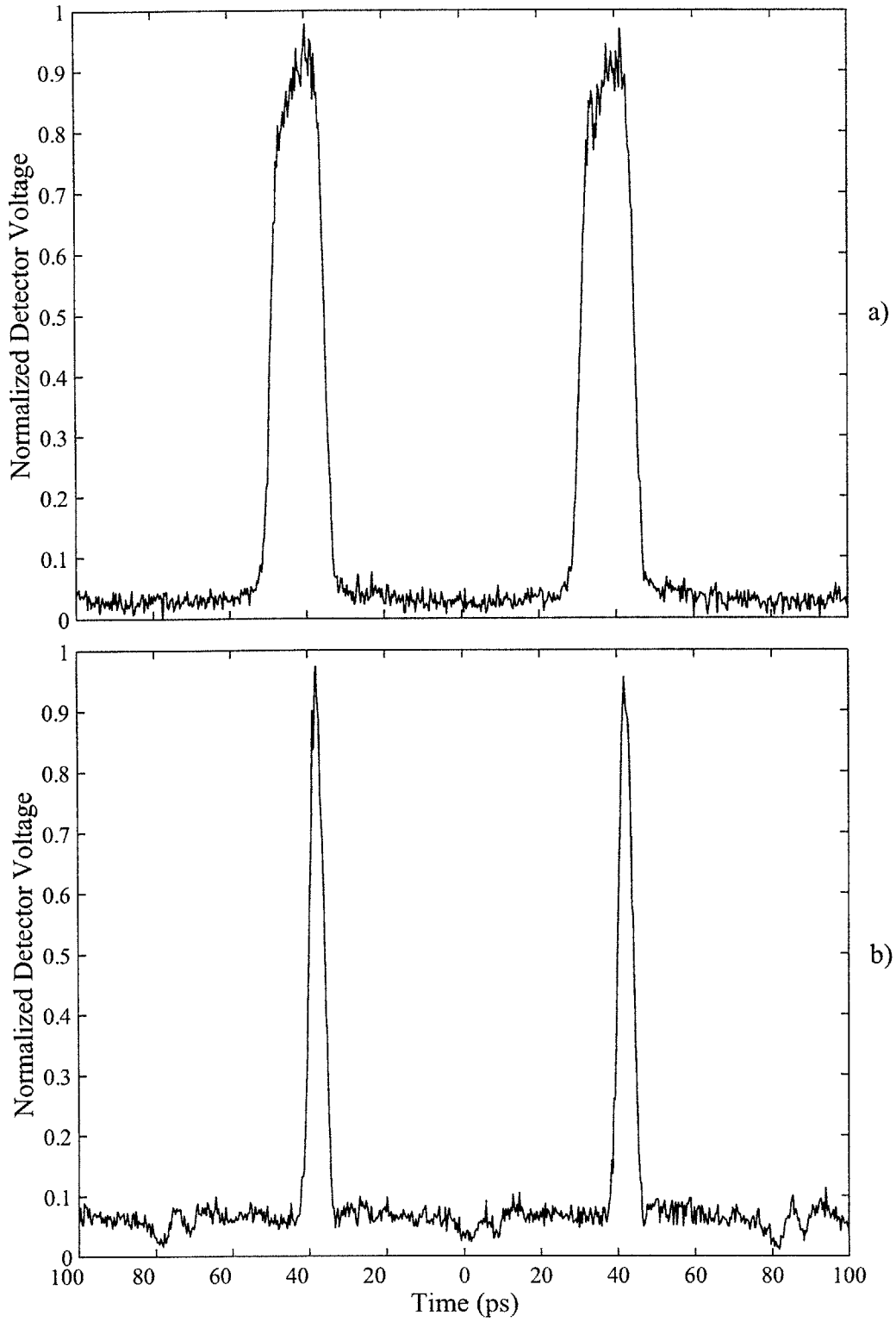


Figure 3-10: Switching windows for a copropagating UNI with signal pulse offsets of a) 16 ps and b) 5 ps measured using difference-frequency sampling.

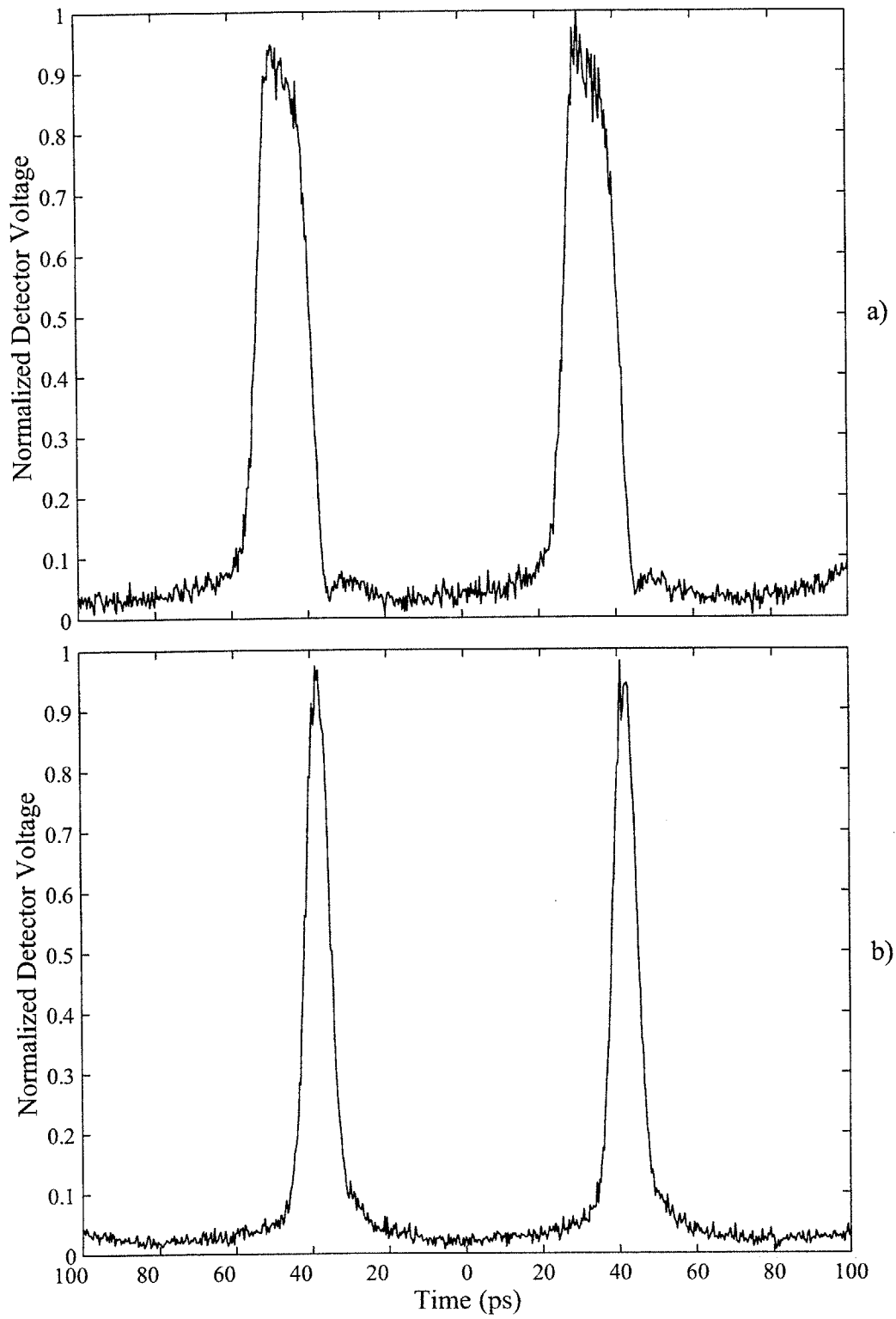


Figure 3-11: Switching windows for a counterpropagating UNI with signal pulse offsets of a) 16 ps and b) 5 ps measured using difference-frequency sampling.

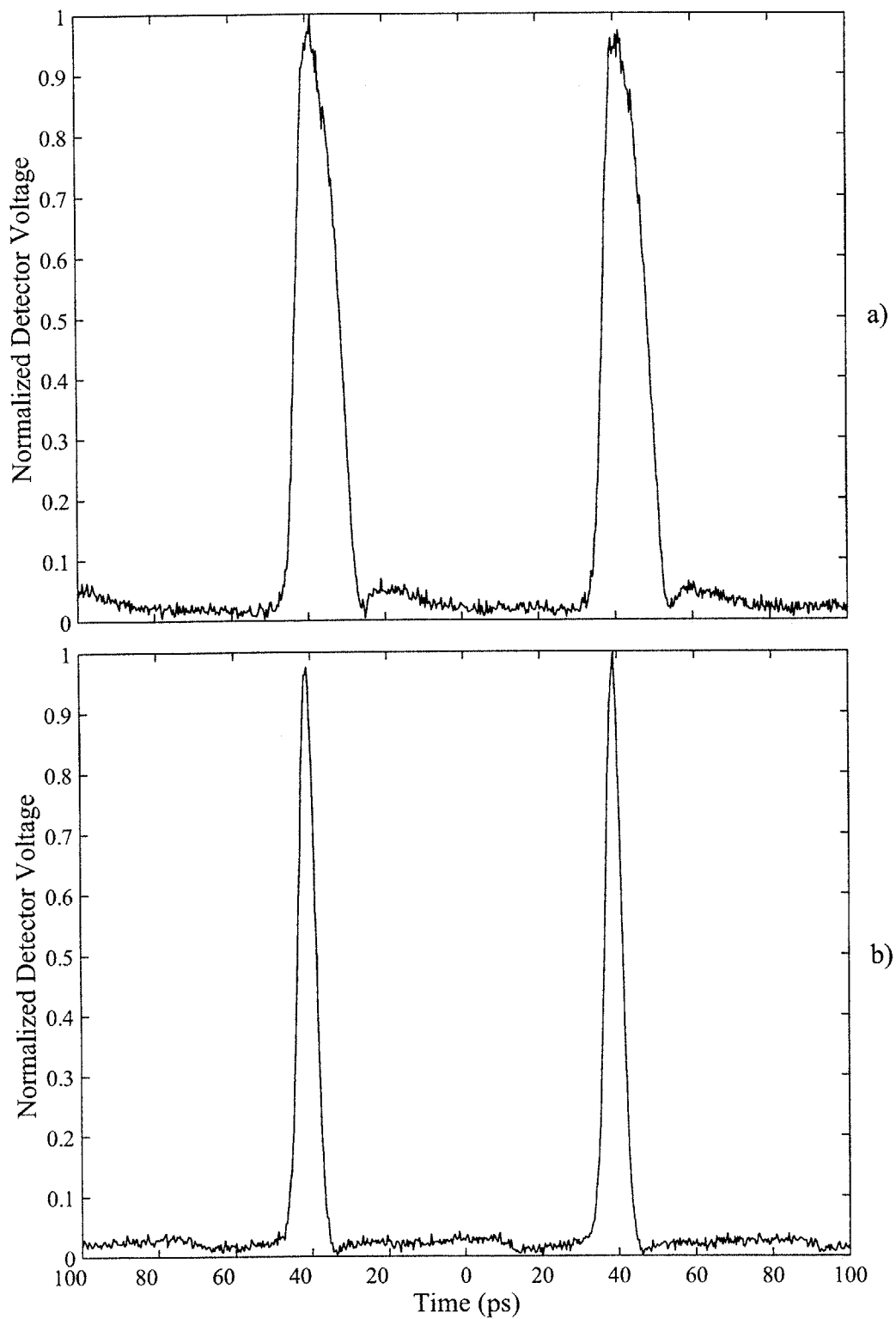


Figure 3-12: Switching windows for TOAD with SOA asymmetries of a) 11 ps and b) 4 ps measured using difference-frequency sampling.

the switch. We have recently proposed a modification of the UNI which helps to reduce these problems [3.25]. The distinguishing traits of the three geometries are apparent in the measured switching windows, with the copropagating UNI displaying the fastest switching transients, followed by the TOAD and the counterpropagating UNI. For the copropagating UNI with a 5-ps signal pulse separation, the observed switching window duration is 4.6 ps. This window is short enough to allow demultiplexing from aggregate data rates as high as 200 Gbit/s.

3.5 Demultiplexing Performance Evaluation

The three interferometer configurations discussed above differ with respect to the direction of propagation of the signal pulses relative to the control pulse. As shown in the simulations and experiments above, these propagation differences lead to differences between the transmission characteristics of the switches. The system impact of these differences has been demonstrated in a 100-Gbit/s OTDM demultiplexing experiment [3.26]. Recall from Chapter 1 that an OTDM demultiplexer is used to de-interleave a low-rate data stream from the higher-rate OTDM data stream. For example, a 12.5-Gbit/s stream may be demultiplexed from a 25-, 50-, or 100-Gbit/s aggregate data stream. The UNI and TOAD switches are particularly well-suited for this task, since the switching window can be made very short relative to the control pulse period. In the experiment described below, we compare the demultiplexing performance of a copropagating UNI and a TOAD using the same SOA.

The experimental setup for the demultiplexing operation is shown in Figure 3-13. The signal pulses are provided by an actively mode-locked fiber laser producing a 12.5-GHz stream of 3-ps pulses with a center wavelength of 1558 nm. The signal pulses are on-off key (OOK) modulated with a 12.5-Gbit/s pseudo-random binary sequence using a LiNbO₃ intensity modulator. The modulated pulses are multiplexed to higher data rates using a passive OTDM multiplexer (MUX). In the multiplexer, the pulse stream is divided into two paths. One path is delayed relative to the other. Then, the two streams are interleaved to form a new stream at twice the data rate.

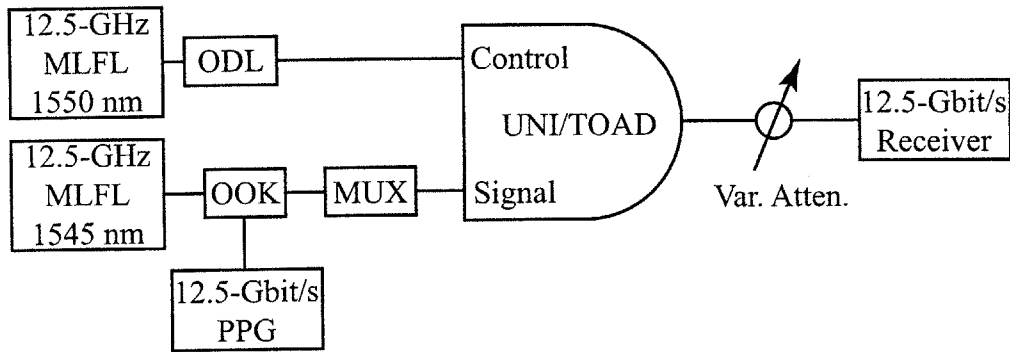


Figure 3-13: Experimental setup for 100-Gbit/s demultiplexing using the UNI and the TOAD.

Thus, for a 12.5-Gbit/s input stream, an output stream at 25 Gbit/s is generated. This process may be repeated to generate signal streams of 50-Gbit/s and 100-Gbit/s data. Note that the delays in the multiplexer must be several bits in duration in order to maintain the pseudo-random nature of the data stream at the output of the multiplexer. For this experiment, the relative delays in the multiplexer are set to 120 ps, 60 ps, and 30 ps. The control pulses are provided by a second actively mode-locked fiber laser producing a 12.5-GHz stream of 2.5-ps pulses at 1545 nm. An optical delay line (ODL) is used to temporally align the control pulses to the desired 12.5-Gbit/s signal data stream. Both the TOAD and the UNI used in this experiment contain a 800- μm -long commercially available SOA (Alcatel 1901). The pulse offset/asymmetry is set to 5 ps for both switches. The demultiplexed pulses at the switch output are input to a 12.5-Gbit/s optically preamplified direct-detection receiver for bit-error rate analysis.

The results of a bit-error rate (BER) analysis performed at the output of the switch are shown in Figure 3-14. Note that the receiver power in these plots refers to the power at the output of the switch, immediately before the 12.5-Gbit/s receiver. Figure 3-14 a) shows the demultiplexing performance of the TOAD with aggregate signal input rates of 25-, 50-, and 100-Gbit/s. Good demultiplexing performance is observed for aggregate data rates of 25- and 50-Gbit/s. At 50-Gbit/s there is a moderate power penalty of 5 dB measured at a sensitivity of 10^{-9} . For the 100-Gbit/s

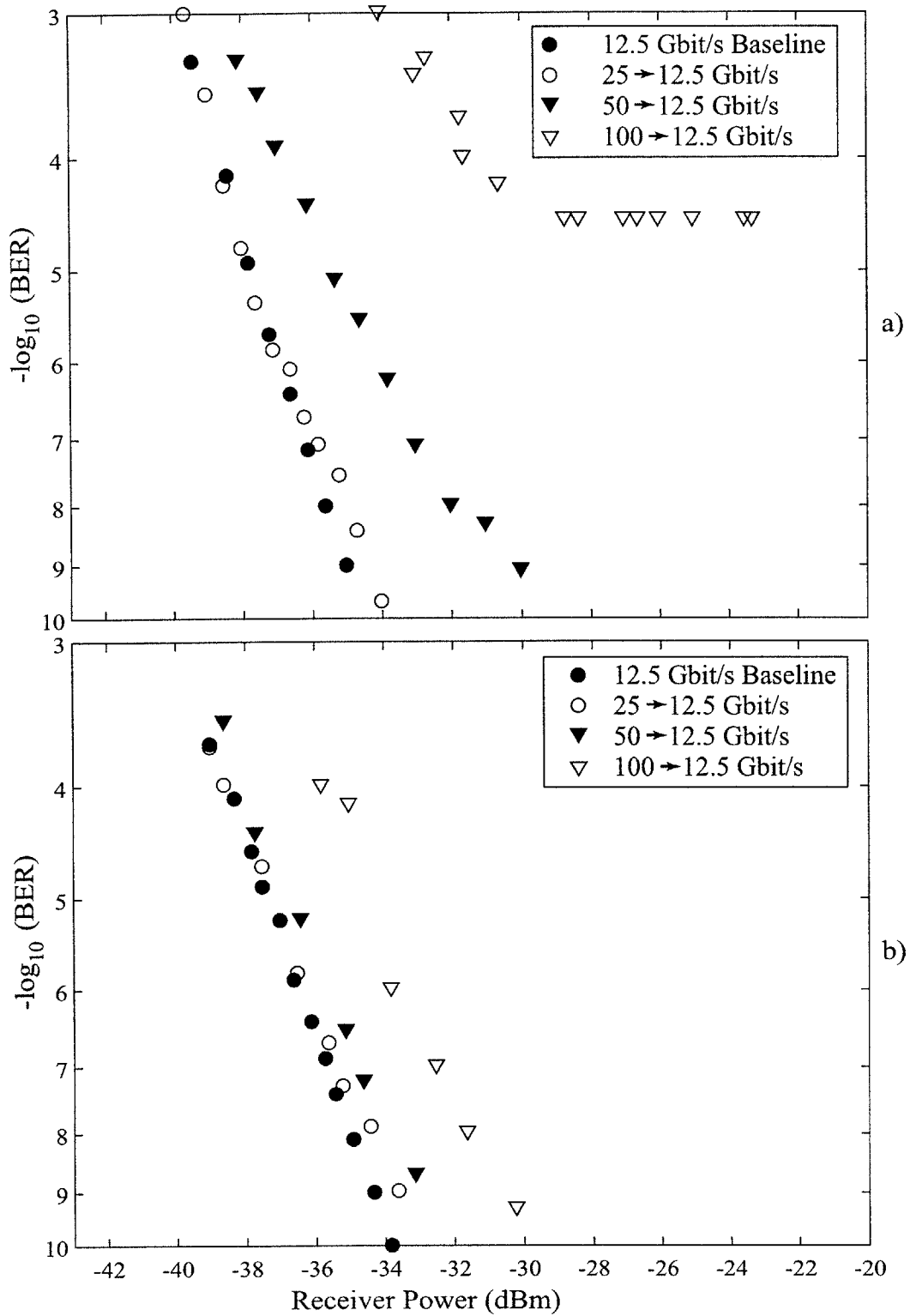


Figure 3-14: Bit-error rate analysis of demultiplexed output of a) TOAD and b) UNI switches operating at aggregate data rates of 25-, 50-, and 100-Gbit/s.

aggregate stream, however, an error floor of $> 10^{-5}$ is observed. In contrast, the copropagating UNI measurements, shown in Figure 3-14 b), reveal good performance for aggregate data rates up to 100 Gbit/s. A slight power penalty of 2 dB is observed for the 50-Gbit/s aggregate stream. At 100 Gbit/s, the penalty is only 4 dB, with no observable error floor.

The differences in the system performance of these two switches may be attributed to the counterpropagating effects in the TOAD. As discussed above, the counterpropagating signal pulse in the TOAD limits the switching transients to approximately two times the transit time of the SOA. For the 800- μm long SOA used in these experiments, the transit time is 9 ps. Thus, switching transients are limited to approximately 18 ps in duration. For aggregate data rates of 50 Gbit/s, the bit period is 20 ps. Thus, we observe significant degradation in the performance of the TOAD at this data rate. For 100-Gbit/s aggregate data rates, the bit period is only 10 ps. In this case, the duration of the TOAD switching window severely limits the switching performance and error-free operation ($\text{BER} < 10^{-9}$) is not achievable.

3.6 Conclusions

In summary, we have demonstrated techniques for utilizing SOAs for ultrafast all-optical switching. In SOA-based switches, balanced interferometers are required to reduce the impact of long-lived index changes, thereby enabling switching at rates much faster than the carrier density recover rate. Implementing a two-arm balanced interferometer in fiber is impractical due to instabilities caused by thermal and acoustic variations between the two arms. Single-arm interferometers eliminate these instabilities by propagating all signal pulses through the same optical path. In these interferometers, signal pulses are distinguished by temporally separation or direction of propagation.

We have investigated the operation three commonly-used single-arm fiber interferometers: the ultrafast nonlinear interferometer, in copropagating and counterpropagating configurations, and the terahertz optical asymmetric demultiplexer. These

switches differ primarily in the relative directions of propagation for the signal and control pulses. Due to longitudinal saturation effects in the semiconductor optical amplifier, the fastest switching transients are observed in the copropagating UNI, where the rise- and fall-times for the switching window are determined by the control pulse duration. Using 2-ps control pulses, we have experimentally observed switching windows as short as 4.5 ps in the UNI. A comparison of the 100-Gbit/s demultiplexing performance of the UNI and the TOAD demonstrated the system impact of the slower switching transients associated with counterpropagating signal and control pulses in the TOAD.

Note that, in this discussion, we have neglected the impact that gain saturation has on the operation of semiconductor-based switches. Gain saturation primarily impacts switching operation in two ways. First, fast gain saturation, such as that due to spectral hole burning and carrier heating, can lead to a difference in the gain observed by the two signal pulses in the interferometer. As is evident from the transmission characteristics for the interferometers, given by Equations 3.5, 3.8, and 3.11, this will lead to a reduction in the achievable extinction ratio of the switch. The second way that gain saturation affects the operation of the switch is through long-lived, changes in the signal gain. These changes are due to saturation of the carrier density and typically recover over a duration of many bit periods at high data rates. Thus, they lead to pattern-dependent amplitude modulation of the signal pulses at the switch output. These effects are addressed in more detail in Chapter 4.

References

- [3.1] A. Lattes, H. A. Haus, F. J. Leonberger, and E. P. Ippen, "An ultrafast all-optical gate," *IEEE J. Quantum Electron.*, vol. QE-19, pp. 1718–23, November 1983.
- [3.2] K. Tajima, "All-optical switch with switch-off time unrestricted by carrier lifetime," *Jpn. J. Appl. Phys., Part 2*, vol. 32, pp. L1746–9, December 1993.
- [3.3] K. Tajima, S. Nakamura, Y. Ueno, J. Sasaki, T. Sugimoto, T. Kato, T. Shimoda, M. Itoh, H. Hatakeyama, T. Tamanuki, and T. Sasaki, "Hybrid inte-

- grated symmetric Mach-Zehnder all-optical switch with ultrafast, high extinction switching,” *Electron. Lett.*, vol. 35, pp. 2030–1, November 1999.
- [3.4] R. Hess, M. Caraccia-Gross, W. Vogt, E. Gamper, P. A. Besse, M. Duellk, E. Gini, H. Melchior, B. Mikkelsen, M. Vaa, K. S. Jepsen, K. E. Stubkjaer, and S. Bouchoule, “All-optical demultiplexing of 80 to 10 Gb/s signals with monolithic integrated high performance Mach-Zehnder interferometer,” *IEEE Photon. Technol. Lett.*, vol. 10, pp. 165–7, January 1998.
- [3.5] M. Shirasaki, H. A. Haus, and D. L. Wong, “Nonlinear fiber interferometer and logic gate,” in *Conference on Lasers and Electro-Optics*, 1987.
- [3.6] N. S. Patel, K. A. Rauschenbach, and K. L. Hall, “40-Gb/s demultiplexing using an ultrafast nonlinear interferometer (UNI),” *IEEE Photon. Technol. Lett.*, vol. 8, pp. 1695–7, December 1996.
- [3.7] M. J. LaGasse, D. Liu-Wong, J. G. Fujimoto, and H. A. Haus, “Ultrafast switching with a single-fiber interferometer,” *Opt. Lett.*, vol. 14, pp. 311–3, March 1989.
- [3.8] K. K. Anderson, M. J. LaGasse, C. A. Wang, J. G. Fujimoto, and H. A. Haus, “Femtosecond dynamics of the nonlinear index near the band edge in AlGaAs waveguides,” *Appl. Phys. Lett.*, vol. 56, pp. 1834–6, May 1990.
- [3.9] K. K. Anderson, *Disordered Quantum Well Waveguide Fabrication and Ultrafast Optical Characterization*. PhD thesis, Massachusetts Institute of Technology, October 1989.
- [3.10] K. Tajima, S. Nakamura, and Y. Sugimoto, “Ultrafast polarization discriminating Mach-Zehnder all-optical switch,” *Appl. Phys. Lett.*, vol. 67, pp. 3709–11, December 1995.
- [3.11] S. A. Hamilton and B. S. Robinson. Unpublished.
- [3.12] K. L. Hall and K. R. Rauschenbach, “100-Gbit/s bitwise logic,” *Opt. Lett.*, vol. 23, pp. 1271–3, August 1998.
- [3.13] A. E. Kelly, I. D. Phillips, R. J. Manning, A. D. Ellis, D. Nasset, D. G. Moodie, and R. Kashyap, “80 Gbit/s all-optical regenerative wavelength conversion using a semiconductor optical amplifier based interferometer,” *Electron. Lett.*, vol. 35, pp. 1477–8, August 1999.
- [3.14] N. S. Patel, K. L. Hall, and K. A. Rauschenbach, “40-Gbit/s cascable all-optical logic with an ultrafast nonlinear interferometer,” *Opt. Lett.*, vol. 21, pp. 1466–8, September 1996.
- [3.15] K. L. Hall, J. P. Donnelly, S. H. Groves, C. I. Fennelly, R. J. Bailey, and A. Napoleone, “40-Gbit/s all-optical circulating shift register with an inverter,” *Opt. Lett.*, vol. 22, pp. 1479–81, October 1997.

- [3.16] N. J. Doran and D. Wood, "Nonlinear-optical loop mirror," *Opt. Lett.*, vol. 13, pp. 56–8, January 1988.
- [3.17] M. Eiselt, "Optical loop mirror with semiconductor laser amplifier," *Electron. Lett.*, vol. 28, pp. 1505–6, July 1992.
- [3.18] M. Eiselt, W. Pieper, and H. G. Weber, "SLALOM: Semiconductor laser amplifier in a loop mirror," *IEEE J. Lightwave Technol.*, vol. 13, pp. 2099–112, October 1995.
- [3.19] J. P. Sokoloff, P. R. Prucnal, I. Glesk, and M. Kane, "A terahertz optical asymmetric demultiplexer (TOAD)," *IEEE Photon. Technol. Lett.*, vol. 5, pp. 787–90, July 1993.
- [3.20] M. G. Kane, I. Glesk, J. P. Sokoloff, and P. R. Prucnal, "Asymmetric optical loop: mirror analysis of an all-optical switch," *Appl. Opt.*, vol. 33, no. 29, pp. 6833–42, 1994.
- [3.21] K. Suzuki, K. Iwatsuki, S. Nishi, and M. Saruwatari, "Error-free demultiplexing of 160 Gbit/s pulse signal using optical loop mirror including semiconductor laser amplifier," *Electron. Lett.*, vol. 30, pp. 1501–3, September 1994.
- [3.22] A. J. Poustie, K. J. Blow, A. E. Kelly, and R. J. Manning, "All-optical parity checker," in *Optical Fiber Communication Conference*, pp. 137–9, 1999.
- [3.23] A. J. Poustie, K. J. Blow, R. J. Manning, and A. E. Kelly, "All-optical pseudo-random number generator," *Opt. Comm.*, vol. 159, pp. 208–14, January 1999.
- [3.24] B. S. Robinson and K. L. Hall, "Experimental analysis of switching windows in semiconductor-based all-optical switches," in *Conference on Lasers and Electro-Optics*, pp. 331–2, 2000.
- [3.25] S. J. Savage, B. S. Robinson, S. A. Hamilton, and E. P. Ippen, "All-optical pulse regeneration in an ultrafast nonlinear interferometer with Faraday mirror polarization stabilization," *Opt. Lett.*, vol. 28, pp. 13–15, January 2003.
- [3.26] K. L. Hall and B. S. Robinson, "Bit error rate characterization of 100 Gb/s all-optical demultiplexers," in *Conference on Lasers and Electro-Optics*, pp. 214–5, 1999.

Chapter 4

Gain Saturation in Semiconductor Optical Amplifiers

4.1 Introduction

The use of semiconductor optical amplifiers in multichannel, high bit rate optical networks is limited due to the nonlinearities and cross talk which arise from the intensity-dependent saturation of the optical gain in the semiconductor. Most optical data transmission systems in use today employ some form of pulse-amplitude modulation (PAM) as the channel modulation format. In these systems, information is conveyed by the intensity of an optical pulse. For instance, in a binary on-off keyed (OOK) system, a one-bit is represented by the presence of a pulse in a bit period while a zero-bit is represented by the absence of a pulse in a bit period. Thus, for time-scales comparable to the bit period, the average power in the optical signal is dependent on the transmitted data sequence. If the semiconductor carrier lifetime is comparable to the bit period of the transmitted data, these fluctuations in average power lead to gain variations arising from the depletion and recovery of the free carrier population in the semiconductor. As discussed in Chapter 2, the carrier lifetime in a semiconductor optical amplifier (SOA) is typically between ~ 100 ps and a few nanoseconds. Thus, linear amplification of optical data streams at data rates in excess of a few Gbit/s leads to undesirable patterning and crosstalk between channels.

By contrast, the spontaneous emission lifetime in an erbium-doped fiber amplifier (EDFA) is approximately 10 ms. Since this time constant is many times longer than the bit period at typical optical transmission data rates, the average power in an optical signal on this time-scale varies little. Thus, the EDFA gain remains saturated at a fairly constant level and pattern-dependent gain saturation effects are negligible. Consequently, the wide-availability of EDFAs has led to decreased interest in SOAs for in-line amplification in optical transmission systems.

Semiconductor optical amplifiers remain useful for other network applications such as optical switching due to their high nonlinearity. The fast carrier dynamics in the semiconductor enable bitwise switching at data rates in excess of 100 Gbit/s. As discussed in Chapter 3, the long-lived index dynamics associated with changes in the carrier density can be compensated using a balanced interferometer such as the ultrafast nonlinear interferometer (UNI) [4.1] or the terahertz optical asymmetric demultiplexer (TOAD) [4.2]. However, the gain dynamics in the SOA remain a problem, especially for applications where the high-power control signal to the switch is modulated with a data pattern. Examples of such applications include wavelength conversion, all-optical logic, and all-optical regeneration. For these applications the varying intensity of the control input to the switch leads to pattern-dependent switch performance and undesirable amplitude modulation at the switch output.

In this chapter, we first present experimental results which illustrate the effect of gain saturation in an SOA-based OTDM demultiplexer. Then, we develop a theoretical model which may be used to quantify the effects of gain saturation in a single-channel optical transmission system. Next we review the various techniques which have been considered for reducing the effects of gain saturation in SOA-based switches. We present experimental work related to optical switching using SOAs biased at the transparency point, where gain fluctuations due to stimulated emission are minimized. Finally, we discuss the use of pulse-position modulation (PPM) to mitigate the problems of gain saturation. PPM is a flexible modulation format that can be readily employed in an optical time-division multiplexed (OTDM) network. We describe techniques for transmitting and receiving optical PPM data streams at

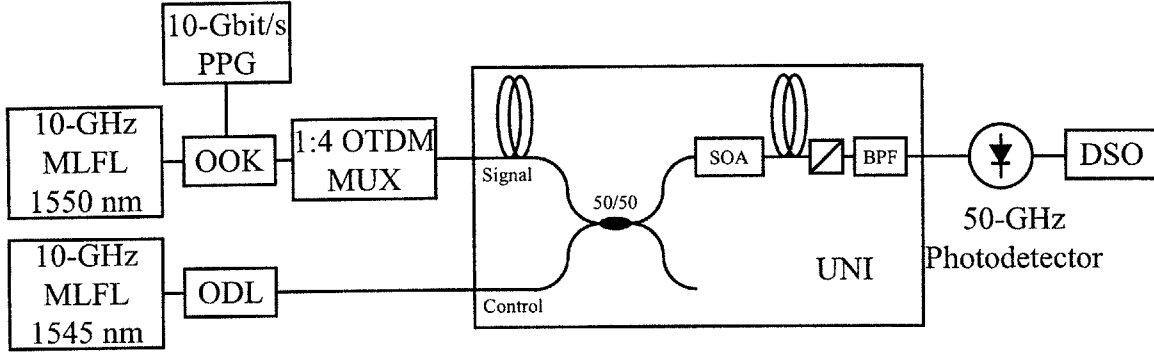


Figure 4-1: Experimental setup for demultiplexing a 10-Gbit/s signal from a 40-Gbit/s data stream. MLFL: Mode-locked fiber laser, ODL: Optical delay line, OTDM MUX: Free-space optical time-division multiplexer, OOK: On-off-keyed modulator, PPG: Pulse-pattern generator, DSO: Digital sampling oscilloscope.

aggregate OTDM data rates. Experimental results for demultiplexing of OTDM PPM data streams and pattern-independent all-optical wavelength and modulation-format conversion are presented.

4.2 Saturation Effects in OTDM Demultiplexing

The effects of gain saturation in a semiconductor optical amplifier may be observed experimentally in a simple demultiplexing experiment. The experimental setup for demultiplexing of a 40-Gbit/s data signal into four 10-Gbit/s signals is shown in Figure 4-1. The 40-Gbit/s data signal is generated from a commercially-available (PriTel) mode-locked fiber laser. The laser produces 2.5-ps pulses at 1550 nm with a 10-GHz repetition rate. The pulses are modulated using a lithium niobate intensity modulator driven by a pulse-pattern generator producing a 10-Gbit/s pseudo-random data pattern of length $2^{31} - 1$. The OOK-modulated pulses are then passively multiplexed to a data rate of 40 Gbit/s in a free-space OTDM multiplexer. The two relative delays in the multiplexer are set to $3/2$ and $3/4$ of the 10-Gbit/s bit period, thus ensuring that adjacent bits in the 40-Gbit/s pattern are uncorrelated.

A UNI demultiplexes a single 10-Gbit/s data stream from the 40-Gbit/s aggregate stream. The 40-Gbit/s data is the signal input to the UNI. A second mode-locked

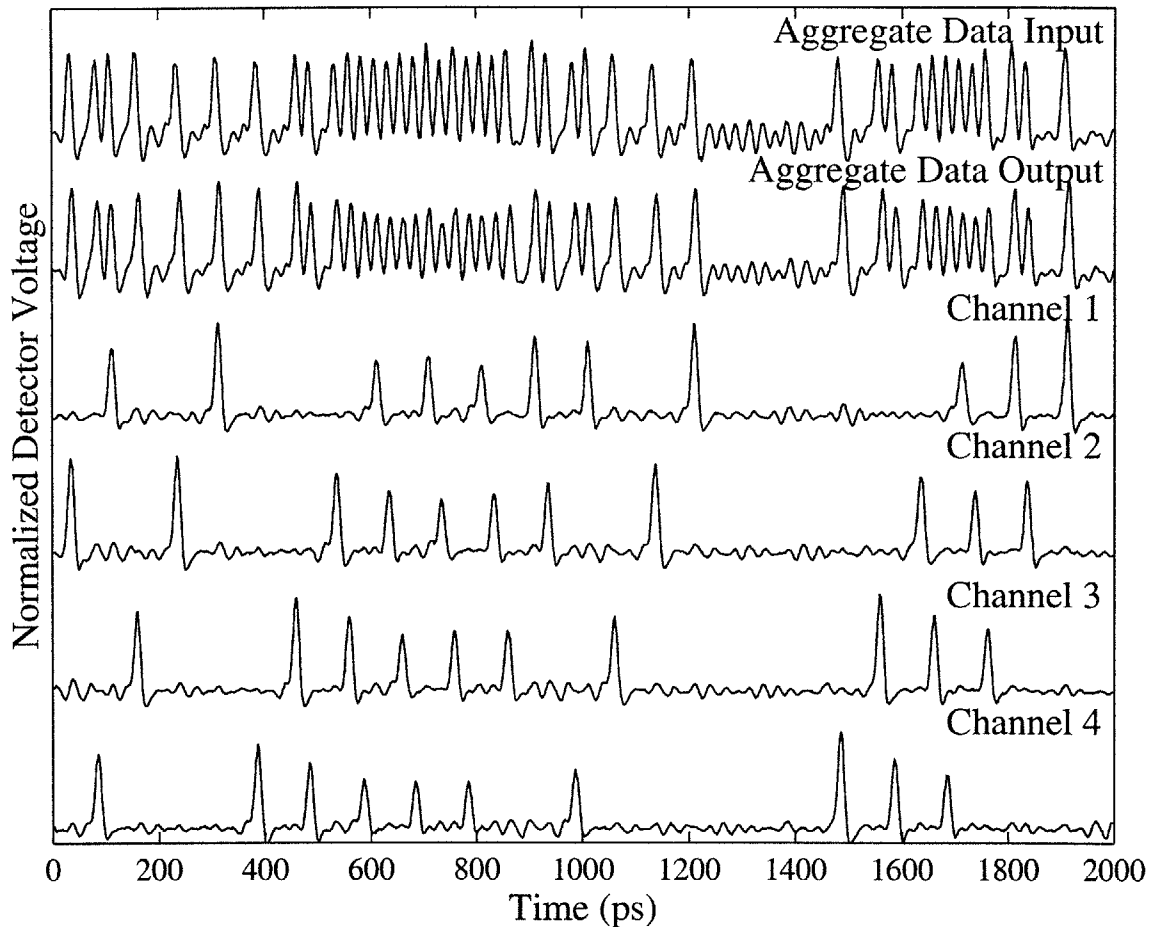


Figure 4-2: Waveforms at input and output of 40-Gbit/s-to-10-Gbit/s demultiplexer measured using a digital sampling oscilloscope.

fiber laser operating at 10 GHz provides a stream of 2.5-ps pulses at 1545 nm for the control input of the UNI. The signal pulse separation in the UNI is set to provide a switching window duration of approximately 5 ps. An optical delay line on the control input allows the relative delay between the control and signal inputs to be varied, enabling any of the four 10-Gbit/s streams at the signal input to be selected by the demultiplexer. The commercially-available SOA (Alcatel) in the UNI is biased with a current of 200 mA. At the UNI inputs, the signal pulse energy is 8.2 fJ and the control pulse energy is 117 fJ.

Figure 4-2 shows waveform traces of the input and output signals in the experiment measured using a 50-GHz photodiode and a digital sampling oscilloscope. The first

trace shows the 40-Gbit/s aggregate data stream at the signal input to the UNI. At this point, any observed non-uniformity in the amplitudes of the pulses is due to imperfections in the modulation and multiplexing of the data. The second trace shows the aggregate data stream after passing through the UNI. This trace is obtained by biasing the UNI in the ON state and passing the signal through with no pulses applied to the control input. The effects of gain saturation in the semiconductor optical amplifier are clearly visible as a compression of the output pulse amplitudes in response to a series of one-bits at the input. The remaining traces show the output of the UNI when it is configured for demultiplexing. In this case, the UNI is biased OFF and the control pulses are used to switch out a 10-Gbit/s data stream from the 40-Gbit/s aggregate stream. The four different channels are obtained by varying the relative delay between the control and signal inputs.

We can make several important observations regarding the gain saturation effects observed in this demultiplexing experiment. First, we observe that amplitude modulation at the output of the demultiplexer is dependent on the incoming data pattern. A series of pulses representing a string of one-bits in the data pattern saturates the gain of the semiconductor optical amplifier, thereby reducing the gain for subsequent pulses. Second, we note that the amplitude modulation in a particular demultiplexed channel is dependent on the data pattern in the channels that are not demultiplexed. This crosstalk between different channels can have serious implications for OTDM networks. In particular, in bit-interleaved OTDM systems (as opposed to slotted OTDM systems), a receiver on the network operates at the bit rate of the demultiplexed channel and, generally, has no information regarding the data pattern in neighboring channels which are not demultiplexed. Therefore, in spite of the fact that gain saturation effects are deterministic based on the history of data passing through the amplifier, at a bit-interleaved OTDM receiver their effect may appear as random amplitude fluctuations which are largely uncorrelated with the demultiplexed data. This means that feed-forward correction schemes which seek to reduce the effects of amplitude patterning by dynamically adjusting the gain or threshold at the receiver in response to the received optical signal (see, for example, [4.3–4.5]) may

not be practical in these systems. Consequently, gain saturation in an in-line SOA can have a severe impact on receiver performance in an OTDM transmission system.

4.3 Statistical Analysis of Gain Saturation

Gain saturation effects in semiconductor optical amplifiers can have considerable impact on end-to-end system performance in an optical link. In order to study the effects of gain saturation on a system performance metric, such as the bit-error rate measured at an optical receiver, a statistical description of the SOA gain in response to a random transmitted data sequence is required. Statistical models describing gain in an SOA have been developed previously. However, these models have been limited to multichannel systems where the bit-period is much longer than the SOA carrier density recovery time [4.6] and systems where the channel number is large enough so that fluctuations in the aggregate optical intensity may be accurately modeled as small-signal deviations from the average intensity [4.7, 4.8]. These models are not necessarily applicable to the study of ultrafast OTDM systems where data with a bitperiod that is typically shorter than the SOA carrier density recovery time is transmitted using a single modulated optical wavelength. Statistical models of SOAs in single-channel systems have been limited to studies of the effects of short sequences of random bits with durations approximately equal to the carrier lifetime [4.9, 4.10]. These models are impractical when the gain recovery time encompasses many bit periods. In this section, we develop a general theoretical model of the SOA gain which may be used to accurately describe the SOA gain statistics for single-channel transmission systems at OTDM data rates. For illustration, we apply this model to study the effects of gain saturation on the receiver sensitivity in the simple optical communication link shown in Figure 4-3. The link consists of a pulse-amplitude modulation transmitter and an optically preamplified direct-detection receiver. An SOA is used for in-line amplification between the transmitter and receiver.

We begin with a model describing the propagation of an optical pulse in an SOA. This model is adapted from the theory presented in [4.11]. In a frame of reference

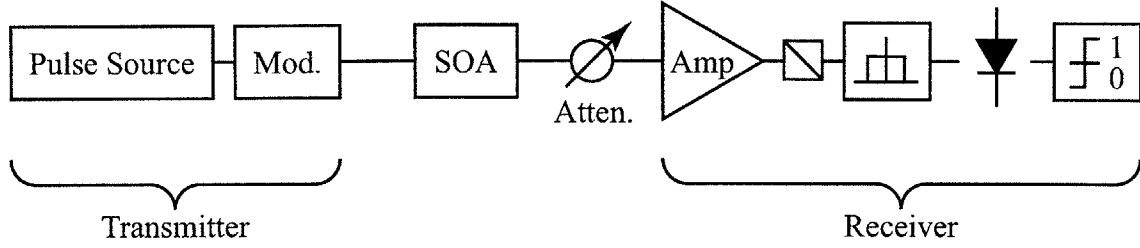


Figure 4-3: Optical transmission system employing a semiconductor optical amplifier for in-line amplification.

moving at the group velocity of the optical signal, the instantaneous intensity of the signal at a longitudinal point in the SOA, z , is $P(z, t)$. Assuming that the gain of the amplifier, $g(z, t)$, is large enough so that scattering and other propagation losses may be neglected, the evolution of the intensity envelope in the amplifier may be described by

$$\frac{\partial P(z, t)}{\partial z} = g(z, t)P(z, t). \quad (4.1)$$

Since the gain saturation effects which give rise to patterning in high bit-rate optical transmission systems occur on time-scales of ~ 100 ps, or greater, we shall employ a simple model for the gain which only includes the effects of the carrier density dynamics in the amplifier. Ultrafast effects which occur on time-scales much shorter than the bit period, such as spectral hole burning and carrier heating, are neglected. These effects can lead to pulsewidth-dependent saturation in the amplification of short pulses [4.12, 4.13]. Thus, we limit the present discussion to pulses with durations of at least 1 picosecond. In this case, the amplifier gain dynamics can be approximately described by [4.11]

$$\frac{\partial g(z, t)}{\partial t} = \frac{g_0 - g(z, t)}{\tau_c} - \frac{g(z, t)P(z, t)}{E_{\text{sat}}}, \quad (4.2)$$

where g_0 is the unsaturated small-signal gain of the amplifier, τ_c is the spontaneous carrier lifetime in the active region, and E_{sat} is the saturation energy of the amplifier.

The first term in Equation 4.2 models recovery of the gain to its unsaturated level, g_0 . The second term represents the gain saturation due to the incident optical field.

The intensity envelope at the output of the amplifier ($z = L$) may be obtained via integration of Equation 4.1 over the length of the amplifier

$$P(z = L, t) = P(z = 0, t)e^{h(t)}. \quad (4.3)$$

Here, $h(t)$ is the integrated gain observed by the pulse at time t ,

$$h(t) = \int_0^L g(z, t) dz. \quad (4.4)$$

Integration of Equation 4.2 over the length of the amplifier yields an ordinary differential equation describing the dynamics of the integrated gain, $h(t)$, [4.11]

$$\frac{dh}{dt} = \frac{g_0 L - h(t)}{\tau_c} - \frac{P(z = 0, t)}{E_{\text{sat}}} [e^{h(t)} - 1]. \quad (4.5)$$

Equations 4.3, 4.4, and 4.5 may be solved to determine the response of the amplifier to a specified input, $P(0, t)$.

We wish to study the dynamics of the integrated gain, $h(t)$, in response to an optical field which is modulated with a random data pattern. For binary pulse amplitude modulation, the optical field at the input to the amplifier may be written as

$$P(0, t) = \sum_{n=-\infty}^{\infty} b_n E_p p(t - nT), \quad (4.6)$$

where $\{b_n\}$ is a random binary data sequence, E_p is the pulse energy, $p(t)$ is the pulse intensity envelope, and T is the bit period. The pulse envelope, $p(t)$, is confined to the bit interval $[0, T]$ and has unit area. We shall assume that the random binary sequence, $\{b_n\}$, is generated by a stationary random process and that b_n and b_m are statistically independent for $n \neq m$.

Now, consider the random sequence, $\{h_n\}$, obtained by sampling the integrated

gain at the beginning of each bit period:

$$h_n = h(nT). \quad (4.7)$$

Note that h_n can, in general, take on any value in the interval $[0, g_0L]$. We will specify the probability density for h_n in this interval as $f_n(h)$. Equation 4.5 may be used to relate h_{n+1} to h_n :

$$h_{n+1} = h_n + \int_{nT}^{(n+1)T} \left\{ \frac{g_0L - h(t)}{\tau_c} - b_n \frac{p(t - nT)}{E_{\text{sat}}} [e^{h(t)} - 1] \right\} dt. \quad (4.8)$$

Thus, h_{n+1} is completely specified in terms of h_n and b_n . Since b_n is statistically independent of all prior bits in the data sequence, the sequence $\{h_n\}$ is a discrete-time continuous-state Markov process. That is, h_{n+1} is independent of h_{n-1}, h_{n-2}, \dots if h_n is known. The probability density for h_{n+1} may be specified in terms of the probability density for h_n via the density propagation equation

$$f_{n+1}(h) = \int_0^{g_0L} \pi(h, h') f_n(h') dh', \quad (4.9)$$

where the transition kernel function, $\pi(h, h')$ is the conditional density function for h_{n+1} given that $h_n = h'$. Since the process generating the data sequence, $\{b_n\}$, is stationary, the transition kernel is temporally homogeneous. Therefore, it does not depend on the index n . If $h_n = h'$, then h_{n+1} will be one of two possible values, $h_1(h')$ or $h_2(h')$, corresponding to the cases where $b_n = 1$ or $b_n = 0$. Thus,

$$\begin{aligned} \pi(h, h') &= f_{n+1|n}(h|h') \\ &= p_1 \delta(h - h_1(h')) + p_0 \delta(h - h_2(h')). \end{aligned} \quad (4.10)$$

The values h_1 and h_2 may be obtained using Equation 4.8. For large n , the density function, $f_n(h)$, converges to the stationary density for the transition kernel, $f_S(h)$. The stationary density does not change from one observation time to the next. Thus,

from Equation 4.9, we find that the stationary density is described by a Fredholm integral equation of the second kind with the transition kernel, π :

$$f_S(h) = \int_0^{g_0L} \pi(h, h') f_S(h') dh'. \quad (4.11)$$

We employ a discrete numerical approximation to solve Equation 4.11 and calculate the stationary distribution, $f_S(h)$. First, the range of possible integrated gains, $[0, g_0L]$, is partitioned into N bins of width $\Delta h = g_0L/N$. The probability density function for h_n is represented using an N -element column vector, F_n , where the k -th element of F_n is:

$$F_n[k] = \int_{(k-1)\Delta h}^{k\Delta h} f_n(h) dh, \quad (4.12)$$

where $k \in \{1, 2, \dots, N\}$. Substituting this definition into Equation 4.9, we obtain

$$\begin{aligned} F_{n+1}[j] &= \int_{(j-1)\Delta h}^{j\Delta h} \pi(h, h') f_n(h') dh' dh \\ &\approx \int_{(j-1)\Delta h}^{j\Delta h} \sum_{k=1}^N \pi\left(h, k\Delta h - \frac{\Delta h}{2}\right) F_n[k] dh \\ &\equiv \sum_{k=1}^N \Pi_{jk} F_n[k]. \end{aligned} \quad (4.13)$$

Thus, the transition kernel π is discretized to form an $N \times N$ matrix, Π , where

$$\Pi_{jk} = \int_{(j-1)\Delta h}^{j\Delta h} \pi\left(h, k\Delta h - \frac{\Delta h}{2}\right) dh. \quad (4.14)$$

With this notation, the stationary density, F_S , is the solution to the matrix equation

$$F_S = \Pi F_S. \quad (4.15)$$

Thus, the stationary state, F_S , is the (normalized) eigenvector for the matrix, Π , which has an eigenvalue of 1. Due to the nature of the transition kernel, as described in Equation 4.10, the transition matrix, Π , is very sparse. Each column in the matrix

has, at most, two non-zero entries. Thus, sparse matrix techniques can be used to solve the eigen equation and find the stationary density for large N .

Figure 4-4 shows two example probability densities for the integrated gain. The densities were calculated for a 1-mm long SOA with a small signal gain, g_0 , of 10,000 m^{-1} , a carrier lifetime, τ_c , of 200 ps, and a saturation energy, E_{sat} , of 1 pJ. The integrated gain range from 0 to 10 was divided into $N = 1000$ bins for the calculation of the stationary state of the gain distribution. The optical pulse intensity envelope, $p(t)$, is a 2-ps gaussian. In both simulations, the peak of the pulse arrives 5 ps after the sample time, so the integrated gain at the sample time is fairly close to the gain seen by the pulse entering the amplifier. In Figure 4-4 a), the integrated gain density is calculated for a 10-Gbit/s random data stream ($T = 100$ ps) with a pulse energy of 100 fJ. In Figure 4-4 b), the same calculation is performed for a 100-Gbit/s random data stream ($T = 10$ ps) with a pulse energy of 10 fJ. In both cases, the average power of the incident optical signal is 1 mW. However, the calculated probability densities for the integrated gain are very different. For the 10-Gbit/s data stream, the probability density function indicates that the integrated gain at the sample time takes on only a few discrete values. This characteristic is due to the fact that the bit period is very close to the carrier lifetime in the SOA. Thus, the gain observed at the sample time is only significantly affected by a few of the previous bits. By contrast, for the 100-Gbit/s data stream, the carrier lifetime in the SOA is many bit periods in duration. Thus, the integrated gain is affected by fluctuations in the signal energy averaged over many bit periods. Since these fluctuations are smaller than the energy fluctuations for the 10-Gbit/s data stream, the variance in the observed gain is also smaller.

Once the stationary density for the integrated gain at the beginning of the bit period is known, the bit-error rate at a receiver may be calculated by conditioning on h

$$P_e = \int_0^{g_0 L} \Pr[\text{error}|h(0) = h'] f_S(h') dh'. \quad (4.16)$$

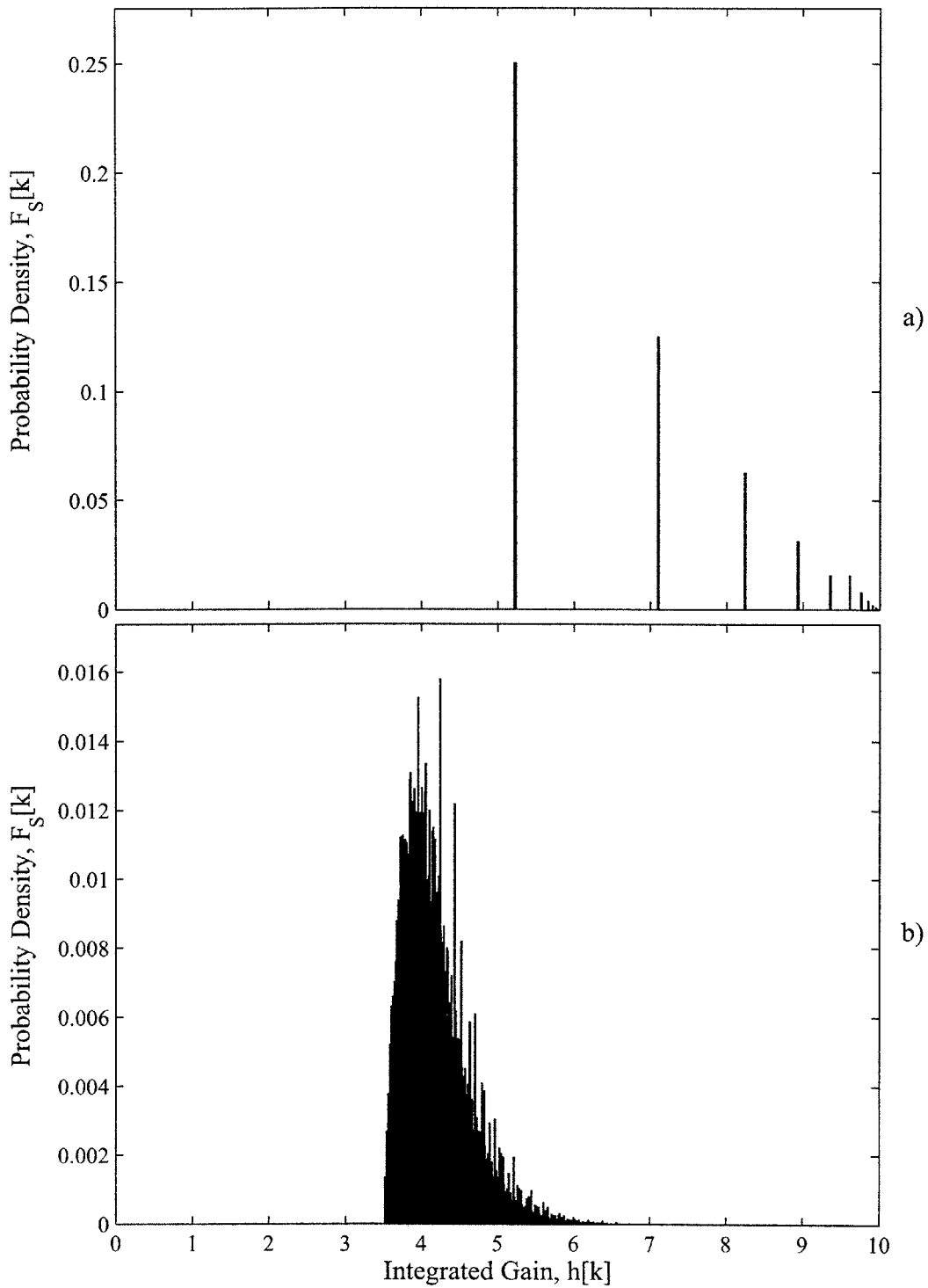


Figure 4-4: Probability density for the sampled integrated gain in an SOA in response to a) a 10-Gbit/s random OOK-modulated data stream with a pulse energy of 100 fJ and b) a 100-Gbit/s random OOK-modulated data stream with a pulse energy of 10 fJ.

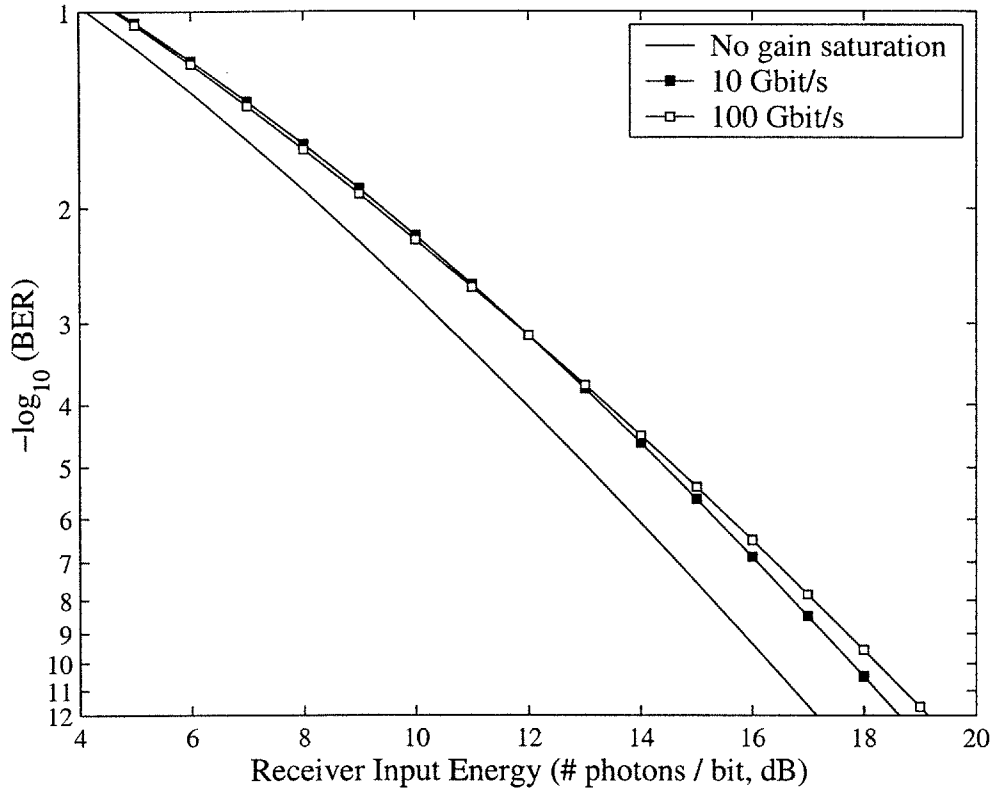


Figure 4-5: Calculated bit-error rate for 10-Gbit/s and 100-Gbit/s transmission systems including the effects of gain saturation in an in-line SOA. The pulse extinction ratio at the SOA input is infinite.

For a specified value of $h(0)$, the conditional probability of error in the integrand is calculated as follows. First, the pulse energies for a one-bit and a zero-bit at the output of the amplifier are obtained using Equations 4.3, 4.4, and 4.5. Then, the probability of error is calculated for a receiver with these pulse energies at the input. The receiver is modeled as an optically preamplified direct-detection receiver with a matched optical filter [4.14]. The resulting bit-error rate as a function of the average number of photons per bit at the receiver input is shown in Figure 4-5. Note, the input power to the optical receiver is varied by including a fixed attenuation between the SOA and the receiver input. The input power to the SOA is not varied.

Figure 4-5 shows the calculated bit-error rate as a function of the number of photons per bit at the receiver input. The solid curve represents the performance

of an ideal direct detection receiver with no amplitude patterning on the incoming data stream. The curves with square markers show the receiver performance for the 10-Gbit/s and 100-Gbit/s data streams described above. At a bit-error rate of 10^{-9} , the sensitivity of the ideal receiver is 38 photons per bit. When the effects of gain saturation are included, the sensitivity degrades to 53 photons per bit for the 10-Gbit/s signal and 59 photons per bit for the 100-Gbit/s, corresponding to power penalties of 1.4 dB and 1.9 dB relative to the ideal receiver sensitivity. This degradation is largely due to the fact that the error performance at the receiver is primarily determined by the lowest energy one-bits that arrive at the receiver input, while the average power at the receiver is affected by the higher energy one-bits.

The receiver performance becomes much worse if the practical limitations of a typical transmitter are included in the analysis. In particular, a finite extinction ratio (defined as the ratio of the energy in a one-bit to the energy in a zero-bit) at the transmitter can have a severe impact on receiver performance when gain saturation effects are included in the link. Typical transmitters in optical transmission links have extinction ratios of 20-30 dB. Gain saturation effects in an in-line amplifier lead to further degradation in the extinction ratio, since a one-pulse may see less gain than a zero-pulse. Figure 4-6 shows the performance of the 10-Gbit/s and 100-Gbit/s links discussed above when the transmitter extinction ratio is limited to 20 and 30 dB. For the 10-Gbit/s system, the sensitivity degrades to 146 photons per bit for an extinction ratio of 30 dB and 419 photons per bit for an extinction ratio of 20 dB, corresponding to power penalties of 5.8 dB and 10.4 dB from the ideal baseline sensitivity. For the 100-Gbit/s system, we calculate sensitivities of 65 photons per bit for an extinction ratio of 30 dB and 179 photons per bit for an extinction ratio of 20 dB, corresponding to power penalties of 2.3 dB and 6.7 dB from the ideal baseline sensitivity. The power penalties at 100 Gbit/s are generally smaller than the penalties at 10 Gbit/s because the variance in the gain is smaller. However, due to the different shape of the probability density function for the integrated gain at the two different data rates, the 100-Gbit/s system has a larger power penalty than the 10-Gbit/s system at low error rates.

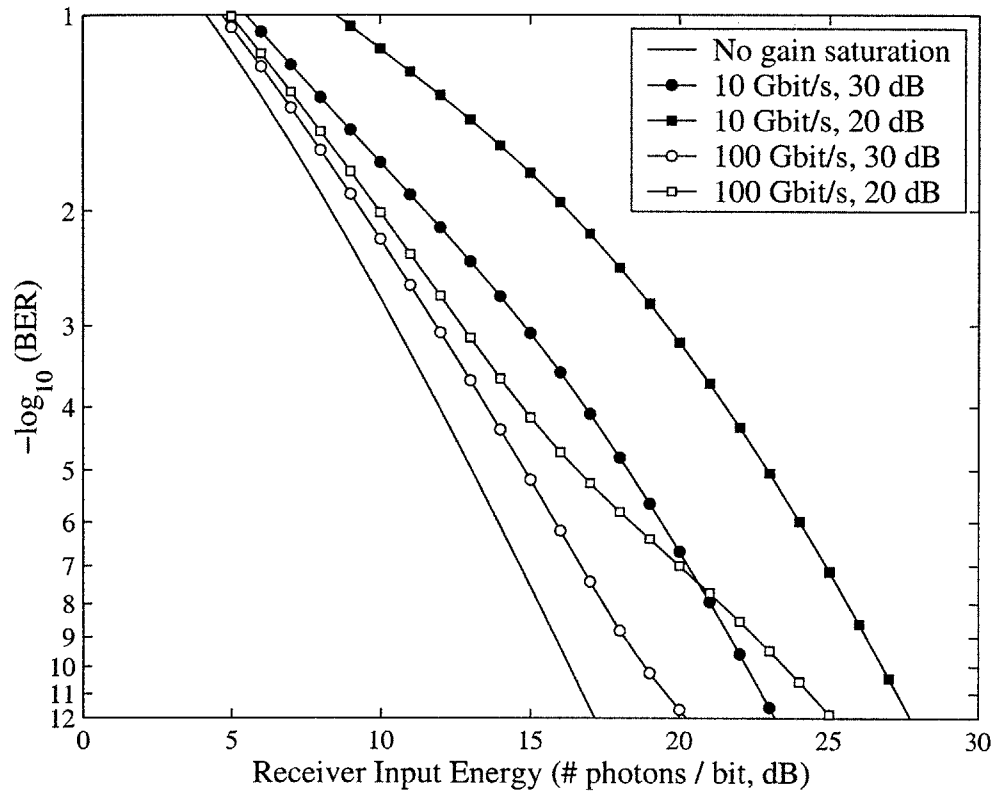


Figure 4-6: Calculated bit-error rate as a function of the receiver input power for 10 Gbit/s and 100 Gbit/s transmission systems with finite extinction ratios of 30 dB and 20 dB at the transmitter.

4.4 Reducing Pattern-Dependent Gain Saturation

Three primary approaches have been considered for reducing the problems of pattern-dependent gain saturation in semiconductor optical amplifiers. First, one can reduce the carrier lifetime of the semiconductor. Ideally, this lifetime should be reduced to much less than the relevant time for energy fluctuations in the signal, thus assuring that the amplifier remains at a constant saturation level. A second approach is to design semiconductor materials such that the intensity fluctuations of the optical signal do not induce appreciable changes in the carrier populations of the semiconductor. Finally, gain fluctuations can be reduced by utilizing a modulation format in which the energy of the signal does not vary appreciably on the time-scale of the carrier lifetime. In this section, we review several implementations of these three approaches and consider their practicality for use OTDM networks.

There are several methods for reducing the recovery time for carrier density changes in an SOA. For instance, the device may be operated at high bias currents, producing high carrier densities in the active region. Under these conditions, Auger recombination can become the dominant recombination mechanism, leading to a carrier lifetime that varies with bias current as $\tau_c \propto I^{-2/3}$ [4.15]. At high bias currents (producing carrier densities $\sim 3 - 6 \cdot 10^{24} \text{ m}^{-3}$), carrier lifetimes of $\sim 100 - 200 \text{ ps}$ are typically observed. This is still not sufficient for operating at bit rates of 10 Gbit/s or higher. The gain recovery time can be reduced further by using an optical holding beam [4.16]. The holding beam typically has a photon energy that is higher than the photon energy of the data signal. It serves to “clamp” the gain at a particular level of saturation. When the carrier density is depleted due to stimulated emission, the holding beam replenishes carriers via stimulated absorption. Holding beams have been used to achieve gain recovery times of $< 20 \text{ ps}$ [4.17, 4.18].

An alternative to speeding up the gain recovery time is to design the semiconductor material so that intensity fluctuations in the optical signal do not induce changes in the free carrier populations. For instance, one can use a passive waveguide where both the signal and control photon energies are below the bandgap of the semiconductor.

In this case, there is no change in the carrier populations due to linear stimulated absorption or emission. Typically, the signal and control energies are set only slightly below the bandgap energy in order to take advantage of the resonant enhancement of the index nonlinearity near the band edge ([4.19, 4.20]). However, at these energies, two-photon absorption can induce unwanted carrier density changes and limit the switching efficiency of the device [4.21, 4.22].

Pattern-dependent gain fluctuations may also be reduced by utilizing the gain-transparent (GT) SOA configuration [4.23, 4.24]. In this scheme, the signal photon energy is below the bandgap of the semiconductor while the control photon energy is above the bandgap of the semiconductor. In practice, SOAs with a bandgap of $1.3 \mu\text{m}$ have been used with signal and control wavelengths of $1.55 \mu\text{m}$ and $1.3 \mu\text{m}$, respectively. GT SOAs have been demonstrated in UNI [4.25], TOAD/SLALOM [4.24, 4.26], and Mach-Zehnder [4.27] switches as well as for four-wave mixing [4.28]. The GT configuration is most useful in demultiplexer applications where the signal contains intensity-modulated data while the control is an unmodulated clock source. Thus, the control pulses induce regular periodic fluctuations of the carrier populations. The index variations which accompany these fluctuations are used to demultiplex the signal data. Since the signal wavelength is below the bandgap of the semiconductor, intensity modulation on the signal does not affect the carrier populations significantly. Indeed, linearity for signal inputs over a power range of more than 50 dB has been demonstrated [4.29].

The GT configuration suffers two potential drawbacks. First, it requires that the signal and control photon energies be widely spaced. Thus, wavelength conversion may be required in order to process two signals whose wavelengths are closely-spaced, as might be the case in a typical transmission system. Second, the GT configuration does not solve the problem of pattern-dependent carrier density fluctuations for the case when the control input to the switch is modulated with data. Thus, its application is limited primarily to the demultiplexing configurations for which it was proposed.

Operation at the transparency point has also been suggested for all-optical switch-

ing situations where the control pulse stream is modulated with a data pattern [4.30, 4.31]. Recall from Chapter 2 that at thermal equilibrium, the free carriers in an active semiconductor have a Fermi distribution. Above-band photon energies near the band edge experience gain via stimulated emission while energies that are much higher than the bandgap energy experience loss due to stimulated absorption. The energy at which the signal experiences equal amounts of stimulated emission and stimulated absorption is known as the transparency point. It is equal to the energy difference between the quasi-Fermi levels in the conduction and valence bands of the semiconductor. Signals at the transparency energy experience neither gain nor loss via linear interactions with the free carriers of the semiconductor. Thus, they do not affect the gain of the semiconductor by changing the carrier densities in the semiconductor. However, index changes do occur in the semiconductor due to the effects two-photon absorption and carrier heating by free carrier absorption. These index changes have been observed experimentally using pump-probe techniques [4.30] and may be utilized to provide all-optical switching in an interferometric configuration such as the UNI.

4.4.1 Demonstration of All-Optical Wavelength Conversion at Transparency Point

We have experimentally investigated the practicality of all-optical switching at the transparency point [4.32, 4.33]. Figure 4-7 shows the experimental setup for demonstrating all-optical wavelength conversion at 10 Gbit/s using the UNI. The control and signal pulse sources are provided by two synchronized 10-GHz gain-switched distributed-feedback lasers. The chirped pulses output from the gain-switched lasers were compressed using a dispersion compensating fiber to produce 11.3-ps signal pulses and 10.4-ps control pulses. Since the losses in the SOA are high when operating at the transparency point, it is preferable to use signal pulses with photon energies less than the control pulse photon energy so that the signal pulses are amplified in the SOA. In this experiment, the signal pulse wavelength is 1551 nm and the control

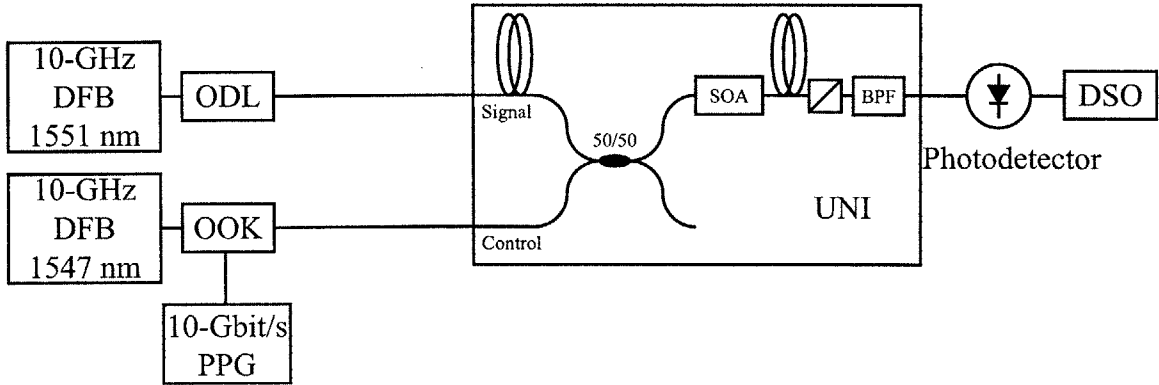


Figure 4-7: Experimental setup for all-optical wavelength conversion using an ultra-fast nonlinear interferometer.

pulse wavelength is 1547 nm. When the SOA is biased at transparency for the control pulse photon energy, the total loss through the UNI at the signal wavelength is 11.5 dB. The control pulses are OOK-modulated with a pseudo-random binary sequence of $2^7 - 1$ bits with an intensity modulator. The UNI is biased off. Hence, a signal pulse only propagates to the output when a control pulse is present. In this manner, the OOK data on the control wavelength is converted to the signal wavelength at the output of the UNI.

As discussed in Chapter 2, the transparency point varies with the injected carrier density in the SOA. In this switching experiment, the bias current in the SOA is adjusted in order to set the transparency point at the control pulse wavelength of 1547 nm. This is done by modulating the control input to the SOA using an optical chopper. When the SOA is biased such that the control photons are in the gain or absorption regimes, stimulated interband transitions may be observed as changes in the junction voltage across the SOA diode [4.34]. A lock-in amplifier is used to detect changes in the junction voltage at the chopper frequency. The SOA current is then adjusted to minimize the signal observed on the lock-in amplifier, thereby setting the transparency point to coincide with the control photon energy.

Figure 4-8 shows input and output waveforms from the wavelength conversion experiment as measured on a digital sampling oscilloscope. The top trace shows the

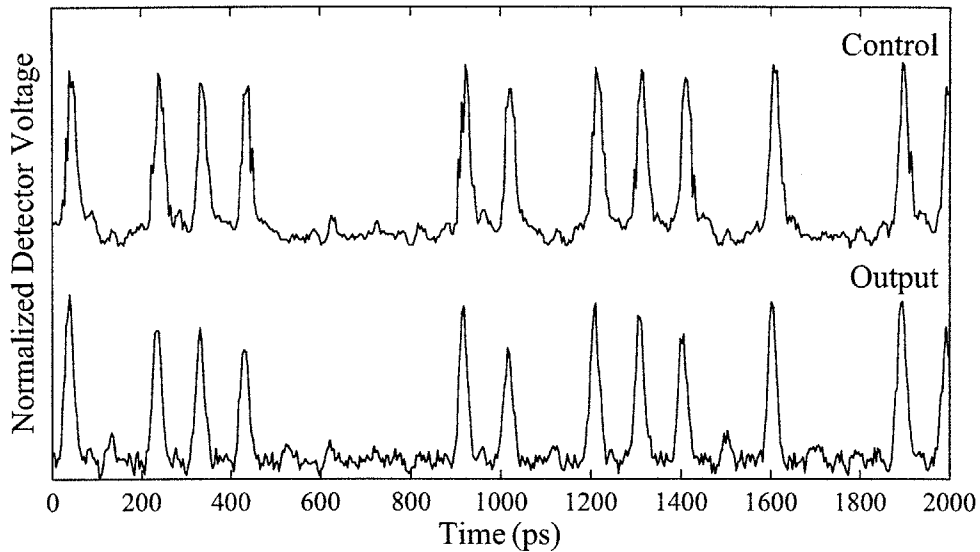


Figure 4-8: Wavelength conversion of a 10-Gbit/s signal using a semiconductor optical amplifier biased at the transparency point.

modulated control pulse stream. The bottom trace shows the modulated signal pulses at the output of the UNI. With the amplifier biased at transparency, we obtained a π phase shift in the signal pulses with control pulse peak powers of approximately 1 W, corresponding to a switching energy of 10 pJ. This high switching energy is due the lack of gain at the control pulse energy. Coupling losses (estimated as ≈ 3 dB per facet) and scattering losses in the SOA waveguide can also be significant.

In spite of the fact that the SOA is biased so that the modulated control pulses are at the transparency point, amplitude patterning is still observed on the signal output. There are several possible explanations for this patterning. First, note that similar patterning is observed in the control pulses at the input of the switch due to imperfect modulation. Additionally, since the transparency point is sensitive to temperature and the SOA bias current, it may have drifted during the course of the experiment. This effect can be mitigated by actively tracking the transparency point with a control loop. Finally, because of the high control pulse intensities required to achieve a π phase shift, interband transitions due to two-photon absorption were probably significant. These transitions cause carrier density changes and associated

saturation of the optical gain. Experimental and theoretical studies suggest that two-photon absorption is a significant limitation for switching at the transparency point [4.35].

4.4.2 Alternative Modulation Formats

As discussed above, the gain saturation problems which arise in transmission systems using standard PAM modulation formats, are largely due to the fact that variations in the modulated signal energy varies on time-scales which are comparable to the gain-recovery time of the amplifier. Thus, a possible solution to these problems is to use a modulation format in which the signal energy varies little on a time-scale comparable to the amplifier gain recovery time. In this manner, the amplifier remains saturated at a constant level and pattern-dependent gain modulation is reduced.

One such modulation format which has been recently demonstrated is the wavelength modulated (WM) signal format [4.36]. This format consists of modulating a non-return-to-zero (NRZ) OOK data pattern on one wavelength and modulating its inverse on a neighboring wavelength. In this manner, the total intensity of the two signals is constant, independent of the data pattern. This modulation is easily generated using a 2x1 LiNbO₃ intensity modulator where the two wavelengths are input to the two separate modulator inputs and the WM signal is obtained at the output. This technique has been used to demonstrate the propagation of eight 10-Gbit/s WDM channels (using a total of 16 wavelengths) over 75 km of dispersion-shifted fiber with in-line SOA amplification [4.36]. The WM signal format resulted in a wider dynamic range of usable input powers at the SOA and better receiver sensitivity as compared to standard NRZ modulation formats. However, because the data and inverse data are modulated on distinct wavelength channels, any chromatic dispersion in the transmission link leads to walk-off between the two signals. Thus, dispersion compensation is required before each amplifier.

A polarization multiplexing scheme has also been recently demonstrated for reducing pattern-dependent gain saturation in an SOA [4.37]. This technique is very similar to the WM format. However, instead of using a second wavelength for each

channel, the data and inverse data are modulated onto orthogonal polarizations at the same wavelength, thereby ensuring a constant, pattern-independent signal intensity at the SOA. This technique was used in a transmission experiment where 2 10-Gbit/s channels were sent over 45 km of standard fiber with in-line SOA amplification [4.37]. In contrast to the WM demonstration, this modulation technique is not adversely affected by chromatic dispersion. However, polarization mode dispersion (PMD) can lead to different group delays and undesirable mixing between the two orthogonal polarizations.

Both of these modulation techniques are very effective in reducing the pattern-dependence of the gain in SOAs. They are attractive due to their simple implementation. The transmission of both the data and the inverse data can also be utilized to obtain improved sensitivity at the receiver with a balanced detection scheme, although this was not demonstrated in the reported experiments. These improvements come at a cost of a factor of 2 reduction in the spectral efficiency of the modulation format (in units of bit/s/Hz/polarization). It should also be noted that the effects of chromatic dispersion and polarization mode dispersion may make the implementation of these modulation formats difficult in real transmission systems. Moreover, these modulation formats, which are NRZ in nature, are not readily extended to OTDM transmission systems which typically utilize return-to-zero (RZ) modulation formats.

4.5 Pulse-Position Modulation

An alternative modulation technique which can be effectively utilized in an OTDM network is pulse-position modulation (PPM). With PPM, pulses are transmitted at a fixed symbol rate and information is conveyed via the temporal placement of a pulse within the symbol period. In M -ary PPM, there are M possible time slots during which a pulse may arrive in each symbol period. In the following discussion, we shall assume that $M = 2^k$, where k is an integer. Thus, each symbol in the M -ary PPM waveform conveys k bits of information. Hence, transmitting a binary sequence at a

bit rate of R_B requires a symbol rate of

$$\begin{aligned} R_S &= \frac{R_B}{k} \\ &= \frac{R_B}{\log_2 M}. \end{aligned} \tag{4.17}$$

The symbol transmission period, T_S , is divided into M slots of duration $\tau = T_S/M$ during which the optical pulse may arrive. Often, the symbol transmission period is set equal to $1/R_S$ in order to maximize the spectral efficiency of the modulated signal. However, since we desire a modulation format that can be used with standard passive time-division multiplexing techniques where symbols from different transceivers or channels may be temporally interleaved on a network bus, we shall allow the symbol transmission period to be a small fraction of $1/R_S$. For instance, if the aggregate network data-rate is N times the individual transceiver rate, R_B , we set the symbol transmission period equal to $1/(N \cdot R_S)$. This condition allows the transmitted symbols from various transceivers in the network to be temporally interleaved in standard OTDM fashion.

Pulse-position modulation in optical transmission systems was first studied as a means for improving receiver sensitivities [4.38, 4.39]. Prior to the development of the EDFA, receiver sensitivities were the primary limitation for unrepeated transmission distances in optical fiber networks. Even today, energy-efficient modulation formats such as PPM may be useful in free-space communications links where mid-span amplification is impossible. As we shall discuss in more detail below, the use of the PPM data format can also be effective in reducing the gain saturation problems which arise in semiconductor optical amplifiers used in optical transmission and switching systems. As long as the symbol rate is comparable to or shorter than the gain-recovery rate in the SOA, the SOA will remain saturated at a fairly constant level since an optical pulse arrives in each symbol period.

Methods for generating optical PPM waveforms at electronic data rates are well-established. Below, we present novel techniques for transmitting and receiving optical PPM signals at OTDM data-rates which may exceed available electronic data rates.

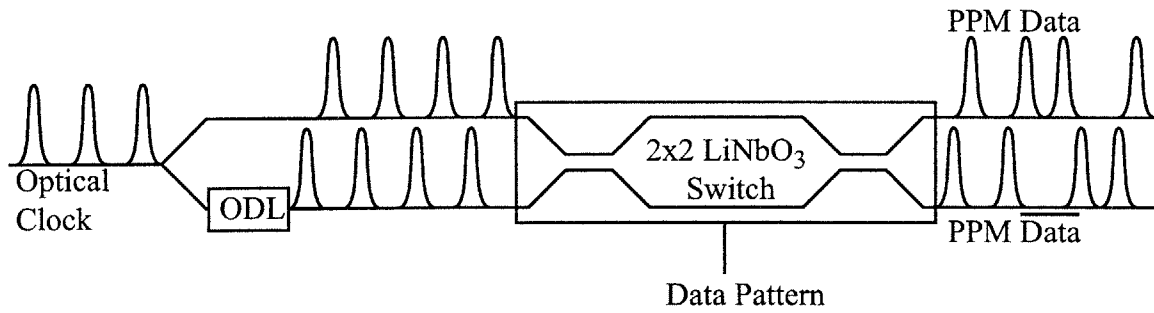
We also discuss the impact of the use of the PPM data-format on spectral efficiency and receiver sensitivities in optical networks.

4.5.1 PPM Waveform Generation

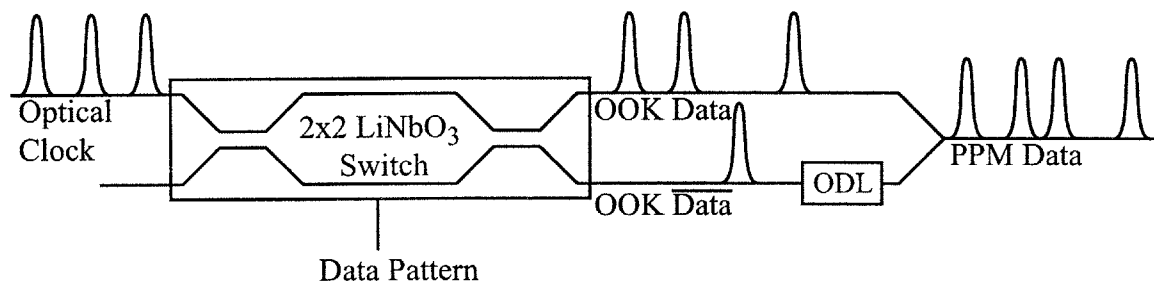
There are several possible techniques for generating an optical PPM data signal. Perhaps the most straightforward method is to generate the PPM waveform using electronics. This waveform can then be used to drive an optical intensity modulator to generate the optical PPM signal. Generating the PPM waveform in this manner allows the designer to take advantage of electronic processing capabilities to design highly-functional transmitters and receivers. For example, a high-sensitivity variable-rate transmission link using binary PPM has been demonstrated [4.40]. The receiver in this demonstration achieved near-quantum-limited performance at multiple bit rates between 51 Mbit/s and 1.244 Gbit/s using a single fixed-bandwidth optical filter. Generating the PPM waveform in this manner also eases the bandwidth requirements for the optical modulator drive electronics. As we will show in Section 4.5.3, for moderate values of M , the use of M -ary PPM reduces contributions from low-frequency components in the electronic waveform. Thus, wide-band modulator drivers that have good performance and gain near DC may not be required. Instead, cheaper narrow-band amplifiers may be utilized.

The primary difficulty associated with generating an electronic PPM waveform is the limitation imposed by the maximum electronic bandwidth. For instance, consider a system for transmitting a 10-Gbit/s stream of data using an optical PPM signal with a symbol rate of 2.5 GHz (400-ps symbol period). In this case, $M = 2^4 = 16$. So, the PPM slot duration is $400 \text{ ps}/16 = 25 \text{ ps}$. The electronics generating the PPM waveform must be able to generate a pulse shorter than the slot duration. Thus, transmission at this modest data rate would require an electronic bandwidth in excess of 40 GHz.

We have proposed and demonstrated several optical modulation techniques for generating an optical PPM waveform at OTDM data-rates which do not require such high electronic bandwidths. Figure 4-9 shows two such techniques for generating



a)



b)

Figure 4-9: Two configurations for producing optical binary PPM waveforms using an electro-optic modulator. In a), the PPM delay is introduced prior to modulation. In b), the PPM delay is introduced after modulation.

binary PPM waveforms. Both techniques use an electro-optic 2x2 switch driven by an NRZ electronic waveform at the base data rate to perform the modulation. In the first technique, an optical pulse source generates pulses at the symbol rate. A 50/50 coupler divides the clock pulses into two arms. One arm is delayed relative to the other using a tunable optical delay line. The relative delay between the two arms is set equal to one PPM time slot (also referred to as the “PPM delay”). For binary PPM, this is generally equal to one-half of the symbol-period at the aggregate data-rate. The two streams of pulses are then used as the two optical inputs to a LiNbO₃ 2x2 modulator. The modulator is driven by an NRZ electronic waveform at the bit-rate. It is biased such that a one-bit places the modulator in the bar-state and a zero-bit places the modulator in the cross-state. In this manner, a one-bit in the data routes the pulse from the upper arm to the upper output while a zero-bit in the data routes the delayed pulse from the lower arm to the upper output. Thus, a binary PPM waveform is created at the output of the modulator. Coincidentally, a PPM waveform representing the inverse data pattern is created at the lower output of the modulator. This modulation technique has been verified in a 12.5-Gbit/s all-optical wavelength-conversion experiment [4.41].

Since the two pulses at the input of the modulator in Figure 4-9 a) arrive at different times, for PPM delays that are a significant fraction of the symbol period, this first modulation technique suffers due to the non-instantaneous switching-time of the modulator. The second modulation technique, shown in Figure 4-9 b), was developed to address this problem. In this technique, the optical clock is input to one arm of the switch. The electronic data pattern drives the switch, producing an OOK-formatted version of the data on the upper output and an OOK-version of the inverse data on the lower output. A tunable optical delay line is used to introduce a relative PPM delay between the two arms. The two arms are then combined in a 50/50 coupler to produce the PPM waveform at the output. In this modulator design, a single optical pulse which is much shorter than the bit-period of the data sequence is used at the input to the modulator. This pulse is timed to fall in the middle of the bit-period so that it is unaffected by the rise- and fall-time of the switch. Since the

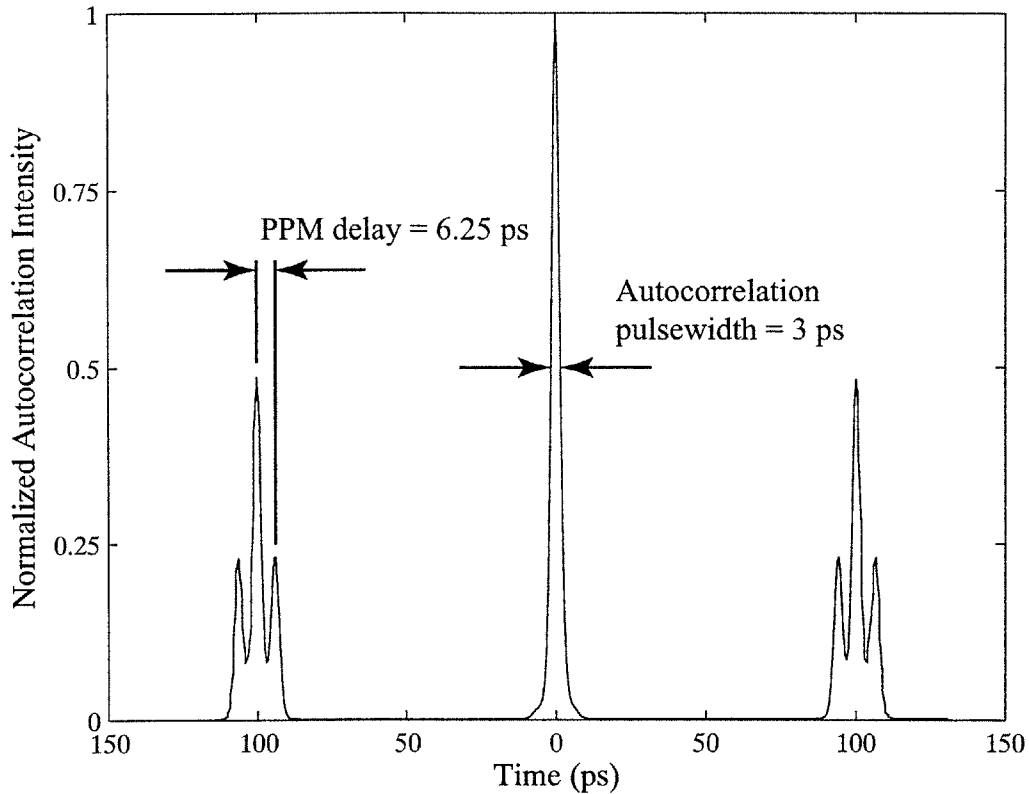


Figure 4-10: Experimental autocorrelation of a 10-Gbit/s pseudo-random binary PPM sequence using 2-ps optical pulses. The PPM delay is 6.25 ps, allowing OTDM multiplexing to rates as high as 80 Gbit/s.

PPM delay is added after the modulator, this second technique can be used to create longer PPM delays than what is possible with the first technique.

Figure 4-10 shows an experimental autocorrelation of the output of a PPM modulator configured as shown in Figure 4-9 a). In this example, the optical source was a mode-locked fiber laser producing 2-ps pulses at a 10-GHz repetition rate. A 10-Gbit/s pseudo-random binary sequence of $2^{31} - 1$ bits was used to drive the 18-GHz LiNbO₃ 2x2 switch in the PPM modulator. The PPM delay was set to 6.25 ps, allowing the modulated waveform to be passively multiplexed to data-rates as high as 80 Gbit/s [4.42]. The pulse at the origin is the autocorrelation of the optical pulses used in the experiment. The next pair of pulses near the origin represent the crosscorrelation between a one-bit and a subsequent zero-bit in the waveform. This pattern

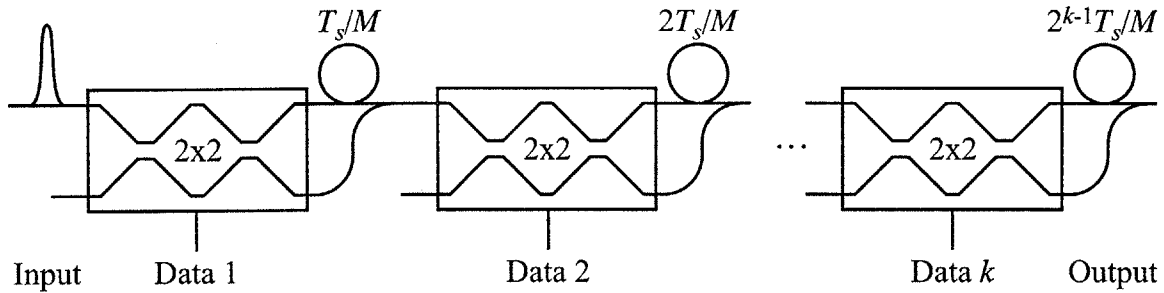


Figure 4-11: An optical M -ary PPM waveform modulator ($M = 2^k$) constructed using k 2×2 switches and a logarithmic series of delay lines.

occurs with probability $1/4$. These pulses are separated by the PPM delay from the $1/2$ height pulses representing a pair of one-bits or a pair of zero-bits in the data sequence. Finally, the pair of pulses furthest from the origin in the autocorrelation trace represent a zero-bit followed by a one-bit in the data sequence.

The two modulators described above are used to create binary PPM optical waveforms. The technique can also be extended to produce M -ary PPM waveforms, where $M = 2^k$, as shown in Figure 4-11. In this case, k binary PPM modulators are cascaded. The first has a PPM delay of T_s/M . Each subsequent modulator has a delay that is twice the delay of the preceding modulator. If each 2×2 switch is driven by a data sequence with a bit-rate equal to the PPM symbol-rate, R_s , the output of the cascaded modulators will be an M -ary PPM waveform at an aggregate data-rate of $k \cdot R_s$.

4.5.2 Demodulation and Detection of Optical PPM Signals

An M -ary PPM waveform detector must decide, for each received symbol, which of the M possible symbols was transmitted. There have been numerous studies of optical PPM receivers (see, for example, [4.39, 4.43, 4.44]). Early studies of PPM-based fiber transmission systems analyzed receivers which determined which PPM symbol was transmitted based on the time at which the received optical intensity first crossed some predefined threshold [4.43]. Such a receiver design is useful when the transmitted

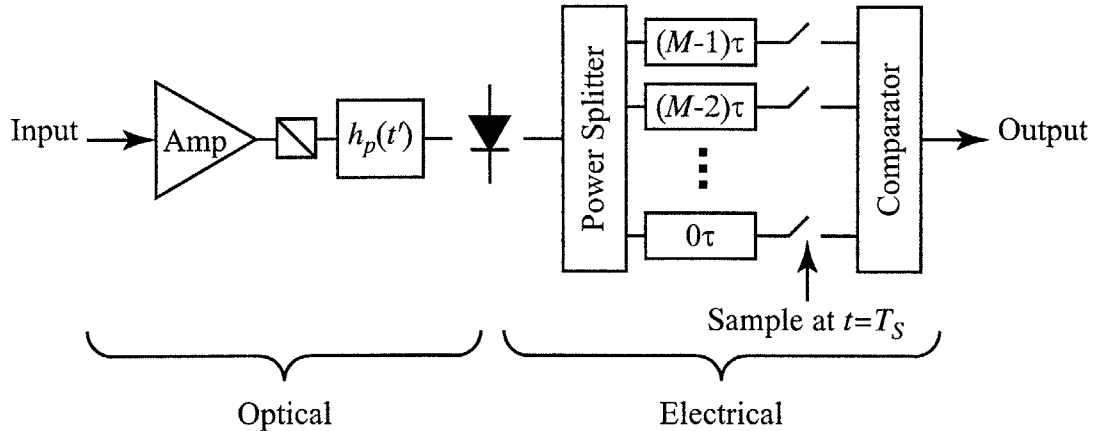


Figure 4-12: Maximum likelihood direct detection M -ary PPM receiver for equal a priori symbol probabilities.

pulse field envelope, $a_p(t)$, is not confined to a single PPM slot time, τ . While this modulation format may relax bandwidth requirements at the transmitter, these receivers are difficult to implement at high data rates since the electrical bandwidth required to detect the threshold transition is inversely proportional to the PPM slot time. Additionally, the non-orthogonal nature of the transmitted signal pulses leads to a penalty in receiver sensitivity relative to transmission systems utilizing orthogonal modulation formats.

When the transmitted pulse field envelope, $a_p(t)$, is confined to the PPM slot time (i.e. $a_p(t) = 0$ for $t < 0$ and $t > \tau$), the PPM symbols are non-overlapping, or orthogonal. If equal a priori symbol probabilities are assumed, the maximum likelihood direct detection M -ary orthogonal PPM receiver design is shown in Figure 4-12. An optical amplifier at the input amplifies the incoming optical signal. While the amplified spontaneous emission (ASE) noise added by this amplifier reduces the ideal sensitivity of the receiver, the amplifier is useful for overcoming the practical limitations of thermal noise and shot noise in the receiver electronics. A polarizer after the amplifier rejects ASE that is orthogonal to the signal polarization. The amplified signal is then filtered with an optical matched filter prior to square-law detection with a photodetector. The photodetector current is then divided among M delay lines. At

the sample time, the current output from these delay lines corresponds to the signal and noise energy in each PPM slot. A comparator samples the detector current at the output of each of the delay lines and selects the symbol corresponding to the largest detector current as the decoded symbol. Below, we analyze the sensitivity of this receiver in the limit of high optical amplifier gain. In this case, the receiver noise is dominated by the amplified spontaneous emission from the optical amplifier.

In our analysis we shall consider the impact that imperfect extinction at the PPM transmitter has on the sensitivity of the receiver. Let r denote the ratio of the energy in the slot containing the PPM pulse to the energy in an empty slot. If m -th symbol is transmitted ($m \in \{0, 1, \dots, M - 1\}$), then the signal at the input to the receiver may be expressed as

$$x_{in}(t) = \text{Re} \{ s_m(t) e^{j\omega_0 t} \}, \quad (4.18)$$

where ω_0 is the angular frequency of the optical carrier. The complex symbol envelope, $s_m(t)$, is the sum of the pulse contributions in each slot:

$$s_m(t) = \sqrt{\frac{2E_S r}{r + M - 1}} a_p(t - m\tau) + \sum_{\substack{n=1 \\ n \neq m}}^M \sqrt{\frac{2E_S}{r + M - 1}} a_p(t - n\tau). \quad (4.19)$$

Here, E_S is the average energy per received symbol. The complex pulse envelope, $a_p(t)$, is normalized so that

$$\int_{-\infty}^{\infty} |a_p(t)|^2 dt = 1. \quad (4.20)$$

The optical preamplifier at the receiver input is treated as a linear amplifier of the optical field with power gain G . After passing through the optical amplifier, the amplified symbol is given by

$$x_A(t) = \text{Re} \left\{ \left[\sqrt{G} s_m(t) + n(t) \right] e^{j\omega_0 t} \right\}, \quad (4.21)$$

where $n(t)$ is the complex envelope of the amplified spontaneous emission noise added

by the amplifier. In this analysis, it is assumed that the signal bandwidth is small compared to the bandwidth of the additive noise. Thus, for time-scales of interest, the noise envelope, $n(t)$, can be modeled as white gaussian noise with a double-sided power spectral density of [4.45]

$$S_n(\omega) = \frac{N_0}{2} = \frac{1}{2}n_{sp}(G - 1)\hbar\omega, \quad (4.22)$$

where $\hbar\omega$ is the photon energy and n_{sp} is the spontaneous emission parameter describing the population inversion of the amplifier.

The optical filter is a bandpass filter centered at the carrier frequency, ω_0 . The envelope of the impulse response of the optical filter is matched to the pulse envelope:

$$h_p(t) = \sqrt{2}\text{Re} \{ a_p^*(\tau - t)e^{-j\omega_0(\tau - t)} \}. \quad (4.23)$$

The impulse response of the matched filter response is delayed by τ to ensure that the filter is causal. Since the optical pulse envelope, $a_p(t)$, is confined to a single slot, the impulse response of the optical filter is zero for $t < 0$ and $t > \tau$. In the narrowband approximation, the field at the output of the bandpass filter is a bandpass signal with an envelope described by the convolution of the envelopes of the filter impulse response and the amplified signal at the input to the filter:

$$x_F(t) = \frac{1}{\sqrt{2}}\text{Re} \left\{ \left[\sqrt{G}s_m(t) + n(t) \right] \otimes a_p^*(\tau - t) \cdot e^{j\omega_0(t - \tau)} \right\}. \quad (4.24)$$

The photodetector produces a current, $x_{PD}(t)$, that is proportional to the square of the magnitude of the filtered envelope:

$$x_{PD}(t) = \frac{1}{2} \left| \left[\sqrt{G}s_m(t) + n(t) \right] \otimes a_p^*(\tau - t) \right|^2. \quad (4.25)$$

The output from the photodetector is divided among M delay lines and the compara-

tor samples each delay line at time $t = T_S = M\tau$. The k -th sample is

$$\begin{aligned} x_k &= x_{PD}((k+1)\tau) \\ &= \frac{1}{2} \left| \int_{k\tau}^{(k+1)\tau} \left[\sqrt{G} s_m(t') + n(t') \right] a_p^*(t' - k\tau) dt' \right|^2. \end{aligned} \quad (4.26)$$

The bounds on the convolution integral in Equation 4.26 are obtained by noting that $a_p(t)$ is time-limited to the interval $(0, \tau)$. Since $a_p(t - k\tau)$ and $a_p(t - m\tau)$ are orthogonal when $k \neq m$, we obtain from Equation 4.19

$$x_k = (\mu_k + n_{I,k})^2 + n_{Q,k}^2. \quad (4.27)$$

Here,

$$\mu_k = \begin{cases} \sqrt{\frac{GE_S \tau}{r+M-1}} & \text{if } k = m \\ \sqrt{\frac{GE_S}{r+M-1}} & \text{if } k \neq m \end{cases} \quad (4.28)$$

and $n_{I,k}$ and $n_{Q,k}$ are the sampled in-phase and quadrature components of the filtered noise process, defined by

$$n_{I,k} = \text{Re} \left\{ \frac{1}{\sqrt{2}} \int_{k\tau}^{(k+1)\tau} n(t') a_p^*(t' - k\tau) dt' \right\} \quad (4.29)$$

and

$$n_{Q,k} = \text{Im} \left\{ \frac{1}{\sqrt{2}} \int_{k\tau}^{(k+1)\tau} n(t') a_p^*(t' - k\tau) dt' \right\}. \quad (4.30)$$

Since $n_{I,k}$ and $n_{Q,k}$ are samples of a filtered zero-mean white gaussian noise process with double-sided power spectral density of $N_0/2$, they are gaussian random variables

with mean and covariance given by:

$$\begin{aligned} E[n_{\alpha,k}] &= 0 \\ E[n_{\alpha,k}n_{\beta,j}] &= \frac{N_0}{2}\delta_{\alpha\beta}\delta_{jk}, \end{aligned} \quad (4.31)$$

where $\alpha, \beta \in \{I, Q\}$. Thus, each sample, x_k , is a sum of the squares of two uncorrelated gaussian random variables. Moreover, the M samples corresponding to a particular transmitted symbol are uncorrelated. It is straightforward to show that the probability density function for the k -th sample is given by the Rician distribution [4.46]

$$f_k(x_k) = \frac{1}{N_0} \exp\left(-\frac{x_k + \mu_k^2}{N_0}\right) I_0\left(\frac{2\mu_k\sqrt{x_k}}{N_0}\right) \quad (4.32)$$

where $x > 0$ and I_0 is the zero-order modified Bessel function.

If each symbol is transmitted with equal probability, the optimum decision rule for the receiver selects the symbol corresponding to the largest sample, x_k . The correct decision will be made when the sample corresponding to the transmitted symbol is larger than the other $M - 1$ samples. Assuming that symbol zero is transmitted, we find that the probability of correctly decoding the received symbol is

$$\begin{aligned} P_{SC} &= \Pr\left(x_0 = \max_k\{x_k\}\right) \\ &= \int_0^\infty f_0(x_0) \prod_{k=1}^{M-1} \left(1 - \int_{x_0}^\infty f_k(x_k) dx_k\right) dx_0 \\ &= \int_0^\infty f_0(x_0) \left[1 - \int_{x_0}^\infty f_1(x_1) dx_1\right]^{M-1} dx_0. \end{aligned} \quad (4.33)$$

The last equality in Equation 4.33 is obtained by noting that x_j and x_k are identically distributed random variables for $k, j \in \{1, 2, \dots, M - 1\}$. A symbol error is made whenever a symbol is not decoded correctly. Thus, the probability of a symbol error

is

$$\begin{aligned}
P_{SE} &= 1 - P_{SC} \\
&= 1 - \int_0^\infty f_0(x_0) \left[1 - \int_{x_0}^\infty f_1(x_1) dx_1 \right]^{M-1} dx_0 \\
&= \int_0^\infty f_0(x_0) \left\{ 1 - \left[1 - \int_{x_0}^\infty f_1(x_1) dx_1 \right]^{M-1} \right\} dx_0.
\end{aligned} \tag{4.34}$$

Equation 4.34 is generally difficult to evaluate when Rician distributions are used for both $f_0(\cdot)$ and $f_1(\cdot)$. In this work, we utilize an upper bound on the probability of symbol error which was first described by Hughes [4.47]. This bound is tighter than the more common union bound (see, for example, [4.48, 4.49]), yet still computationally tractable. It is obtained by noting that the function $f(y) = 1 - [1 - y]^{M-1}$ is concave on the region $y \in [0, 1]$. Thus, Jensen's inequality [4.50] may be applied to bound the expected value of $f(y)$ for y in this range as $E[f(y)] \leq f(E[y])$. Defining

$$y = \int_{x_0}^\infty f_1(x_1) dx_1, \tag{4.35}$$

we find that the symbol error probability in Equation 4.34 may be expressed as the expectation of $f(y)$ over the random variable x_0 , $P_{SE} = E[f(y)]$. Applying Jensen's inequality, we obtain

$$\begin{aligned}
P_{SE} &\leq f(E[y]) \\
&= 1 - [1 - E[y]]^{M-1}.
\end{aligned} \tag{4.36}$$

It can be shown that this bound is always less than the bound obtained using the union bound [4.47]. Substituting the definition of y into $E[y]$, we find

$$\begin{aligned}
E[y] &= \int_0^\infty f_0(x_0) \int_{x_0}^\infty f_1(x_1) dx_1 dx_0 \\
&= \Pr(x_1 > x_0).
\end{aligned} \tag{4.37}$$

Thus, the expected value of y over x_0 is the probability that x_1 is greater than x_0 . Since this term is typically very small at high photon counts, the bracketed term in Equation 4.36 is very close to 1. This can limit the accuracy of the numerical evaluation of the error probability. For this reason, we expand the power series to obtain

$$P_{SE} \leq \sum_{n=1}^{M-1} \binom{M-1}{n} (-1)^{n-1} [\Pr(x_1 > x_0)]^n \quad (4.38)$$

The probability that x_1 is greater than x_0 is the probability that the current sampled in a slot without a pulse is larger than the current sampled in a slot with a pulse. Using Equation 4.32, we find that this probability can be expressed as [4.51, 4.52]

$$\Pr(x_1 > x_0) = \frac{1}{2} \left\{ \left[1 - Q_1 \left(\sqrt{\frac{E_1}{N_0}}, \sqrt{\frac{E_0}{N_0}} \right) \right] + Q_1 \left(\sqrt{\frac{E_0}{N_0}}, \sqrt{\frac{E_1}{N_0}} \right) \right\}, \quad (4.39)$$

where E_0 is the average amplified energy in the slot containing the pulse,

$$E_0 = \frac{GE_S r}{r + M - 1}, \quad (4.40)$$

and E_1 is the average amplified energy in a slot without a pulse,

$$E_1 = \frac{GE_S}{r + M - 1}. \quad (4.41)$$

Note that for large amplifier gain, G , and extinction, r , the ratio E_0/N_0 approaches the number of photons per symbol at the receiver input. In Equation 4.39, Q_1 is the first-order generalized Marcum Q -function, defined as

$$Q_m(\alpha, \beta) = \int_{\beta}^{\infty} u \left(\frac{u}{\alpha} \right)^{m-1} \exp \left(-\frac{u^2 + \alpha^2}{2} \right) I_{m-1}(\alpha u) du. \quad (4.42)$$

The Marcum Q -function has been tabulated extensively [4.53]. To numerically evaluate the Marcum Q -function, we implement an algorithm [4.54] based on a power

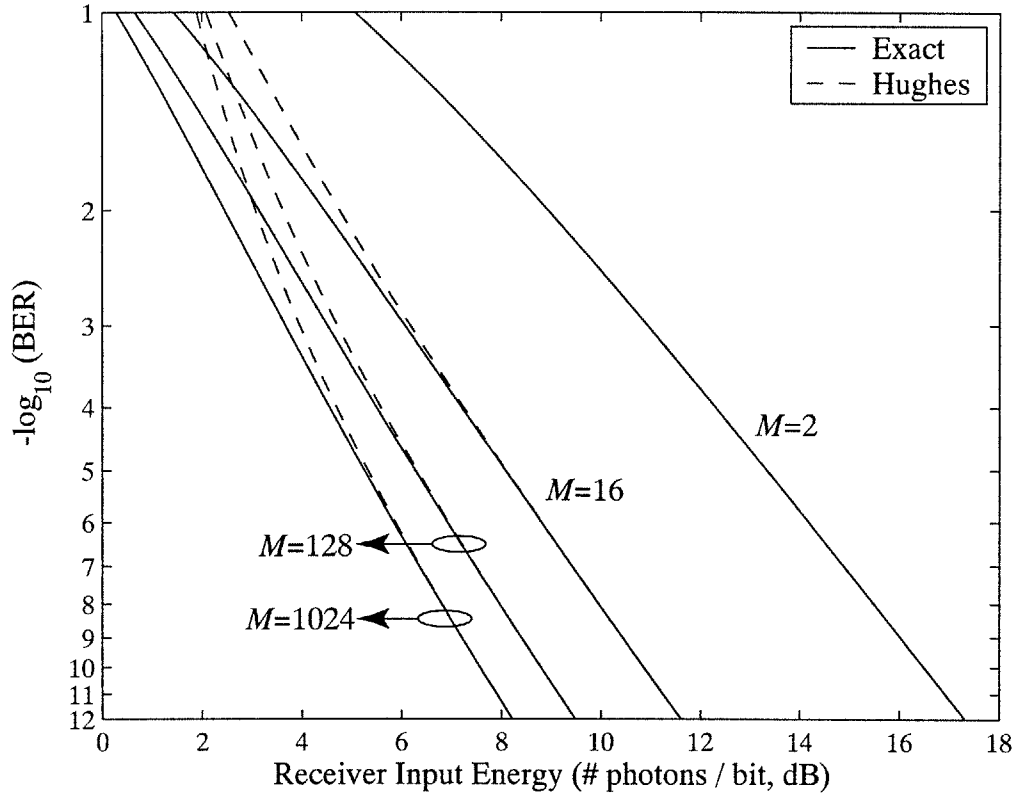


Figure 4-13: Calculated bit-error rate for an ideal noncoherent M -ary PPM receiver as a function of the number of photons per bit at the receiver input.

series approximation to the function developed by Fehlner [4.55] and Dillard [4.56].

We must now calculate the expected bit-error rate as a function of the symbol error probability. When a symbol error is made in an M -ary orthogonal modulation scheme, such as PPM, each of the $M - 1$ incorrect symbols is likely to be detected with equal probability. A particular bit in the decoded symbol will be incorrect in $(M/2)$ of the $M - 1$ incorrect codewords. Assuming that each symbol is transmitted with equal probability, the probability of a bit error is given by

$$P_E = \frac{1}{2} \frac{M}{M-1} P_{SE} = \frac{2^{k-1}}{2^k - 1} P_{SE}. \quad (4.43)$$

Figure 4-13 shows the calculated bit-error rate as a function of the number of received photons per bit for the case of perfect extinction at the transmitter ($r \rightarrow \infty$).

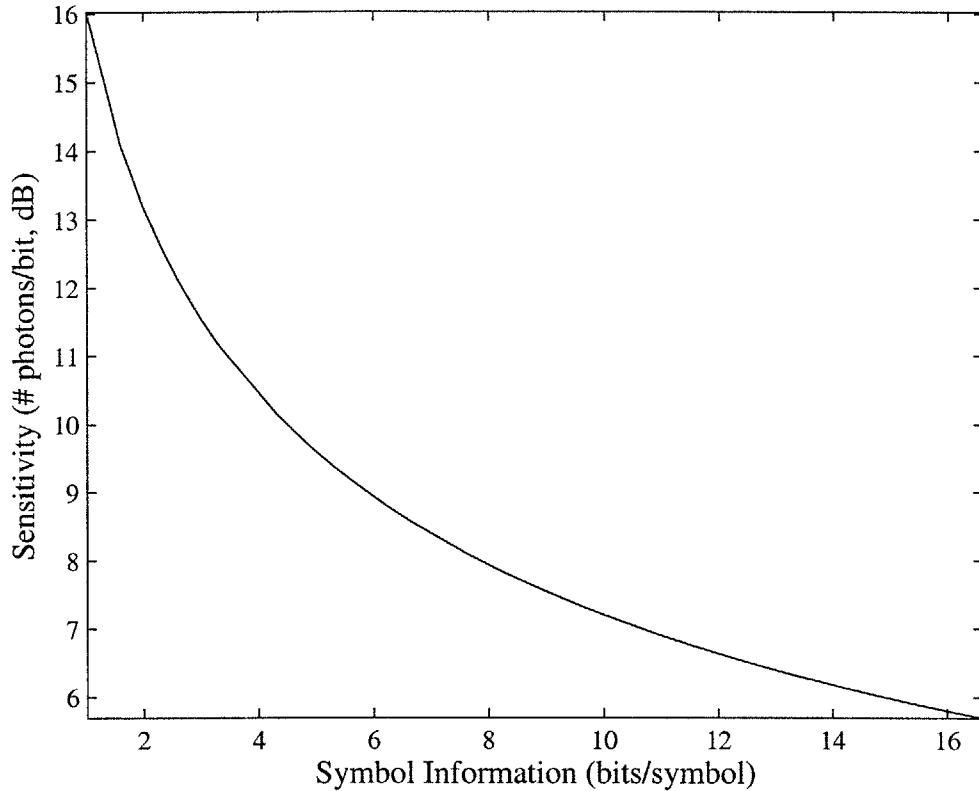


Figure 4-14: Required number of photons per bit to achieve a BER of 10^{-9} as a function of the number of bits per transmitted symbol, $k = \log_2 M$.

The solid lines show the exact bit-error rate obtained via numerical integration of Equation 4.34. The dashed lines show the upper bound on the bit-error rate calculated using Equation 4.38. For $M = 2$ (binary PPM), the upper bound provided by the Hughes approximation is equal to the exact bit-error rate. For larger values of M , the upper bound asymptotically approaches the exact value of the bit-error rate at low error rates. Since receiver performance is typically characterized at error rates of $< 10^{-9}$, we use the Hughes bound in the receiver sensitivity calculations discussed below.

As Figure 4-13 illustrates, the receiver power required to achieve a particular error rate decreases as the symbol alphabet size, M , increases. This is one of the primary benefits of an orthogonal M -ary modulation scheme such as PPM. The receiver sensitivity is defined as the required number of photons per bit to achieve a

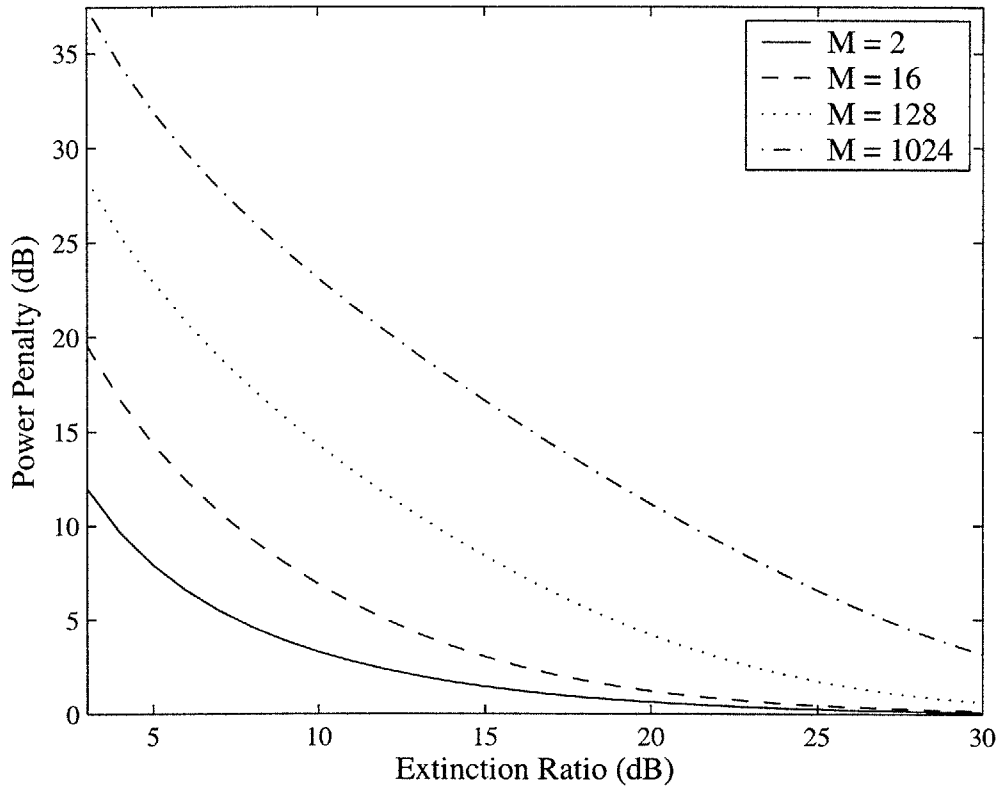


Figure 4-15: Receiver power penalty at a bit-error rate of 10^{-9} as a function of the pulse extinction ratio at the transmitter.

bit-error rate of 10^{-9} . For binary PPM ($M = 2$), the ideal noncoherent PPM receiver described here requires 40 photons/bit to achieve this error rate. For $M = 1024$, approximately 5 photons/bit are required to obtain the same performance. Figure 4-14 shows the calculated receiver sensitivity as a function of the number of bits per symbol ($\log_2 M$). The receiver sensitivity decreases monotonically as M is increased. Ultimately, the sensitivity asymptotically approaches a limit of $\ln 2$ bits (= one “nat”) per photon [4.57, 4.58].

Next, we consider the effect of a finite extinction ratio in the detected PPM symbols. Figures 4-15 and 4-16 illustrate the impact of a finite pulse extinction ratio on receiver performance. In Figure 4-15 the receiver power penalty is plotted as a function of the extinction ratio, r , for several values of M . The power penalty is the fractional increase in receiver power required to achieve a bit-error rate of 10^{-9} as

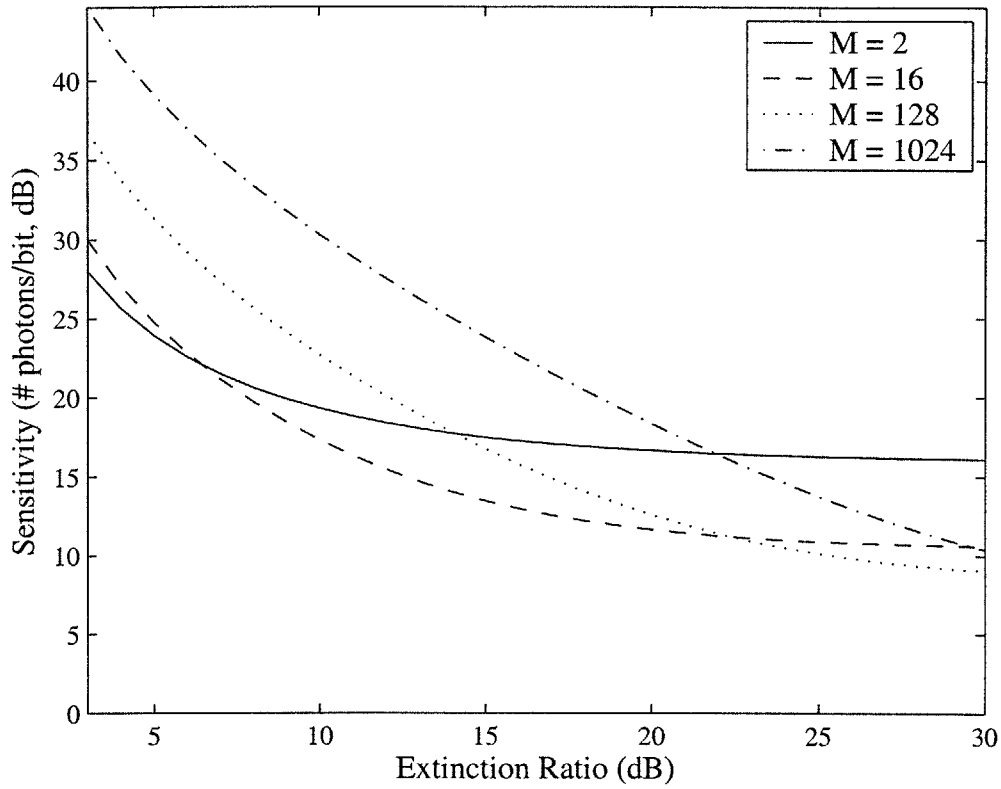


Figure 4-16: Receiver sensitivity as a function of the transmitted pulse extinction ratio.

compared to the ideal receiver sensitivity. As expected, the required receiver power increases as the extinction ratio decreases. The impact of the finite pulse extinction ratio becomes more severe as M is increased. These effects are illustrated in Figure 4-16, where the receiver sensitivity is shown as a function of the transmitter pulse extinction ratio. The impact of a finite extinction ratio is an important consideration in the design of a PPM transmission system. In a practical system with a finite transmitter extinction ratio, increasing the PPM alphabet size does not always lead to an improvement in receiver sensitivity. For instance, if the transmitter pulse extinction ratio is limited to 20 dB ($r = 100$), a binary PPM system will outperform an 1024-ary PPM system in terms of receiver sensitivity, even though the ideal sensitivity of the 1024-ary PPM is ≈ 9 dB better than the binary system.

The optimum receiver design shown in Figure 4-12 is attractive for its relatively

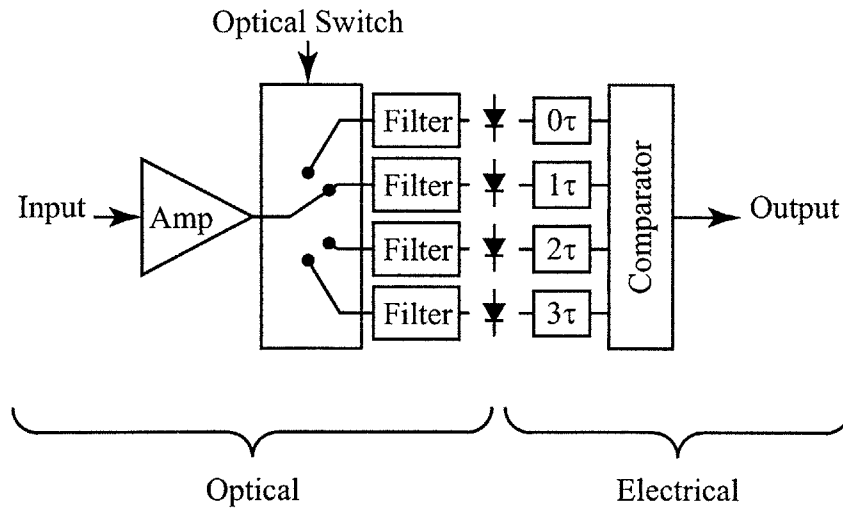


Figure 4-17: A PPM receiver with an optical front-end.

simple implementation. Even the parallel delay-line structure, which can place scalability constraints on the size PPM symbol space, M , can be implemented serially if the comparator can sample at the slot rate. However, the electrical bandwidth requirements of the components in this receiver design place severe limitations on the data rate and PPM alphabet size, M . In particular, in order to ensure orthogonality and prevent intersymbol interference at the receiver, the current sampler at the input to the comparator must have a bandwidth that is significantly larger than the slot rate of the PPM data signal. The slot rate, $1/\tau$, is related to the bit rate, R_B and the symbol rate, R_S by

$$\begin{aligned} \frac{1}{\tau} &= MR_S \\ &= \frac{MR_B}{\log_2 M}. \end{aligned} \tag{4.44}$$

As seen in the discussion of PPM transmitter designs above, even moderate values for M and R_B can lead to impractical electrical bandwidth requirements.

An alternative optical PPM receiver which can potentially be used at much higher data rates is shown in Figure 4-17. In this receiver, the slots are demultiplexed in the optical domain using an optical switch. Optical pulses at the input pass through an

optical preamplifier and are directed to one of M parallel optical receivers using an optical switch. The switch starts in the top position at the beginning of each PPM symbol transmission period. At the end of the each PPM slot, the switch moves to next position, progressing through each of the M positions during the symbol transmission period. At high data rates, this switch is likely to be an all-optical switch or an optical demultiplexer. Each of the parallel receivers at the output of the switch consists of an an optical filter matched to the transmitted pulse, a square-law photodetector, and an integrator which integrates the output of the photodetector over one symbol transmission period. The output voltages from the integrators are sampled during each symbol transmission period by the comparator. The output with the largest voltage is selected as the decoded symbol. The performance analysis of this receiver is similar to the analysis of the ideal PPM receiver outlined above. However, the effects of post-detection filtering due to the reduced electronic bandwidth of the receiver must be included.

Note that the electrical bandwidths required by this receiver are inversely proportional to the symbol transmission period. Thus, for the same data rate, R_B , the required electrical bandwidth is reduced by a factor of M as compared to the first design. The primary drawback in the implementation of this receiver is the complexity of its parallel architecture. However, it is still practical for moderate values of M . In the experiments described below and in Chapter 5, we demonstrate a simplified version of this receiver for binary PPM with symbol rates of 10 GHz and 12.5 GHz using a UNI as the optical switch. Rather than using both outputs of the switch (representing the one-pulse and the zero-pulse), we only detect the output corresponding to the one-pulse. Thus, the receiver performance resembles that of a binary OOK receiver.

4.5.3 Spectral Efficiency

Pulse-position modulation offers the possibility of higher receiver sensitivity and reduced patterning from SOAs. However, one of the potential drawbacks of using pulse-position modulation is the accompanying decrease in spectral efficiency as compared

to other modulation formats. This increase in bandwidth is primarily due to the fact that shorter optical pulses must be used to transmit the data. In binary PPM, for instance, the pulsewidth must be short enough so that the energy is confined to approximately one half of the bit period.

Here, let us consider the spectral efficiency of a PPM transmission system in more detail by calculating the spectrum of a random M -ary PPM signal. We shall proceed by first calculating the autocorrelation function of a random PPM waveform. Using the Wiener-Khinchin theorem, we may then calculate the power spectral density of a random PPM waveform by taking the Fourier transform of the time-average of the autocorrelation function. A sample, $s(t)$, of a random process which produces M -ary PPM waveforms, $S(t)$, may be written as:

$$s(t) = \sum_{m=-\infty}^{\infty} a_p \left(t - mT_S - a_m \frac{T_S}{M} \right) \quad (4.45)$$

where $\{a_m\}$ is a random sequence of M -ary symbols ($a_m \in \{0, 1, \dots, M-1\}$) and $a_p(t)$ is the pulse envelope. Alternatively, this waveform may be expressed using indicator random variables, $I_{(a_m=i)}$, where $I_{(a_m=i)} = 1$ if $a_m = i$, otherwise $I_{(a_m=i)} = 0$:

$$s(t) = \sum_{m=-\infty}^{\infty} \sum_{i=0}^{M-1} a_p \left(t - mT_S - i \frac{T_S}{M} \right) I_{(a_m=i)}. \quad (4.46)$$

The autocorrelation of the random process $S(t)$ is then expressed as

$$\begin{aligned} R_S(t + \tau, t) &= E [S(t + \tau)S(t)] \\ &= E \left[\left\{ \sum_{m=-\infty}^{\infty} \sum_{i=0}^{M-1} a_p \left(t - mT_S - i \frac{T_S}{M} + \tau \right) I_{(a_m=i)} \right\} \right. \\ &\quad \left. \times \left\{ \sum_{n=-\infty}^{\infty} \sum_{j=0}^{M-1} a_p \left(t - nT_S - j \frac{T_S}{M} \right) I_{(a_n=j)} \right\} \right] \\ &= \sum_{m,n=-\infty}^{\infty} \sum_{i,j=0}^{M-1} p \left(t - mT_S - i \frac{T_S}{M} + \tau \right) p \left(t - nT_S - j \frac{T_S}{M} \right) \times \\ &\quad E [I_{(a_m=i)} I_{(a_n=j)}]. \end{aligned} \quad (4.47)$$

We shall assume that the process generating the symbols $\{a_m\}$ has stationary mean and uniform distribution and that a_m and a_n are independent for $m \neq n$. These assumptions have two useful consequences. First, it can be shown that

$$R_S(t + \tau + T_S, t + T_S) = R_S(t + \tau, t). \quad (4.48)$$

Thus, the process $S(t)$ is cyclostationary with period T_S . Moreover, we find that the expectation value in Equation 4.47 is only dependent on the differences $m - n$ and $i - j$:

$$\begin{aligned} E [I_{(a_m=i)} I_{(a_n=j)}] &= \Pr (a_m = i \cap a_n = j) \\ &= \begin{cases} \frac{1}{M} \delta_{ij} & m = n \\ \frac{1}{M^2} & m \neq n \end{cases} \\ &\equiv R_a(m - n, i - j), \end{aligned} \quad (4.49)$$

where δ_{ij} is the discrete Kronecker delta function (i.e., $\delta_{ij} = 1$ if $i = j$, otherwise $\delta_{ij} = 0$). The function R_a is the sequence autocorrelation.

Thus, the time-average of the autocorrelation is given by

$$\begin{aligned} \langle R_S(\tau) \rangle &= \frac{1}{T_S} \int_{-T_S/2}^{T_S/2} R_S(t + \tau, t) dt \\ &= \frac{1}{T_S} \int_{-T_S/2}^{T_S/2} \sum_{m,n=-\infty}^{\infty} \sum_{i,j=0}^{M-1} R_a(m - n, i - j) a_p \left(t - mT_S - i \frac{T_S}{M} + \tau \right) \\ &\quad \times a_p \left(t - nT_S - j \frac{T_S}{M} \right) dt \\ &= \frac{1}{T_S} \sum_{m'=-\infty}^{\infty} \sum_{j=0}^{M-1} \sum_{i'=-j}^{M-1-j} R_a(m', i') R_p \left(\tau - m'T_S - i' \frac{T_S}{M} \right) \end{aligned} \quad (4.50)$$

where $m' = m - n$, $i' = i - j$ and $R_p(\tau)$ is the autocorrelation of the pulse envelope:

$$R_p(\tau) = \int_{-\infty}^{\infty} a_p(t + \tau) a_p(t) dt. \quad (4.51)$$

Further simplification using the definition of the sequence autocorrelation given by

Equation 4.49 and setting $k = Mm' + i'$ yields

$$\begin{aligned} \langle R_S(\tau) \rangle &= \frac{1}{T_S} R_p(\tau) + \frac{1}{T_S M^2} \sum_{k=-M}^M |k| R_p \left(\tau - k \frac{T_S}{M} \right) \\ &+ \frac{1}{T_S M} \sum_{|k| > M} R_p \left(\tau - k \frac{T_S}{M} \right) \end{aligned} \quad (4.52)$$

Using the Weiner-Khinchin theorem, we can now find the power spectral density of the random process S by taking the Fourier transform of Equation 4.52

$$\begin{aligned} S(f) &= \frac{M-1}{T_S M} |A_p(f)|^2 - \frac{2}{T_S M^2} |A_p(f)|^2 \sum_{k=1}^{M-1} (M-k) \cos \left(2\pi k \frac{T_S}{M} f \right) \\ &+ \frac{1}{T_S^2} \sum_{k=-\infty}^{\infty} \left| A_p \left(k \frac{M}{T_S} \right) \right|^2 \delta \left(f - k \frac{M}{T_S} \right), \end{aligned} \quad (4.53)$$

where $A_p(f)$ is the Fourier transform of the pulse, $a_p(t)$. The first two terms in Equation 4.53 represent the continuous portion of the power spectral density. The third term is a comb of discrete delta functions at harmonics of the slot frequency. We shall neglect this discrete comb in the following discussion. In fact, its contribution in the optical domain can be minimized by randomly varying the phase of the optical carrier in each symbol.

Figure 4-18 shows the continuous portion of the spectrum in Equation 4.53 for a random PPM modulation with $M = 2$ and $M = 16$. The pulse shape, $a_p(t)$ for these calculations is a raised cosine with a duration equal to the slot time, T_S/M . The frequency axis in the plot is normalized to the bit rate, $R_B = R_S \log_2 M$. For comparison, the power spectral density for a random OOK signal with the same pulse shape is also shown. As expected, the PPM spectra are wider than the OOK signal due to the shorter pulses which are required. The spectral width of the different modulation formats may be compared using the bandwidth expansion factor, defined as the ratio of the spectral width of the signal under consideration to the spectral width of the OOK signal of the same data rate at some specified power level relative to the peak. At a power level of -30 dB from the peak of the spectra, the $M = 2$

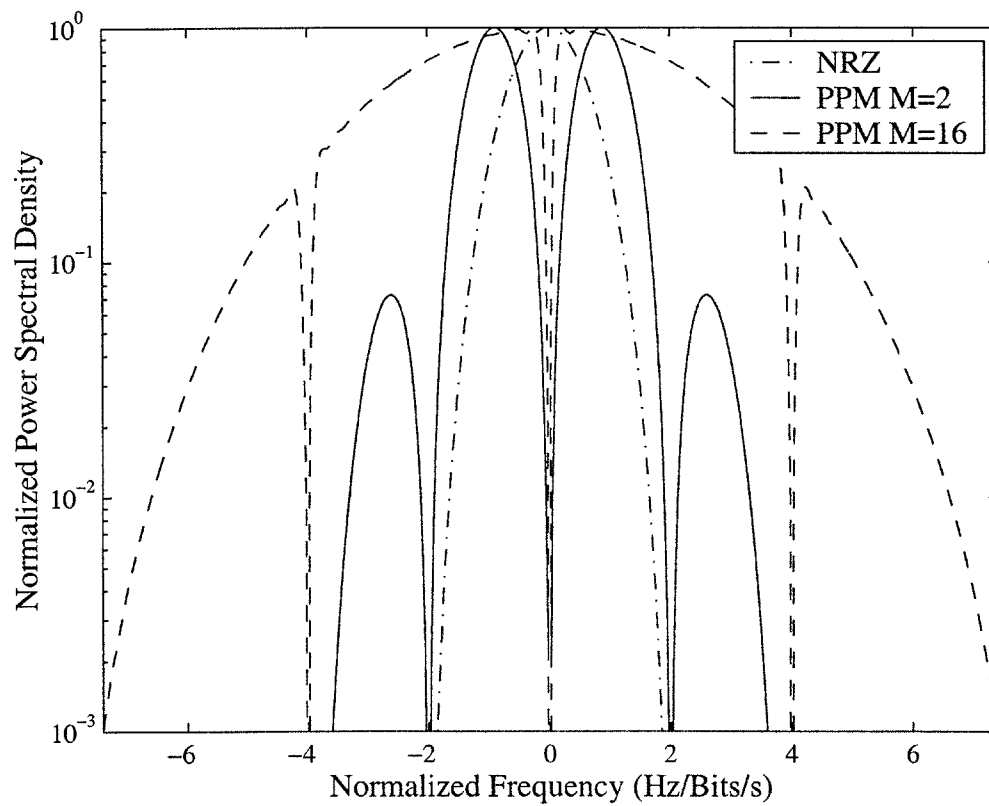


Figure 4-18: Calculated power spectral densities for NRZ and PPM waveforms with a raised cosine pulse shape. The PSD is plotted as a function of the frequency normalized to the data rate.

PPM signal has a bandwidth expansion factor of 1.9. The $M = 16$ signal has a bandwidth expansion factor of 4. The $M = 2$ signal has a slightly smaller bandwidth expansion factor due to the small number of cosine terms subtracted in the second term of Equation 4.53. In the limit of large M , these cosine terms sum to a train of narrow peaks at harmonics of the slot rate with height equal to the power spectral density of the pulse at that harmonic. Thus, for large M , the shape of the power spectral density becomes very close to the power spectral density of the transmitted pulse, with discontinuities at the harmonics of the slot rate. Since the width of this pulse is $\tau = T_S/M = \log_2 M/(R_B M)$, the bandwidth expansion factor for an M -ary PPM signal is very close to $M/\log_2 M$ for large values of M .

4.6 Demultiplexing of PPM Data

The use of the pulse-position modulation format at symbol rates higher than the gain recovery time is expected to reduce the deleterious effects of pattern-dependent gain fluctuations in SOA-based switching systems. To investigate the impact of the use of the PPM data format in an OTDM demultiplexer, we have repeated the demultiplexing experiment described in Section 4.2. The experimental setup for this test is the same as that shown in Figure 4-1, only the OOK modulator has been replaced with the binary PPM modulator shown in Figure 4-9 b). The 10-GHz stream of 2.5-ps pulses at 1550 nm is PPM-modulated with a 10-Gbit/s data pattern of length $2^{31} - 1$. The PPM delay is set to 12.5 ps. Since this delay is much shorter than the carrier lifetime in the SOA, the SOA gain should remain saturated at a fairly constant level. The modulated data stream is then passively multiplexed to produce a 40-Gbit/s binary PPM data stream which is incident at the signal input to the UNI. The control input to the UNI is provided by a second laser producing a 10-GHz stream of 2.5-ps pulses at 1545 nm. As in the previous experiment, the signal and control pulse energies are set to 8.2 fJ and 117 fJ, respectively. Because a pulse is present in every bit period with the binary PPM data format, the average power in the signal stream in this experiment is doubled compared to the OOK experiment.

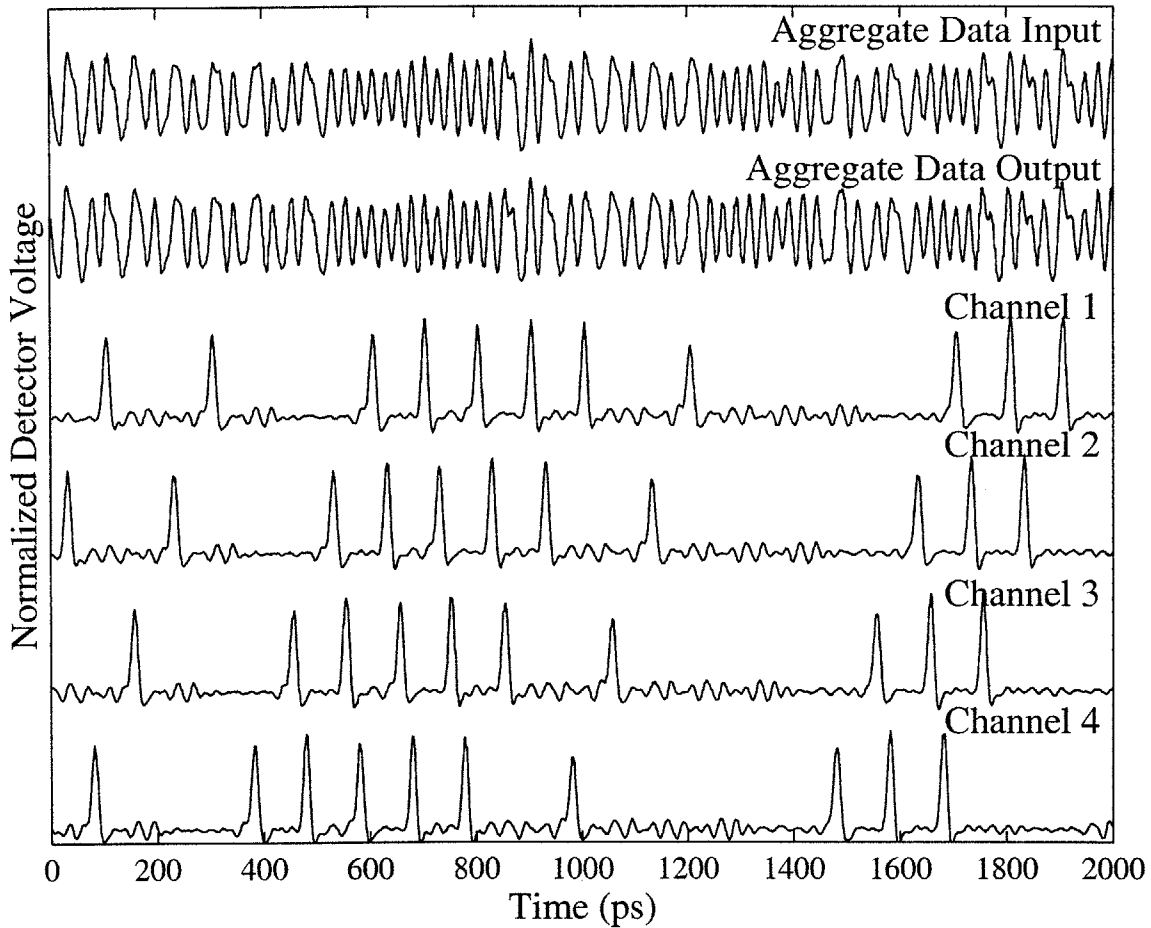


Figure 4-19: Waveforms at input and output of 40-Gbit/s-to-10-Gbit/s PPM UNI demultiplexer measured using a digital sampling oscilloscope. The UNI is used for both demultiplexing and format-conversion from PPM to OOK modulation.

The signal pulse separation in the UNI is set to provide a switching window duration of approximately 5 ps. As in the previous demultiplexing experiment, the 10-GHz control pulse stream demultiplexes a single 10-Gbit/s data sequence from the aggregate 40-Gbit/s data at the signal input to the UNI. Because the switching window duration is shorter than the PPM delay in the modulated data, either the pulses representing the one-bits or the pulses representing the zero-bits may be selected in the demultiplexed stream. In this manner, the data format of the demultiplexed stream is converted from PPM to OOK.

Figure 4-19 shows the waveforms at the input and output of the UNI demulti-

plexer as measured with a 50-GHz photodiode. The first trace shows the aggregate 40-Gbit/s PPM data stream. Due to the limited bandwidth of the photodiode, not all of the pulses are resolved. The second trace shows the output of the demultiplexer in the absence of control pulses when the UNI is biased so that the entire aggregate signal stream passes to the output of the switch. The pattern-dependent gain-compression effects observed in the previous experiment are greatly reduced. The remaining four traces show the four demultiplexed 10-Gbit/s data channels at the switch output. Note that the PPM data format has been converted to OOK format by the demultiplexer. Additionally, the amplitude patterning that was observed in the OOK demultiplexer demonstration is negligible in this case. Thus, the use of the PPM data format has effectively mitigated the effects of gain saturation in an OTDM demultiplexer. The results of bit-error rate testing of the demultiplexer output for aggregate PPM data rates up to 80 Gbit/s are reported in Chapter 5.

4.7 All-Optical Wavelength Conversion of OOK and PPM Data Formats

All-optical wavelength conversion is usually performed using a high-power intensity-modulated pump signal to modulate a lower-power probe signal via a nonlinear optical interaction between the two signals. When an SOA is used for the nonlinear medium, the effects of gain saturation can be especially deleterious due to the high power of the modulated pump. In experimental wavelength conversion demonstrations, these pattern-dependent effects have been observed as a degradation of the bit-error rate performance at the output of the wavelength converter for long test pattern lengths [4.59]. These experiments demonstrate the importance of using long data patterns to test the low-frequency characteristics of semiconductor-based all-optical gates.

We have experimentally verified the utility of the PPM data format for reducing the pattern-dependent operation of an interferometric SOA-based wavelength

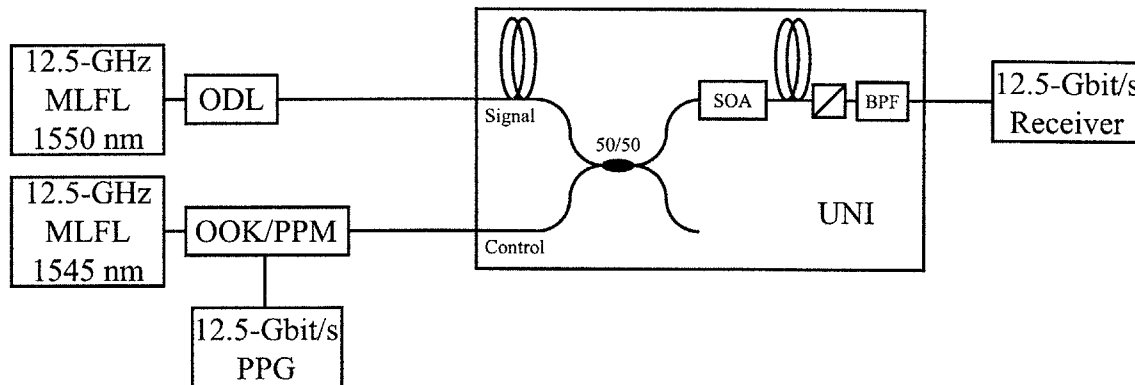


Figure 4-20: Experimental setup for OOK/PPM wavelength conversion.

converter operating at 12.5 Gbit/s [4.41]. The experimental setup for wavelength conversion using the UNI is shown in Figure 4-20. A 12.5-GHz stream of 2.5-ps pulses from a modelocked-fiber laser operating at 1545 nm is intensity modulated with a 12.5-Gbit/s data pattern. The modulation format can be either OOK or binary PPM with a PPM delay of 15 ps. The pattern length from the pulse pattern generator can be varied in order to characterize the pattern-dependent operation of the switch. The signal input to the UNI consists of a 12.5-GHz stream of 2.5-ps pulses at 1550 nm. The signal and control pulse energies at the input to the UNI are 35 fJ and 70 fJ, respectively. The UNI is biased so that a signal pulse propagates to the output port only when a control pulse is present. Thus, the control data pattern is modulated onto the output signal pulses. The UNI switching window duration is set to 5 ps. Since this response is shorter than the PPM delay, only the one-bits in the PPM-formatted control stream are modulated onto the signal pulses. Thus, the format of the PPM stream is converted to OOK at the output of the switch, allowing for bit-error rate characterization of the switch operation using a 12.5-Gbit/s optically preamplified direct-detection receiver.

Figure 4-21 shows the bit-error rate performance measured as a function of input power to the receiver at the output of the wavelength converter. The baseline performance is measured by injecting the OOK-modulated control stream directly into the receiver. After the wavelength converter, a power penalty of 4.5 dB at an error rate

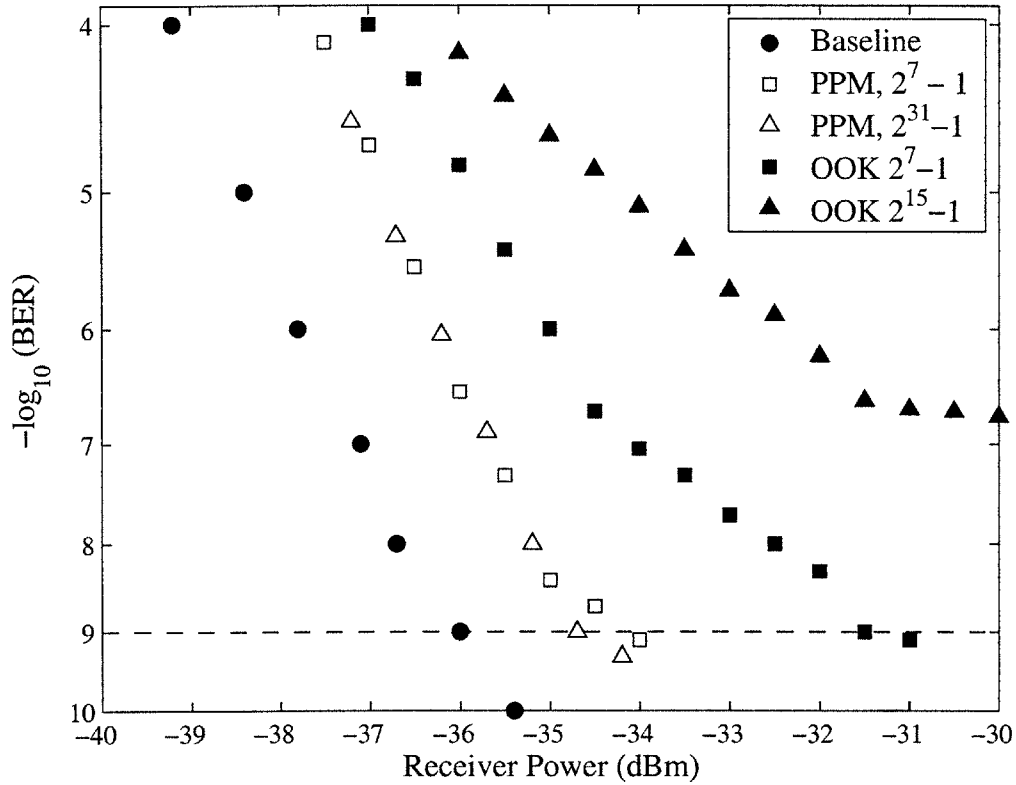


Figure 4-21: Bit-error rate performance of wavelength conversion of OOK and PPM waveforms of various pattern lengths.

of 10^{-9} is measured for the OOK data pattern with $2^7 - 1$ bits. When the pattern length is increased to $2^{15} - 1$ bits, the error performance degrades and the receiver performance is limited to a bit-error rate of $\sim 10^{-7}$. The reason for this degradation is that the longer data pattern contains longer sequences of consecutive one-bits and zero-bits. Thus, the variance of the SOA gain in the wavelength converter is larger due to increased recovery and saturation in response to these sequences. The wavelength converter performance is improved when the PPM data format is used for the control input. In this case, the power penalty from the baseline performance is only 1.3 dB at an error rate of 10^{-9} . The error rate performance was almost identical for input pattern lengths of $2^7 - 1$ bits and $2^{31} - 1$ bits, verifying the pattern-independent operation of the switch for the PPM data format.

4.8 Conclusions

As we have shown above, gain saturation in semiconductor optical amplifiers can lead to significant performance degradation in optical communications systems. These problems arise because the carrier lifetime in an SOA is comparable to the bit period for moderate transmission rates (~ 10 Gbit/s). This makes SOAs impractical for use as in-line amplifiers for optical transmission systems, since the free carrier populations fluctuate in response to the data pattern producing pattern-dependent gain and intersymbol interference for intensity-modulated signals. For these applications, the EDFA is much more useful due to its long carrier lifetime of several milliseconds. However, the shorter carrier lifetime of the SOA makes it more attractive for optical switching applications in future all-optical networks. In this chapter, we have considered the impact of SOA gain saturation on these applications.

We have developed a statistical model of the gain saturation process which can be used to study its impact on system performance in OOK transmission links. We model the stochastic gain process as a discrete-time Markov process. This allows the steady-state probability density function for the gain to be calculated. This probability density function can then be used to calculate bit-error rates at a receiver. In contrast to previous models that have been developed, this model can be used to calculate system performance for a wide range of data rates. We have applied the model to study the impact of SOA gain saturation on the in-line amplification of single-channel optical transmission systems at 10-Gbit/s and 100-Gbit/s.

We propose the use of pulse-position modulation as a practical means for mitigation of gain saturation effects in OTDM networks. Optical PPM was first developed as an energy-efficient modulation format which is useful in communications systems where mid-span amplification or regeneration are not possible. The PPM data format is also useful in reducing gain saturation effects since a pulse is present in every symbol period. When the symbol period is less than the gain recovery time, pattern-dependent gain in the SOA is greatly reduced. One of the drawbacks to using PPM is the large transmitter and receiver bandwidths required for high data rate operation

with moderate alphabet sizes. To address these problems, we have presented several optical techniques which can be used to transmit and receive binary PPM signals at aggregate data rates up to 80 Gbit/s. We have also analyzed the performance of optically preamplified PPM receivers in detail and considered the system impact of imperfect extinction in the transmitted signal.

Lastly, we have presented experimental evidence of the utility of the PPM data format in various optical switching applications using SOAs. We have compared the performance of a 40-Gbit/s OTDM demultiplexer with OOK and PPM data formats. We have also experimentally studied all-optical wavelength conversion of 12.5-Gbit/s OOK- and PPM-formatted data streams in a semiconductor-based interferometer. In both of these experiments, the pattern-dependent performance of the switch associated with the OOK-formatted data was greatly reduced by the use of the PPM data format. Further examples of the use of the PPM data format are explored in Chapter 5, where we discuss an all-optical transmitter and receiver for a slotted OTDM network utilizing binary PPM data format.

References

- [4.1] N. S. Patel, K. A. Rauschenbach, and K. L. Hall, "40 Gbit/s demultiplexing using an ultrafast nonlinear interferometer (UNI)," *IEEE Photon. Technol. Lett.*, vol. 8, pp. 1695–7, December 1996.
- [4.2] J. P. Sokoloff, P. R. Prucnal, I. Glesk, and M. Kane, "A terahertz optical asymmetric demultiplexer (TOAD)," *IEEE Photon. Technol. Lett.*, vol. 5, pp. 787–90, July 1993.
- [4.3] A. A. M. Saleh, R. M. Jopson, and T. E. Darcie, "Compensation of nonlinearity in semiconductor optical amplifiers," *Electron. Lett.*, vol. 24, pp. 950–2, July 1988.
- [4.4] T. E. Darcie, R. M. Jopson, and A. A. M. Saleh, "Electronic compensation of saturation-induced crosstalk in optical amplifiers," *Electron. Lett.*, vol. 24, pp. 1154–6, September 1988.
- [4.5] M. Shtaif and G. Eisenstein, "Analysis of bit error rate performance signal processing schemes exploiting semiconductor optical amplifiers," in *15th IEEE International Semiconductor Laser Conference*, pp. 117–8, 1996.

- [4.6] K. Inoue, "Crosstalk and its power penalty in multichannel transmission due to gain saturation in a semiconductor laser amplifier," *J. Lightwave Technol.*, vol. 7, pp. 1118–24, July 1989.
- [4.7] Q. Xu, M. Yao, M. Chen, and Y. Gao, "Statistical analysis on the reduction of pattern effect in semiconductor in-line amplifier for multi-channel systems," in *Optical Amplifiers and Their Applications*, pp. 88–90, 2000.
- [4.8] Q. Xu, M. Yao, M. Chen, and J. Zhang, "Analytical calculation based on probability model for the pattern effect of SOA as in-line amplifier for WDM system," *Opt. Comm.*, vol. 195, pp. 159–66, August 2001.
- [4.9] S. Bischoff, B. Lading, and J. Mork, "BER estimation for all-optical regenerators influenced by pattern effects," *IEEE Photon. Technol. Lett.*, vol. 14, pp. 33–5, January 2002.
- [4.10] M. Shtaif and G. Eisenstein, "Improved bit-error-rate performance in frequency conversion of high-bit-rate data based on cross gain compression in semiconductor optical amplifiers," *IEEE Photon. Technol. Lett.*, vol. 8, pp. 1474–6, November 1996.
- [4.11] G. P. Agrawal and N. A. Olsson, "Self-phase modulation and spectral broadening of optical pulses in semiconductor laser amplifiers," *IEEE J. Quantum Electron.*, vol. 25, pp. 2297–306, November 1989.
- [4.12] Y. Lai, K. L. Hall, E. P. Ippen, and G. Eisenstein, "Short pulse gain saturation in InGaAsP diode laser amplifiers," *IEEE Photon. Technol. Lett.*, vol. 2, pp. 711–3, October 1990.
- [4.13] A. Uskov, J. Mork, and J. Mark, "Theory of short-pulse gain saturation in semiconductor laser amplifiers," *IEEE Photon. Technol. Lett.*, vol. 4, pp. 443–6, May 1992.
- [4.14] P. A. Humblet and M. Azizoglu, "On the bit error rate of lightwave systems with optical amplifiers," *J. Lightwave Technol.*, vol. 9, pp. 1576–82, November 1991.
- [4.15] G. Eisenstein, R. S. Tucker, J. M. Wiesenfeld, P. B. Hansen, G. Raybon, B. C. Johnson, T. J. Bridges, F. G. Storz, and C. A. Burrus, "Gain recovery time of traveling-wave semiconductor optical amplifiers," *Appl. Phys. Lett.*, vol. 54, pp. 454–6, January 1989.
- [4.16] D. M. Patrick and R. J. Manning, "20 Gbit/s wavelength conversion using semiconductor nonlinearity," *Electron. Lett.*, vol. 30, pp. 252–3, February 1994.
- [4.17] R. J. Manning, D. A. O. Davies, and J. K. Lucek, "Recovery rates in semiconductor laser amplifiers: Optical and electrical bias dependencies," *Electron. Lett.*, vol. 30, pp. 1233–5, July 1994.

- [4.18] R. J. Manning and G. Sherlock, "Recovery of a π phase shift in ~ 12.5 ps in a semiconductor laser amplifier," *Electron. Lett.*, vol. 31, pp. 307–8, February 1995.
- [4.19] H. Q. Le and S. DiCecca, "Ultrafast, room-temperature, resonance-enhanced third-order optical susceptibility tensor of an AlGaAs/GaAs quantum well," *Opt. Lett.*, vol. 4, pp. 901–3, 1991.
- [4.20] J. P. Donnelly, H. Q. Le, E. A. Swanson, S. H. Groves, A. Darwish, and E. P. Ippen, "Nondegenerate four-wave mixing wavelength conversion in low-loss passive InGaAsP-InP quantum-well waveguides," *IEEE Photon. Technol. Lett.*, vol. 8, pp. 623–5, May 1996.
- [4.21] V. Misrahi, K. W. DeLong, G. I. Stegeman, M. A. Saifi, and M. J. Andrejco, "Two-photon absorption as a limitation to all-optical switching," *Opt. Lett.*, vol. 14, pp. 1140–2, October 1989.
- [4.22] K. W. DeLong and G. I. Stegeman, "Two-photon absorption as a limitation to all-optical waveguide switching in semiconductors," *Appl. Phys. Lett.*, vol. 57, pp. 2063–4, November 1990.
- [4.23] S. Diez, R. Ludwig, and H. G. Weber, "All-optical switch for TDM and WDM/TDM systems demonstrated in a 640 Gbit/s demultiplexing experiment," *Electron. Lett.*, vol. 34, pp. 803–4, April 1998.
- [4.24] S. Diez, R. Ludwig, and H. G. Weber, "Gain-transparent SOA-switch for high-bitrate OTDM add/drop multiplexing," *IEEE Photon. Technol. Lett.*, vol. 11, pp. 60–2, January 1999.
- [4.25] C. Schubert, S. Diez, J. Berger, R. Ludwig, U. Feiste, , G. Toptchiyski, H. G. Weber, K. Petermann, and V. Krajinovic, "160-Gb/s all-optical demultiplexing using a gain-transparent ultrafast nonlinear interferometer (GT-UNI)," *IEEE Photon. Technol. Lett.*, vol. 13, pp. 475–7, May 2001.
- [4.26] G. Toptchiyski, S. Randel, K. Petermann, S. Diez, E. Hilliger, C. Schmidt, C. Schubert, R. Ludwig, and H. G. Weber, "Analysis of switching windows in a gain-transparent-SLALOM configuration," *IEEE J. Lightwave Technol.*, vol. 18, pp. 2188–95, December 2000.
- [4.27] S. Diez, C. Schubert, R. Ludwig, H. J. Ehrke, U. Feiste, C. Schmidt, and H. G. Weber, "160 Gbit/s all-optical demultiplexer using hybrid gain-transparent SOA Mach-Zehnder interferometer," *Electron. Lett.*, vol. 36, pp. 1484–6, August 2000.
- [4.28] S. Diez, R. Ludwig, C. Schmidt, U. Feiste, and H. G. Weber, "160-Gb/s optical sampling by gain-transparent four-wave mixing in a semiconductor optical amplifier," *IEEE Photon. Technol. Lett.*, vol. 11, pp. 1402–4, November 1999.

- [4.29] S. Diez, C. Schubert, R. Ludwig, H. J. Ehrke, U. Feiste, C. Schmidt, and H. G. Weber, "160 Gb/s all-optical demultiplexer using a hybrid gain-transparent SOA Mach-Zehnder-interferometer," in *Optical Amplifiers and Their Applications*, pp. 195–7, 2000.
- [4.30] K. L. Hall, G. Lenz, A. M. Darwish, and E. P. Ippen, "Subpicosecond gain and index nonlinearities in InGaAsP diode lasers," *Opt. Comm.*, vol. 111, pp. 589–612, October 1994.
- [4.31] Y. H. Kao, I. V. Goltser, M. N. Islam, and G. Raybon, "Ultrafast optical logic gate using a semiconductor laser amplifier operating at transparency in a loop mirror," in *Conference on Lasers and Electro-Optics*, pp. 94–5, 1997.
- [4.32] B. S. Robinson and K. L. Hall, "Interferometric all-optical switching using nonlinearities in semiconductor optical amplifiers biased at transparency," in *Conference on Lasers and Electro-Optics*, p. 2, 1998.
- [4.33] B. S. Robinson, "All-optical switching using semiconductor amplifiers biased at transparency," Master's thesis, Massachusetts Institute of Technology, June 1998.
- [4.34] K. L. Hall, E. P. Ippen, and G. Eisenstien, "Bias-lead monitoring of ultrafast nonlinearities in InGaAsP diode laser amplifiers," *Appl. Phys. Lett.*, vol. 57, pp. 129–31, July 1990.
- [4.35] Y. H. Kao, T. J. Xia, M. N. Islam, and G. Raybon, "Limitations on ultrafast optical switching in a semiconductor laser amplifier operating at transparency current," *J. Appl. Phys.*, vol. 86, pp. 4740–7, November 1999.
- [4.36] H. K. Kim and S. Chandrasekhar, "Reduction of cross-gain modulation in the semiconductor optical amplifier by using wavelength modulated signal," *IEEE Photon. Technol. Lett.*, vol. 12, pp. 1412–4, October 2000.
- [4.37] A. K. Srivastava, S. Banerjee, B. R. Eichenbaum, C. Wolf, Y. Sun, J. W. Sulhoff, and A. R. Chraplyvy, "A polarization multiplexing technique to mitigate WDM crosstalk in SOAs," *IEEE Photon. Technol. Lett.*, vol. 12, pp. 1415–6, October 2000.
- [4.38] R. M. Gagliardi and S. Karp, "*M*-ary Poisson detection and optical communications," *IEEE Trans. Communication Technology*, vol. COM-17, pp. 208–16, April 1969.
- [4.39] S. Karp and R. M. Gagliardi, "The design of a pulse-position modulated optical communication system," *IEEE Trans. Communication Technology*, vol. COM-17, pp. 670–6, December 1969.
- [4.40] M. L. Stevens, D. M. Boroson, and D. O. Caplan, "A novel variable-rate pulse-position modulation system with near quantum limited performancs," in *IEEE Lasers and Electro-Optics Society 12th Annual Meeting*, vol. 1, pp. 301–2, 1999.

- [4.41] B. S. Robinson, J. D. Moores, and D. T. Moriarty, "Pattern independent semiconductor-based interferometric all-optical switching using pulse-position modulation," in *Conference on Lasers and Electro-Optics*, pp. 690–1, 2000.
- [4.42] B. S. Robinson, S. A. Hamilton, and E. P. Ippen, "Demultiplexing of 80-Gbit/s pulse-position modulated data with an ultrafast nonlinear interferometer," *IEEE Photon. Technol. Lett.*, vol. 14, pp. 206–8, February 2002.
- [4.43] I. Garrett, "Pulse-position modulation for transmission over optical fibers with direct or heterodyne detection," *IEEE Trans. Commun.*, vol. COM-31, pp. 518–27, April 1983.
- [4.44] A. J. Phillips, R. A. Cryan, and J. M. Senior, "Performance evaluation of optically pre-amplified PPM systems," *IEEE Photon. Technol. Lett.*, vol. 6, pp. 651–3, May 1994.
- [4.45] P. S. Henry, "Error-rate performances of optical amplifiers," in *Conference on Optical Fiber Communication*, p. THK3, 1989.
- [4.46] S. O. Rice, "Mathematical analysis of random noise," *Bell Sys. Tech. J.*, vol. 24, pp. 46–156, January 1945.
- [4.47] L. W. Hughes, "A simple upper bound on the error probability for orthogonal signals in white noise," *IEEE Transactions on Communications*, vol. 40, p. 670, April 1992.
- [4.48] R. M. Gagliardi and S. Karp, *Optical Communications*. Series in Telecommunications and Signal Processing, New York: Wiley, 2nd ed., 1995.
- [4.49] J. Wozencraft and I. Jacobs, *Principles of Communication Engineering*. New York: Wiley, 1965.
- [4.50] J. L. W. V. Jensen, "Sur les fonctions convexes et les inégalités entre les valeurs moyennes," *Acta Math.*, vol. 30, pp. 175–93, 1906.
- [4.51] C. W. Helstrom, *Statistical Theory of Signal Detection*. New York: Oxford, 2nd ed., 1968. Appendix F, The Q -Function.
- [4.52] L. C. Maximon, "On the representation of indefinite integrals containing Bessel functions by simple Neumann series," *Proc. Amer. Math. Soc.*, vol. 7, pp. 1054–62, 1956.
- [4.53] J. I. Marcum, "Table of Q -functions," Tech. Rep. RM-339, RAND Corp., Santa Monica, CA, January 1950.
- [4.54] D. A. Shnidman, "The calculation of the probability of detection and the generalized marcum Q -function," *IEEE Trans. Inform. Theory*, vol. 35, pp. 389–400, March 1989.

- [4.55] L. F. Fehlner, "Marcum's and Swerling's data on target detection by pulsed radar," Tech. Rep. TG-451, Applied Physics Laboratory, Johns Hopkins University, Silver Spring, MD, July 1962.
- [4.56] G. M. Dillard, "Recursive computation of the generalized Q -function," *IEEE Trans. Aerosp. Electron. Syst.*, vol. AES-9, pp. 614-5, July 1973.
- [4.57] G. L. Turin, "The asymptotic behavior of ideal M -ary systems," *Proc. IRE (Correspondence)*, vol. 47, pp. 93-4, January 1962.
- [4.58] F. G. Splitt, "A limit for the probability of error for largest-of-selection," *IEEE Trans. on Communication Systems (Correspondence)*, vol. CS-11, pp. 494-6, December 1963.
- [4.59] J. M. Wiesenfeld, J. S. Perino, A. H. Gnauck, and B. Glance, "Bit error rate performance for wavelength conversion at 20 Gbit/s," *Electron. Lett.*, vol. 30, pp. 720-1, April 1994.

Chapter 5

Slotted OTDM Networking Demonstrations

5.1 Introduction

In recent years, increases in single-fiber point-to-point optical transmission capacities have outpaced electronic processing capabilities. Wavelength-division multiplexed (WDM) transmission links have been demonstrated with aggregate capacities in excess of 10 Tbit/s [5.1, 5.2]. Bit-interleaved optical time-division multiplexed (OTDM) links utilizing a single wavelength for transmission have been demonstrated at rates as high as 1.28 Tbit/s [5.3]. These capacities far exceed current electronic capabilities for processing and routing. This has prompted a transition from first-generation, point-to-point, optical networks to second-generation optical networks where limited network functionality such as multiplexing and routing is provided at the optical layer. Two approaches to optical multiplexing have been studied extensively: WDM and OTDM. In a WDM network, multiplexing is accomplished by combining many low data rate channels modulated onto distinct wavelengths in a single fiber. In OTDM networks, low data rate channels are modulated on streams of short optical pulses which are then temporally interleaved in a single fiber. Routing in second-generation optical networks is limited to circuit-switching of individual low data rate channels. In these networks, end-to-end bandwidth provisioning is accomplished on time-scales

ranging from minutes to milliseconds, depending on the network design.

As a consequence of the enormous growth of the internet, global telecommunications traffic will soon be predominantly electronic data, rather than voice traffic. Packet-oriented data traffic tends to have very bursty bandwidth requirements, especially at the low levels of user aggregation that are typical in local- or metro-area networks. Present-day technologies for allocating bandwidth in optical networks are not fast enough to satisfy these bursty demands. For example, a 1500-byte Ethernet packet transmitted on a 10-Gbit/s fiber channel has a duration of only 1.2 microseconds. Since this is much shorter than the time required for bandwidth provisioning in present optical networks, network designers must provide links with much more bandwidth than is actually needed on average in order to satisfy peak capacity demands and quality-of-service agreements. Recent studies suggest that allocated bandwidths in today's private-line data networks are 15 to 30 times greater than average network demands [5.4].

Slotted OTDM networks can potentially utilize network bandwidth resources much more efficiently than WDM or bit-interleaved OTDM multiplexing schemes by utilizing packet-based statistical multiplexing techniques [5.5, 5.6]. In a slotted OTDM network, many transceivers share a single wavelength channel operating at aggregate media rates which are much higher than single-channel electronic processing rates and the average traffic rates of the nodes (e.g., > 100 Gbit/s). Time on the network is divided into slots during which a particular transmitter may burst packets of data onto the network at the aggregate media rate. Slotted OTDM networks potentially provide maximally efficient use of network bandwidth since transmitters only use slots when they have data to send, leaving unused slots available for use by other network nodes. Moreover, slotted OTDM networks have many potential benefits when serving diverse user populations since they can provide variable quality-of-service and they offer flexible bandwidth provisioning at a much finer granularity than other multiplexing techniques.

Slotted OTDM networks are challenging to implement because the physical layer optical interface requires certain processing capabilities at the aggregate media rate.

In this chapter, we will describe efforts to utilize the ultrafast optical logic functionality provided by semiconductor-based switches, such as the UNI, to provide basic physical layer functionality in a slotted OTDM network. We begin with a general discussion of network architecture for ultrahigh-speed multiaccess networks where high latency necessitates the design of novel media access control protocols in order to ensure efficient and fair access to the network medium by all network nodes. The helical local area network (HLAN) is presented as a candidate architecture for such networks. Next, we discuss the design and experimental verification of the optical interface for various functional nodes in an HLAN network. We present designs of simplified head-end and transmitter nodes. These nodes simulate the transmission of fully-loaded network slots and test the operation of the receiver node. Finally, we describe the implementation of a fully-functional optical interface for a receiver node. This node utilized optical logic gates for the three primary tasks required for physical layer access in an ultrahigh speed multiaccess network: synchronization, header processing, and data rate conversion.

5.2 HLAN Architecture

The design of a multi-access slotted OTDM network operating at aggregate single-stream data rates in excess of 100 Gbit/s must address two important issues. First, because of the high data rate, the network must be designed to operate fairly and efficiently when many packets are in flight simultaneously on the network bus. At lower data rates, contention-based media access control (MAC), such as the Carrier Sense Multiple Access with Collision Detection (CSMA/CD) used in Ethernet networks, work well since the network is engineered so that the average packet duration is much longer than the maximum transmission time between distant transceivers on the network. This allows collisions, which occur when two transmitters attempt to transmit data on the network bus simultaneously, to be detected and dealt with in an efficient manner. The performance of the CSMA/CD MAC protocol (in terms of system utilization as a function of the offered load from the transmitters) degrades

significantly when the transmission latency becomes comparable to or longer than the packet duration (see, for example, [5.7, 5.8]). This limits 100-Mbit/s Ethernet to shared-bus lengths of less than 100 m, for example. At 100 Gbit/s, an Ethernet packet with the maximum size of 1500 bytes, would have a duration of only 120 ns. The requirement that the maximum bus transmission time be much less than the average packet duration would limit the shared-bus length to a few meters, at best, using CSMA/CD. This constraint is unacceptable, even for local-area networks. Thus, the MAC protocol for a multi-access slotted OTDM network must operate well in a high-latency environment where many (> 1000) packets may be in flight simultaneously.

A second constraint that must be considered in the design of multi-access slotted OTDM networks operating at 100-Gbit/s data rates is the limited availability of complex logical processing at those data rates. Ultrafast all-optical switches, such as the UNI, can be used to provide simple logical functionality (e.g., AND or XOR) at data rates in excess of 100 Gbit/s. However, these fiber-based interferometers are presently quite large, making integration of many gates difficult. Semiconductor interferometers have been monolithically integrated on a single chip. However, complex processing capabilities at such high data rates are presently unavailable since the necessary integration of multi-gate logic on a single chip has not been demonstrated. Thus, network protocols that require only simple processing at the data rate must be developed.

The Helical Local-Area Network (HLAN) architecture [5.5, 5.9], shown in Figure 5-1, was developed with these constraints in mind in order to provide fair, efficient use of network resources in a multi-access slotted OTDM local-area network operating at data rates in excess of 100 Gbit/s. HLAN provides both guaranteed bandwidth (GBW) and contention-free bandwidth-on-demand (BOD) services to a heterogeneous population of users. The network topology consists of transmitters and receivers which are connected via a unidirectional “helical” bus. Time on the network is divided into fixed-length slots. A head-end node at the beginning of the bus demarcates the slot boundaries and controls access to the network bus. The network transmitters

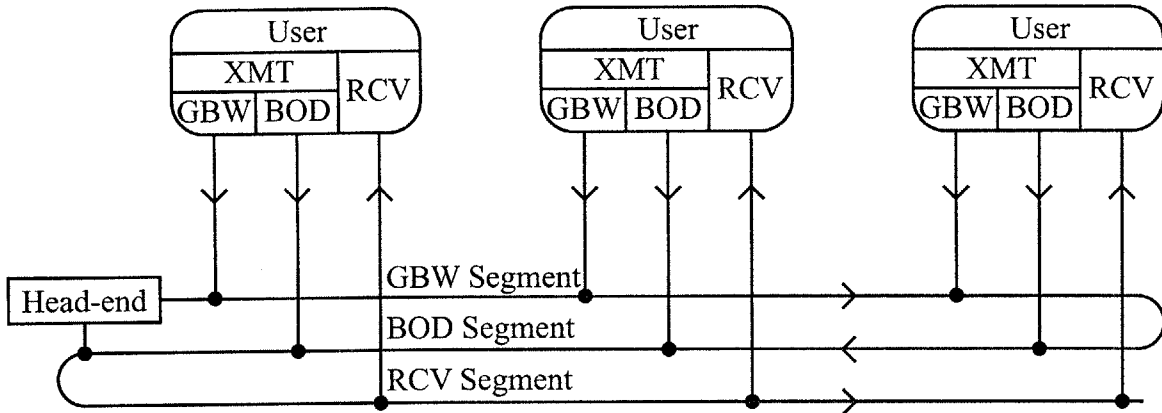


Figure 5-1: Helical local area network consisting of a head-end and three users connected via a unidirectional folded bus. Here, a folded linear bus is shown. A helical-shaped bus is also possible, but it may be less practical to implement. XMT: Transmitter, RCV: Receiver, GBW: Guaranteed Bandwidth, BOD: Bandwidth-on-Demand.

then synchronize to the slot timing and transmit data in empty slots.

The network transceivers are each connected to the helical bus at three points. The first segment provides GBW services. On this segment, media access is controlled by the head-end which allocates slots for use by specific transmitters which require GBW. This allocation information is encoded in an optical header which is processed by the transmitters to determine whether transmission of data is allowed in a particular slot.

The second network segment provides BOD services. On this segment, transmitters may transmit data in any empty slot, including unused slots which were designated for GBW services. Due to the high-latency nature of HLAN, fairness on the BOD segment can be an issue as the first node on the segment can potentially fill all of the available slots. This behaviour is prevented by using credits to regulate access to the BOD segment. The head-end distributes credits to all users on the network at an equal rate via the optical slot headers or some other communications channel. Nodes with data available for transmission accumulate credits and use a credit for each slot of transmitted data. The head-end monitors the number of empty slots at the end of the BOD segment. If no empty slots are available, the rate of credit distribution is reduced. Under light loads, the network access resembles the greedy

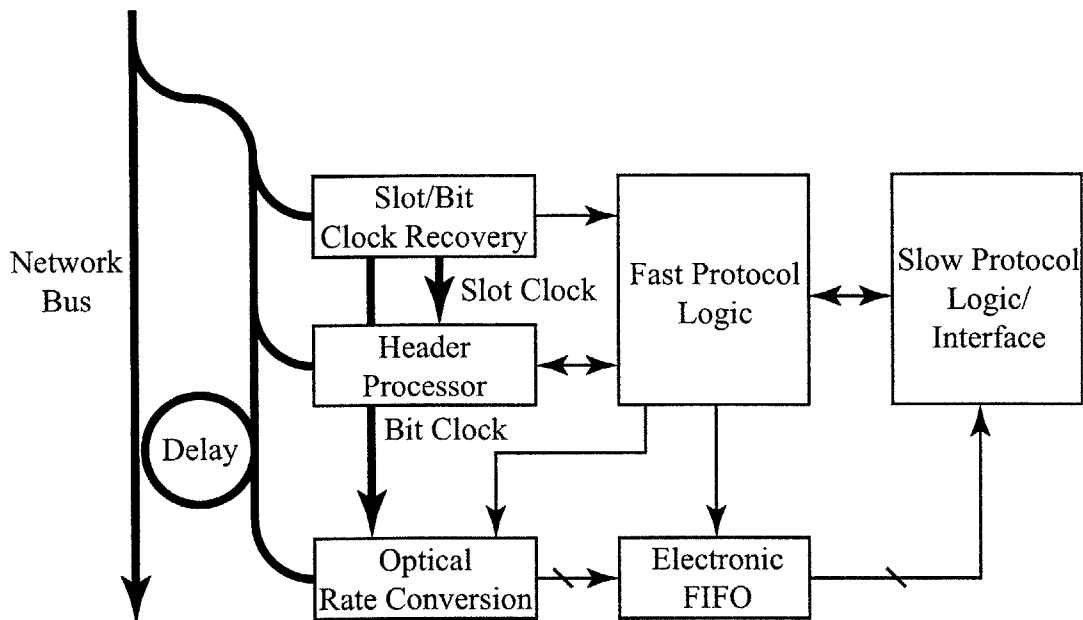


Figure 5-2: HLAN receiver block diagram. The heavy lines represent optical connections, while the light lines represent electrical connections.

algorithm, where each node transmits its data as soon as it is available. Under heavy loads, the credit distribution rate is reduced until the network access resembles a fair TDM algorithm, with the slots evenly divided between the different transmitters. In this manner, the network capacity is efficiently utilized while providing fair BOD services.

The final network segment is the receive (RCV) segment. On this segment, the receivers process address information encoded in the optical header of full slots to determine their destination. Note that because of the three-pass unidirectional nature of the HLAN, all of the receivers are downstream from all of the transmitters.

Figure 5-2 shows a block diagram of an HLAN receiver node. The heavy lines represent optical transmission paths, while the light lines represent baseband electrical transmission paths. A fraction of the optical signal on the network bus is routed into the optical receiver using a passive tap coupler. This signal is then routed into three optical processors within the receiver. The first processor recovers the slot- and bit-clocks from the network signal and synchronizes the receiver to these clocks.

The slot-clock is sent to the optical header processor unit which performs address recognition and empty/full slot detection. The bit-clock is used by the optical rate-conversion unit to convert the incoming slot data from the media data rate down to electronic processing rates. The optical rate-conversion unit may include optical buffers to store slot data during the time required for rate conversion. The rate-converted optical data is then detected and the resulting electronic data is buffered in an electronic first-in-first-out (FIFO) buffer for use by higher network layers. The functions of these three optical processors are coordinated by a fast protocol logic unit operating at the slot rate which implements the MAC protocol. This unit also interfaces with slower protocol logic in higher network layers. The HLAN transmitter schematic is very similar to the receiver design shown here.

The folded-bus architecture of HLAN is best-suited for local- and metropolitan-area networks where the maximum separation between network nodes is typically less than 100 km. While the HLAN MAC protocol can scale to longer transmission distances, the longer feedback delay between the transmitters and the head-end would slow the responsiveness of the network to bursty traffic demands. Additionally, transmission impairments such as chromatic dispersion and polarization-mode dispersion make long distance propagation of high-bandwidth OTDM signals difficult. Despite these challenges, several methods have been proposed for extending the HLAN to wide-area network operation [5.10].

5.3 Slotted OTDM System Implementation

Here, we describe the experimental implementation of a slotted OTDM network testbed based on the HLAN architecture consisting of a head-end, a single transmitter, and a single receiver. Since the focus of this work is on the use of semiconductor-based optical switches to provide essential physical layer functionality in HLAN, the full HLAN MAC protocol is not presently implemented. In particular, implementation of the credit distribution scheme for BOD has not been demonstrated. Additionally, assignment of GBW slots by the head-end and header processing by the transmitter

is not demonstrated. However, the essential optical technology required to provide these functionalities is demonstrated, reducing the full implementation of the HLAN MAC protocol to an electronic hardware and/or software problem that can be readily solved using presently available electronics technology.

In the following sections, we describe the implementation of reduced-functionality head-end and transmitter nodes and a fully-functional receiver node. The primary purpose of the head-end and transmitter nodes in this work is to simulate the construction of fully-loaded HLAN slots which are then processed by the receiver node. The receiver node consists of three layers of optical logic which are used for synchronization, address processing, and rate conversion of incoming network data. Below, we describe these operations and present experimental results to illustrate their functionality. Note that the network nodes discussed here have been demonstrated at data rates of 40 Gbit/s [5.11, 5.12] and 100 Gbit/s [5.13, 5.14]. Unless otherwise specified, the data presented below were obtained during operation at 100 Gbit/s.

5.4 Head-End

As discussed above, the head-end in a HLAN is responsible for defining the slot structure for the network and managing bandwidth allocation on the GBW and BOD segments of the network. For the purposes of this study, the head-end simply defines the slot structure. The bandwidth management features of the head-end can be developed using some of the techniques described in the transmitter and receiver designs. The slot structure for the network is shown in Figure 5-3. A global clock consisting of a stream of short optical pulses at a repetition rate that is a sub-harmonic of the aggregate media rate is distributed to all of the nodes in the network. This clock serves two purposes. First, it provides bit-level synchronization for all nodes on the network. Second, it eliminates the need for a local pulse source in the transmitter. There is a bandwidth overhead associated with transmitting the global clock in addition to the network data. However, this overhead can be reduced by making the ratio of the clock frequency to the data rate small. A single pulse is eliminated from this

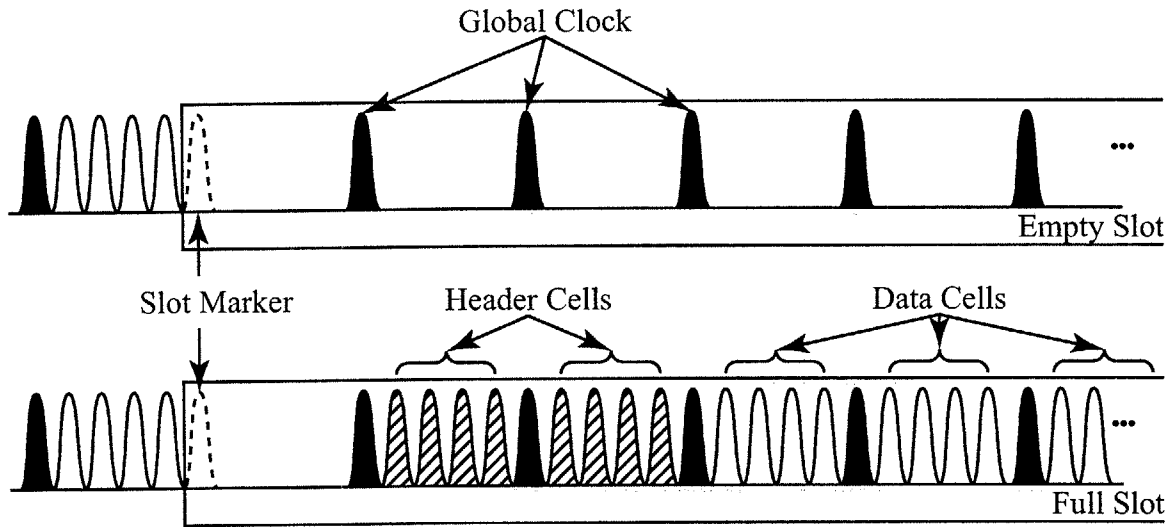


Figure 5-3: Illustration of slot structure for an empty and a full slot.

global clock stream to indicate the beginning of a slot. This missing pulse is referred to as the slot-marker. The transmitters in the network, interleave cells of data pulses between the clock pulses in an empty slot. The first few cells in a slot contain the optical header information. The remaining cells contain data. In the work shown here, the global clock frequency is 12.5 GHz. We utilize constant-length slots with a duration of 100 ns (corresponding to a slot frequency of 10 MHz). Eight data pulses are interleaved between each clock pulse. This gives an aggregate data rate of 100 Gbit/s (8 data pulses every 80 ps) and an aggregate media rate of 112.5 GHz (9 total pulses every 80 ps). Each full slot contains up to 10,000 data pulses. The overhead associated with the global clock distribution scheme in this system is $\approx 11\%$.

A schematic of the head-end configuration is shown in Figure 5-4. This simplified head-end generates the global clock for distribution on the network bus and defines the slot boundaries by eliminating a single clock pulse at 100-ns intervals. The global clock is generated by a commercially-available (PriTel) mode-locked fiber laser (MLFL) which produces a 12.5-GHz stream of nearly transform-limited 2.5-ps optical pulses with a center wavelength of 1550 nm. A 10-MHz frequency synthesizer synchronized to the 12.5-GHz MLFL is used as the slot clock. The Avtech sine-to-TTL convertor

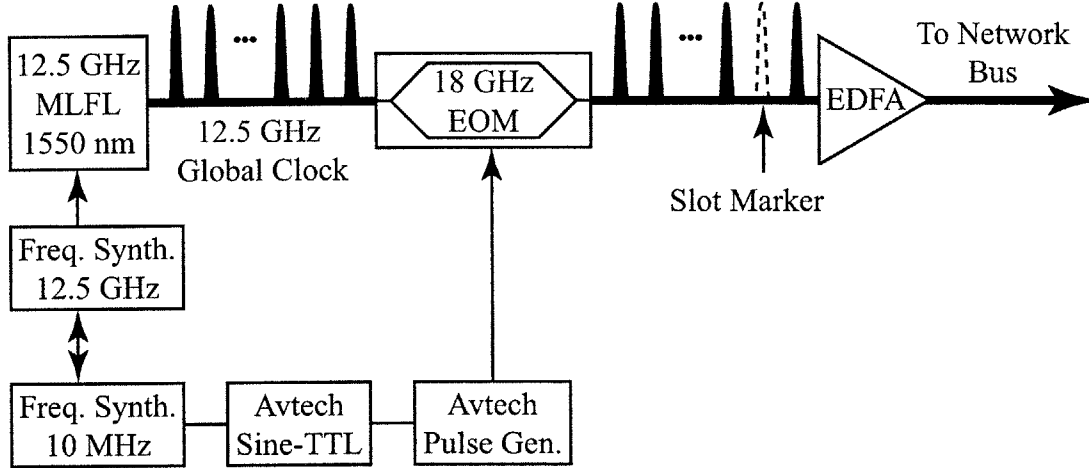


Figure 5-4: Head-end experimental implementation. MLFL: Mode-locked fiber laser; EOM: Electro-optic intensity modulator; EDFA: Erbium-doped fiber amplifier.

(AV-148-PS-MITB) converts the 10-MHz clock to a 10-MHz stream of 20-ns TTL-level (0 to +3 V) pulses. These pulses are input to an Avtech pulse generator (AVM-2-C) which produces electrical pulses with a duration of ≈ 100 ps. The output from the pulse generator drives a LiNbO_3 electro-optic modulator to gate out a single pulse from the 12.5-GHz optical clock every 100 ns, thus defining the beginning of a slot. Finally, the optical pulses are amplified in an erbium-doped fiber amplifier (EDFA) prior to transmission onto the network bus. Figure 5-5 shows a waveform trace of the empty slots generated by the head-end as measured on a digital sampling oscilloscope.

5.5 Transmitter

We have also implemented a transmitter for the slotted OTDM network testbed. As with the head-end implementation, the transmitter considered here is not a fully-functional HLAN transmitter. In particular, the transmitter does not process headers for empty/full detection and GBW services. It also does not keep track of credits. Since there is only one transmitter on the network testbed, these functions are not required. The transmitter in this study modulates the global clock pulses to generate

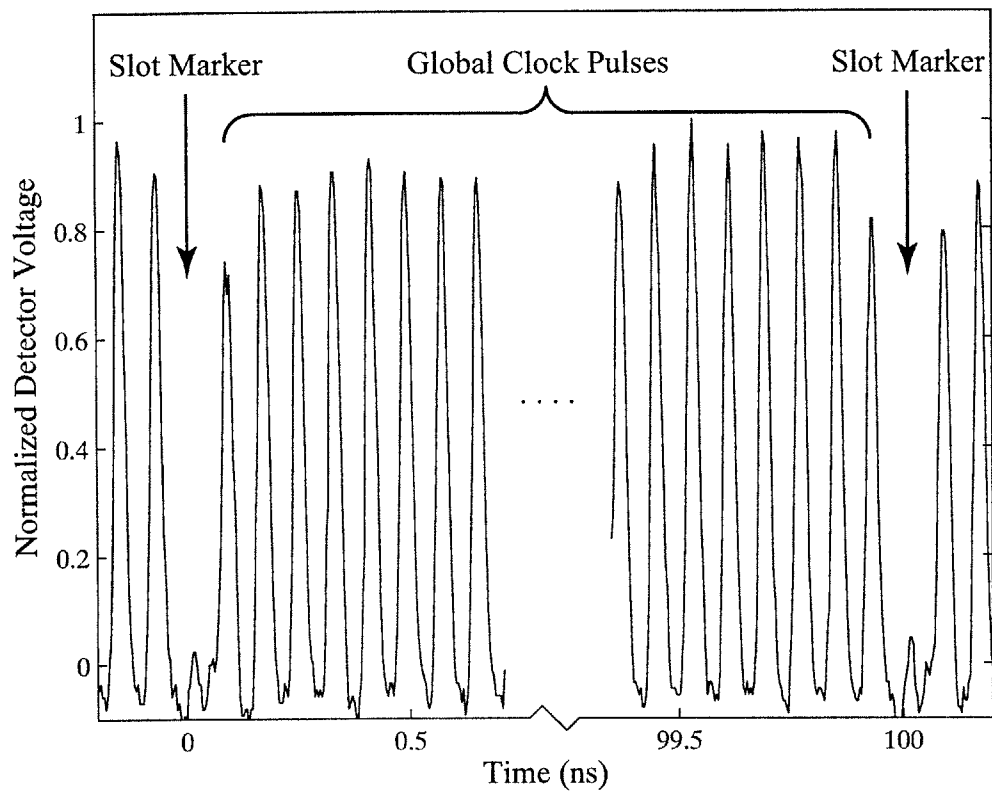


Figure 5-5: Head-end waveform trace. A single pulse is eliminated from the 12.5-GHz global clock stream every 100 ns to demarcate the beginning of a slot.

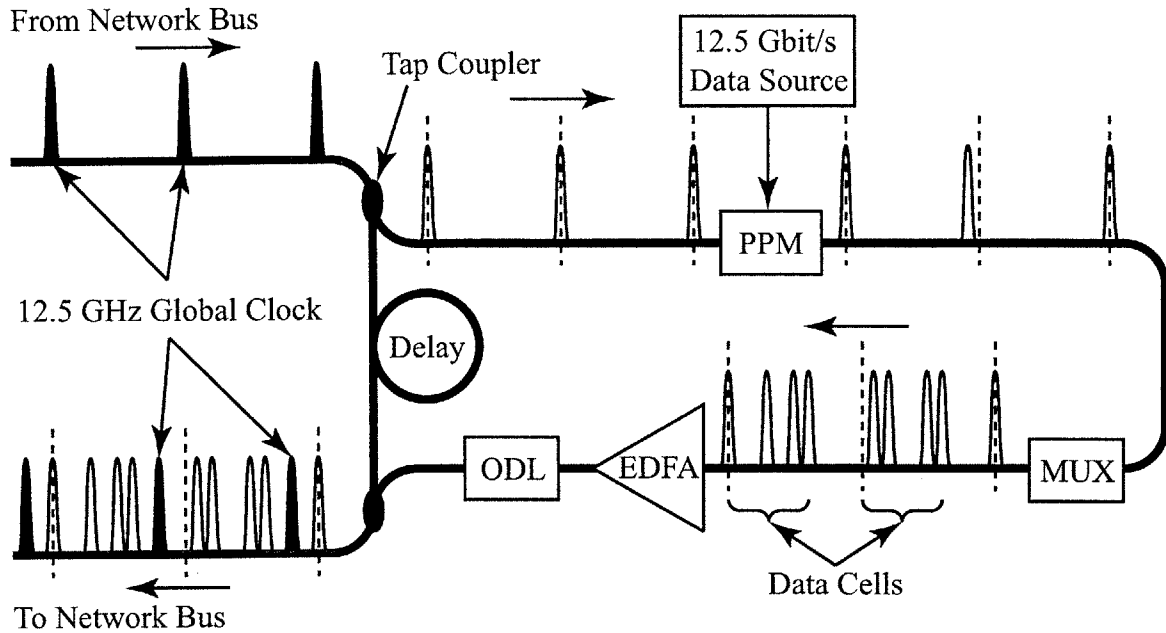


Figure 5-6: Transmitter experimental implementation. PPM: Pulse-position modulator; MUX: Passive OTDM multiplexer; EDFA: Erbium-doped fiber amplifier; ODL: Tunable optical delay line.

header and data cells which are then interleaved with the global clock pulses on the network bus. Transmission of real data would require rate conversion from electronic processing rates to the optical transmission data rate. Several techniques for performing this rate conversion have been reported [5.15, 5.16]. However, this functionality is not required for testing receiver operation in the network testbed. Thus, in this demonstration, fully-loaded high data rate slots are simulated using standard OTDM passive multiplexing techniques [5.17].

A schematic of the transmitter design is shown in Figure 5-6. A tap coupler is used to passively tap a portion of the optical power on the network bus for use in the transmitter. The use of passive taps is important in a unidirectional multi-access bus architecture, such as HLAN, so that a single transmitter node failure does not disable the entire network bus. The global clock pulses are modulated with a pseudo-random binary sequence using a pulse-position modulator (PPM) driven by a data source (Anritsu MP 1763B Pulse Pattern Generator) operating at the clock repetition rate.

The PPM delay is set to approximately one half of the bit-period at the aggregate media rate. For example, at an aggregate media rate of 112.5 Gbit/s, we use a PPM delay of 4.4 ps. Fully-loaded data cells are then generated by passively multiplexing the PPM data from the clock repetition rate to the aggregate network data rate. This is done by successive stages of an OTDM multiplexer. In each stage, the incoming stream of modulated pulses is split into two spatially-distinct beam paths using a polarizing beam splitter (PBS). The two beams traverse different path lengths prior to being recombined using a PBS. The relative delay between the two paths results in a doubling of the data rate at the output of the stage. Two issues must be considered in choosing the lengths of the differential delays in the passive multiplexer. First, the relative path lengths must be long enough so that the pseudo-random nature of the data is maintained at the higher data rate (i.e., adjacent bits should not be correlated). Second, the path lengths must be designed to leave a gap between the data cells for the global clock pulses. A two-stage multiplexer with relative delays of $7T/5$ and $4T/5$, where $T = 100$ ps, is used for multiplexing from a data rate of 10 Gbit/s to a data rate of 40 Gbit/s. Multiplexing from a data rate of 12.5 Gbit/s to 100 Gbit/s requires a 3-stage multiplexer. The relative optical delays used in this multiplexer were $7T/9$, $10T/9$, and $14T/9$, where $T = 80$ ps is the bit-period at 12.5 Gbit/s. After multiplexing, the data pulses are amplified to match the energy of the clock pulses on the network using an EDFA. The amplified pulses are then interleaved with the clock pulses on the network bus using an optical delay line and a second passive coupler.

Figure 5-7 shows two experimental traces of the output of the transmitter. Figure 5-7 a) shows operation at an aggregate media rate of 50 Gbit/s (40-Gbit/s data rate) as measured on a digital sampling oscilloscope. The trace resolution is limited by the bandwidth of the 40-GHz photodiode used in the measurement. In this demonstration, the global clock frequency is 10 GHz, giving rise to clock pulses separated by 100 ps. Four-pulse PPM data cells with a PPM delay of 10 ps are interleaved between the clock pulses. The second trace shows the transmitter operation at an aggregate media rate of 112.5 Gbit/s. Here, the clock frequency is 12.5 GHz and the

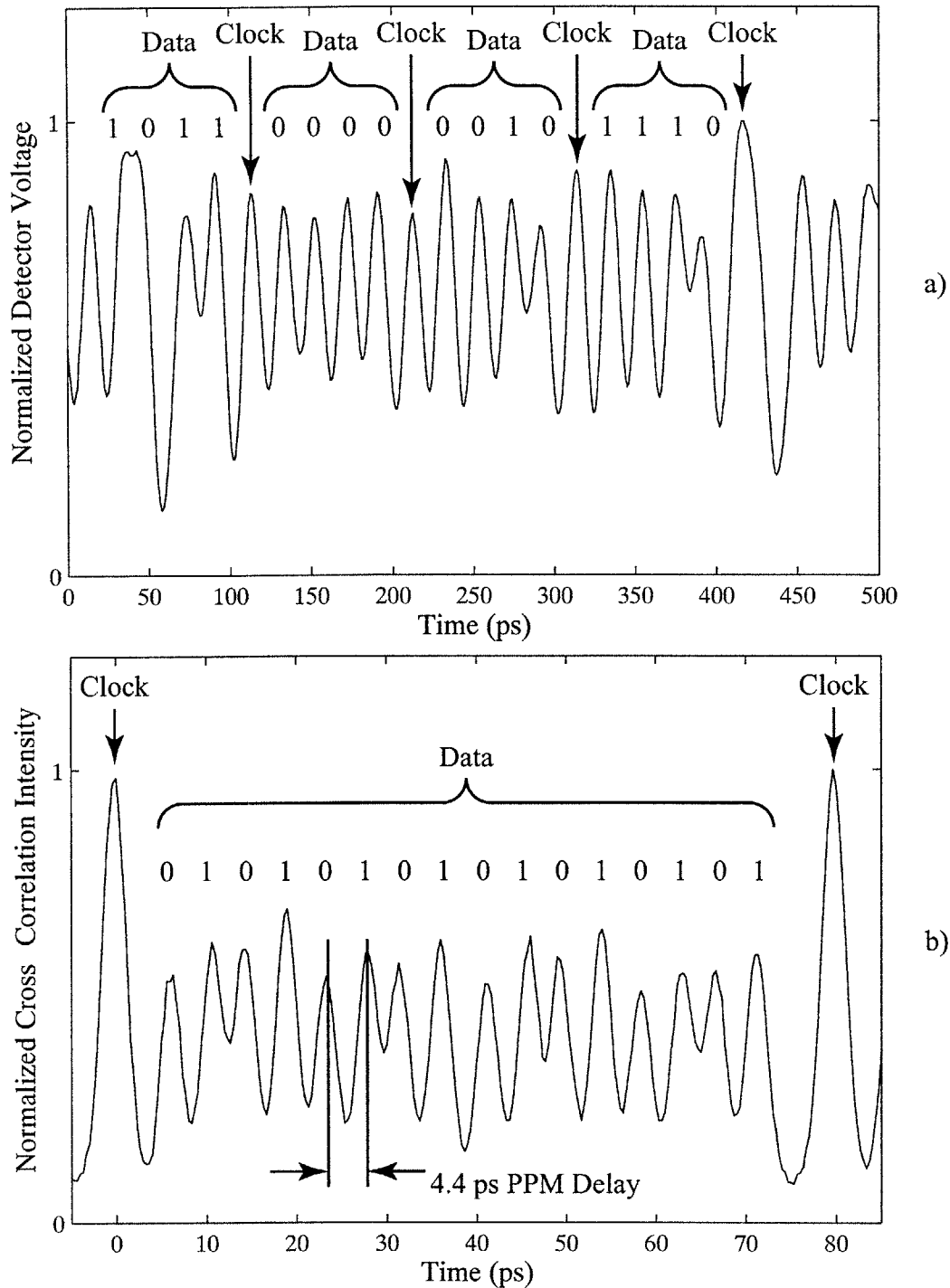


Figure 5-7: Experimental waveforms demonstrating transmitter operation at aggregate media rates of a) 50 Gbit/s and b) 112.5 Gbit/s. The 50-Gbit/s waveform is measured using a 40-GHz photodiode and a digital sampling oscilloscope. The 112.5-Gbit/s waveform is measured via cross-correlation with a 12.5-GHz stream of 2.5-ps optical pulses.

data rate is 100 Gbit/s (corresponding to 8 pulses per data cell). The measured trace is obtained via optical cross-correlation of the transmitter output with a 12.5-GHz stream of 2.5-ps pulses using sum-frequency generation in a nonlinear crystal [5.18]. Due to the PPM data format and the pseudo-random nature of the data, two pulses are observed in the cross-correlation for each pulse in the data cell. The PPM delay is set to 4.4 ps. The data pulses are approximately half the height of the clock pulses in the cross correlation due to the equal probability of a 1 and 0 in the binary data. The additional height fluctuations observed in the data are due to imperfect alignment of the OTDM multiplexer.

5.6 Receiver

In this section, we describe the design of an optical front-end for a slotted OTDM receiver node. As discussed in Section 5.2, the receiver front-end consists of three optical processors. These processors are used for synchronization, address processing, and rate conversion at the receiver node. Below, we detail each of these tasks and demonstrate how optical logic implemented using the ultrafast nonlinear interferometer (UNI) design can be used to accomplish each of these tasks in a functional receiver node.

5.6.1 Synchronization

The optical receiver node in a slotted OTDM network must be synchronized to both the slot-clock for the network and the bit-clock for an individual slot. Numerous techniques for slot-clock synchronization have been proposed and demonstrated. Most of these involve placing a unique identifier which may be identified by the receiver at the beginning of a slot. This identifier can take several forms. For instance, a unique codeword can be placed at the beginning of the slot [5.19, 5.20]. These methods are potentially easy to implement at the transmitter, since they do not require complicated modulation techniques. However, encoding the data at the transmitter may be complicated by the requirement that the codeword for the slot beginning cannot

appear in the modulated data. Alternatively, a single pulse with a polarization that is orthogonal to the data stream polarization may be placed at the beginning of the slot [5.21, 5.22]. This scheme potentially simplifies the detection procedure in the receiver as a polarizer can be used to detect the slot beginning. However, such a modulation format requires careful control of signal polarization at the input to the receiver and may be further impaired by polarization-mode dispersion during propagation. Synchronization schemes which take advantage of the saturation induced in a semiconductor optical amplifier (SOA) by the onset of the optical packet have also been proposed [5.23, 5.24]. These schemes require sufficiently long guard bands between packets to allow for gain recovery in the SOA. Their performance may also be degraded by long series of ones in on-off keyed (OOK) intensity-modulated data.

In this work, we present a straightforward scheme for bit- and slot-clock synchronization which overcomes some of the limitations of the aforementioned techniques. As we have discussed above, in the HLAN network architecture, the head-end demarcates the slot boundaries. In our implementation, the head-end distributes a 12.5-GHz global clock stream of 2.5-ps optical pulses. The beginning of a slot is indicated by a missing pulse in the 12.5-GHz global clock stream distributed by the head-end. Bit-clock synchronization is accomplished at the receiver by synchronizing a local 12.5-GHz clock to the globally distributed clock. Slot-clock synchronization is obtained by detecting the missing pulses in the global clock stream. Both of these tasks are performed using a single UNI as shown in Figure 5-8. A mode-locked fiber laser provides a local optical clock at the receiver. The laser produces a 12.5-GHz stream of 2-ps pulses at 1545 nm which is used as the signal input to the UNI. A passive tap from the network bus provides the control input to the UNI. The local clock pulses are temporally aligned with the global clock pulses in the network data stream at the input to the UNI. The UNI is configured as an AND gate with an inverted control input. Thus, a signal pulse is routed to the output only when the slot-marker arrives at the control input. This pulse provides the slot-clock timing reference at the receiver. Figure 5-9 shows an experimental trace of the output of the slot-marker detection UNI. In this experiment, the slot-synchronization UNI was used to detect

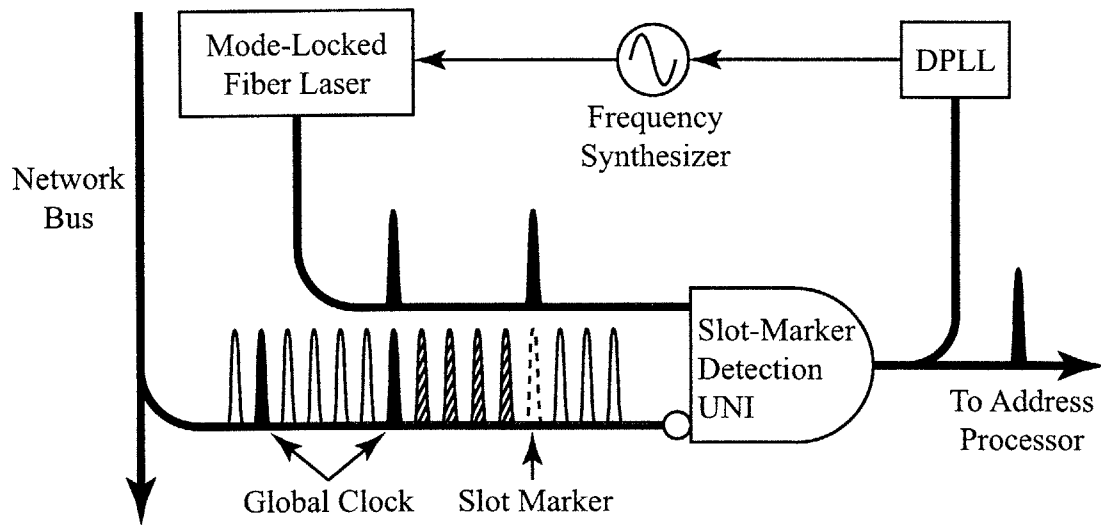


Figure 5-8: Block diagram of synchronization unit for a receiver node in a slotted OTDM network. The UNI output provides a slot-synchronization signal as well as a feedback to the dithering phase-locked loop (DPLL) which is used for bit synchronization.

the beginning of slots produced by the head-end and transmitter operating at an aggregate media rate of 112.5 Gbit/s. The UNI used in the experiment had a 2.5-ps switching window duration which allowed the global slot clock to be distinguished from the neighboring data pulses. An extinction ratio of 8.5 dB is measured using 7-fJ signal pulses and 24-fJ control pulses.

Synchronization with the bit clock is maintained using a dithering phase-locked loop (DPLL) which synchronizes the local receiver clock to the incoming global clock. The DPLL works by applying a 1-kHz phase dither to the frequency synthesizer driving the fiber laser in the receiver. This dither subsequently produces a small modulation in the timing of the local receiver pulses of about 100 fs, peak-to-peak. Due to the temporal shape of the UNI switching window, this timing variation may be detected as a 1-kHz intensity modulation at the output of the UNI. The DPLL adjusts the phase of the local frequency synthesizer to minimize this intensity modulation, thereby synchronizing the local clock pulses with the global clock pulses. Note that in the present configuration, only the phase of the incoming global clock is recovered. Frequency synchronization is obtained using a 10-MHz reference signal between the

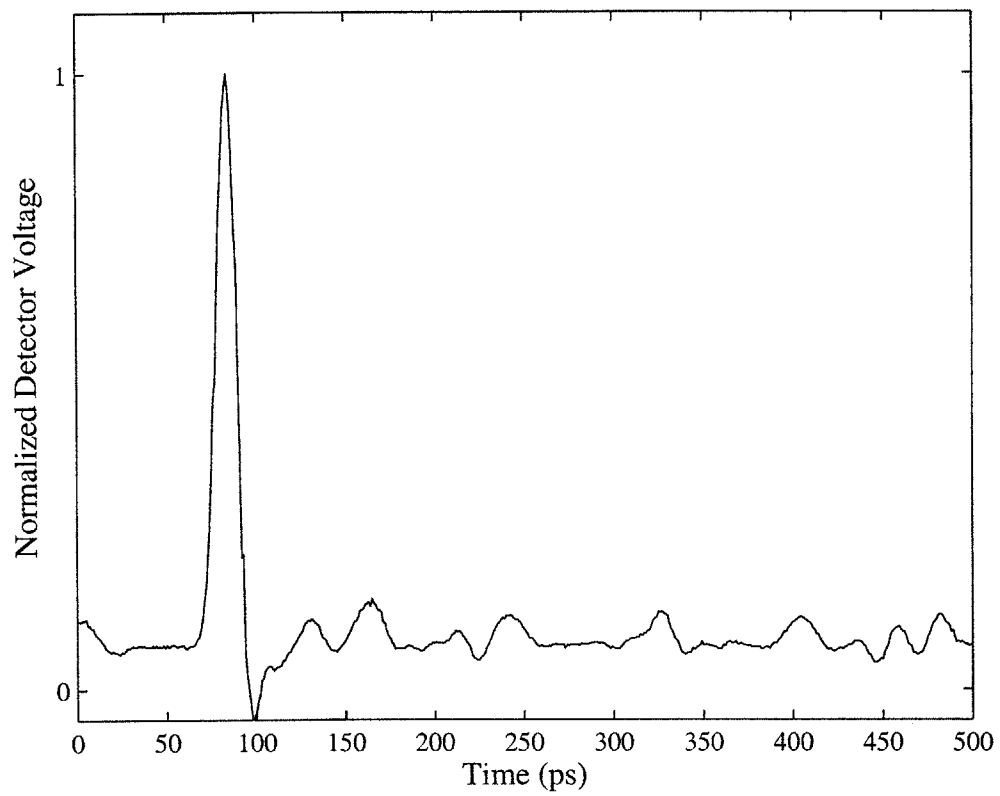


Figure 5-9: Output pulse from slot-synchronization UNI operating at an aggregate media rate of 112.5 Gbit/s.

frequency synthesizer for the receiver clock and the head-end clock. However, this scheme may be modified to provide both frequency- and phase-recovery.

This synchronization scheme is advantageous for several reasons. First, in contrast to other schemes, it does not require special coding or modulation formats at the transmitter. There is no limitation on codewords or data patterns which the transmitter may send. Since the network data is used as the control input to the UNI, the synchronization scheme is largely polarization independent. Additionally, this technique does not require the use of guard bands. Moreover, while fixed-length slots were used in this demonstration, this scheme can also be used to process variable-length slots. The major drawback to the scheme is the additional bandwidth required to interleave the global clock with the transmitted data. As discussed previously, in the 112.5-Gbit/s networking demonstration, there is an 11-percent bandwidth overhead associated with the global clock distribution. This reduces the spectral efficiency of the network transmissions. However, when the aggregate media rate is large compared to the global clock rate, this overhead becomes acceptable.

5.6.2 Optical Address Processing

Optical address processing is an important task in a slotted OTDM transceiver. Numerous techniques have been developed for processing electronic-rate optical addresses. Here, we will focus on all-optical techniques for address comparison that are readily scalable to the data rates required in slotted OTDM networks. Address-processing requirements at a network node can vary greatly, depending on the network type and the functional role of the node within the network. For instance, a receiver node in a broadcast-select network (such as the HLAN) may simply compare the address on the incoming slot to the local receiver address. The result of this comparison determines the state of a optical pass-gate or 2 x 2 switch which off-loads the packet into the receiver terminal for further processing. On the other hand, an optical packet switch in the core of the network may require more complex processing to determine the proper routing for a slot within the switch. Here, we will focus on the simple address processing required in the broadcast-select network scenario, although the

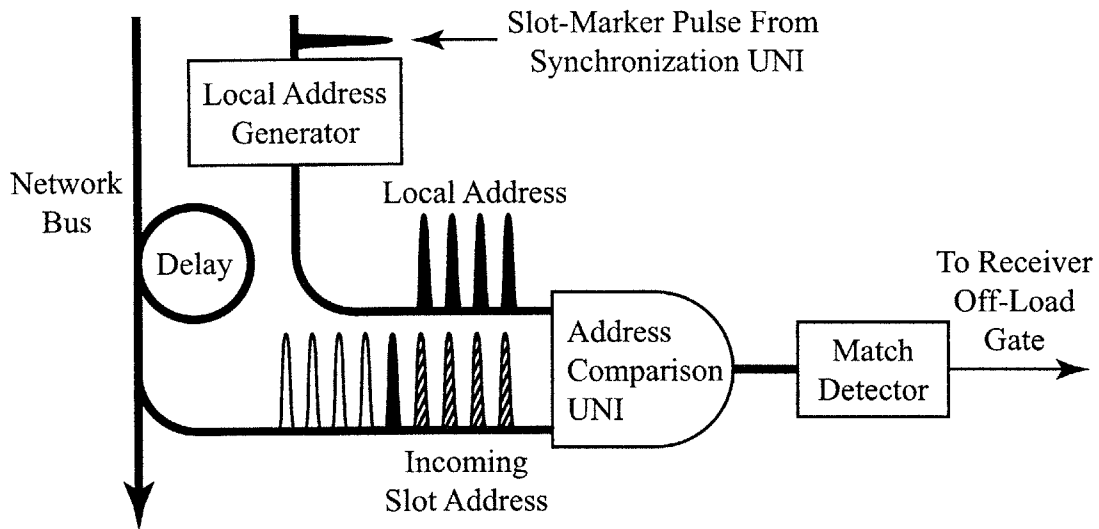


Figure 5-10: Block diagram of address processor for slotted OTDM receiver node.

techniques which we present can be extended to more complex routing scenarios (see, for example [5.25]).

An all-optical address processor in such a network must provide three important functions: synchronization, local address generation, and address comparison. The optical receiver must synchronize its operation to the timing of the incoming optical slot in order to correctly locate the address within the slot for further processing. Next, the receiver must generate a representation of the local address. Finally, the local address must be compared with the incoming slot address to determine whether the two match. A block diagram of the address processing technique demonstrated here is shown in Figure 5-10. Synchronization of the receiver node to the slot timing has been discussed above. The address processor in the OTDM receiver node is synchronized to the incoming slot-clock by using the slot-marker pulse obtained at the output of the synchronization UNI to generate the local receiver address. Fiber propagation delays in the receiver are set to ensure overlap of the locally-generated address with the incoming slot address at the address-comparison UNI. The two addresses are compared bitwise using a UNI AND gate. However, as we discuss below, the UNI provides XOR functionality due to the PPM data format. After bitwise

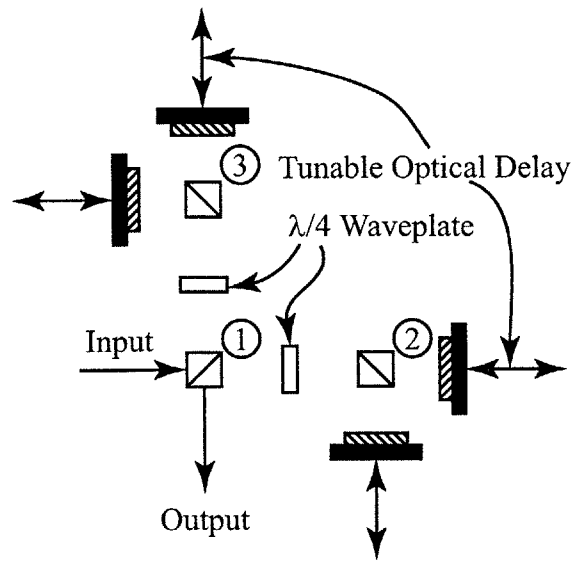


Figure 5-11: 4-bit PPM optical address generator.

comparison, the resulting “match-bits” are sent to a match detector to determine whether the two addresses match. Below, we describe each of these components in more detail and provide experimental evidence of their operation.

The local receiver optical address is produced from the slot-marker synchronization pulse using passive bulk optics as shown in Figure 5-11. The use of the slot-marker pulse in generating the local address accomplishes two tasks. First, it guarantees synchronization with the incoming packet, so no additional circuitry or variable optical delays are required to synchronize the local address with the incoming slot address. As such, it is well suited for networks with diverse packet routes and variable-length packets. Second, since the slot-marker synchronization pulse is produced locally at the receiver, its polarization can be controlled. This is important, since both the optical address generator and the address-comparison UNI are polarization sensitive. The incoming pulse polarization is aligned at 45 degrees with respect to the axis of the first PBS. Consequently, the pulse power is divided evenly into two pulses at the reflection and transmission ports of the PBS. These pulses then pass through quarter-wave plates to produce a circular polarization which causes each pulse to be equally divided (into 4 total pulses) among the outputs of the second and third PBSs. The

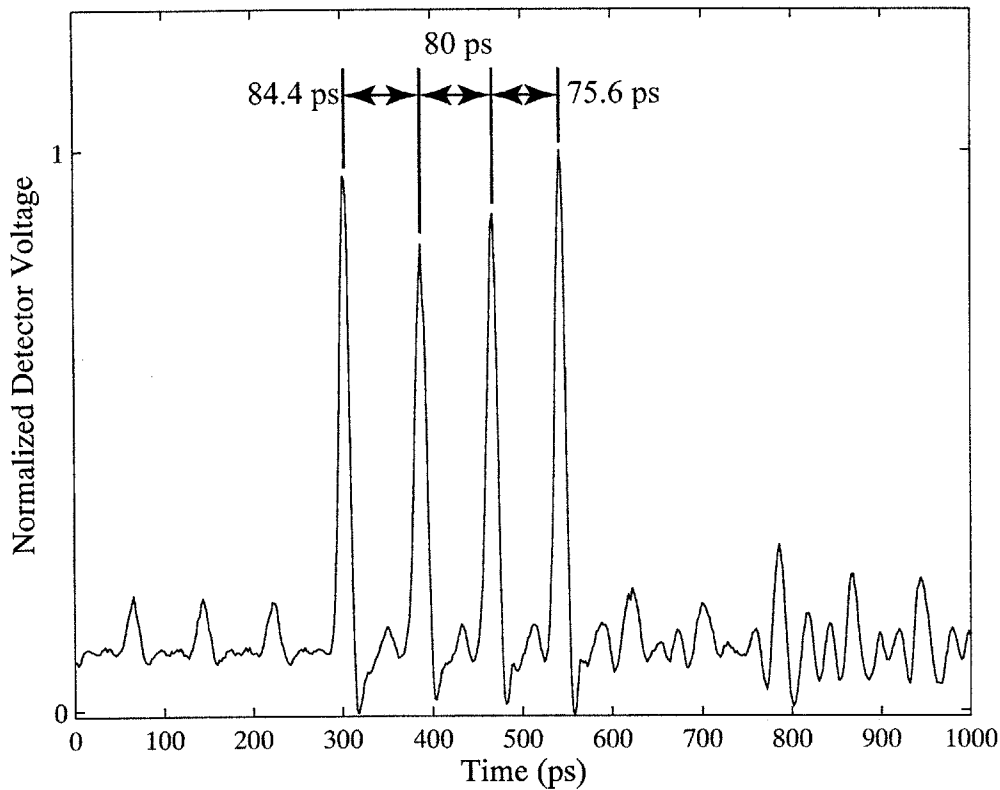


Figure 5-12: Experimental trace of a 4-bit PPM local address, [1001]. The address rate is 12.5 Gbit/s. The PPM delay is set to 4.4 ps, or one-half of the bit-period at the aggregate media rate of 112.5 Gbit/s.

four pulses then reflect off separate mirrors and pass back through the PBS. A second pass through the quarter-wave plate then aligns the polarization such that the four pulses are directed to the output port of the first PBS.

The four mirror-delay paths are adjusted to produce four pulses, each separated by one bit-period, at the output of the address generator. These delays can be adjusted to provide the PPM delay on any of the paths, enabling any 4-bit optical address to be produced. Note that while this mechanical design is inherently slow, it is likely that the address could be changed on a fast enough time-scale to perform necessary network functions, such as updating a routing table in an optical packet router. It could also potentially be integrated as a planar lightwave circuit with temperature-controlled delays. Figure 5-12 shows an experimental 4-bit address of [1001] produced

from a slot-marker synchronization pulse by the address generator. In this case, the address bit rate is 12.5 Gbit/s and the PPM delay is 4.4 ps.

Once the receiver address recognition unit is synchronized and a local address is generated, the local address must be compared to the incoming slot address. Multiple techniques have been demonstrated for optical address comparison in an optical transceiver. For example, a network address can be compared to a local address using an optical AND gate [5.21, 5.26]. This technique is particularly attractive for implementation using ultrafast optical logic since it does not require the use of exclusive-OR (XOR) logic, which is difficult to achieve. Instead, bits from the two addresses are compared using an AND gate and the address space is limited to keywords that are distinguishable using this comparison method. In this addressing scheme, the addresses are restricted such that an N -bit address has exactly $N/2$ ones and $N/2$ zeros. This limitation reduces the efficiency of the address coding (i.e., for an N -bit address, fewer than 2^N codewords are available). Improved address-matching performance can be obtained by further restricting the address space to increase the minimum distance between address codewords, but this reduces the efficiency even further [5.27].

Optimal efficiency in address coding is only obtained by bitwise comparison using XOR logic. In this case, the match signal for a network address and a local address, represented by the binary digits $\{n_i\}$ and $\{l_i\}$, respectively, is given by

$$M = \prod_{i=1}^n n_i \otimes l_i, \quad (5.1)$$

where \otimes represents the exclusive-OR operation. Figure 5-13 shows two possible methods for comparing an incoming network address in a slot to a local receiver address. In the first method, the two 4-bit addresses arrive via two parallel buses. Each bit of the network address is compared to the local address using an XOR gate. The match signal is generated using a 4-input AND gate on the outputs of the XOR gates. This circuit, while simple to implement in electronics where large-scale integration is possible, is difficult to implement using ultrafast optical logic due to the number

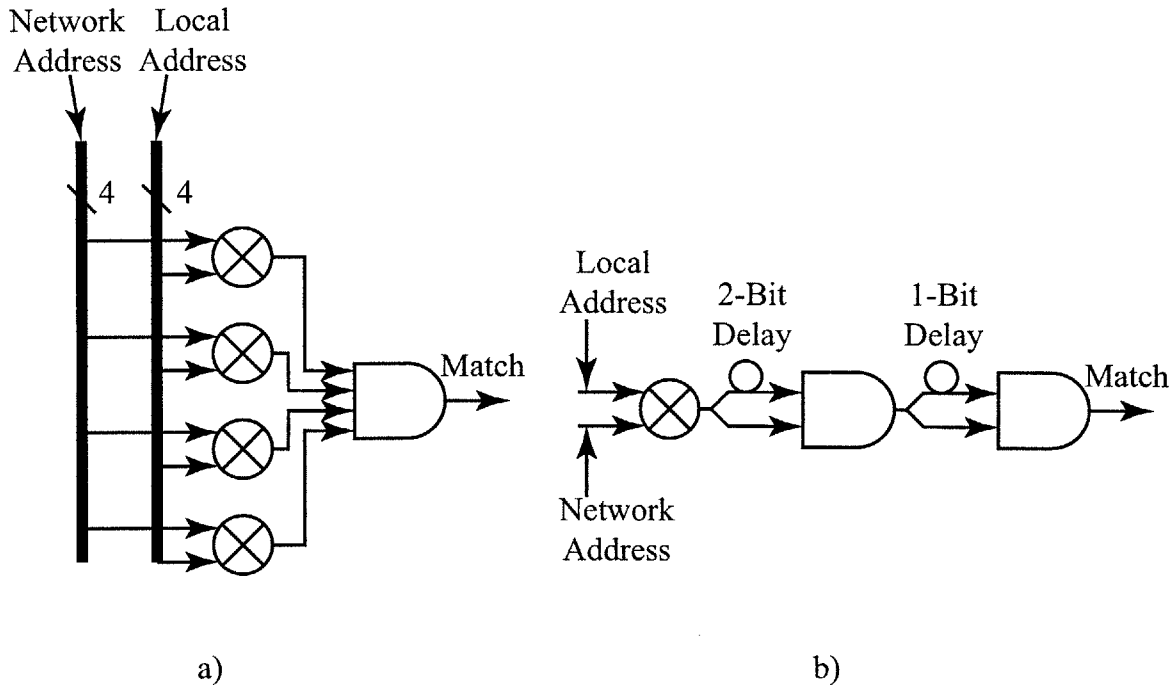


Figure 5-13: Two techniques for detecting a 4-bit address match. In the parallel comparator, a), four 2-input XOR gates and one 4-input AND gate are required. In b), the process is serialized, requiring a single 2-input XOR gate and two 2-input AND gates.

of components involved. An N -bit address would require N XOR gates. Additionally, since most optical logic demonstrated to date has only two inputs, the N -input AND gate required would have to be constructed from $N - 1$ dual-input AND gates. Using current optical logic technologies, implementing even a 4-bit address would be difficult. By contrast, the second technique shown is much more attractive due to the serial nature of the optical address in the slotted OTDM system. In this case, an XOR gate compares the serial network and local address. The four serial match bits at the output of the XOR are then combined using two dual-input AND gates to produce the match signal.¹ This technique requires a total of three dual-input gates operating at the aggregate address rate in order to perform the 4-bit address comparison. Additionally, the technique scales well to higher address spaces— an N -bit address requires one dual-input XOR gate and $\log_2 N$ dual-input AND gates.

¹The serial AND gate comparison technique presented here was designed by R. Magliocco, MIT Lincoln Laboratory.

Several experimental demonstrations of ultrafast dual-input XOR functionality at rates up to 100 Gbit/s have been carried out using fiber-based switches, such as the nonlinear optical loop mirror [5.28, 5.29]. This XOR gate has been used for header recognition in an all-optical packet-switched OTDM receiver node [5.30]. Additionally, we have verified the fidelity of the XOR operation in dual-input fiber-based switches via bit-error rate testing at rates up to 50 Gbit/s of the output of the XOR operation on two fully-loaded pseudo-random binary sequences performed with a folded ultrafast nonlinear interferometer (FUNI) [5.31]. However, these switches are not very compact due to the long lengths of fiber required. XOR functionality has also been demonstrated in semiconductor-based switches. A Sagnac interferometer with a semiconductor optical amplifier was used as an XOR gate in a recirculating configuration to generate long pseudo-random binary sequences at 1 Gbit/s [5.32]. Symmetric Mach-Zehnder and UNI XOR gates have been demonstrated at rates as high as 20 Gbit/s [5.33, 5.34]. However, these semiconductor-based XOR gates are inherently limited to operational speeds where the bit-period is less than the recovery time for carrier density changes in the SOA due to the imbalanced nature of the XOR configuration. Recently, a balanced XOR interferometer configuration which has potential for operating at much higher rates has been proposed [5.35]. However, the pattern-independent operation of this switch has not yet been experimentally verified.

The use of the PPM data format allows binary XOR functionality to be obtained using an AND gate, such as the UNI. In this case, the two PPM-formatted optical data signals are used as the control and signal inputs to the UNI. If the UNI has a switching window that is less than the PPM delay, then a pulse at the signal input will propagate to the output only when it arrives at the same time as a pulse on the control input. Due to PPM data format, this scenario only arises when the signal and control inputs are both a logical zero, or when both inputs are a logical one. If a pulse at the output of the gate represents a one, then the gate computes the logical inverse of the XOR of the signal and control inputs. Traditional XOR operation can also be obtained by adjusting the bias of the UNI to perform the AND of the signal

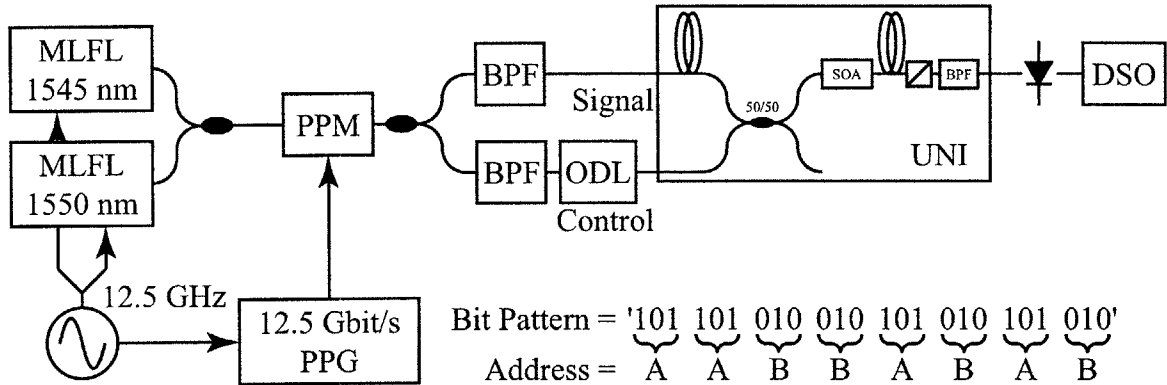


Figure 5-14: Experimental setup for demonstrating address matching functionality using PPM XOR in a UNI at 12.5 Gbit/s. MLFL: Mode-locked fiber laser; BPF: Bandpass filter; ODL: Optical delay line; PPG: Pulse-pattern generator; DSO: Digital sampling oscilloscope.

and the inverse of the control inputs.

We have demonstrated the use of PPM XOR to perform all-optical address comparison of two complementary 3-bit addresses at 12.5 Gbit/s using the experimental setup shown in Figure 5-14. The control and signal inputs to the UNI are provided by two synchronized 12.5-GHz mode-locked fiber lasers producing 2.5 ps pulses at 1550 nm and 1545 nm, respectively. The outputs of these lasers are coupled together using a 50/50 optical tap coupler. In this experiment, we use the UNI to compare two 3-bit addresses, $A = [101]$ and $B = [010]$. The pattern generator produces a repeating stream of the two addresses, $[AABBABAB]$, which is modulated onto the two streams of optical pulses at 12.5 Gbit/s. The modulator produces PPM-formatted data with a PPM delay of 20 ps. After the modulator, the two pulse streams are separated using a 50/50 coupler and two bandpass filters. The control data stream is delayed by five addresses (1.2 ns at 12.5 Gbit/s) relative to the signal stream in order to decorrelate the two inputs to the switch. The UNI has a switching window duration of 16 ps. Since this is less than the PPM delay in the modulated data, the UNI computes the logical XOR of the two input streams.

The output of the UNI is detected using a 30-GHz photodiode and displayed on a digital sampling oscilloscope. These waveforms are shown in Figure 5-15. In this

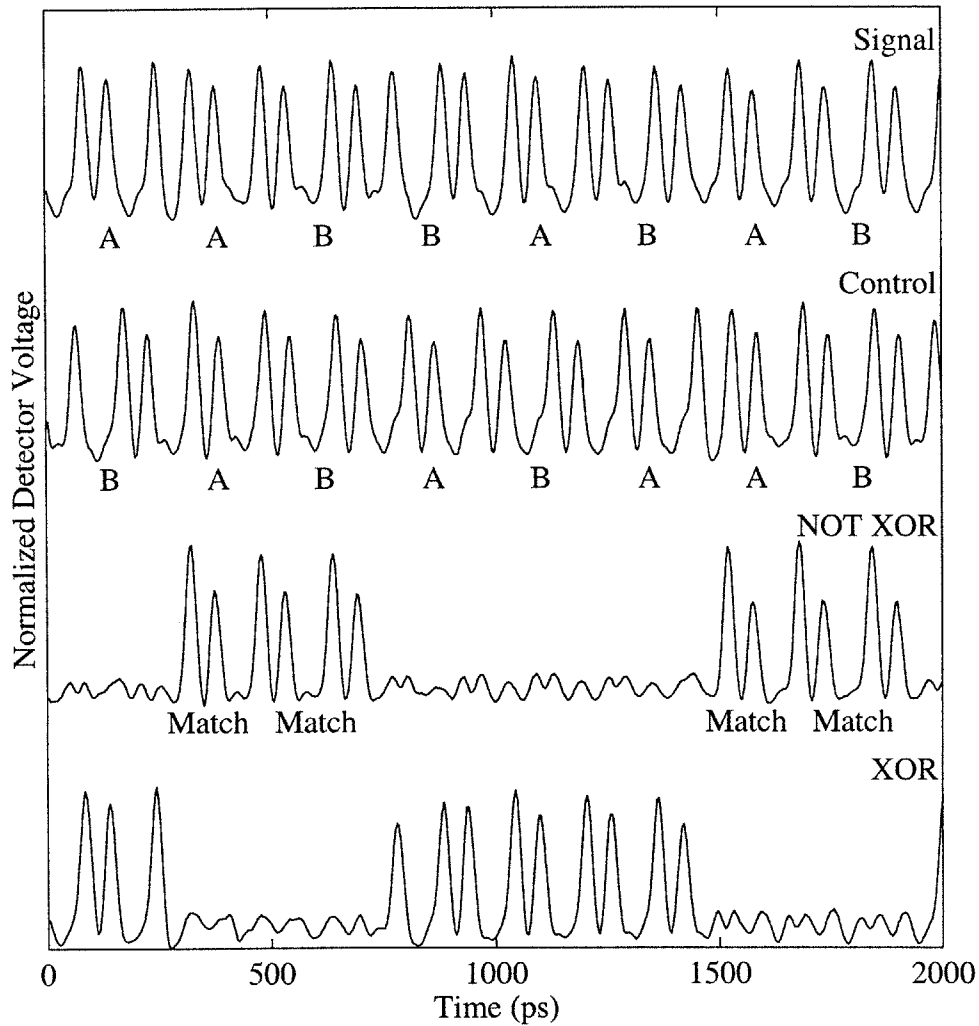


Figure 5-15: Waveforms from all-optical address matching demonstration at 12.5 Gbit/s. The control and signal inputs to the UNI each consist of a repeating stream of 3-bit complementary binary PPM addresses, A and B, where $A = [101]$ and $B = [010]$. A 20-ps PPM delay is used. When the addresses on the inputs match, the NOT XOR output of the UNI produces three match bits. When they do not match, no match bits are produced.

experiment, all possible combinations of binary inputs to the switch are tested. Good performance is obtained in all cases. The amplitude patterning at the output of the switch is primarily due to imperfect modulation at the input. The NOT XOR output provides a pulse when the two input address bits match. Because of the orthogonal nature of the addresses used in this experiment, three match pulses are obtained when the control and signal addresses match and no match pulses are observed when the addresses differ. In this case, a simple match detection scheme consisting of an integrator (e.g., a slow detector) and a thresholder can be used to determine whether or not the addresses match. For non-orthogonal addresses, the serial AND gate scheme discussed above can be used for this purpose.

Address comparison functionality has also been tested using the full address processor setup shown in Figure 5-10 together with the head-end and transmitter described above at aggregate media rates of 50 Gbit/s [5.12] and 112.5 Gbit/s [5.14]. In the 112.5-Gbit/s experiment, the head-end distributed a global clock of 2.5-ps pulses at repetition rate of 12.5 GHz. The slot duration was fixed at 100 ns for a slot rate of 10 MHz. The transmitter modulated a 9-bit repeating data pattern of [100101101] at 12.5 Gbit/s onto the tapped portion of the global clock pulses. The modulated data pulses were then multiplexed to a data rate of 100 Gbit/s and interleaved with the global clock pulses on the network bus to create an aggregate media rate of 112.5 Gbit/s. Each slot contains 1,250 data bits at 12.5 Gbit/s (or, 10,000 data bits at 100 Gbit/s). Thus, each slot contains 138 copies of the 9-bit data pattern, with eight remaining bits at the end of each slot. Therefore, in each consecutive slot, the 9-bit pattern is shifted by 1 bit. In this manner, 9 different slots with 7 distinct 4-bit addresses ([1001], [1100], [0110], [1011], [1101], [0101], and [0010]) are created.

The receiver node synchronizes to the global clock as discussed above. The slot-marker pulse produced by the synchronizer is used to generate a 12.5-Gbit/s PPM local receiver address of [1001]. This address is then compared to the incoming slot address using a UNI with a 2.5-ps switching window duration. The locally generated address is used as the signal input and the incoming 112.5 Gbit/s network slot is used as the control input. This configuration is necessary to ensure that the SOA in

the UNI remains in saturation. The locally-generated address has a low duty cycle consisting of 4 pulses at the beginning of every 100 ns slot. If this were used as the control input on the UNI, the SOA gain would recover between addresses, leading to unpredictable performance. By contrast, even an empty slot on the network bus has a 12.5 GHz stream of clock pulses which serve to keep the SOA saturated. At the input to the UNI, the signal pulse energy is 1 fJ and the control pulse energy is 19 fJ. The results of the address comparison for the seven distinct slot addresses are shown in Figure 5-16. The extinction ratio in all cases was 6.4 dB or better.

The XOR output from the UNI is treated as OOK-formatted data. Thus, the presence of a pulse within a bit-period represents a bit match in the address comparison, while the absence of a pulse represents a bit mismatch. Note that the timing of the match pulse within the bit period is not fixed, however, due to the use of PPM-formatted data at the input to the UNI. Thus, a pulse representing a match between two zero-bits arrives at a different time within the bit-period than a pulse representing a match between two one-bits. It is important to consider the effect of this timing variation in subsequent processing elements, such as the serial AND operation in the address comparator.

In the slotted OTDM address comparison experiment discussed above, the effect of this timing variation will likely be small due to the fact that the PPM delay (4.4 ps) is a small fraction of the address bit-period (80 ps at 12.5 Gbit/s). Figure 5-17 illustrates this point by comparing simulated eye diagrams after direct-detection and filtering in an electronic receiver for the case of standard OOK-formatted and OOK data with PPM delays. The eye diagrams are simulated using a 12.5-Gbit/s PRBS data pattern of length $2^7 - 1$ which is intensity modulated on a stream of 2.5-ps optical pulses. The extinction ratio of the modulator is set to 6.5 dB for comparison with the output from the UNI in the address comparison experiment. To simulate the PPM-formatted data at the detector input, a delay of 4.4 ps is randomly added to half of the data pulses. After detection, a fifth-order Bessel low-pass filter with a 3-dB cutoff of 7.5 GHz is used to model electronic filtering in the receiver. Noise sources are not included in the simulation. However, both signal-dependent and signal-independent

Network Address

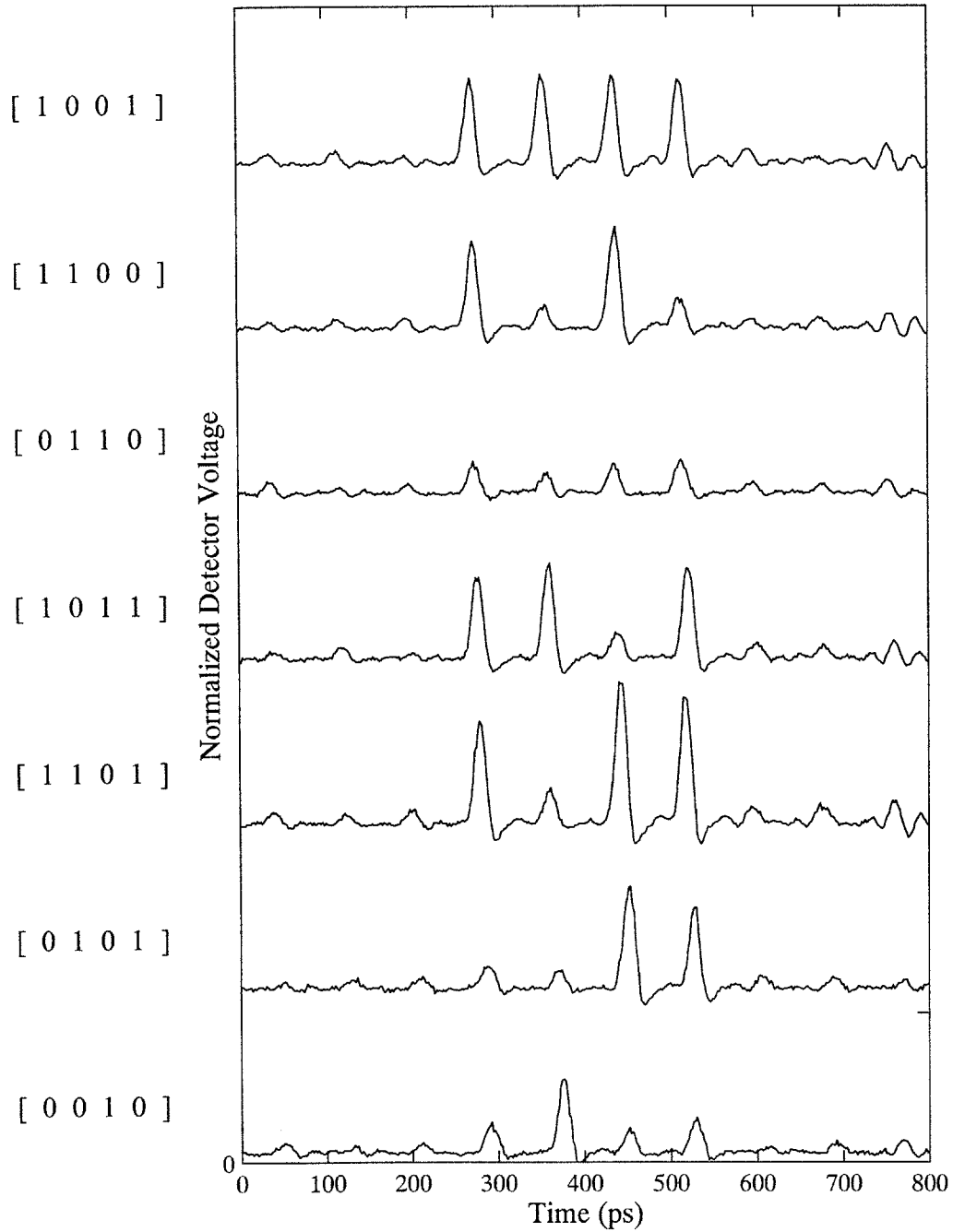


Figure 5-16: Experimental waveforms at output of address-comparison UNI operating at an address rate of 12.5 Gbit/s with an aggregate media rate of 112.5 Gbit/s. The network addresses are compared with a local receiver address of [1001]. The waveforms are measured on a digital sampling oscilloscope with a 30-GHz photodiode.

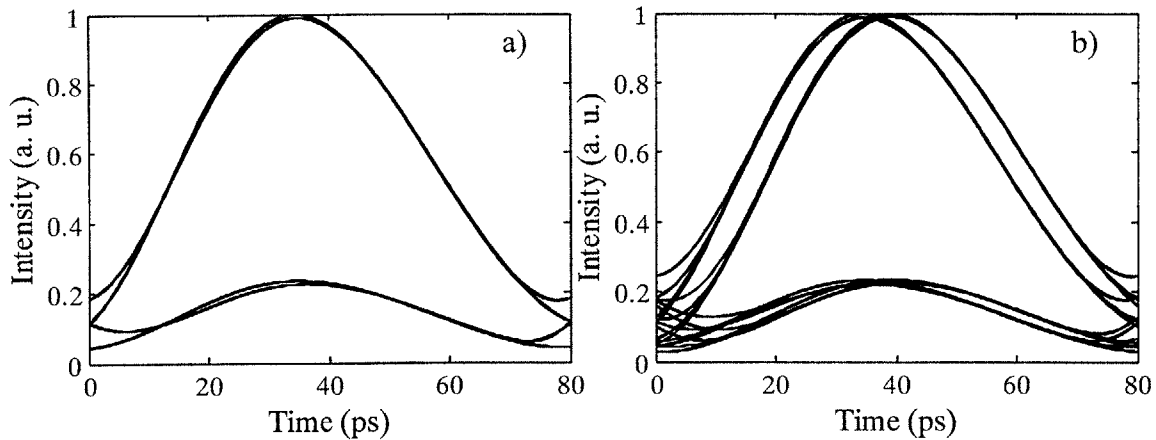


Figure 5-17: Simulated 12.5 Gbit/s receiver eye diagrams at output of address comparison XOR gate after direct-detection and filtering for a) OOK and b) PPM data formats.

noise terms can be added to the present simulation in order to calculate the signal-to-noise ratio or bit-error rate at the receiver (see, for example [5.36, 5.37]). As seen in the simulation results, the addition of a 4.4 ps time delay does not significantly degrade the opening of the eye at the optimum sampling point. The temporal width of the eye is reduced by the PPM time delay, however, and greater sensitivity to clock jitter in the receiver is expected.

5.6.3 Rate Conversion

Since OTDM networks operate at aggregate data rates which are much higher than electronic processing speeds, optical rate conversion is essential in OTDM receiver nodes. In a bit-interleaved OTDM network, rate conversion is achieved using an optical demultiplexer which selects one particular channel from the several temporally-interleaved channels on the network bus. In contrast to this, in a slotted OTDM network, all of the serial data in an incoming slot must be converted down to electronic rates.

Figure 5-18 illustrates two techniques for rate converting a slot from the aggregate network data rate of R Gbit/s down to the electronics processing rate of R/N Gbit/s. The first is a serial-to-serial technique where the incoming (serial) slot data is directly converted into a single serial data stream at the lower data rate. With this technique,

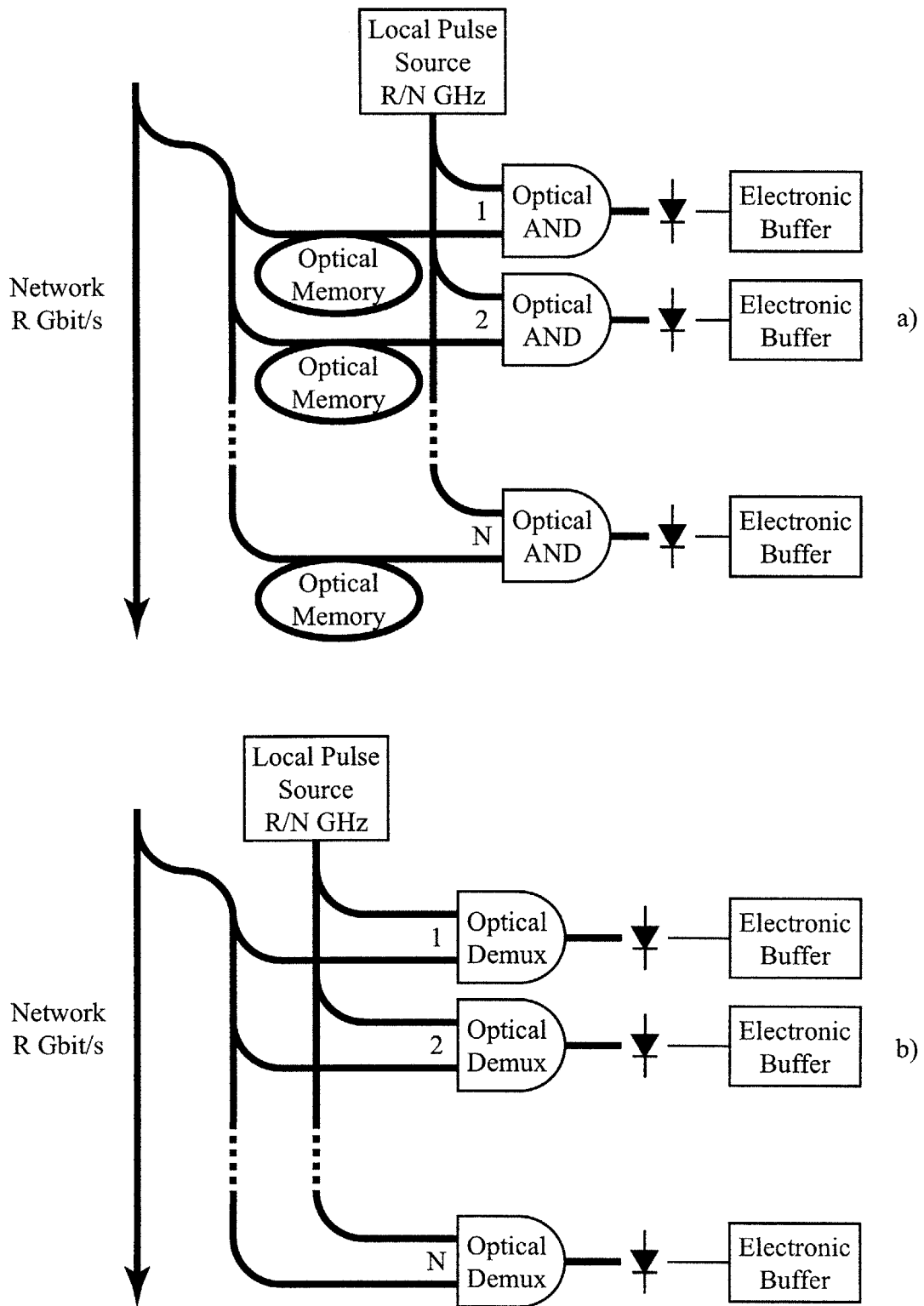


Figure 5-18: Techniques for optical rate conversion of OTDM slots: a) serial-to-serial conversion, b) serial-to-parallel conversion.

the incoming slot is loaded into an optical loop memory. As the slot propagates around the memory, the data pulses are optically sampled at a rate of R/N GHz using an optical AND gate. The sampled pulses are then detected and stored in an electronic buffer. On each pass through the memory, successive streams of optical bits in the slot are sampled. After N passes, the slot is completely converted and serially stored in the electronic buffer. Thus, the total time required for conversion of the slot is equal to N times the duration of the slot. If a second slot arrives at the receiver during this conversion time, it must be loaded into a second optical buffer for conversion. Hence, the optical buffer depth may limit the peak rate at which the receiver can accept slots using this configuration. Recently, several optical memory-based rate convertors have been proposed and demonstrated [5.6, 5.38, 5.39].

The second rate conversion technique shown in Figure 5-18 is a serial-to-parallel scheme where the incoming slot at the aggregate network data rate, R , is treated as N bit-interleaved slots, each with a data rate of R/N Gbit/s. Each of these slots is separated from the others using N optical demultiplexers. The demultiplexed optical data is then detected and stored in N parallel electronic buffers. In contrast to the serial rate conversion technique, this converts the entire slot to electronic data rates within duration of the slot. Therefore no optical buffering is required and the peak rate at which slots can be accepted by the node is limited only by the electronic buffer depth. However, N demultiplexers are required in order to rate convert a slot.

In this work, we focus on the serial-to-parallel technique. We demonstrate two techniques for demultiplexing OTDM PPM data and converting it to a OOK format for detection at 80 Gbit/s using the UNI [5.40, 5.41]. Note that with the parallel rate-conversion technique, even low-bandwidth receivers on the network must have an optical front-end that is capable of receiving data at the full aggregate data rate. While this may seem to be an inefficient use of resources, we demonstrate below a multiple-wavelength demultiplexer that can simultaneously demultiplex multiple OTDM channels with a single all-optical logic gate [5.42]. This greatly simplifies the OTDM receiver architecture. Note that these experiments were not performed using the slotted OTDM architecture described above. Instead, the demultiplexing

was done on continuous streams of OTDM data, rather than actual slots with data cells interleaved between clock pulses. However, the techniques demonstrated here are readily applicable to the slotted OTDM receiver using the rate-conversion architectures discussed above.

Figure 5-19 shows the experimental setup for demultiplexing of an 80-Gbit/s stream of PPM data using the standard demultiplexing configuration for the UNI. In this setup, the data at the aggregate OTDM rate of $N \cdot 10$ Gbit/s is used as the signal input to the UNI. Control pulses at a repetition rate of 10 GHz gate the incoming signal data, routing every N -th pulse to the output of the switch. Pulses from a mode-locked fiber laser (MLFL) producing a 10-GHz stream of transform-limited 2-ps pulses at 1550 nm are modulated with a 10-Gbit/s PPM data pattern consisting of $2^{31} - 1$ bits. The PPM delay is set to 6.25 ps. These pulses are then passively multiplexed to rates of 10, 20, 40, or 80 Gbit/s using a free-space multiplexer with multiple-bit delays between the tributaries. The output of the multiplexer provides the signal input to the UNI. A second MLFL producing a 10-GHz stream of 2-ps pulses at 1545 nm is used as the control input to the UNI. A dithering phase-locked loop (DPLL) maintains the bit-phase alignment between the control and signal pulses. The DPLL applies a 1-kHz phase modulation to the RF synthesizer driving the control MLFL. The temporal shape of the UNI switching window converts the 1-kHz bit-phase modulation to an amplitude modulation at the output of the UNI. The DPLL adjusts the DC signal into the phase modulator to minimize the 1-kHz tone at the output, thereby aligning the signal pulses to the maximum transmission point of the switching window. The commercially-available SOA (Alcatel 1901) used in the experiment is a 1-mm-long InGaAsP device. The SOA bias current is 150 mA, providing a small-signal fiber-to-fiber gain of 28 dB at 1550 nm.

The UNI in this experiment has a switching window duration of 5 ps. Because the switching window duration is less than the PPM delay, the control pulses may be temporally aligned to gate exclusively the one-bits in the overlapped channel of the aggregate OTDM data. In this manner, the demultiplexer converts the demultiplexed channel modulation format to 10-Gbit/s OOK, as illustrated in Figure 5-19. This

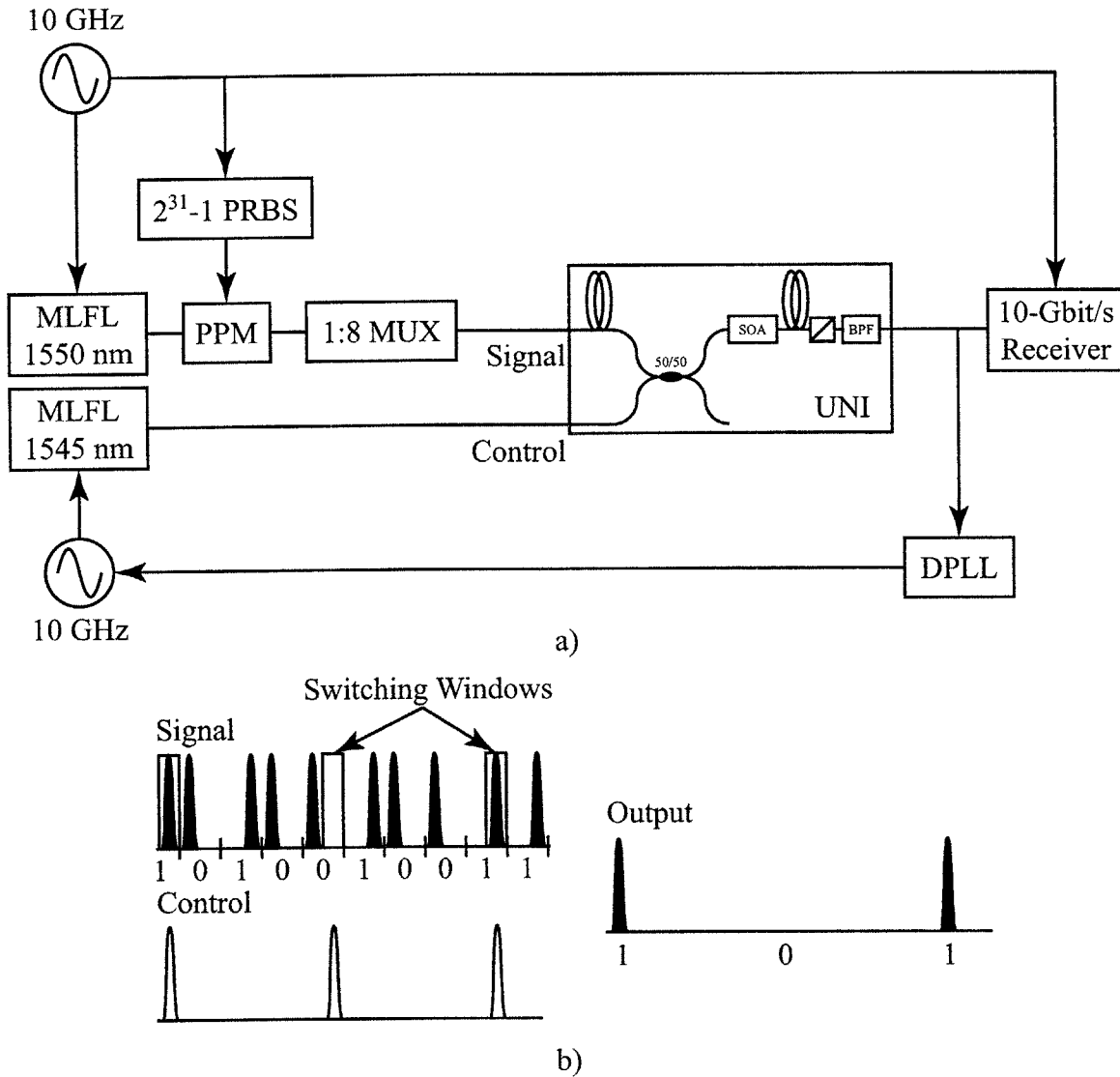


Figure 5-19: Demultiplexing of OTDM PPM data at rates up to 80 Gbit/s with the aggregate data input to the signal port of the UNI. The experimental setup is shown in a). MLFL: Mode-locked fiber laser. PPM: Pulse-position modulator. DPLL: Dithering phase-locked loop; MUX: OTDM passive multiplexer; PRBS: Pseudo-random binary sequence. In b), an illustration of the switch operation at 40 Gbit/s is provided. Each control pulse opens a switching window for the signal path. Only signal pulses that are coincident with a switching window pass to the output of the switch.

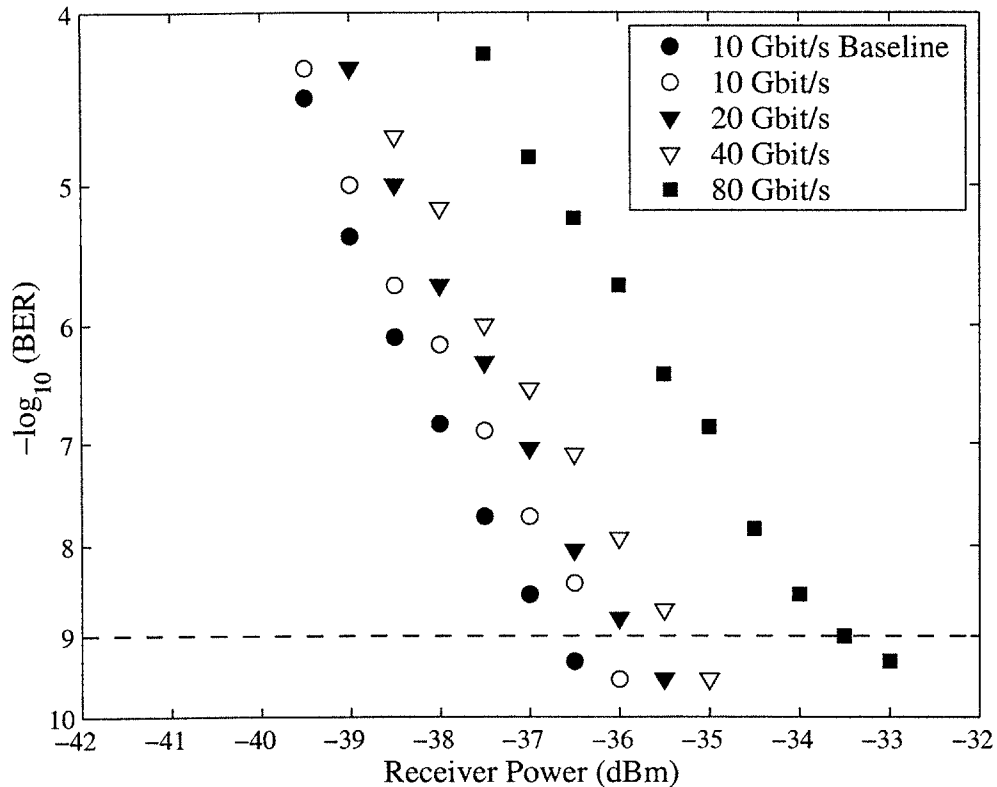


Figure 5-20: Bit-error-rate performance for demultiplexing from aggregate PPM data rates of 10, 20, 40 and 80 Gbit/s on signal input to UNI.

allows bit-error rate (BER) testing at the output of the switch with a standard OOK receiver. A longer switching window could be used to maintain the PPM format.

The results of BER tests performed at the attenuated output of the switch using a 10-Gbit/s OOK optically preamplified receiver are shown in Figure 5-20. The baseline is measured using the OOK data directly from one of the arms in the PPM modulator. The control pulse and signal pulse energies in the demultiplexing experiments were maintained at 500 fJ and 12.5 fJ, respectively. For aggregate PPM data rates up to 40 Gbit/s, a maximum power penalty of 1.2 dB at a BER of 10^{-9} is observed. This penalty is largely due to the wavelength selectivity of the receiver, imperfect contrast of the demultiplexer and increased saturation of the SOA as the signal data rate is increased. At 80 Gbit/s, a power penalty of 3 dB is observed. We believe that this power penalty is a result of intersymbol interference (ISI). This effect is discussed in

more detail below.

Demultiplexing of PPM data may also be performed in a configuration where the aggregate OTDM data is input to the control port of the UNI demultiplexer as illustrated in Figure 5-21. In this configuration, the UNI acts as a wavelength converter, converting every N -th control pulse to the signal wavelength. This configuration is generally avoided in semiconductor-based demultiplexers because data modulation on the control input leads to severe gain saturation effects in the switch at high data rates. The use of the PPM data format reduces these effects, making switching at high data rates practical with modulated data on the control input. Here we demonstrate demultiplexing in this manner from aggregate data rates as high as 80 Gbit/s. As in the previous demonstration, signal and control pulses are provided at 10-GHz repetition rates by two MLFLs producing 2-ps pulses at 1550 nm and 1545 nm, respectively. The control pulses are modulated with a PPM data pattern using a 6.25 ps PPM delay. To demonstrate the pattern-independent operation of the switch, a long data pattern of length $2^{31} - 1$ is used. The PPM data is then passively multiplexed to rates of 10, 20, 40, and 80 Gbit/s, and input to the control port of the UNI. As in the first demonstration, the UNI switching window duration of 5 ps provides a format conversion from PPM to OOK at the output of the UNI. In this setup, maintaining the PPM data format at the output of the switch would require splitting each signal pulse into two pulses separated by the PPM offset.

The results of BER tests at the output of this demultiplexer are shown in Figure 5-22. Error free operation ($\text{BER} < 10^{-9}$) is obtained for all aggregate data rates with control and signal pulses energies of 25 fJ and 12.5 fJ, respectively. Because the signal pulses are at the demultiplexed rate, the contrast ratio of the demultiplexer between signal pulses is not as important in this experiment. Thus, good performance is obtained with significantly reduced control pulse energies. For aggregate control pulse data rates of up to 40 Gbit/s, a small power penalty of < 0.5 dB from baseline is observed. Since the data pulses on the control input are not temporally separated in the UNI, the intersymbol interference observed in the first demultiplexing experiment is not present in this experiment. At 80 Gbit/s the observed power penalty of 2 dB is

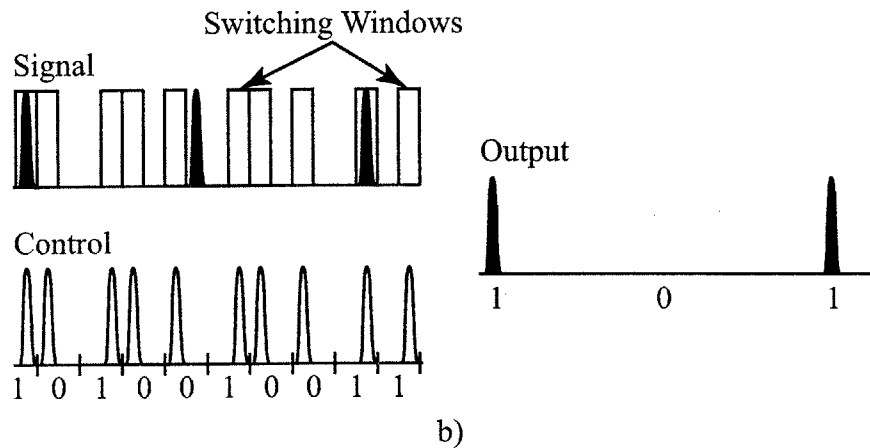
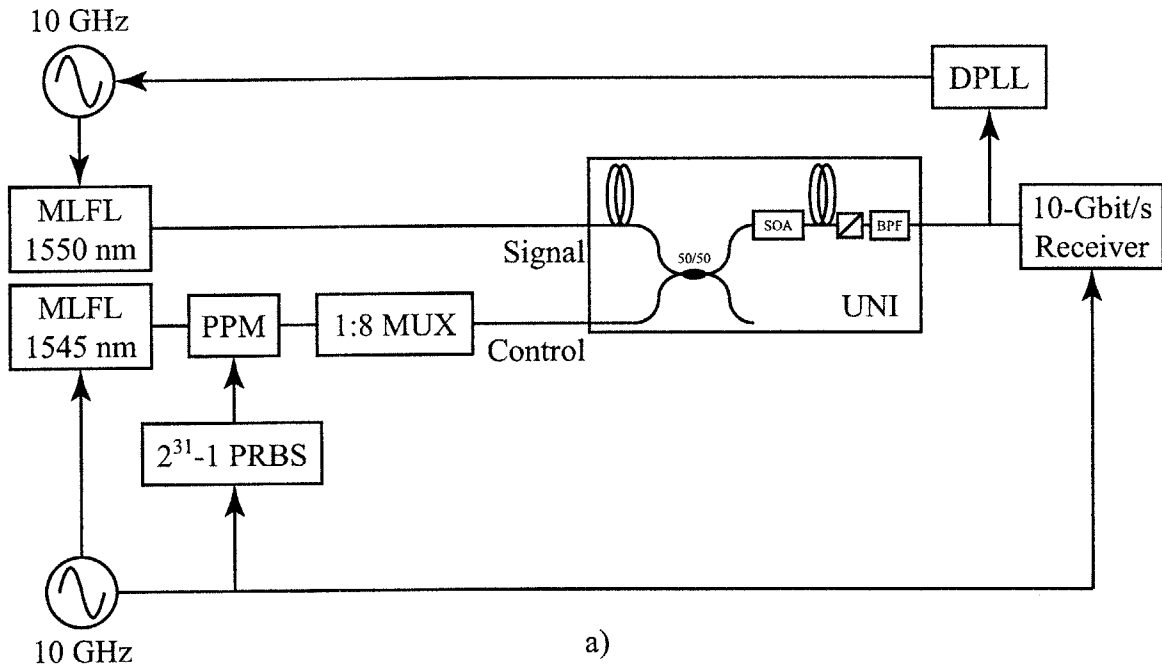


Figure 5-21: Demultiplexing of OTDM PPM data at rates up to 80 Gbit/s with the aggregate data input to the control port of the UNI. The experimental setup is shown in a). MLFL: Mode-locked fiber laser. PPM: Pulse-position modulator. DPLL: Dithering phase-locked loop; MUX: OTDM passive multiplexer; PRBS: Pseudo-random binary sequence. In b), an illustration of the switch operation at 40 Gbit/s is provided. Each control pulse opens a switching window for the signal path. Only signal pulses that are coincident with a switching window pass to the output of the switch.

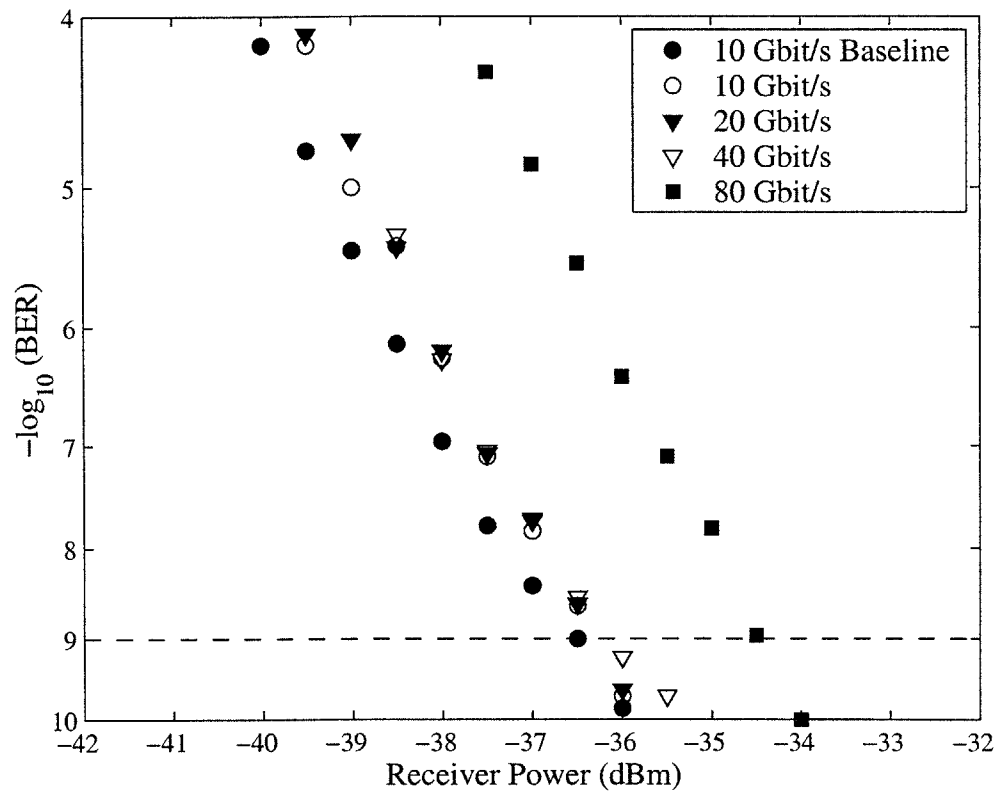


Figure 5-22: Bit-error-rate performance for demultiplexing from aggregate PPM data rates of 10, 20, 40, and 80 Gbit/s on control input to UNI.

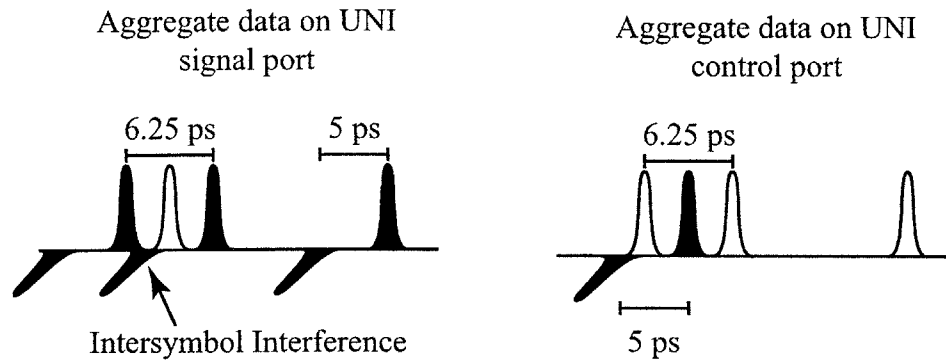


Figure 5-23: Origin of intersymbol interference in demultiplexing of 80-Gbit/s PPM data using a UNI with 5-ps signal pulse separation. The filled pulses represent the signal input to the UNI while the unfilled pulses represent the control input.

thought to be a result of the increased saturation of the SOA due to the high average power of the control pulses.

The large power penalty of 3 dB observed at 80 Gbit/s in Figure 5-20 when the aggregate data is on the signal input to the UNI, as shown in Figure 5-19 a), is due to ISI. This interference is a consequence of the PPM data format in the UNI as shown in Figure 5-23. ISI arises due to the fact that, as discussed in Chapter 3, signal pulses in the UNI are split by the birefringent fiber into orthogonally polarized pairs, temporally separated by 5 ps. Because of the PPM data format, pulses in the data stream may be separated by as little as 6.25 ps. Thus, adjacent pulse overlap may occur in the UNI leading to the observed ISI. This effect may be mitigated by reducing the length of birefringent fiber in the UNI, thereby reducing the temporal separation of the signal pulse pairs in the SOA. Note that this effect does not occur when demultiplexing is performed with the modulated data on the control input to the UNI. In this case, the PPM-modulated data pulses are not split in the UNI, so overlap between neighboring pulses is non-existent.

These two PPM demultiplexing demonstrations show that significant performance gain can be obtained by using a wavelength-converting demultiplexing configuration where the aggregate data is used as the control input to the ultrafast switch and a lower-rate clock is used as the signal input. This configuration also offers the

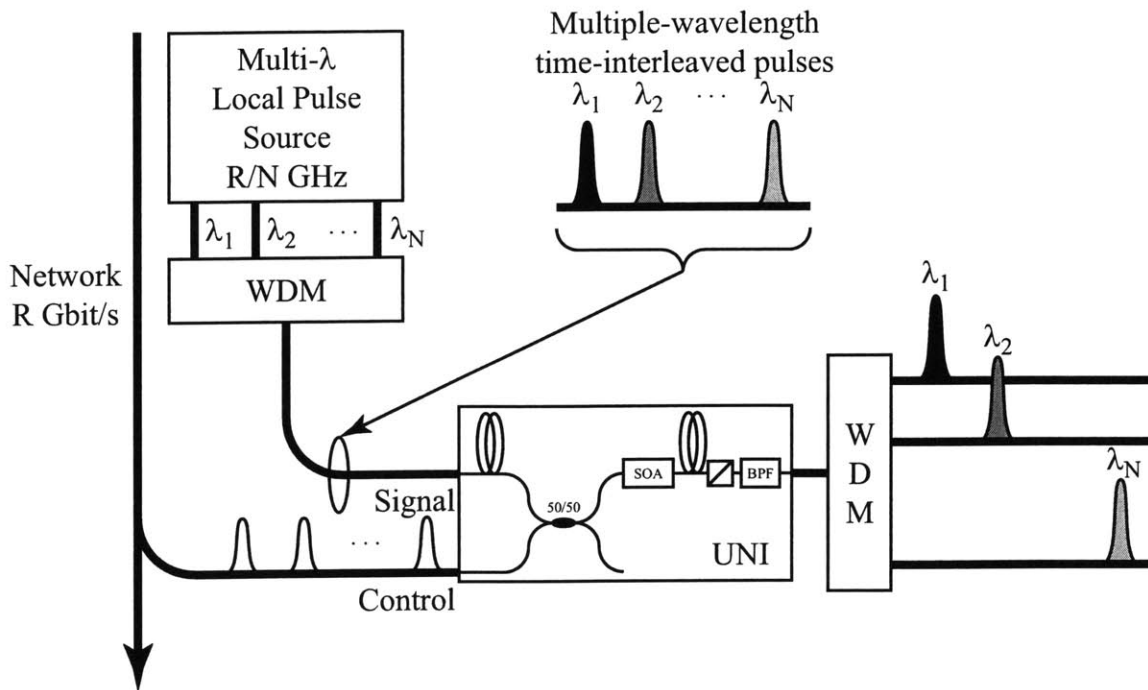


Figure 5-24: Schematic for slotted OTDM rate conversion utilizing multiple wavelength demultiplexing in a single UNI. WDM: Wavelength-division multiplexer.

possibility of simplifying the rate-conversion process by simultaneously demultiplexing multiple OTDM channels using a single all-optical demultiplexer together with standard wavelength-demultiplexing techniques. Figure 5-24 shows a schematic of a rate converter utilizing multiple-wavelength demultiplexing in a single UNI [5.42]. In this configuration, the local clock source generates N optical clocks with repetition rate R/N at N distinct wavelengths. These clocks are then combined and time-interleaved using a wavelength-division multiplexer (WDM). Several multiple-wavelength clock sources which may be useful in this application have been recently demonstrated [5.43, 5.44]. Alternatively, a chirped supercontinuum pulse may be used instead of N distinct clock pulses (see, for example [5.45]). This multiple-wavelength OTDM clock is used as the signal input to the UNI. The network data at the aggregate rate of R Gbit/s provides the control input to the UNI. The multiple-wavelength signal pulses are each aligned with a distinct sub-rate channel within the control data stream, similar to the serial-to-parallel rate conversion technique. The UNI then

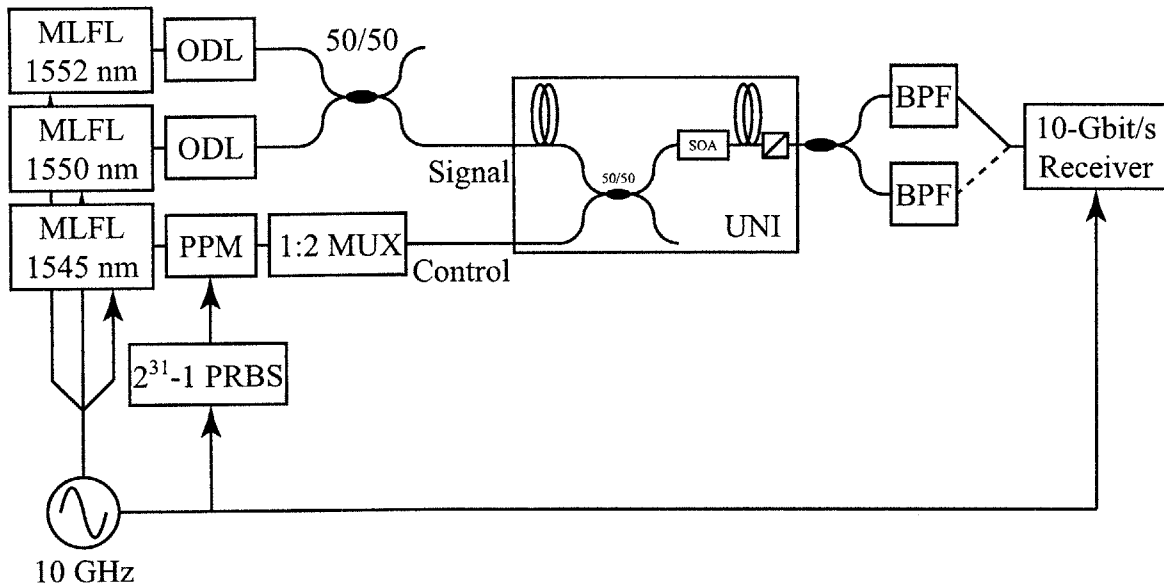


Figure 5-25: Schematic of experimental setup for multiple-wavelength demultiplexing of 20-Gbit/s aggregate data on control input of UNI. MLFL: Mode-locked fiber laser; PPM: Pulse-position modulator; ODL: Optical delay line; MUX: OTDM passive multiplexer; PRBS: Pseudo-random binary sequence.

acts as a wavelength converter, converting each channel of the control data into the wavelength of the overlapped signal pulse. The signal pulses are then separated at the output of the UNI using a second WDM to provide the N demultiplexed parallel channels.

Previously, multiple-channel demultiplexing has been demonstrated using cross-phase modulation-induced chirp compensation in fiber [5.46, 5.47] and four-wave mixing in fiber [5.45] and semiconductor optical amplifiers [5.48]. Multiple-channel interferometric demultiplexing has been limited to fiber-based switches such as the nonlinear loop mirror [5.49] due to the pattern-dependent gain saturation effects which degrade performance in SOA-based interferometers when the control input is modulated. However, SOA-based interferometers can have significant advantages over alternative demultiplexers in terms of size and required switching energies. Here, we report on multiple-channel demultiplexing experiments using the UNI [5.42].

Figure 5-25 shows a schematic of the experimental setup for multiple-wavelength

demultiplexing using the UNI. In this demonstration, an aggregate network data rate of 20 Gbit/s is demultiplexed into two 10-Gbit/s streams. The control pulse source is a mode-locked fiber laser producing a 10-GHz stream of 2-ps pulses at 1545 nm. These pulses are pulse-position modulated with a 10-Gbit/s pseudo-random bit sequence of length $2^{31} - 1$. The PPM delay in this experiment is 6.25 ps. We optically multiplex the modulated pulses to create a 20-Gbit/s OTDM data stream. Two additional mode-locked fiber lasers producing 10-GHz streams of 2-ps pulses at 1550 nm and 1552 nm provide the signal pulse sources. A 50/50 coupler combines the two streams of signal pulses. No clock recovery is performed in this experiment. Instead, a single 10 GHz synthesizer provides a frequency reference to each of the fiber lasers and the receiver. Optical time delays on the signal pulse sources are used to temporally interleave the two signal pulse streams and overlap the signal pulses with the corresponding control pulse streams. The UNI has a switching window duration of 5 ps. As in the previous experiment, since the switching window duration in the UNI is less than the PPM delay, the demultiplexer converts the data format from PPM to OOK. At the output of the UNI, the two signal wavelengths are separated using a 50/50 coupler together with two bandpass filters. These two outputs are then sent to a 10-Gbit/s optically preamplified OOK receiver for BER analysis.

Figure 5-26 shows the results of the BER tests for multiple wavelength operation. In each of these experiments, the individual signal powers at the input of the UNI are -5 dBm, corresponding to a pulse energy of 31 fJ. The control stream average power is 0 dBm, corresponding to a switching energy of 50 fJ. The baseline is measured using the OOK-formatted data at 1545 nm obtained from one arm of the PPM modulator. The unfilled points represent the BER performance of the switch when only a single wavelength is used for demultiplexing while the filled points show the BER performance when both signal wavelengths are used for simultaneous demultiplexing. The maximum observed power penalty for a BER of 10^{-9} was 1.5 dB. This is likely due to the increased saturation of the SOA in the multiple-wavelength experiment and the wavelength-sensitivity of the receiver.

Assuming that multiple-wavelength clock sources are available, the multiple chan-

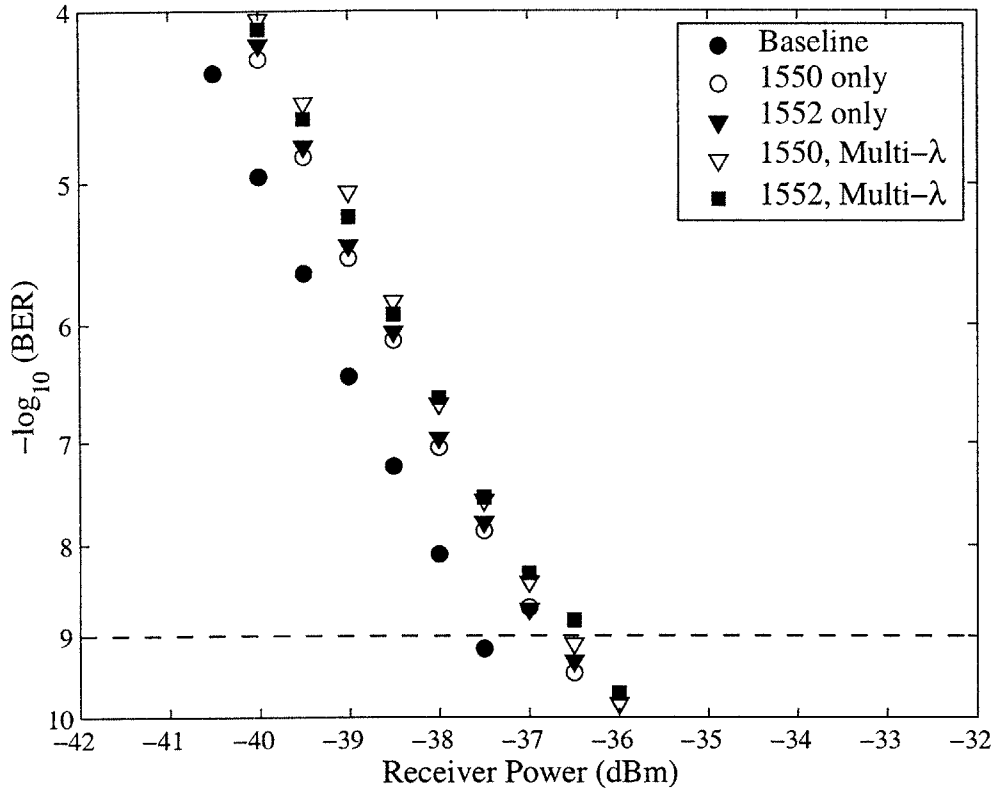


Figure 5-26: Bit-error rate test results at UNI output for multiple-wavelength demultiplexing of a 20-Gbit/s OTDM signal. The solid symbols represent single-wavelength operation and the open symbols represent multiple wavelength operation.

nel demultiplexing technique presented here can significantly reduce the complexity of a slotted OTDM rate converter. However, it is worth considering the spectral requirements of these multiple-channel demultiplexing techniques. Let R_O and R_E denote the optical and electronic processing rates (R_O is equal to the aggregate network data rate, R). The number of optical clock wavelengths required is $N = R_O/R_E$. Since each of the optical clock pulses must have a duration shorter than the bit-period at the aggregate network data rate, the bandwidth of each optical clock is proportional to $R_O = NR_E$. Thus, the total optical bandwidth required by the multiple wavelength optical clock is proportional to $N^2R_E = R_O^2/R_E$. If the electronic and optical processing rates scale at the same rate, then the required bandwidth for the multiple-wavelength demultiplexer is directly proportional to the optical processing

rate. However, in recent years, the optical data rate has been increasing at a rate much faster than the electronic processing rates. In this situation, the optical bandwidth of the multiple-wavelength demultiplexer increases at a rate proportional to the square of the optical data rate. Thus, this is not a very scalable solution at high optical data rates. In these cases, a hybrid combination of standard serial-to-parallel rate conversion together with multiple-wavelength demultiplexing would likely be employed for slotted OTDM rate conversion.

5.7 Conclusions

In summary, we have presented a functional optical interface for an ultrahigh-speed multi-access slotted OTDM network, such as HLAN. We have demonstrated network operation at aggregate media rates as high as 112.5 Gbit/s. Simplified head-end and transmitter designs have been used to simulate fully-loaded slots on the network and fully test receiver operation. In the receiver, we have demonstrated the essential functions of synchronization, optical header processing, and optical rate conversion using as few as three semiconductor-based optical logic gates. The synchronization technique that we have employed is resistant to transmission impairments such as group velocity dispersion and polarization-mode dispersion. While we have used fixed-length slots in this work, the slot-synchronization technique can also be used in a network with variable length packets. We have also demonstrated a novel optical address comparison technique. We have demonstrated XOR logic functionality for address comparison using a single optical AND gate with a PPM-formatted optical header. The use of the PPM data format also reduces patterning effects in SOA-based switches and makes possible a unique wavelength-converting demultiplexing operation where the aggregate data stream is used as the control input to the optical switch. We have demonstrated demultiplexing in this manner at aggregate rates up to 80 Gbit/s. With this configuration, multiple wavelengths can be used to simultaneously demultiplex the aggregate data rate signal into several lower rate signals using a single optical switch. We have demonstrated simultaneous demultiplexing of a 20-Gbit/s

aggregate signal into two 10-Gbit/s signals using this technique.

It should be noted that the receiver design presented here is largely insensitive to the polarization of the incoming network data. The semiconductor optical amplifiers used in the UNI data processors in the receiver are bulk active region devices. Lattice strain in the active region is used to achieve approximately equal gain for both TE and TM modes. Less than 1-dB polarization sensitivity was observed in the devices used in these experiments. Consequently, the operation of the UNI devices is fairly insensitive to the polarization of the control input. The network data is used as the control input for both the slot-synchronization and the address-comparison UNIs. As we have shown, the use of the PPM data format also allows the network data to be used as the control input to the rate-conversion UNI, making the entire optical front-end insensitive to the incoming network signal polarization. The UNI is sensitive to the polarization of the signal input. This polarization must be aligned at 45 degrees relative to the birefringent axes of the polarization maintaining fiber at the input to the UNI. However, since the signal inputs to the UNI devices in the receiver are all generated locally, their polarization can be easily controlled within the receiver using polarization maintaining fiber.

Finally, we note that the network architecture presented in this work is readily scalable, both in number of users and data rate. The address-processing scheme that we have demonstrated enables maximum efficiency in address coding, providing 2^N possible addresses with N address bits. Moreover, the number of logic gates required for address comparison scales efficiently as $\log_2 N$. This sub-linear scaling is especially well-suited for all-optical header processing since technology for integration of multiple optical logic gates is only beginning to develop. Of course, scaling the number of users on the network also requires increases in available network bandwidth in order to satisfy peak demands. We have presented experimental demonstrations at media rates as high as 112.5 Gbit/s. However, much higher rates are possible with this network design. The optical front-end design that we have presented ensures that required electronic serial data rates in the receiver are limited to 12.5 Gbit/s for buffering of rate-converted data and several hundred Mbit/s for MAC protocol

implementation. Thus, peak network media rates are only limited by the optical switching technology. Using the UNI switching technology presented in this work, we have experimentally observed switching windows with durations as short as 2.5 ps. This should enable network operation at aggregate rates as high as 200 Gbit/s. Scaling to higher rates will require optical pulses shorter than than the 2-ps pulses used here.

References

- [5.1] S. Bigo, Y. Fignac, G. Charlet, W. Idler, S. Borne, H. Gross, R. Dischler, W. Poehlmann, P. Trann, C. Simonneau, D. Bayart, G. Veith, A. Jourdan, and J. P. Hamaide, "10.2 Tbit/s (256x42.7 Gbit/s PDM/WDM) transmission over 100 km TeraLight fiber with 1.28 bit/s/Hz spectral efficiency," in *Conference on Optical Fiber Communication*, pp. PD25-1-3, 2001.
- [5.2] K. Fukuchi, T. Kasamatsu, M. Morie, R. Ohhira, T. Ito, K. Sekiya, D. Ogasahara, and T. Ono, "10.92 Tb/s (273 x 40 Gb/s) triple-band/ultra-dense WDM optical repeatered transmission experiment," in *Conference on Optical Fiber Communication*, pp. PD24-1-3, 2001.
- [5.3] M. Nakazawa, T. Yamamoto, and K. R. Tamura, "1.28 Tbit/s-70 km OTDM transmission using third- and fourth-order simultaneous dispersion compensation with a phase modulator," *Electron. Lett.*, vol. 36, pp. 2027-9, November 2000.
- [5.4] "Fiber optic network capacity and utilization." White paper, Telecommunications Industry Association, September 2002.
- [5.5] R. A. Barry, V. W. S. Chan, K. L. Hall, E. S. Kintzer, J. D. Moores, K. A. Rauschenbach, E. A. Swanson, L. E. Adams, C. R. Doerr, S. G. Finn, H. A. Haus, E. P. Ippen, W. S. Wong, and M. Haner, "All-optical network consortium- ultrafast TDM networks," *IEEE J. Sel. Areas Commun.*, vol. 14, pp. 999-1013, June 1996.
- [5.6] A. Hasegawa and H. Toda, "A feasible all optical soliton based inter-LAN network using time division multiplexing," *IEICE Trans. Commun.*, vol. E81-B, pp. 1681-5, August 1998.
- [5.7] V. W. S. Chan, K. L. Hall, E. Modiano, and K. A. Rauschenbach, "Architectures and technologies for high-speed optical data networks," *IEEE J. Lightwave Technol.*, vol. 16, pp. 2146-68, December 1998.
- [5.8] D. Bertsekas and R. Gallager, *Data Networks*. Prentice Hall, 2nd ed., 1992.

- [5.9] S. G. Finn, "HLAN— an architecture for optical multi-access networks," in *IEEE/LEOS 1995 Summer Topical Meetings*, pp. 45–6, 1995.
- [5.10] J. D. Moores, J. Korn, K. L. Hall, S. G. Finn, and K. A. Rauschenbach, "Ultrafast optical TDM networking: extension to the wide area," *IEICE Trans. Commun.*, vol. E82-B, pp. 209–21, February 1999.
- [5.11] S. A. Hamilton, B. S. Robinson, J. D. Moores, F. Hakimi, and P. A. Schulz, "Ultrafast synchronous all-optical time division multiplexing system demonstration," in *Optical Fiber Communication Conference*, pp. WO4–1–3, 2001.
- [5.12] S. A. Hamilton and B. S. Robinson, "40-Gb/s all-optical packet synchronization and address comparison for OTDM networks," *IEEE Photon. Technol. Lett.*, vol. 14, pp. 209–11, February 2002.
- [5.13] S. A. Hamilton and B. S. Robinson, "100 Gbit/s synchronous all-optical time-division multiplexing multi-access network testbed," in *Optical Fiber Communication Conference*, pp. 602–5, 2002.
- [5.14] S. A. Hamilton, B. S. Robinson, T. E. Murphy, S. J. Savage, and E. P. Ippen, "100 Gb/s optical time-division multiplexed networks," *IEEE J. Lightwave Technol.*, vol. 20, December 2002.
- [5.15] K. L. Deng, K. I. Kang, I. Glesk, P. R. Prucnal, and S. Shin, "Optical packet compressor for ultrafast packet-switched optical networks," *Electron. Lett.*, vol. 33, pp. 1237–8, July 1997.
- [5.16] H. Toda, F. Nakada, M. Suzuki, and A. Hasegawa, "An optical packet compressor based on a fiber delay loop," *IEEE Photon. Technol. Lett.*, vol. 12, pp. 708–10, June 2000.
- [5.17] K. Suzuki, K. Iwatsuki, S. Nishi, M. Saruwatari, and T. Kitoh, "160 Gb/s sub-picosecond transform-limited pulse signal generation utilizing adiabatic soliton compression and optical time-division multiplexing," *IEEE Photon. Technol. Lett.*, vol. 6, pp. 352–4, March 1994.
- [5.18] H. Takara, S. Kawanishi, T. Morioka, K. Mori, and M. Saruwatari, "100 Gbit/s optical waveform measurement with 0.6 ps resolution optical sampling using subpicosecond supercontinuum pulses," *Electron. Lett.*, vol. 30, pp. 1152–3, July 1994.
- [5.19] M. Shabeer, J. K. Lucek, K. Smith, and D. Cotter, "Self-synchronisation scheme for high-speed photonic networks," *Electron. Lett.*, vol. 31, pp. 1476–8, August 1995.
- [5.20] M. C. Cardakli and A. E. Willner, "Synchronization of a network element for optical packet switching using optical correlators and wavelength shifting," *IEEE Photon. Technol. Lett.*, vol. 14, pp. 1375–7, September 2002.

- [5.21] D. Cotter, J. K. Lucek, M. Shabeer, K. Smith, D. C. Rogers, D. Nesses, and P. Gunning, "Self-routing of 100 Gbit/s packets using 6 bit 'keyword' address recognition," *Electron. Lett.*, vol. 31, pp. 2201–2, December 1995.
- [5.22] I. Glesk, J. P. Solokoff, and P. R. Prucnal, "All-optical address recognition and self-routing in a 250 Gbit/s packet-switched network," *Electron. Lett.*, vol. 30, pp. 1322–3, August 1994.
- [5.23] Y. H. Kao, Y. Liang, T. J. Xia, K. H. Ahn, J. W. Lou, G. A. Nowak, O. Boyraz, and M. N. Islam, "Self-synchronization of 100-Gbit/s TDM packets using a semiconductor optical amplifier and an intensity discriminator," in *Conference on Lasers and Electro-Optics*, p. CFB6, 1998.
- [5.24] H. J. Lee, H. G. Kim, J. Y. Choi, and K. Kim, "A simple packet-level clock extraction scheme using a terahertz optical asymmetric demultiplexer," *IEEE Photon. Technol. Lett.*, vol. 11, pp. 1310–2, October 1999.
- [5.25] S. A. Hamilton and B. S. Robinson, "OTDM packet networking devices at 100 Gbit/s and beyond," in *IEEE/LEOS 2002 Summer Topical Meeting*, pp. 19–20, 2002.
- [5.26] D. Cotter and S. C. Cotter, "Algorithm for binary word recognition suited to ultrafast nonlinear optics," *Electron. Lett.*, vol. 29, pp. 945–7, May 1993.
- [5.27] S. Bernstein, "Codes for TDMA 'keyword' address recognition." Lincoln Laboratory Internal Memorandum, March 2000.
- [5.28] K. L. Hall and K. A. Rauschenbach, "All-optical bit pattern generation and matching," *Electron. Lett.*, vol. 32, pp. 1214–5, June 1996.
- [5.29] X. D. Cao, M. Jiang, K. H. Ahn, Y. Liang, B. C. Barnett, and M. N. Islam, "High-speed header processing using synchronized fiber lasers driving all-optic logic gates," in *IEEE/LEOS 1996 Summer Topical Meetings*, pp. 18–9, 1996.
- [5.30] T. J. Xia, Y. Liang, K. H. Ahn, J. W. Lou, O. Boyraz, Y. H. Kao, X. D. Cao, S. Chaikamnerd, J. K. Andersen, and M. N. Islam, "All-optical packet-drop demonstration using 100-Gb/s words by integrating fiber-based components," *IEEE Photon. Technol. Lett.*, vol. 10, pp. 153–5, January 1998.
- [5.31] B. S. Robinson, S. A. Hamilton, S. J. Savage, and E. P. Ippen, "40 Gbit/s all-optical XOR using a fiber-based folded ultrafast nonlinear interferometer," in *Optical Fiber Communication Conference*, pp. 561–2, 2002.
- [5.32] A. J. Poustie, K. J. Blow, R. J. Manning, and A. E. Kelly, "All-optical pseudorandom number generator," *Opt. Commun.*, vol. 159, pp. 208–14, 1999.
- [5.33] T. Fjelde, D. Wolfson, A. Kloch, B. Dagens, A. Coquelin, I. Guillemot, F. Gaborit, F. Poingt, and M. Renaud, "Demonstration of 20 Gbit/s all-optical logic XOR in integrated SOA-based interferometric wavelength convertor," *Electron. Lett.*, vol. 36, pp. 1863–4, October 2000.

- [5.34] C. Bintjas, M. Kalyvas, G. Theophilopoulos, T. Stathopoulos, H. Avramopoulos, L. Occhi, L. Scares, G. Guekos, S. Hansmann, and R. Dall'ara, "20 Gb/s all-optical XOR with UNI gate," *IEEE Photon. Technol. Lett.*, vol. 12, pp. 834–6, July 2000.
- [5.35] H. Chen, G. Zhu, Q. Wang, J. Jaques, J. Leuthold, A. B. Piccirilli, and N. K. Dutta, "All-optical logic XOR using differential scheme and Mach-zehnder interferometer," *Electron. Lett.*, vol. 38, pp. 1271–3, October 2002.
- [5.36] P. J. Winzer and A. Kalmar, "Sensitivity enhancement of optical receivers by impulsive coding," *IEEE J. Lightwave Technol.*, vol. 17, pp. 171–7, February 1999.
- [5.37] M. Pauer, P. J. Winzer, and W. R. Leeb, "Bit error probability reduction in direct detection optical receivers using RZ coding," *IEEE J. Lightwave Technol.*, vol. 19, pp. 1255–62, September 2001.
- [5.38] N. S. Patel, K. L. Hall, J. D. Moores, K. A. Rauschenbach, and B. S. Robinson, "All-optical rate conversion," in *Optical Fiber Communication Conference*, pp. 87–8, 1997.
- [5.39] N. S. Patel, K. L. Hall, and K. A. Rauschenbach, "Optical rate conversion for high-speed TDM networks," *IEEE Photon. Technol. Lett.*, vol. 9, pp. 1277–9, September 1997.
- [5.40] B. S. Robinson, S. A. Hamilton, and E. P. Ippen, "Demultiplexing of 80-Gbit/s pulse-position modulated data with an ultrafast nonlinear interferometer," *IEEE Photon. Technol. Lett.*, vol. 14, pp. 206–8, February 2002.
- [5.41] B. S. Robinson, S. A. Hamilton, and E. P. Ippen, "Demultiplexing of 80 Gbit/s pulse-position modulated data with an ultrafast nonlinear interferometer," in *Optical Fiber Communication Conference*, pp. WO4–1–3, 2001.
- [5.42] B. S. Robinson, S. A. Hamilton, and E. P. Ippen, "Multiple wavelength demultiplexing using an ultrafast nonlinear interferometer," in *Conference on Lasers and Electro-Optics*, p. 528, 2001.
- [5.43] J. W. Lou, T. F. Carruthers, and M. Currie, "Mode-locked multiple-wavelength erbium-doped fiber laser in a sigma configuration," *IEEE Photon. Technol. Lett.*, vol. 14, pp. 281–3, March 2002.
- [5.44] K. L. Lee, C. Shu, and H. F. Liu, "10 Gsample/s photonic analog-to-digital converter constructed using 10-wavelength jitter-suppressed sampling pulses from a self-seeded laser diode," in *Conference on Lasers and Electro-Optics*, pp. 67–8, 2001.
- [5.45] T. Morioka, S. Kawanishi, H. Takara, and M. Saruwatari, "Multiple-output, 100 Gbit/s all-optical demultiplexer based on multichannel four-wave mixing

pumped by a linearly chirped pulse,” *Electron. Lett.*, vol. 30, pp. 1959–60, November 1994.

- [5.46] K. Uchiyama, S. Kawanishi, and M. Saruwatari, “Multiple channel output all-optical OTDM demultiplexer using XPM-induced chirp compensation (MOXIC),” *Electron. Lett.*, vol. 34, pp. 575–6, March 1998.
- [5.47] K. Uchiyama, H. Takara, K. Mori, and T. Morioka, “160 Gbit/s all-optical time-division demultiplexing utilising modified multiple-output OTDM demultiplexer (MOXIC),” *Electron. Lett.*, vol. 38, pp. 1190–1, September 2002.
- [5.48] K. Uchiyama, S. Kawanishi, and M. Saruwatari, “100-Gb/s multiple-channel output all-optical OTDM demultiplexing using multichannel four-wave mixing in a semiconductor optical amplifier,” *IEEE Photon. Technol. Lett.*, vol. 10, pp. 890–2, June 1998.
- [5.49] K. Uchiyama, H. Takara, T. Morioka, S. Kawanishi, and M. Saruwatari, “100 Gbit/s multiple-channel output all-optical demultiplexing based on TDM-WDM conversion in a nonlinear optical loop mirror,” *Electron. Lett.*, vol. 32, pp. 1989–91, October 1996.

Chapter 6

Conclusion

The primary goal of the work presented in this dissertation was to investigate the utility of semiconductor-based all-optical switching for applications in future slotted optical networks operating at data rates which exceed electronic processing speeds. Our comprehensive study began with the development of a detailed model of the saturation dynamics in a semiconductor optical amplifier (SOA) and progressed through the demonstration of a fully functional optical front-end for a receiver in a slotted optical time-division multiplexed (OTDM) network. In this chapter, we review the primary contributions of this work. We conclude with a brief discussion of a few of the possible applications for semiconductor-based all-optical switches in future packet-switched optical networks.

6.1 Summary of Contributions

We have developed a detailed numerical model for the dynamic gain and index saturation in an SOA for the purpose of evaluating the performance of SOA-based all-optical switches. In order to assess the effects of counterpropagating pulses in an optical switch, we carefully model the longitudinal saturation effects in the SOA. The model includes an accurate description of the dynamics of the carrier distributions in the conduction and valence bands in the semiconductor. In contrast to many of the dynamic SOA models which have been previously reported, the model developed in this

work does not attempt to describe these dynamics in terms of statistical parameters, such as the carrier temperatures in the bands. Rather, the dynamic state of the SOA is represented using physical parameters such as the carrier density and the carrier energy densities in the bands. We present a technique for inverting the Fermi-Dirac integrals which describe the carrier density and the carrier energy density to obtain the quasi-Fermi energies and carrier temperatures for the bands. These statistical parameters can then be used to evaluate the SOA gain and refractive index. Such a description provides an accurate model of the frequency-dependent effects of carrier density saturation and carrier heating in the SOA. This is particularly important for optical switching applications where the various optical signals in the switch may have different carrier wavelengths. We have validated the qualitative accuracy of this model by performing a high repetition rate pump-probe analysis on a commercial SOA.

We have described various techniques for utilizing semiconductor optical amplifiers to construct interferometric optical switches. Balanced interferometers may be used to mitigate the effects of long-lived refractive index changes in the SOA, enabling switching at rates which exceed the recovery rate for carrier density changes in the SOA. We have presented three semiconductor-based balanced fiber interferometers which are commonly used for ultrafast all-optical switching. These switches differ primarily in the relative directions of propagation for the signal and control pulses. We have used our SOA model to evaluate the switching dynamics of these different interferometer configurations. The fastest switching speeds are obtained using a co-propagating geometry, such as the ultrafast nonlinear interferometer (UNI), where the speed of the switching transients is determined primarily by the duration of the control pulses. With the 2-ps optical pulses used in this work, switching windows as short as 4.5 ps have been observed, enabling demultiplexing from aggregate data rates as high as 200 Gbit/s. We have also investigated the performance of different interferometer configurations for demultiplexing of 100-Gbit/s OTDM data streams.

The gain saturation dynamics of the semiconductor optical amplifier present the greatest challenge to their wide application in optical networks. Changes in gain

caused by fluctuations in the carrier density require several hundred picoseconds to recover to their unsaturated state. This leads to pattern-dependent gain saturation for intensity-modulated signals at data rates in excess of ~ 1 Gbit/s. We have developed a statistical model based on Markov chains to evaluate the effect of pattern-dependent gain saturation on the performance of an optical transmission system. The effects of gain saturation are strongly dependent on signal characteristics such as data rate and average power. In general, only small penalties are incurred if the transmitter extinction ratio is infinite. A finite transmitter extinction ratio, however, leads to significant power penalties when the signal bit period is comparable to the carrier lifetime in the SOA.

We have proposed the use of pulse-position modulation (PPM) as a signal format for high data rate OTDM networks. With PPM, the variation in the signal energy over a time period comparable to the SOA lifetime is small. Thus, the effects of gain saturation are greatly reduced with the PPM data format. The PPM data format can also be time-division multiplexed to high data rates. We have demonstrated straightforward techniques for creating binary PPM signals at OTDM data rates as high as 112.5 Gbit/s. All-optical switching of PPM signals using intensity-dependent nonlinearities in an SOA is also possible. We have demonstrated all-optical wavelength conversion of PPM signals at 12.5 Gbit/s as well as all-optical demultiplexing of PPM signals from aggregate data rates as high as 80 Gbit/s. While the use of PPM reduces the bandwidth efficiency of an optical transmission system, this small penalty may be outweighed by its potential benefits in terms of system performance and its ability to enable the use of semiconductor optical amplifiers for a variety of novel all-optical processing applications.

Finally, we have demonstrated the use of SOA-based switches in providing essential optical processing for a scalable slotted OTDM network based on the helical local area network architecture. We have implemented reduced functionality head-end and transmitter nodes and a fully functional receiver node operating at data rates as high as 112.5 Gbit/s. The use of PPM as the network data format provides enhanced functionality in the receiver node. In particular, we have demonstrated all-optical

XOR functionality for address comparison using an ultrafast optical AND gate with PPM data inputs. Moreover, we have demonstrated novel techniques techniques for demultiplexing and format conversion of PPM data, including a multiple-wavelength demultiplexing configuration which could be used for low-latency all-optical data rate conversion in a receiver node.

6.2 Optical Packet Switching

The 100-Gbit/s HLAN networking technologies developed in this work are primarily applicable to local area networks which have a small to moderate number of closely located users. HLAN is a broadcast-and-select network where all of the transceivers are interconnected via a single fiber bus. This type of network does not scale well to large user populations, since all of the traffic must processed by all of the nodes. Moreover, the helical bus may be impractical to implement for user populations which are spread over large geographic areas. Networks which serve these types of populations are usually “switched” networks where all of the nodes are not simultaneously connected. In a switched network, connections between particular nodes are only constructed as they become needed, leading to more efficient utilization of the network resources.

Modern networks are primarily constructed of point-to-point optical transmission links. Switching services are provided in electronics, before and after optical transmission. New systems being deployed utilize circuit switching of wavelengths for bandwidth provisioning in a WDM network. These systems provide many improvements over static point-to-point links. However, the granularity of the bandwidth provisioning in these networks is limited to the capacity of a single wavelength channel (e.g. 10-40 Gbit/s). Additionally, the time required for bandwidth provisioning in these networks (i.e. the time required to establish a new connection between nodes) is long compared to typical packet durations on the channels. Thus, packet-routing data services are still provided in electronics. Electronic routers do not scale in capacity as readily as WDM transmission systems. Consequently, in future optical networks,

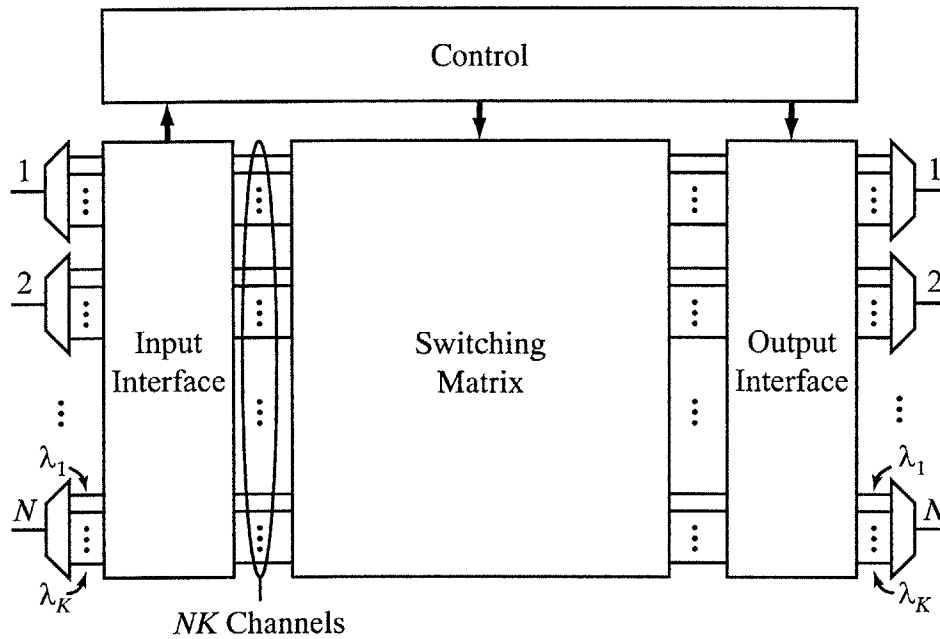


Figure 6-1: Schematic of a generalized optical packet switch.

packet-routing services may be provided in the optical domain [6.1]. Many of the switching techniques studied in this work may be useful in enabling optical packet routing.

Figure 6-1 shows a schematic of a generalized optical packet switch for a wavelength division multiplexed network. N fibers, each of which carries K wavelengths, enter and exit the switch. The switch consists of four primary functional blocks: the input interface, the control unit, the switching matrix, and the output interface. The input interface provides synchronization and buffering of the incoming data packets. The control unit processes the headers of the incoming packets in order to provide control signals to the switch matrix. The switch matrix forwards the packets to the desired destination port. The output interface prepares the packets for transmission to the next node, possibly replacing the optical header and/or providing optical signal regeneration.

Many different architectures have been proposed for the implementation of an all-optical packet switch (e.g. [6.1–6.3]). These architectures, while often providing transparent routing of packet payloads, are typically designed to operate at WDM

channel rates which are limited to electronic processing speeds. The immediate benefit of using a slotted OTDM network architecture capable of operating at data rates which exceed electronic processing speeds becomes clear when the scalability of such a packet switch is considered. For example, in the packet switch shown in Figure 6-1, the switching matrix must be able to route packets from the $N \cdot K$ inputs to any permutation of the $N \cdot K$ outputs (assuming that the switching matrix is non-blocking). Thus, the switching matrix must have at least $(N \cdot K)!$ states. If the switching matrix is constructed using 2x2 unit cells, each switching cell has 2 possible states. Thus, the minimum number of unit cells required to construct a matrix with $(N \cdot K)!$ states is

$$\begin{aligned} N_{2 \times 2} &= \log_2(N \cdot K)! \\ &\approx (N \cdot K) \log_2(N \cdot K) - \frac{N \cdot K}{\ln 2}, \end{aligned} \tag{6.1}$$

where the approximation is obtained using Stirling's approximation and is valid for large $(N \cdot K)$. For a fixed transmission capacity per fiber, the number of wavelengths on each fiber, K , is inversely proportional to the channel data rate. Considering the first term on the right hand side of equation 6.1, we find that increasing the data rate by a factor of M reduces the number of required switching elements by a factor of $M/(1 - \log_2 M / \log_2(N \cdot K))$. For example, in a switch with 8 input and output fibers, if the electronics data rate is 10 Gbit/s and the total transmission capacity on each fiber is 1 Tbit/s (100 channels), operating at an optical data rate of 100 Gbit/s reduces the number of required switching elements by a factor of 20 compared to operating the switch with electronic-rate channels. Note that the number of unit cells required by Equation 6.1 is a necessary condition for constructing such the switching matrix. It is not necessarily sufficient. In fact, the scaling of non-blocking switch matrix architectures is often much worse than what is predicted by Equation 6.1, making the necessity of operating at high channel rates even more apparent.

The optical processing technologies we have developed in this work have many possible applications in an optical packet switch operating with channel data rates

in excess of 100 Gbit/s [6.4]. For example, the optical address processing techniques using the UNI which were described in Chapter 5 may be utilized to process optical addresses at the aggregate channel data rate. Some justification for encoding addresses at the aggregate data rate is required. Since the amount of information contained in the optical header is small compared to the payload, this information can potentially be encoded at a lower data rate (e.g. [6.1, 6.5]), enabling cost-effective electronic processing of the headers. However, there are several drawbacks to implementing the optical headers in this manner. There is a higher latency associated with reading the header at the slower data rate. This can slow header processing times, requiring optical buffering of the packets. If the slower data rate header is implemented serially, the system efficiency is reduced due to the overhead associated with the header transmission time. Encoding the headers serially at the line rate reduces the latency in reading the headers, leading to potentially faster switching and better utilization of network resources. For channel rates of 100 Gbit/s, optical processing of the header is required. For the HLAN receiver implementation described in Chapter 5, optical logic was used to compare an optical address on an incoming slot with a local address. Similar optical processing techniques may be used to determine control signals for forwarding slots through an optical switch matrix with a Banyan configuration [6.4].

SOA-based optical switching may also be useful in implementing the switch matrix in an optical packet switch. In Chapter 3, we described how the UNI may be used as a cross-bar switch. Cross-bar switches using an alternate configuration of the UNI have recently been demonstrated [6.6]. These switches can switch between the cross and bar states on a bit-by-bit basis at data rates in excess of 100 Gbit/s. Typically, a unit-cell in a packet switching matrix is only required to switch between states on time-scales comparable to the packet durations in the network. However, the ability to switch between states at the bit rate enables new switching functionality. For example, an ultrafast cross-bar switch can be operated in 4 possible states, providing a “speed-up” in the switch matrix, as shown in Figure 6-2. This speed-up may be used to resolve contention and reduce complexity in the switch matrix, po-

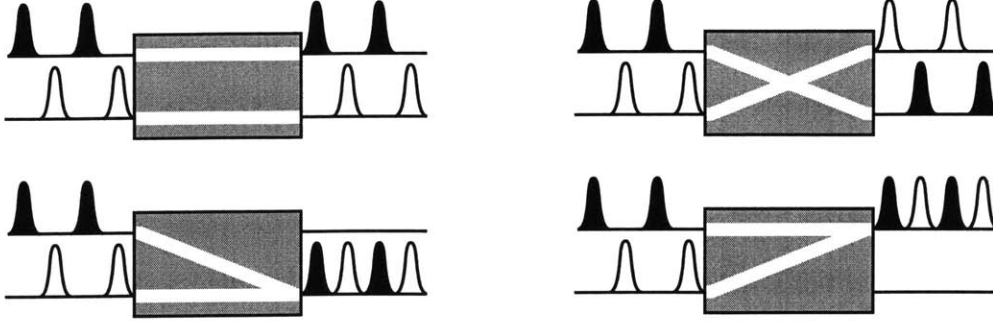


Figure 6-2: Four operational states of an ultrafast cross-bar switch.

tentially increasing scalability and reducing optical buffer requirements in the switch.

The input interface is, perhaps, the most technically challenging component to implement in an optical packet switch. The input interface must synchronize the incoming packets to the local clock and, possibly, buffer incoming packets to prevent packet loss due to contention at the output ports. Both of these tasks are difficult due to the lack of an optical equivalent to electronic random access memory. Most often, buffering and synchronization of optical packets are accomplished using an optical delay line, such as a length of fiber. Variable delays with durations on the order of the packet length can be achieved using a cascade of optical switches connected via logarithmically decreasing fiber delays [6.7, 6.8]. Variable delays on the order of a bit-period can be achieved using mechanical delays [6.9, 6.10], wavelength-dependent propagation delays in a dispersive medium [6.11], or optical modulators [6.12]. A technique for utilizing phase delays in an optical carrier to produce envelope delays in a modulated signal has also been recently demonstrated [6.13].

In Chapter 5, we demonstrated the use of the UNI as an all-optical phase detector which can be used in an electro-optic feedback loop to synchronize a local optical clock to the clock for an incoming packet. This synchronization technique is useful in broadcast-and-select networks where all packets are transmitted on a common bus and transceiver nodes need only synchronize to a single incoming clock. By contrast, an optical packet switch must simultaneously synchronize packets on many

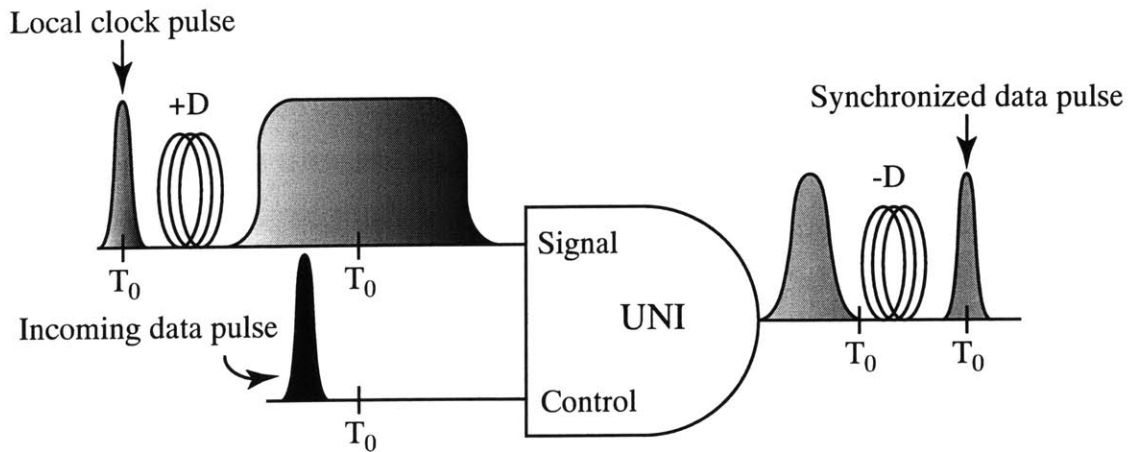


Figure 6-3: All-optical synchronization with an ultrafast nonlinear interferometer.

incoming channels. Optical gates, such as the UNI, may be used to provide bit-level synchronization for an incoming packet. One method for accomplishing this synchronization is shown in Figure 6-3. In this configuration, the optical gate is used to retim the incoming data pulses relative to the locally-generated clock pulses. The local clock pulse is chirped in a positive dispersion medium and input to the signal port of the UNI. This chirped pulse is gated by the incoming data pulse which is input to the UNI control port. Thus, the portion of the local clock pulse spectrum which propagates to the UNI output is determined by the relative timing between the local clock pulse and the incoming data pulse. At the output of UNI the gated pulse is retimed to the center of the local clock pulse period via propagation in a negative dispersion medium. In this manner, incoming data pulses are all-optically synchronized to a locally generated clock.

These examples are but a few of the many possible applications of semiconductor-based all-optical switching technologies in future packet-switched optical networks.

References

- [6.1] G. Guillemot, M. Redaud, P. Gambini, C. Janz, I. Andonovic, R. Bauknecht, B. Bostica, M. Burzio, F. Callegati, M. Casoni, D. Chiaroni, F. Clèrot, S. L. Danielsen, F. Dorgeuille, A. Dupas, A. Franzen, P. B. Hansen, D. K. Hunter, A. Kloch, R. Krähenbühl, B. Lavigne, A. L. Corre, C. Raffaelli, M. Schilling, J. C. Simon, and L. Zucchelli, "Transparent optical packet switching: The European ACTS KEOPS project approach," *J. Lightwave Technol.*, vol. 16, pp. 2117–34, December 1998.
- [6.2] J. Gripp, M. Duell, J. Simsarian, S. Chandrasekhar, P. Bernasconi, A. Bhardwaj, Y. Su, K. Sherman, L. Buhl, E. Laskowski, M. Cappuzzo, L. Stulz, M. Zirngibl, O. Laznicka, T. Link, R. Seitz, P. Mayer, and M. Berger, "Demonstration of a 1.2 Tb/s optical packet switch fabric (32×40 Gb/s) based on 40 Gb/s burst-mode clock-data recovery, fast tunable lasers, and a high-performance NxN AWG," in *Proc. 27th ECOC'01*, October 2001.
- [6.3] A. Carena, M. D. Vaughn, R. Gaudino, M. Shell, and D. J. Blumenthal, "OPERA: An optical packet experimental routing architecture with label swapping capability," *J. Lightwave Technol.*, vol. 16, pp. 2135–45, December 1998.
- [6.4] S. A. Hamilton and B. S. Robinson, "OTDM packet networking devices at 100 Gbit/s and beyond," *IEEE LEOS Newsletter*, vol. 16, pp. 33–5, October 2002.
- [6.5] A. E. Willner, "Implementing subcarrier-based control in optical networking," in *International Microwave Symposium (MTT 2002)*, vol. 3, pp. 1697–90, 2002.
- [6.6] G. Theophilopoulos, M. Kalyvas, C. Bintjas, N. Pleros, K. Yiannopoulos, A. Stavdas, H. Avramopoulos, and G. Guekos, "Optically addressable 2×2 exchange/bypass packet switch," *IEEE J. Lightwave Technol.*, vol. 14, pp. 998–1000, July 2002.
- [6.7] D. K. Hunter, W. D. Cornwell, T. H. Gilfedder, A. Franzen, and I. Andonovic, "SLOB: A switch with large optical buffers for packet switching," *J. Lightwave Technol.*, vol. 16, pp. 1725–36, October 1998.
- [6.8] D. K. Hunter, D. Cotter, R. B. Ahmad, W. D. Cornwell, T. H. Gilfedder, P. J. Legg, and I. Andonovic, "Buffered switch fabrics for traffic routing, merging and shaping in photonic cell networks," *J. Lightwave Technol.*, vol. 15, pp. 86–101, January 1997.
- [6.9] P. Klovenkorn and J. Munch, "Variable optical delay line with diffraction-limited autoalignment," *Appl. Opt.*, vol. 37, no. 10, pp. 1903–4, 1998.
- [6.10] K. T. Cornett, P. M. Hagelin, J. P. Heritage, O. Solgaard, and M. Everett, "Miniature variable optical delay using silicon micromachined scanning mirrors," in *Conference on Lasers and Electro-Optics*, pp. 383–4, 2000.

- [6.11] P. Blixt and J. E. Bowers, "An optical technique for bit and packet synchronization," *IEEE Photon. Technol. Lett.*, vol. 7, pp. 123–5, January 1995.
- [6.12] B. C. Wang, I. Glesk, R. J. Runser, and P. R. Prucnal, "Fast tunable parallel optical delay line," *Optics Express*, vol. 8, pp. 599–604, May 2001.
- [6.13] K. L. Hall, D. T. Moriarty, H. Hakimi, F. Hakimi, B. S. Robinson, and K. A. Rauschenbach, "An ultrafast variable optical delay technique," *IEEE Photon. Technol. Lett.*, vol. 12, pp. 208–10, February 2000.

Appendix A

Pulse Propagation in an Active Semiconductor Waveguide

In this section, we develop a traveling wave equation which can be used to describe the propagation of a short optical pulse in a semiconductor waveguide. Optical fields propagating in a semiconductor are described classically by Maxwell's equations:

$$\nabla \times \vec{E}(\vec{r}, t) = -\frac{\partial \vec{B}(\vec{r}, t)}{\partial t} \quad (\text{A.1})$$

$$\nabla \times \vec{H}(\vec{r}, t) = \frac{\partial \vec{D}(\vec{r}, t)}{\partial t} + \vec{J}(\vec{r}, t) \quad (\text{A.2})$$

$$\nabla \cdot \vec{D}(\vec{r}, t) = \rho(\vec{r}, t) \quad (\text{A.3})$$

$$\nabla \cdot \vec{B}(\vec{r}, t) = 0 \quad (\text{A.4})$$

Here, \vec{E} is the electric field and \vec{H} is the magnetic field. The displacement field, \vec{D} , and the magnetic flux, \vec{B} , are related to the electric field, the material polarization, \vec{P} , and the magnetic field via the constitutive relations:

$$\vec{D} = \epsilon_0 \vec{E} + \vec{P} \quad (\text{A.5})$$

$$\vec{B} = \mu_0 \vec{H} \quad (\text{A.6})$$

where ϵ_0 is the permittivity of free space and μ_0 is the permeability of free space. In obtaining equation (A.6), we have assumed a non-magnetic medium.

In a source free region ($\vec{J} = 0$ and $\rho = 0$), the wave equation describing the propagation of the electric field in the medium is obtained using Equations (A.1), (A.2), (A.5), and (A.6):

$$\nabla^2 \vec{E}(\vec{r}, t) - \frac{1}{c^2} \frac{\partial^2 \vec{E}(\vec{r}, t)}{\partial t^2} = \mu_0 \frac{\partial^2 \vec{P}(\vec{r}, t)}{\partial t^2} \quad (\text{A.7})$$

where $c = 1/\sqrt{\mu_0\epsilon_0}$ is the speed of light in a vacuum. In obtaining (A.7), we have assumed that the electric field is divergence-free ($\nabla \cdot \vec{E} = 0$). Transforming Equation A.8 into the frequency domain, we obtain

$$\nabla^2 \tilde{E}(\vec{r}, \omega) + \frac{\omega^2}{c^2} \tilde{E}(\vec{r}, \omega) = \mu_0 \omega^2 \tilde{P}(\vec{r}, \omega), \quad (\text{A.8})$$

where $\tilde{E}(\vec{r}, \omega)$ is related to $\vec{E}(\vec{r}, t)$ via the Fourier transform

$$\tilde{E}(\vec{r}, \omega) = \int_{-\infty}^{\infty} \vec{E}(\vec{r}, t) e^{i\omega t} dt. \quad (\text{A.9})$$

The polarization induced in the semiconductor is related to the electric field via the complex electrical susceptibility tensor, χ . Assuming a that the material response is linearly related to the electric field, we have in the time domain

$$\vec{P}(\vec{r}, t) = \epsilon_0 \int_{-\infty}^{\infty} \hat{\chi}(\vec{r}, t - \tau) \vec{E}(\vec{r}, \tau) d\tau. \quad (\text{A.10})$$

In the frequency domain, we obtain

$$\tilde{P}(\vec{r}, \omega) = \epsilon_0 \chi(\vec{r}, \omega) \tilde{E}(\vec{r}, \omega), \quad (\text{A.11})$$

where $\chi(\vec{r}, \omega)$ is the Fourier transform of $\hat{\chi}(\vec{r}, t)$. The susceptibility tensor may be expressed as a sum of the background susceptibility and the susceptibility arising

from the field interaction with the free carriers in the semiconductor

$$\chi(\vec{r}, \omega) = \chi_b(\vec{r}, \omega) + \chi_{fc}(\star, \vec{r}, \omega). \quad (\text{A.12})$$

The background susceptibility is a function of the material composition of the semiconductor waveguide. It is assumed to be a function of the transverse coordinates, x and y , only.

There are many parameters which may affect the free carrier susceptibility tensor. Examples of these parameters include the density of free carriers in the semiconductor and the energy distribution of these carriers within the conduction and valence bands of the semiconductor. In general, these parameters may vary with time and depend on the intensity of the electric field in the medium. For example, a short optical pulse propagating in a semiconductor may temporarily increase the carrier density in the semiconductor via stimulated absorption. The increased carrier density then recovers to the equilibrium density over time via various recombination processes. In Equation A.12, we indicate the dependence of χ_{fc} on these and other parameters via the \star argument. The explicit functional dependence of χ_{fc} on these parameters is described in more detail in Chapter 2.

Because of the time-dependence of these parameters, some caution must be employed in determining $\chi_{fc}(\star, \vec{r}, \omega)$ from $\hat{\chi}_{fc}(\star, \vec{r}, t)$. We define $\chi_{fc}(\star, \vec{r}, \omega)$ to be the frequency-dependent susceptibility for a specific value of the time-dependent parameters, \star . Thus, it is obtained by taking the Fourier transform with respect to the third argument of $\hat{\chi}_{fc}(\star, \vec{r}, t)$ while keeping the first two arguments constant. The time-dependence of parameters such as the carrier density then leads to a time-dependent susceptibility in the frequency domain. This approach is valid as long as the time-dependent quantities which affect the susceptibility vary slowly in comparison to the duration of the induced polarization response of the medium. In a semiconductor this duration is governed by the free carrier scattering times which lead to dephasing and relaxation of the induced polarization. This typically occurs on a time scale of less than 100 fs. Since the time-dependent parameters such as the carrier density vary

with the optical pulse envelope, the theory developed here accurately describes the propagation of pulses of duration greater than a few hundred femtoseconds.

In a manner similar to [A.1], we express the field traveling in the $+z$ direction in the amplifier as a product of the transverse mode profile, F , and a slowly varying envelope, \tilde{A}

$$\tilde{E}(\vec{r}, \omega) = \frac{\hat{e}}{2} \left\{ F(x, y) \tilde{A}(z, \omega - \omega_0) \exp(i\beta_0 z) + F^*(x, y) \tilde{A}^*(z, -\omega - \omega_0) \exp(-i\beta_0 z) \right\}, \quad (\text{A.13})$$

where \hat{e} is a unit vector expressing the field polarization, and ω_0 is the angular frequency of the optical carrier. In Equation A.13, the field envelope, A , has units of $W^{1/2}$. The propagation constant in the semiconductor, β_0 , is related to ω_0 as $\beta_0 = \bar{n}\omega_0/c$, where \bar{n} is the effective index, to be determined below. We assume that the transverse mode profile is normalized so that

$$\int_{-\infty}^{\infty} \int_{-\infty}^{\infty} |F(x, y)|^2 dx dy = 1. \quad (\text{A.14})$$

Substituting this solution into Equation A.8, we obtain two equations describing the transverse mode profile and the slowly varying envelope

$$\frac{\partial^2 F}{\partial x^2} + \frac{\partial^2 F}{\partial y^2} + \frac{\omega^2}{c^2} \epsilon(\omega) F = \tilde{\beta}^2(\omega) F \quad (\text{A.15})$$

$$2i\beta_0 \frac{\partial \tilde{A}}{\partial z} - \beta_0^2 \tilde{A} = -\tilde{\beta}^2 \tilde{A}, \quad (\text{A.16})$$

where $\epsilon = 1 + \chi_b + \chi_{fc}$.

Equation A.15 can be solved to determine the transverse mode profile, F , and the eigen value $\tilde{\beta}$. This can be done using a perturbational approach [A.2]. We write

$$\epsilon = \epsilon_b + \delta\epsilon \quad (\text{A.17})$$

where $\epsilon_b = 1 + \text{Re} \{ \chi_b \}$ is the background dielectric constant. The background loss and field interaction with the free carriers are treated as a perturbation $\delta\epsilon = i\text{Im} \{ \chi_b \} + \chi_{fc}$.

The zero-order solution is first obtained by solving the eigen equation with only the background dielectric response

$$\frac{\partial^2 F^{(0)}}{\partial x^2} + \frac{\partial^2 F^{(0)}}{\partial x^2} + \frac{\omega^2}{c^2} \epsilon_b(\omega) F^{(0)} = \beta^{(0)2}(\omega) F^{(0)} \quad (\text{A.18})$$

To first order in the perturbation, the eigenvalue $\tilde{\beta}^2(\omega)$ is given by $\tilde{\beta}^2(\omega) \approx \beta^{(0)2}(\omega) + \delta\beta^2$, where

$$\delta\beta^2(\omega) = \frac{\omega^2 \int_{-\infty}^{\infty} \int_{-\infty}^{\infty} \delta\epsilon(x, y, \omega) |F(x, y)|^2 dx dy}{c^2 \int_{-\infty}^{\infty} \int_{-\infty}^{\infty} |F(x, y)|^2 dx dy}. \quad (\text{A.19})$$

Assuming that χ_{fc} is uniform over the dimensions of the waveguide, the perturbation may be written as

$$\delta\beta^2(\omega) = \frac{\omega^2}{c^2} (\Gamma \chi_{fc}(\omega) + i\alpha_{\text{int}}), \quad (\text{A.20})$$

where α_{int} is the internal loss arising from the imaginary part of χ_b and the mode confinement fact, Γ , is defined as

$$\Gamma = \frac{\int_{-d/2}^{d/2} \int_{-w/2}^{w/2} |F(x, y)|^2 dx dy}{\int_{-\infty}^{\infty} \int_{-\infty}^{\infty} |F(x, y)|^2 dx dy} \quad (\text{A.21})$$

and w and d are the transverse dimensions of the waveguide.

Substituting this perturbed eigenvalue into the equation for the slowly varying envelope, we find

$$\frac{\partial \tilde{A}}{\partial z} = i(\beta^{(0)} - \beta_0) \tilde{A} + \frac{i}{2\beta_0} \delta\beta^2(\omega) \tilde{A} \quad (\text{A.22})$$

Next, we expand the zero-order propagation constant as a Taylor series around ω_0

$$\beta^{(0)} = \beta_0 + (\omega - \omega_0)\beta_1 + \frac{1}{2}(\omega - \omega_0)\beta_2 \dots \quad (\text{A.23})$$

Substituting this expression into Equation A.22, taking the inverse Fourier transform, and neglecting second-order and higher derivatives of the envelope, A , we obtain

$$\frac{\partial A}{\partial z} + \frac{1}{v_g} \frac{\partial A}{\partial t} = \frac{i\omega_0 \Gamma}{2\bar{n}c} \chi_{fc}(z, t, \omega_0) A - \frac{1}{2} \alpha_{\text{int}} A. \quad (\text{A.24})$$

Changing the coordinates to a reference frame traveling with the optical field ($t \rightarrow t - z/v_g$, $z \rightarrow z$), we obtain the traveling wave equation for the slowly varying field envelope

$$\frac{\partial A}{\partial z} = \frac{i\omega_0 \Gamma}{2\bar{n}c} \chi_{fc}(\omega_0) A - \frac{1}{2} \alpha_{\text{int}} A. \quad (\text{A.25})$$

We can write A in terms of the photon density S , and the carrier phase ϕ as

$$A = \sqrt{\frac{\hbar\omega_0 w d v_g}{\Gamma}} S \exp(i\phi). \quad (\text{A.26})$$

Substituting this definition into Equation A.25, and equating the real and imaginary parts, we obtain traveling wave equations for the photon density,

$$\frac{\partial S}{\partial z} = (\Gamma g(z, t, \omega_0) - \alpha_{\text{int}}) S \quad (\text{A.27})$$

and the carrier phase,

$$\frac{\partial \phi}{\partial z} = \frac{2\pi}{\lambda} n(z, t, \omega_0), \quad (\text{A.28})$$

where the gain, g , and index, n , are related to the free carrier susceptibility as

$$g = -\frac{\omega_0}{\bar{n}c} \text{Im} \{ \chi_{fc} \} \quad (\text{A.29})$$

and

$$n = \frac{1}{2} \text{Re} \{ \chi_{fc} \}. \quad (\text{A.30})$$

These traveling wave equations are used in Chapters 2 and 3 to describe the propagation of optical fields in a semiconductor optical amplifier.

References

- [A.1] G. P. Agrawal and N. A. Olsson, "Self-phase modulation and spectral broadening of optical pulses in semiconductor laser amplifiers," *IEEE J. Quantum Electron.*, vol. 25, pp. 2297–306, November 1989.
- [A.2] G. P. Agrawal, *Nonlinear Fiber Optics*. Academic Press, 2001.

Appendix B

Chebyshev Approximation for the Reduced Fermi Energy

As discussed in Section 2.6.1, the reduced Fermi energy is calculated as a function of the dimensionless quantity, ν , as

$$\mu(\nu) \approx \begin{cases} \frac{1}{2} \ln \nu + \sqrt{\nu} g_1(t_1(\sqrt{\nu})), & \text{if } 0 < \nu \leq a, \\ g_2(t_2(\nu)), & \text{if } a < \nu \leq b, \\ \frac{1}{\sqrt{\nu_{\max} - \nu}} g_3(t_3(\nu_{\max} - \nu)), & \text{if } b < \nu < \nu_{\max}, \end{cases} \quad (\text{B.1})$$

where $a = 0.4$, $b = 3$ and $\nu_{\max} = 250/9\pi$. The functions $t_i(x)$ are linear transformations from the range of x to the interval $[-1, 1]$. For example, $t_1(x) = 1 + 2x/\sqrt{a}$. The functions $g_i(x)$ are truncated series of Chebyshev polynomials

$$g_i(x) = \frac{1}{2} c_{i,0} T_0(x) + \sum_{n=1}^{N_i-1} c_{i,n} T_n(x) \quad (\text{B.2})$$

The Chebyshev polynomial of degree n , $T_n(x)$, can be expressed compactly as

$$T_n(x) = \cos(n \arccos x) \quad (\text{B.3})$$

k	$c_{1,k}$	$c_{2,k}$	$c_{3,k}$
0	1.33211710437662	2.62638273269644	16.58884403091866
1	0.04950859993362	1.13740738729839	-2.30306759454136
2	0.00227671331467	-0.11394304775945	-0.23038727041104
3	$1.13886219776122 \cdot 10^{-4}$	0.04360572632115	-0.02596376173518
4	$5.95796894907074 \cdot 10^{-6}$	-0.01390575345885	-0.00483346873209
5		0.00513791947224	-0.00148391398007
6		-0.00195535095581	$-6.31081618407591 \cdot 10^{-5}$
7		$7.70990105474104 \cdot 10^{-4}$	$-7.94893421647202 \cdot 10^{-5}$
8		$-3.10803351143896 \cdot 10^{-4}$	
9		$1.27512335632574 \cdot 10^{-4}$	
10		$-5.30300515102362 \cdot 10^{-5}$	
11		$2.22976306377011 \cdot 10^{-5}$	
12		$-9.46041051937036 \cdot 10^{-6}$	
13		$4.04423381614260 \cdot 10^{-6}$	
14		$-1.73997066413688 \cdot 10^{-6}$	
15		$7.52724355353191 \cdot 10^{-7}$	

Table B.1: Coefficients used in Chebyshev expansion for $\mu(\nu)$.

The optimal coefficients in the Chebyshev expansion for $g_i(x)$, $c_{i,k}$ are calculated using an algorithm described in [B.1]. In order to obtain a maximum relative error of 5×10^{-6} we use $N_1 = 5$, $N_2 = 16$, and $N_3 = 8$ terms in the expansions for g_1 , g_2 , and g_3 . These coefficients are listed Table B.1. An algorithm utilizing Clenshaw's recurrence formula is utilized to efficiently calculate the truncated Chebyshev series in Equation B.2 [B.1].

References

- [B.1] W. H. Press, B. P. Flannery, S. A. Teukolsky, and W. T. Vetterling, *Numerical Recipes in C: The Art of Scientific Computing*, ch. 5. Cambridge University Press, 2nd ed., 1993.